Synthesis of stimuli responsive nanoparticles for electrocatalysis

Guillaume Crochet

Sorbonne Université

Ecole doctorale Physique et Chimie des Matériaux (ED 397)

Laboratoire de Chimie de la Matière Condensée de Paris

Synthesis of stimuli responsive nanoparticles for electrocatalysis

Par Guillaume CROCHET

Thèse de doctorat de Physique et Chimie des Matériaux

Dirigée par David Portehault

Présentée et soutenue publiquement le 10 décembre 2021

Devant un jury composé de :

Mme. Dubau Laetitia	Chargée de recherche Grenoble INP-UGA	Rapporteuse
M. Gaudon Manuel	Maître de conférence Université Bordeaux, ICMCB	Rapporteur
Mme. Ménager Christine	Professeure Sorbonne Université, PHENIX	Examinatrice
M. Portehault David	Directeur de recherche CNRS, LCMCP	Directeur de thèse

À ma Madame la Lune, Mémone.

« Moi j'veux pas être au-dessus, je veux être à la hauteur. » Nekfeu

Remerciements

Cette thèse a été réalisée au Laboratoire Chimie de la Matière Condensée de Paris et je tenais à remercier les anciens et nouveaux directeurs Florence Babonneau, Christian Bonhomme et François Ribot de m'avoir accueilli et permis que cette thèse se déroule dans les meilleures conditions possibles.

Je remercie Laetitia Dubau, Manuel Gaudon et Christine Ménager d'avoir accepté d'être membre du jury et de lire et évaluer mes travaux de thèse

J'aimerai tout particulièrement remercier mon Directeur de thèse David Portehault, tout d'abord pour m'avoir donné cette chance de réaliser cette thèse mais aussi pour sa patience incommensurable avec moi. Pour avoir su canaliser mes passages sporadiques de folie scientifique mais aussi m'avoir fait confiance tout au long de cette thèse. Un grand merci d'avoir su être disponible et à l'écoute, que ça ait été pour une question stupide comme une idée éclair, les discussions scientifiques enrichissantes comme frustrantes. Merci pour ces 3 années à travailler à tes côtés se fut un immense et réel plaisir.

Merci aux personnes ayant ajouté leurs pierres à l'édifice de cette thèse, Francisco Gonell, Christel Laberty, Vincent Vivier, Peter Dunne, Bernard Doudin, Sandra Casale, David Montero, Antoine Miche et Goeffrey Cabasson.

Un immense merci à cette formidable équipe de gestionnaires du laboratoire, Hélène pour ton aide et ta patience avec moi mais aussi d'avoir été toujours aussi fan de mes chants de couloir ! Enfin Corinne, malgré peu de commandes merci pour tous ces moments de rires, de gêne, nos discussions et surtout ton soutient. Merci beaucoup.

Merci à Diana pour avoir toujours fait en sorte que nous ne manquions de rien durant ces 3 années.

Je tenais aussi à remercier Sophie Carenco et Florian D'Accriscio sans qui je n'aurai jamais pu écrire ces remerciements, merci de m'avoir fait confiance et d'avoir pu me permettre de réaliser tout ça. Merci aussi à Richard Villanneau et Rania Makrygenni sans qui ce goût pour les nanoparticules n'aurait pas été aussi développé.

Merci à Olivier Durupthy, Laurence Rozes et Corinne Chanéac pour ces discussions et surtout ces rires partagés.

A l'équipe Nano, anciens comme nouveau merci à toutes et tous de l'accompagnement, des questions et l'intérêt personnelle comme scientifique que vous avez su me porter.

Aux anciens, Simon, Lionel, Nadège, Xavier, Francisco, Aude et Kim, merci pour la rapide formation à l'arrivée, tant scientifique qu'alcoolique.

Aux doctorants du « carreau », merci pour ces 3 années riche en émotions, en rire et en groupement –OH.

Au bureau Corgi (oui oui je l'ai dit) merci, Elora, Maxime et mon Tac sans vous je n'ose même pas imaginer comment la vie du quotidien aurait été, et on aura formé une sacrée équipe, bravo à nous (Faudra tout de même penser à vider les cadeaux, les jeux de fléchettes, la piste de course à escargot, les nerfs et j'en passe avant de partir hein !).

Bon, aux Isl…… non d'abord à mon Alex-Tac, merci amigo d'avoir été mon acoolyte, merci pour ta personnalité, tes qualités comme tes défauts qui font ton charme et surtout merci pour tous ces moments passés, tous ces beaux souvenirs de Tic & Tac. Mais ce n'est pas un au revoir, j'ai entendu dire que tu avais des cailloux à bouger ? Ah et j'allais oublier, merci pour tes velours côtelés qui m'auront toujours fait me sentir jeune !

A ma petite Tallinn Vilnius Riga, merci d'avoir toujours été là dans les bons comme les mauvais moments. Je m'excuse pour les larmes aux tarots mais tu faisais vraiment n'imp ! Merci aussi d'avoir déménagé en face de chez moi, la lessive est devenue plus facile et moins chère à faire ! Plus sérieusement, je ne ferai pas un monologue de peur que tu pleures mais tu sauras lire entre les lignes. Merci Tata.

Mon petit T-Baõ, à croire qu'on est destiné à se côtoyer pour la vie, ça me va, ton tact légendaire et tes conventions sociales sans pareilles me feront toujours passer de bon moments avec toi. Merci d'avoir été une oreille à l'écoute pour tout, mais surtout l'électrochimie quand clairement tu avais autre chose à faire. Enfin merci pour ta passion Mylène non partagée, il faut bien de tout pour faire un monde !

A Gatou, merci pour ta bonne humeur, tes excès de joies que j'aurai réussi à finalement te faire contenir. Merci pour toutes nos discussions débiles comme plus sérieuses, je tenais aussi à me remercier pour tes choix en matière de cœur parce qu'après tout le choix est plus que bon ! Pour éviter les effusions d'émotion incontrôlable à la lecture de tes remerciements, je te dis donc à très vite en Charente ma Gatou ! FunFact, il paraît que tu as aussi des cailloux à bouger ?

A mon Rafiki, merci d'avoir toujours voulu me faire partager tes passions bien que je reste convaincu que le festival de Cannes c'est non. Merci aussi d'avoir bien voulu partager les miennes, et le Set 6 s'annonce passionnant. Merci d'avoir toujours été là, de parfois t'être forcé pour moi sans néanmoins te débiner. Merci aussi pour la quantité de choses probablement inutiles mais culturellement intéressante que tu auras su m'apprendre sans t'en apercevoir !

Last but not least as they say, mon Francesco, j'aimerai te remercier pour nos discussion houleuses ou non partagées, fin' tu vois quoi. Fin'toutes nos bonnes blagues ou heureusement que tu étais là autrement la solitude aurait été grande, fin' tu vois quoi. Merci pour toutes ces expos que quelque part j'aurai aimé faire mais n'ai jamais su trouver le temps pour. Merci d'être comme la mer, parfois déchainé parfois calme, parfois dur et quelques fois douce.

Enfin merci à Vincent, Anaïs, Swann, Marguerite, Perrine, Lalou, Clement, Lau et Sam de m'avoir appris la vulgarisation scientifique.

A ma famille, merci d'avoir toujours été présent et aimant.

A ma douce et tendre Louve, merci d'avoir su me botter les fesses lorsque tu le pensais nécessaire, merci de ta présence, ton aide et tes conseils. Milles merci pour tout et plus que tout je dirai même. L'avenir nous appartient. I.W.Y.

Merci à vous tous.

General introduction……13

Chapter I: Magnetic properties and electrocatalytic properties of manganese perovskites

I. Introduction……19

II. Magnetic properties……20

1. Doping ratio 21
2. Doping cation's size..... 22
3. A-site disorder..... 23
4. Nanoscale effect on magnetotransport: the case of $La_{0.7}Sr_{0.3}MnO_3$ nanocrystals . 24
5. Conclusion on magnetism in perovskite 28

III. Manganase perovskite electrocatalysis……28

1. Oxygen reduction reaction (ORR)..... 29
2. Influencing factors..... 31
3. External stimuli for enhance electrocatalysis 34
4. Conclusion on electrocatalysis on perovskites…… 39

IV. The exsolution process……42

1. Introduction..... 42
2. Mechanistic approach 46
3. Alternative methods to trigger exsolution 49
4. Conclusion on exsolution in perovskite..... 56

V. Conclusion.....56

References.....58

Chapter II: Synthesis of quaternary phase manganite perovskite $La_{0.33}Pr_{0.33}Ca_{0.33}MnO_3$ using molten salt

I. Introduction.....79

II. Original synthesis.....79

1. Influence of the reaction temperature 81

2. Influence of the reaction time 82
3. Influence of the reagent ratios 84
4. Influence of the reagents concentration 86
5. Influence of the heating process: microwave heating 93
III. Conclusion 98
References 99

Chapter III: $La_{0.7}Sr_{0.3}MnO_3$ nanoparticles, towards interplay between magnetic fields and the oxygen reduction reaction electrocatalysis

I. Introduction 103
II. Synthesis of $La_{0.7}Sr_{0.3}MnO_3$ nanoparticles 104
III. Electrochemical behavior of LSMO in a rotating disk electrode (RDE) configuration 106
IV. Cyclic voltammetry studies of LSMO using a microelectrode (ME) 109
1. ORR activity in ME configuration 110
2. Purity of the electrolyte 110
3. Impact of the magnetic field 111
4. Impact of the magnetic field on the ORR 112
5. Concentration of the electrolyte 116
IV. Conclusion 117
References 119

Chapter IV: The exsolution process, towards enhanced new catalysts

I. Introduction 123
II. $SrTiO_3$ synthesis 123
III. $SrTi_{1-x}O_3$ doped with platinum 124
1. Exsolution assisted by transmission electron microscopy 127
2. Exsolution under reductant atmosphere 131
3. Exsolution of other doping metals 135

IV. Synthesis of $La_{0.7}Sr_{0.3}MnO_3$ doped for the exsolution process.....138

V. Conclusion.....141

References.....143

General conclusion.....147

Materials and methods.....151

Appendix.....169

General introduction

Due to the emerging crisis arising from the depletion of fossil fuel resources, the need of new energy sources, energy storage and conversion systems has increased. Fuel cells are one of the trending energy storage devices. However, the performances of these devices are restrained by the sluggish kinetics of the chemical reactions involved, especially the oxygen reduction reaction at the cathode.[1] The need to synthetize sustainable electrocatalysts has then grown. Perovskites are a family of materials englobing a large number of compositions, which are exempt of precious metals.[2] From this compositional diversity, numerous properties are found in the perovskite family. Especially, some perovskites have emerged as efficient electrocatalyst for the oxygen reduction reaction, possibly competitive *versus* current noble metal electrocatalysts used, like e.g. Pt/C, Pd.

In this context of search for new electrocatalysts, our primary goal was to develop oxygen reduction reaction electrocatalysts among perovskite materials. Several pathways were then identified. The first one was the search for new electrocatalyst compositions among perovskites. The second route was to address already known electrocatalysts and to tune their intrinsic electrocatalytic properties by adjusting their compositions, or to increase the number of active sites per mass unit. Finally, a third way was considered, relying on the use of external stimuli to enhance the electrocatalytic properties of the materials. This last pathway has emerged recently from several groups, which were mostly interested in the effect of magnetic fields on the electrolyte or on the gaseous species involved during electrocatalysis.[3–5] The approach that we selected and that is presented in this thesis combines the three aforementioned pathways in order to develop new electrocatalysts and new electrocatalytic set-ups.

We particularly aimed at manganese perovskites for their numerous properties, which encompass electrochemical and magnetic properties, already widely reported in the literature.[2-6] In order to develop new nanoscaled catalysts, we employed molten salts syntheses, as an emerging synthesis route towards nanomaterials design.[11,12]

We then sought to investigate the interplay that may reside at the crossing road between electrocatalysis and magnetic properties, in order to trigger enhancement of electrocatalytic properties with external magnetic fields.

In parallel, we have capitalized on the ability of molten salts synthesis to deliver a wide range of perovskite nanomaterials, in order to explore another way to modify the intrinsic electrochemical properties of perovskites with external stimuli. Indeed, reducing conditions can be used to exsolute reduced metal particles from metal ions doping perovskite matrices.[13,14] This process, already reported for bulk perovskite oxides, has never been reported on nanoscaled perovskites. Molten salts synthesis provides access to a wide range of possible

cationic substitutions in perovskite nano-objects, and is then an ideal platform to trigger exsolution of electrocatalytic nanoparticles at the surface of perovskite nano-objects, to assess the mechanisms of this process and how it could improve electrocatalytic properties.

This manuscript then resides at the crossroad between the development of synthesis strategies and the design of nanomaterials interacting with their environment and exhibiting stimuli-dependent electrocatalytic properties. We structured this work through 4 chapters:

The first chapter is a bibliographic survey of the magnetic and electrocatalytic properties of manganese perovskites followed by an investigation of the current approaches using external fields for electrocatalysis purposes. This chapter underlines the complexity of perovskite oxides regarding their intertwined properties. The applications and limitations of electrocatalysis under external stimuli are presented. This chapter enables identifying the most promising tracks of research to be explored. It then sets the foundations of the approach we address in the following chapters.

The second chapter of the manuscript is dedicated to the synthesis of nanoparticles of $La_{0.33}Pr_{0.33}Ca_{0.33}MnO_3$, which to our knowledge are not reported in the literature. This perovskite was targeted because it is reported to exhibit interesting electronic phase separation properties in the bulk state,[9,10] which might exacerbate the impact of magnetic fields on the electrocatalytic properties of nano-objects.

The third chapter is dedicated to $La_{0.7}Sr_{0.3}MO_3$ nanoparticles: their synthesis at the nanoscale, their magnetic and electrocatalytic properties. This nanomaterial with already well documented magnetic[15,16] and oxygen reduction reaction electrocatalytic properties[17,18] offers an ideal platform to study the interplay between electrocatalytic properties and magnetism.

The fourth chapter addresses the exsolution process in nanoscaled perovskites, from the doping of perovskite nanocrystals by molten salts synthesis, to the exsolution itself by using various stimuli.

Finally, we draw conclusion from this work and identify future perspectives.

(1) Nørskov, J. K.; Rossmeisl, J.; Logadottir, A.; Lindqvist, L.; Kitchin, J. R.; Bligaard, T.; Jónsson, H. Origin of the Overpotential for Oxygen Reduction at a Fuel-Cell Cathode. *J. Phys. Chem. B* **2004**, *108* (46), 17886–17892. https://doi.org/10.1021/jp047349j.

(2) Hong, W. T.; Risch, M.; Stoerzinger, K. A.; Grimaud, A.; Suntivich, J.; Shao-Horn, Y. Toward the Rational Design of Non-Precious Transition Metal Oxides for Oxygen Electrocatalysis. *Energy Environ. Sci.* **2015**, *8* (5), 1404–1427. https://doi.org/10.1039/c4ee03869j.

(3) Wang, M.; Wang, Z.; Guo, Z. Understanding of the Intensified Effect of Super Gravity on Hydrogen Evolution Reaction. *Int. J. Hydrogen Energy* **2009**, *34* (13), 5311–5317. https://doi.org/10.1016/j.ijhydene.2009.05.043.

(4) Ragsdale, S. R.; Grant, K. M.; White, H. S. Electrochemically Generated Magnetic Forces. Enhanced Transport of a Paramagnetic Redox Species in Large, Nonuniform Magnetic Fields. *J. Am. Chem. Soc.* **1998**, *120* (51), 13461–13468. https://doi.org/10.1021/ja982540q.

(5) Chaure, N. B.; Rhen, F. M. F.; Hilton, J.; Coey, J. M. D. Design and Application of a Magnetic Field Gradient Electrode. *Electrochem. commun.* **2007**, *9* (1), 155–158. https://doi.org/10.1016/j.elecom.2006.08.059.

(6) Xu, X.; Wang, W.; Zhou, W.; Shao, Z. Recent Advances in Novel Nanostructuring Methods of Perovskite Electrocatalysts for Energy-Related Applications. *Small Methods* **2018**, *2* (7), 1–35. https://doi.org/10.1002/smtd.201800071.

(7) Rao, C. N. R. Colossal Magnetoresistance in Rare Earth Manganates. *Mater. Today* **1998**, *1* (3), 9–13. https://doi.org/10.1016/s1369-7021(98)80004-7.

(8) Loktev, V. M.; Pogorelov, Y. G. Peculiar Physical Properties and the Colossal Magnetoresistance of Manganites (Review). *Low Temp. Phys.* **2000**, *26* (3), 171–193. https://doi.org/10.1063/1.593890.

(9) Shao, J.; Liu, H.; Zhang, K.; Yu, Y.; Yu, W.; Lin, H.; Niu, J.; Du, K.; Kou, Y.; Wei, W.; Lan, F.; Zhu, Y.; Wang, W.; Xiao, J.; Yin, L.; Plummer, E. W.; Shen, J. Emerging Single-Phase State in Small Manganite Nanodisks. *Proc. Natl. Acad. Sci.* **2016**, *113* (33), 9228–9231. https://doi.org/10.1073/pnas.1609656113.

(10) Zhu, Y.; Du, K.; Niu, J.; Lin, L.; Wei, W.; Liu, H.; Lin, H.; Zhang, K.; Yang, T.; Kou, Y.; Shao, J.; Gao, X.; Xu, X.; Wu, X.; Dong, S.; Yin, L.; Shen, J. Chemical Ordering Suppresses Large-Scale Electronic Phase Separation in Doped Manganites. *Nat. Commun.* **2016**, *7*, 1–6. https://doi.org/10.1038/ncomms11260.

(11) Portehault, D.; Delacroix, S.; Gouget, G.; Grosjean, R.; Chan-Chang, T. H. C. Beyond the Compositional Threshold of Nanoparticle-Based Materials. *Acc. Chem. Res.* **2018**, *51* (4), 930–939. https://doi.org/10.1021/acs.accounts.7b00429.

(12) Gupta, S. K.; Mao, Y. Recent Developments on Molten Salt Synthesis of Inorganic Nanomaterials: A Review. *J. Phys. Chem. C* **2021**, *125* (12), 6508–6533. https://doi.org/10.1021/acs.jpcc.0c10981.

(13) Mizuki, J.; Akao, T.; Tanaka, H.; Uenishi, M.; Kimura, M.; Okamoto, T.; Hamadak, N. Self-Regeneration of a Pd-Perovskite Catalyst for Automotive Emissions Control. *Nature* **2002**, *418* (x), 12–15. https://doi.org/10.1038/nature00875.1.

(14) Neagu, D.; Oh, T. S.; Miller, D. N.; Ménard, H.; Bukhari, S. M.; Gamble, S. R.; Gorte, R. J.; Vohs, J. M.; Irvine, J. T. S. Nano-Socketed Nickel Particles with Enhanced Coking Resistance Grown in Situ by Redox Exsolution. *Nat. Commun.* **2015**, *6*. https://doi.org/10.1038/ncomms9120.

(15) Thi N'Goc, H. Le; Mouafo, L. D. N.; Etrillard, C.; Torres-Pardo, A.; Dayen, J. F.; Rano, S.; Rousse, G.; Laberty-Robert, C.; Calbet, J. G.; Drillon, M.; Sanchez, C.; Doudin, B.; Portehault, D. Surface-Driven Magnetotransport in Perovskite Nanocrystals. *Adv. Mater.* **2017**, *29* (9), 1–9. https://doi.org/10.1002/adma.201604745.

(16) Rostamnejadi, A.; Venkatesan, M.; Salamati, H.; Ackland, K.; Gholizadeh, H.; Kameli, P.; Coey, J. M. D. Magnetic Properties, Exchange Bias, and Memory Effects in Core-Shell Superparamagnetic Nanoparticles of La0.67Sr0.33MnO3. *J. Appl. Phys.* **2017**, *121* (17), 0–7. https://doi.org/10.1063/1.4982893.

(17) Suntivich, J.; Gasteiger, H. A.; Yabuuchi, N.; Nakanishi, H.; Goodenough, J. B.; Shao-Horn, Y. Design Principles for Oxygen-Reduction Activity on Perovskite Oxide Catalysts for Fuel Cells and Metal-Air Batteries. *Nat. Chem.* **2011**, *3* (7), 546–550. https://doi.org/10.1038/nchem.1069.

(18) Gonell, F.; Sánchez-Sánchez, C. M.; Vivier, V.; Méthivier, C.; Laberty-Robert, C.; Portehault, D. Structure-Activity Relationship in Manganese Perovskite Oxide Nanocrystals from Molten Salts for Efficient Oxygen Reduction Reaction Electrocatalysis. *Chem. Mater.* **2020**, *32* (10), 4241–4247. https://doi.org/10.1021/acs.chemmater.0c00681.

Chapter I:

Magnetic properties and electrocatalytic properties of manganese perovskites

I. Introduction

The term perovskite originally refers to a mineral calcium titanium oxide, $CaTiO_3$, which was discovered in 1839 by Gustav Rose and later named after Russian mineralogist Lev Perovski. It then ended up englobing all compounds with the composition ABX_3, where B is a transition metal and X is an anion. The perovskite family encompasses two groups, the perovskite oxides and the perovskite halides. In the context of the depletion of fossil fuel resources, the need to find energy storage, conversion devices and energy sources, has drawn attention in the scientific community towards the perovskite family. Halide perovskite have found a recent renewal of interest for their use in solar cells. Concerning the oxide perovskite family, they have been studied for decades for their magnetic properties but more recently their electrocatalytic properties have been deeply investigated and shown promising results. As electrode material, perovskite oxides are very interesting due to their thermal stability required in solid oxide fuel cells (SOFC) but also to their ability to sustain deformation (i.e. thermal expansion in SOFC). Moreover, some perovskites are composed of cheap abundant elements, which is a major advantage with the current awareness that resources in precious metals are limited.

In this chapter, the basics for understanding the magnetic properties of manganese perovskites are shown, especially in relation with the colossal magnetoresistance (CMR) and electronic phase separation (EPS). We describe how these properties arise and are modified by doping with divalent A' cations in the A-site of the perovskite structure. We also explain how these properties are intertwined with manganese perovskites electronic conductivity and can be stimulated by external stimuli with the case study of $La_{0.7}Sr_{0.3}MnO_3$ (LSMO). Besides their magnetic properties, manganese perovskites are promising electrocatalysts for the oxygen reduction reaction involved in fuel cells and metal-air batteries. We thus in a second part describe the different mechanisms involved in this reaction. Since the electronic transport in manganese perovskites is influenced by their magnetic properties the coupling of electrocatalysis under external stimuli could be of great interest. Therefore, we present in a third part how electrocatalytic properties can be influenced by external stimuli. Finally, a fourth part is allocated to a concept discovered on bulk perovskites, the exsolution. This process uses external reducing conditions to trigger a phase separation in perovskites. Like in the properties derived from magnetic fields mentioned in the previous parts, exsolution relies on the response of a material to its environment. We will discuss it in this context.

II. Magnetic properties

Bulk manganese perovskites composed of mixed-valence $Mn^{3+/4+}$ exhibit numerous and complex phenomena such as colossal magnetoresistance (CMR),[1–5] electronic phase separation (EPS),[6–9] and metal-insulator (M-I) transition.[10,11] These effects have been also found at the nanoscale, and thus brought a renewed interest for the scientific community. Manganate perovskites such as $La_{2/3}Sr_{1/3}MnO_3$ or $La_{1/3}Pr_{1/3}Ca_{1/3}MnO_3$[1,6,9,12,13] possess such magnetic properties that of course depend on the application of magnetic fields. In this part, we will focus principally on two of these magnetic properties, the colossal magnetoresistance (CMR), and later on briefly, the electronic phase separation (EPS).

The colossal magnetoresistance effect has been discovered in the 1950s by Van Santen and Jonker.[14] It consists in a change of resistance of several orders of magnitude of the material due to the modification of the magnetic alignment of neighbor Mn cations[15] under the influence of a magnetic field. The authors discovered the CMR when experimenting with changes in the chemical composition of manganese perovskites. By replacing A^{3+} cations with alkaline earth elements (A=Ca^{2+}, Sr^{2+} or Ba^{2+}) they observed a change of the magnetic properties of the perovskites, from paramagnetic to ferromagnetic under Curie temperatures.[1,14] The ferromagnetic properties arise from the formation of $Mn^{3+/4+}$ mixed-valences in these perovskites. The chemical composition has thus an important impact on manganates magnetic properties and will be developed in the following part. In this section, we will summarize the different factors involved in the appearance of CMR in manganese perovskites.

Perovskites of composition $A_{1-x}A'_xMnO_3$ where A is a rare earth metal, A' an alkaline earth elements present a distorted structure due to the Jahn Teller effect of Mn^{3+}.[16] Introducing divalent A' cations directly affect the electronic state occupancy by creating Mn^{4+} cations. Moreover, the ionic size mismatch in the A-site modulates the Mn-O-Mn bond angle.[8] It has been found that to obtain the CMR effect, these Mn-O-Mn chains need to be linear, with an angle between Mn^{3+}, O^{2-} and Mn^{4+} of 180°. This yields an overlapping of the $3d_{Mn}$ and $2p_O$ orbitals, allowing the e_g electrons from Mn^{3+} to be delocalized, thus resulting in the ferromagnetic interaction.[17–19] Several factors are involved in the apparition of magnetic order and have an influence on the Curie temperature of the perovskites, i.e the doping ratio, the doping cation size, and the A-site disorder within the lattice. Noteworthy the same parameters, especially size and concentration of the divalent cations, impact the strength of the CMR.

1. Doping ratio

The original theory explaining this CMR effect and the coupled ferromagnetism in manganites was based on the double-exchange interaction conceptualized by Zener[3]. The Mn cations in the perovskites present three different interactions, Mn^{3+}-Mn^{3+}, Mn^{3+}-Mn^{4+}, Mn^{4+}-Mn^{4+}. Let's take $LaMnO_3$ and $La_{1-x}Sr_xMnO_3$ and their Curie temperatures as examples to understand the effect of these interactions on the magnetic properties of manganite perovskites. The Mn^{3+}-Mn^{3+} interaction present in $LaMnO_3$ is weak, thus resulting in an insulating behavior. Moreover, the Curie temperature is impacted by this single Mn^{3+}-Mn^{3+} interaction and is below room temperature. Doping with A' divalent cations results in the two other interactions involving the Mn^{3+}-Mn^{4+}, so-called strong positive interaction, which leads to a strong increase of the Curie temperature and ferromagnetic properties above x>0.08. Finally, the Mn^{4+}-Mn^{4+}, so-called negative interaction, occurs for A' doping rates above x>0.4, resulting in a decrease in the Curie temperature.[14] The phase diagram in **Figure 1** illustrates the importance of the chemical composition for obtaining ferromagnetism in the $La_{1-x}Sr_xMnO_3$ perovskite family.[20]

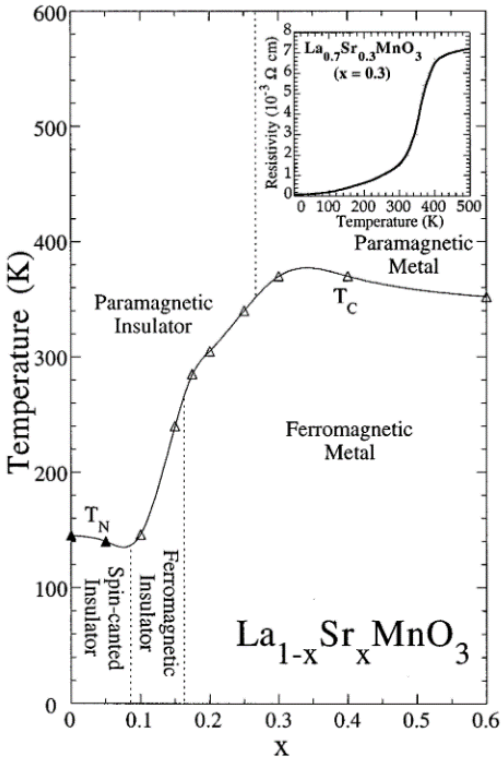

Figure 1. Electronic and magnetic phase diagram of $La_{1-x}Sr_xMnO_3$.[20] Inset shows the resistivity of the x=0.3 crystal used in the present study from Urushibara *et al*.[10]

2. Doping cation's size

However, the simplicity of the Zener model does not grasp the whole complexity of the manganese perovskite magnetic properties, for example the difference of Curie temperatures for different A' cations. Indeed, A^{2+} cations size is also of importance to stabilize the lattice. This is reflected by the Goldshmidt tolerance factor f_{gt}, which helps predicting the stability of the perovskite structure: $f_{gt} = (r_A + r_o)/\sqrt{2}(r_{Mn} + r_O)$ where r_A, r_O and r_{Mn} are the average radii of the A-site cations, oxygen and manganese respectively. A Goldschmidt factor f_{gt} = 1 corresponds to the most stable state the perovskite can obtain, with an Mn-O-Mn bond angle θ=180°, which as mentioned above is optimal for electron hopping from Mn^{3+} to Mn^{4+}.[21] The A-site cations size has then an effect on the magnetic[22] and electrocatalytic properties.[23] At constant doping ratio, the Curie temperature and thus the M-I transition temperature increase with the mean A-site cation radius ($<r_A>$) values.[24,25] For example, $La_{0.75}Sr_{0.25}MnO_3$ has a Curie temperature of 348 K, but by replacing some Sr^{2+} by Ca^{2+} in $La_{0.75}Sr_{0.25-y}Ca_yMnO_3$ the Curie temperature decreases down to 283 K (y=0.125) ($r_{Sr} > r_{Ca}$).[26]

Figure 2 sums up the effect of $<r_A>$ at a constant doping value x = 0.3 on the Curie temperature (T_c) for manganese perovskites. The f_{gt} being below the perfect size match value of 1, the Mn-O-Mn bond has an angle θ<180° due to tilting of the MnO_6 octahedra. This tilting compensates for the space provoked by the too small A^{2+} cations. Thus, the more space created by the doping cations sizes, the more the octahedra tilt, leading to a decrease of the Mn-O-Mn bond angle θ and of T_c. By increasing the f_{gt} and thus the average radius $<r_A>$, T_c increases up to a maximum for $La_{0.7}Sr_{0.3}MnO_3$ (LSMO). However, for f_{gt} above 0.93, the Curie temperature decreases with the average radius increasing. This is most likely due to a transition from the orthorhombic to a trigonal structure, or to a too large size mismatch between A and A' cations.[27]

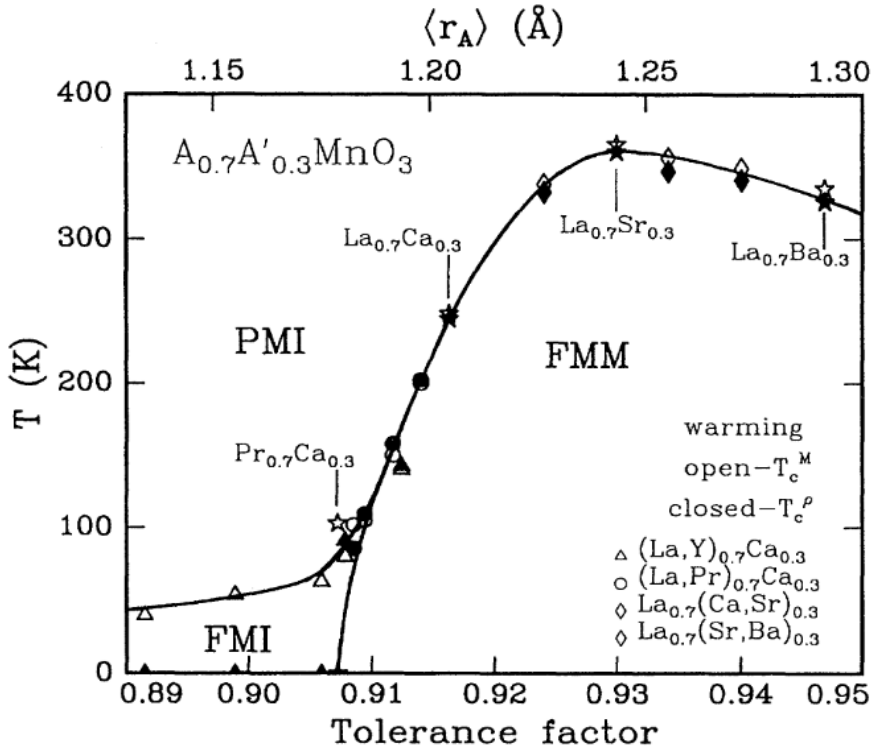

Figure 2. Phase diagram of temperature vs tolerance factor for the system $A_{0.7}A'_{0.3}MnO_3$, where A is a trivalent rare earth ion and A' is a divalent alkali earth cation. Open symbols denote T_c^M measured at 100 Oe. Closed symbols denote T_c^p.[24]

3. A-site disorder

Another important factor involved in the overall magnetic properties of manganese perovskites is the A-site disorder induced by the doping of divalent A' cations. The randomness of the doping leads to the formation of different phases inside the material in the case of LSMO. This induced disorder breaks the symmetry at the surface of the material, which disturbs the double exchange interaction and leads to the formation of an insulating "dead magnetic layer".[28] More generally, the coexistence of several magnetic domains in bulk perovskites is also called electronic phase separation (EPS). This phenomenon has been deeply investigated[6,13,29,30] and its length scale was found to range from few tens of nanometers up to microns in some cases. Zhu *et al.*[8] have investigated the effect of dopant ordering onto the EPS. The authors focused on $(La_{1-y}Pr_y)_{1-x}Ca_xMnO_3$ (LPCMO), which presents one of the largest EPS length scales. They synthesized an ordered LPCMO (O-LPCMO) by growing alternatively unit cells of $La_{0.625}Ca_{0.375}MnO_3$ (LCMO) and of $Pr_{0.625}Ca_{0.375}MnO_3$ (PCMO). Then they compared the EPS domain size with a randomly doped LPCMO (R-LPCMO) with the same nominal composition ($La_{0.44}Pr_{0.22}Ca_{0.33}MnO_3$), synthesized by conventional methods. Magnetic force microscopy

(MFM) (**Figure 3**) showed that ordering LPCMO drastically decreases the EPS scale. However, the ferromagnetic metallic (FMM) volume fraction is up to three-time larger in O-LPCMO than in R-LPCMO despite the smaller sizes of the domains.

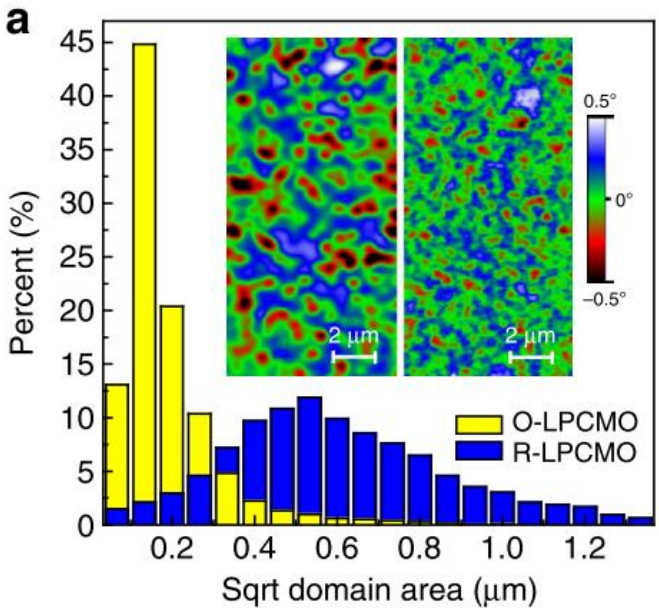

Figure 3. Ferromagnetic metallic (FMM) domain size distribution of O-LPCMO (yellow) and R-LPCMO (blue). The domain size was analyzed from five MFM images for both samples at each temperature. The scanning region is 20 x 20 µm for each image. Insets show MFM images (7 x 14 µm) of R-LPCMO at 140 K and O-LPCMO at 220 K under 1 T field.

The random distribution of the divalent A-site cations inside manganese perovskites can therefore be considered as one of the major parameters influencing the magnetic properties of manganese perovskites, alongside the doping ratio and the size of the doping cations.

4. Nanoscale effect on magnetotransport: the case of $La_{0.7}Sr_{0.3}MnO_3$ nanocrystals

4.1 Magnetic properties of LSMO

The magnetic behavior of LSMO nanocrystals have been reported by Thi N'Goc *et al.*[15] Magnetoresistance curves (**Figure 4**) show that under an applied magnetic field, the resistance of LSMO nanoparticles decreased by one order of magnitude at 7 T (**Figure 4**a). This phenomenon is a magnetoresistance effect (MR). The origin of this decrease of the electrical resistance has been searched for. By normalizing the magnetoconductance from **Figure 4**a and **Figure 4**b as a function of the sample magnetic moment the identification of two MR responses

were observed (**Figure 4**d). One low-field magnetoresistance (LFMR) response ascribed to the alignment of the core moments and a second response at higher field from a paramagnetic-like shell. The LFMR response exhibits few to no change under magnetic field whereas the high-field magnetoresistance (HFMR) response of the shell of LSMO showed a large increase of the conductivity. Hence, the change in electrical resistivity was ascribed to change of the shell from a paramagnetic to a ferromagnetic-like behavior. This magnetoresistance effect is explained by the magnetic alignment under magnetic field of the paramagnetic component. Therefore, under magnetic field, the material is approaching a fully ferromagnetic state. The presence of two distinct magnetic responses suggested the presence of a core-shell magnetic structure of the LSMO nanoparticles.[31] Such peculiar response of the surface has been reported for LSMO thin films possessing the core shell model mentioned above. The surface has been designated as the "dead magnetic layer"[28] or surface antiferromagnetic/spin glass-like phases.[32] The origin of such a different magnetic response of the surface has been investigated by analyzing of the surface of the LSMO nanocrystals.

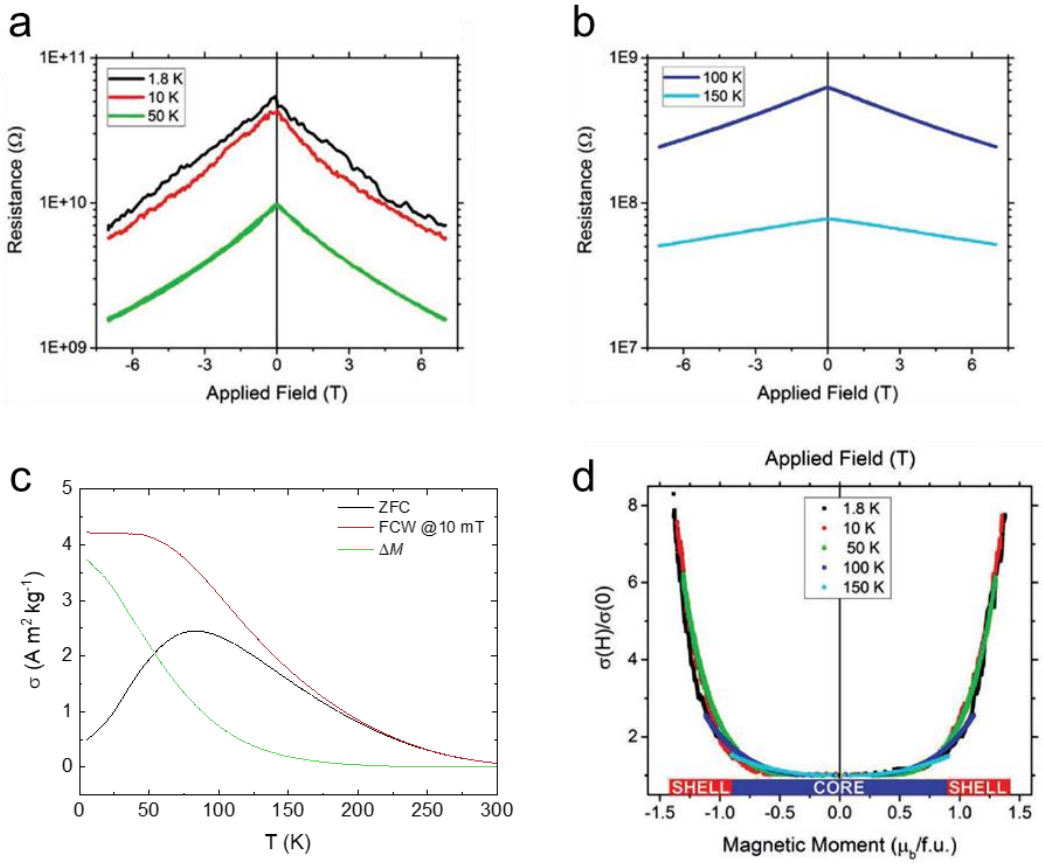

Figure 4. Electrical properties of LSMO nanoparticles. (a-b) Magnetoresistance curves at several temperatures for an applied bias of 2 V. (c) magnetoconductance (d) Normalized magnetoconductance (from a and b) as a function of the sample magnetic moment shown in (a), with bottom colored areas as a reminder of the dominant magnetic nanoparticles component contributing to the moment (blue: ferromagnetic core, red: paramagnetic shell).[15]

4.2. LSMO surface investigation

Thi N'Goc *et al.*[15] investigated by STEM-HAADF, STEM-EDS and STEM-EELS. The structural and compositional characteristics of the aforementioned paramagnetic LSMO shell. They showed the presence of the crystal structure up to the outer surface layer of the cubes (**Figure 5**a), thus indicating that the 2 magnetic phases mentioned above did not originate from surface amorphization. EELS measurements (**Figure 5**b) from the surface of the cube to the core showed an Mn average charge value of $+3.3 \pm 0.1$, except for the outer two unit cells closer to the surface where manganese oxidation state was found to be of $+2.8 \pm 0.1$. These 2 unit cells with a different oxidation state were ascribed to a 0.8 nm thick layer homogeneous over the particle. The origin of such differences in the Mn oxidation state was searched for. The Sr:La ratio was measured by EELS and EDS (**Figure 5**c) across the nanoparticle. The results were in agreement with ICP-OES measurements of the nominal composition. Hence the difference in oxidation state of the manganese at the surface could not be related to the segregation of Sr as observed in the literature.[33] The oxygen content was analyzed as a possible cause of the lower manganese oxidation state of the surface. **Figure 5**d shows that the 2 unit cells possessing lower oxidation state manganese also present a slightly higher Mn:O ratio, hence a decrease in the oxidation state of manganese can only be attributed to an increase in oxygen vacancies at the surface of the particles.

Thi N'Goc *et al.*[15] showed that a layer in average 1 nm thick at the surface of LSMO nanocubes presented higher content in oxygen vacancies than the rest of the particles. This resulted in a decrease in the Mn oxidation state contained in that layer. The magnetic properties of the particles being directly linked to the manganese oxidation state, this 1 nm-thick layer led to the formation of a paramagnetic-like shell for LSMO nanocubes.

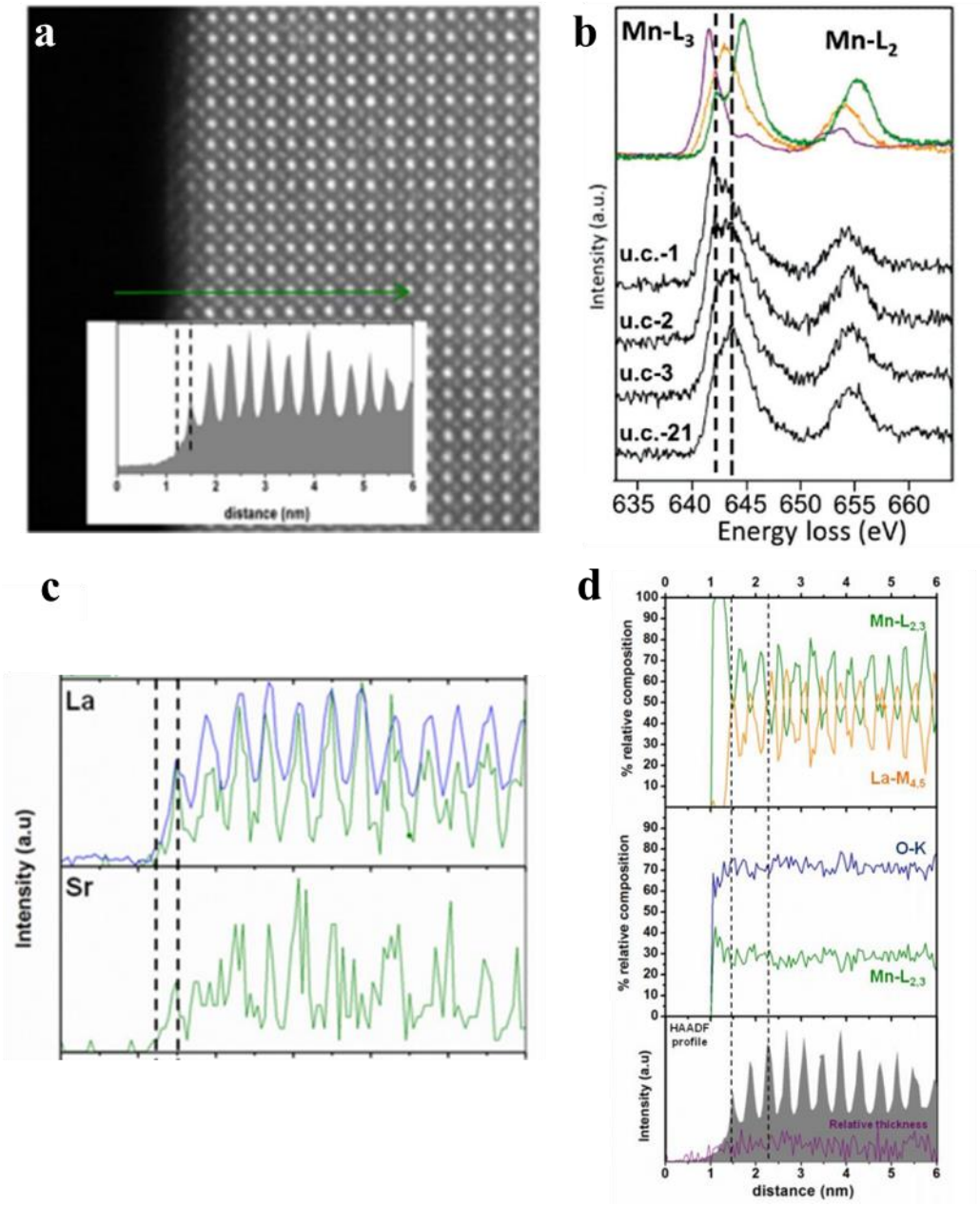

Figure 5. Electron microscopy study of LSMO nanocrystals. STEM analysis of the particles edges. (a) STEM-HAADF image of the edge of a nanocube where high energy resolution EELS spectra have been recorded along a scan line (green line). Inset shows the HAADF signal recorded during the simultaneous acquisition of EELS and EDS line spectra. (b) EELS spectra of selected unit cells (black) and references of Mn^{2+} (purple), Mn^{3+} (orange), and Mn^{4+} (green) oxidation state (c) Signal profiles of the different elements obtained from EDS (green) and EELS (blue) signal and the black dashes lines are included to better identify the first two unit cells. (d) La:Mn and Mn:O relative compositions (%) obtained from EELS signals. The HAADF signal and the black dashed lines are included to better identify the first Mn-O and La/Sr-O planes, as well as the two first unit cells in the STEM-HAADF image.[15]

5. Conclusion on magnetism in perovskite

We have shown in this part how several parameters are critical for obtaining and tuning the magnetic properties of manganese perovskites. The first one, doping ratio, has an impact on the core behavior of the material explained by the Zener double exchange model. It also allows to specifically target a chemical composition to obtain precise magnetic properties. Secondly, we have discussed the size of the divalent A-site cation A', which influences directly the stability of the lattice through the Goldschmidt factor (f_{gt}). This factor translates the ease for the electrons hopping in the Mn-O-Mn bond when approaching the perfect match value ($f_{gt} = 1$). We also underlined the wide changes of *Tc* in manganese perovskites induced by the average radius of the cations on the A site. Finally, the effect of the A-site disorder on the electronic phase separation is such that by ordering the system, the EPS length scale decreases but the volume fraction of ferromagnetic domains increases. One can see that these parameters are entangled and that a small change in one of them will ineluctably result in changes for the others.

III. Manganese perovskite electrocatalysis

Besides the interesting magnetic properties depicted above, manganese perovskites are also of great interest for catalysis. The emerging energy crisis due to the depletion of fossil resources has motivated scientists to find new energy sources, energy storage, and conversion systems. Fuel cells and aqueous metal-air batteries fit within this trend. The performance of these devices relies on two reactions. The first one is the oxygen evolution reaction (OER), used during batteries charge or water splitting. OER is the half redox reaction generating molecular O_2 from water. The second reaction is the oxygen reduction reaction (ORR) involved in batteries discharge and fuell cells. ORR is the half redox reaction of O_2 reduction to water. However, the use of fuel cells, water electrolysers and metal-air batteries on a global scale is tempered by the slow kinetics of these reactions.[34,35] Therefore, the use of sustainable electrocatalysts exempt from noble metals and able to speed up the reactions by reducing the energy barrier of short-lived transition states is nowadays necessary. Perovskite oxides and more specifically manganese perovskites have shown promising performances towards ORR in alkaline media.[36] Some manganese perovskites exhibit an activity towards ORR equivalent to the currently used electrocatalyst (Pt/C, Pd).[37,38] As more than 90% of the metallic elements in the periodic table can form a perovskite structure, a wide variety of tunable systems are achievable for electrocatalysis.[39] This possibility to chemically tailor perovskites for targeting specific

reactions, combined with the elemental abundance and the low cost of the constitutive elements make perovskite oxides promising materials for electrocatalysis. This chapter attempts to give a brief understanding of ORR where manganese perovskite oxides can be used as potential decisive electrocatalysts. Several groups have reported the electrochemical activity toward ORR of manganese oxides such as Mn_5O_8, Mn_3O_4, Mn_2O_3, MnO_2, MnO(OH) and their polymorphs.[37,40–45] A wide number of manganese perovskites has also been investigated, as discussed below.

1. Oxygen reduction reaction (ORR):

The equation of the oxygen reduction reaction in alkaline aqueous media is:

$$O_2 + 2H_20 + 4e^- \rightarrow 4OH^-$$

The ORR is a cathodic chemical process composed of several steps where electrons are transferred. In a fuel cell these reactions are occurring at the cathode and usually in alkaline media. The use of an alkaline media at ambient temperature prevents the adsorption of spectator ions onto the surface of the electrocatalysts, thus enhancing the kinetics of the reaction.[46] Moreover, if one wants to use manganese perovskites, alkaline media become mandatory since manganese perovskites amorphize and dissolve in acidic media. The mechanism of ORR is still widely investigated, two different pathways have been proposed on perovskites:

The first pathway is a 4-electrons direct mechanism involving a 4-electron transfer leading to hydroxides (**Figure 6**).[47–52] (1) The O_2 molecule adsorbs as OO^{2-} onto an Mn site, an OH^- group from the surface is displaced. (2) the peroxo group is protonated and forms OOH^-. (3) An OH^- group is removed from the OOH^- at the surface, leaving a superoxo O^{2-}. (4) This superoxo group is protonated to reproduce the hydroxyl-covered starting surfaces. The kinetically limiting step of the four electron pathway is ascribed to the adsorption of O_2 replacing the OH group in step (1). In this pathway, the B-site cation Mn undergoes a redox switch.

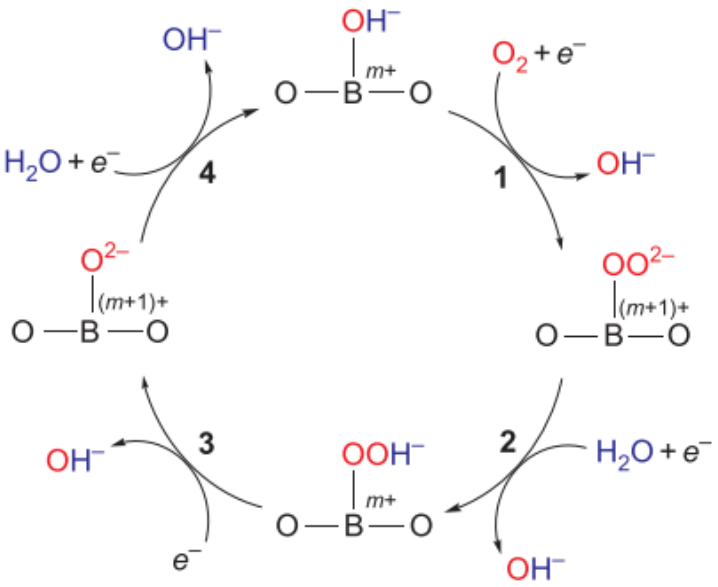

Figure 6. Four-electron pathway reducing O_2 to hydroxides.[47]

The second pathway (**Figure 7**) follows the same steps (1) and (2) of the four-electron mechanism. This pathway arises from difficulties to cleave the O-O bond at (2) and results in the desorption of the protonated group as hydroperoxide HO_2^-.[37,50–53]

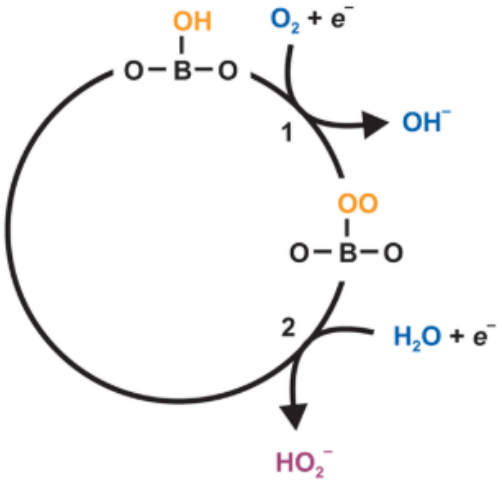

Figure 7. Two-electron pathway reducing O_2 to peroxide. Orange denotes species on the catalyst surface, and blue/purple denotes species in solution.[37]

The desorption of the hydroperoxide group can then either lead to a two electrons reduction or to the peroxide disproportionation. The first case (**Figure 8**a) arises from re-adsorption of the HO_2^- on the catalyst surface followed by its reduction by an additional 2-electron pathway presented in (2) and (3). This leads to the production of 3 OH^- species.[37,50–53] The second

possible case (**Figure 8**b) is the chemical disproportionation of HO_2^- species resulting in formation of $2OH^-$ and O_2.[53]

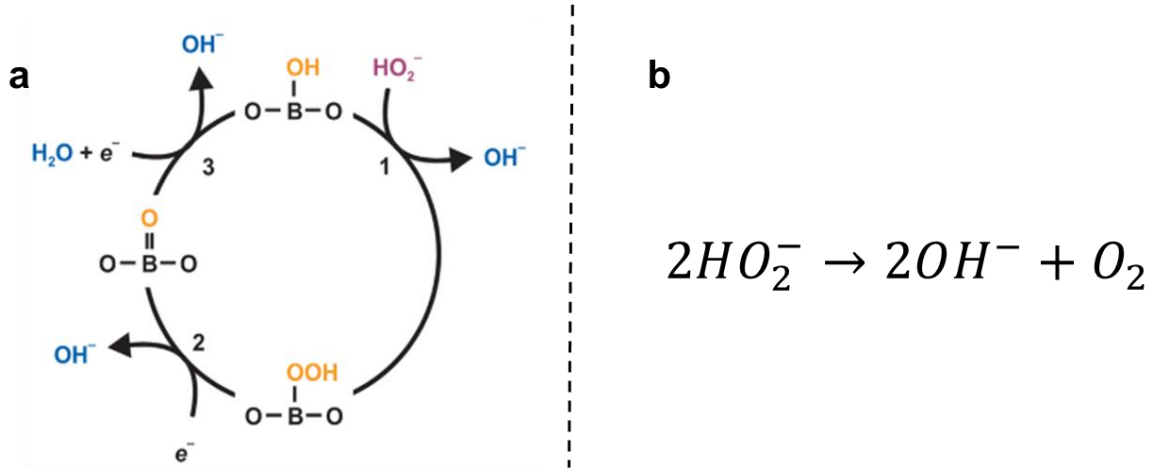

Figure 8. (a) two-electron reduction of peroxide. Orange denotes species on the catalyst surface, and blue/purple denotes species in solution.[37] (b) chemical disproportionation of HO_2^- species.

Amongst these pathways the four-electron route is the most desirable for energy conversion, because the generation of peroxide species during the ORR in fuel cell is detrimental to the overall performances and lifetime due to chemical attack of the catalysts[54,55], the catalyst support[56] or the ion-conducting membrane.[57,58] However, it has been recently proved by experimental study and mathematical modeling that these different pathways may occur simultaneously and compete with each other.[59] Aside from the complexity intrinsic to the ORR, the choice of the electrocatalysts is of great importance to enhance the efficiency of the reaction. The selection of adequate elements composing the perovskite can greatly affect their reactivity.

2. Influencing factors

Manganese perovskites and generally perovskites can adapt to substitution on their A and B sites at various concentrations, thus a wide pool of compositions is accessible for electrocatalysis.[21] A or B site cationic substitutions yield perovskite formula $A_{1-x}A'_xB_{1-y}B'_yO_3$, leading to different oxidation states of the metallic B sites. It is admitted that the B-site cations play a dominant role in the catalytic properties of perovskites.[60] In manganese perovskites, the involvement of Mn(IV)/Mn(III) species in ORR electrocatalysis has been demonstrated by an *in situ* X-Ray absorption near edge structure (XANES) study.[40] The presence of divalent Mn is key to achieve high ORR activities in manganese perovskites.[37,47] It can be obtained by partial substitution of the A-site.

The A-site cation is not involved as an active site in the ORR. However, it plays an important role in tailoring the oxidation state of the B-site cations and thus the B-O bond strength. The effect of A-site cations on the ORR activity has been investigated by Yamazoe *et al.*[61] The authors found out that for $LnMnO_3$ (Ln = La, Pr, Nd, Sm, Gd, Dy, Yb or Y), the ORR activities decreased with the ionic radius of the A-site element (La > Pr > Nd > Sm > Gd > Dy > Y > Yb). Out of these perovskites, $LaMnO_3$ exhibited the highest current density at a given overpotential. The authors ascribed this observation to the increase of the A-site cations radius, which increases the tolerance factors approaching thus a quasi-perfect perovskite structure with higher electronic transport. In addition, Sr^{2+} doping results in the formation of B-site metal ions with different oxidation states (B^{3+}/B^{4+}), thus changing the electronic state of the B-site cations of the perovskite.[62] Therefore, the doping rate of divalent A' cations has a direct impact on the electronic transport and thus the electrocatalytic activity, for example amongst seven different Sr doped $La_{1-x}Sr_xMnO_3$ perovskites, $La_{0.67}Sr_{0.33}MnO_3$ exhibited the highest ORR activity.[47,63,64]

Shao-Horn *et al.*[47] have proposed a way to identify the potentially most active electrocatalysts for ORR by highlighting the relationship of 3d electrons of the B-site ions and the ORR activity. Indeed, the authors highlighted that these 3d electrons were antibonding electrons of the B-O bond and that they can influence the $B-O_2$ bond strength.[65] This hypothesis is based on the fact that the $B-O_2$ adsorption energy is directly correlated to the B-O bond energy.[66] According to this relationship, Shao-Horn *et al.* observed that the ORR activity of perovskites was higher for average d^4 and d^7 configuration of B-site cations (**Figure 9**). [47]

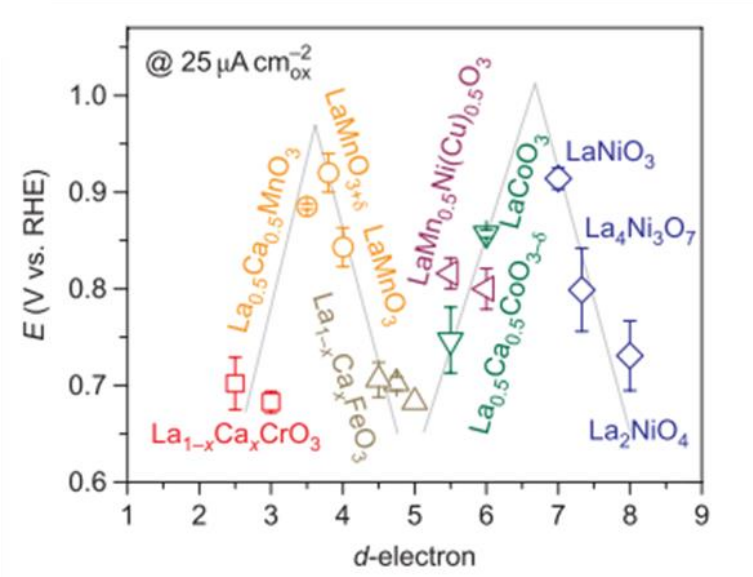

Figure 9. ORR activity of perovskite transition-metal-oxide catalysts. Potentials at 25 μA cm^{2-}_{ox} of the perovskite oxides as function of the average d-electron number of B-site cations. Data symbols vary with type of B ions (Cr, red; Mn, orange; Fe, grey; Co, green; Ni, blue; mixed compounds, purple), where x = 0 and 0.5 for Cr, and 0, 0.25 and 0.5 for Fe. Errors bars represent standard deviations of at least three measurements.[47]

The authors further investigated the relationship between the number of d electrons and the ORR activities of perovskites. They proposed an orbital model to explain these preferential systems. When the O_2 adsorbs on the surface via the B-sites, the B-e_g orbital overlaps with the O-2p_σ more strongly than the B-t_{2g} with the O-2p_π. Therefore, the energy gained by adsorption/desorption of the oxygen on B ions depends on the B-e_g filling. A too low B-e_g filling for example in $La_{1-x}Ca_xCrO_3$ ($t_{2g}^3 e_g^0$ for x = 0, $t_{2g}^{2.5} e_g^0$ for x = 0.5) leads to a B-O_2 bonding too strong. On the contrary, a high occupancy B-e_g in $La_{1-x}Ca_xFeO_3$ ($t_{2g}^3 e_g^2$ for x = 0, $t_{2g}^3 e_g^{1.75}$ for x = 0.25, $t_2^3\, e_g^{1.5}$ for x = 0.5) results in a O-O bond too weak. Finally, $La_{1-x}Ca_xMnO_3$ ($t_{2g}^3 e_g^1$ for x = 0, $t_2^3\, e_g^{0.5}$ for x = 0.5) (**Figure 10**), corresponds to a balance between these two previous cases and gives the highest activity. The strong correlation between e_g electrons and the ORR activity suggests that the e_g filling can be considered as a primary descriptor of ORR effective catalysts.

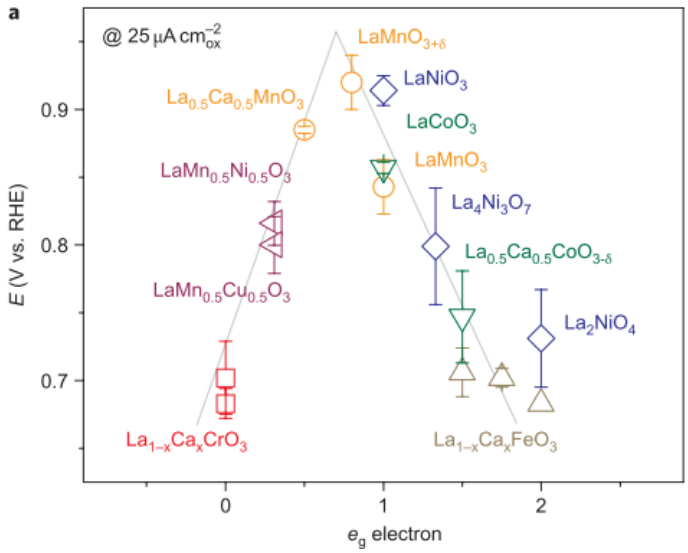

Figure 10. Role of e_g electron filling on ORR activity of perovskite oxides. Potential at 25 μA cm_{ox}^{2-} as a function of e_g orbital in perovskite-based oxides. Data symbols vary with type of B ions (Cr, red; Mn, orange; Fe, grey; Co, green; Ni, blue; mixed compounds, purple), where x = 0 and 0.5 for Cr, and 0, 0.25 and 0.5 for Fe. Errors bars represent standard deviations of at least three measurements.[47]

So far in this electrocatalysis part, enhancement of the ORR activity through the perovskites structural changes have been depicted, however, other strategies are possible. First by increasing the active sites of the catalysts, secondly by the use of external stimuli.

Traditionally to increase the amount of actives sites, researchers have searched nanostructured catalysts. Indeed, the change from bulk to nanoparticles results in an increased surface-to-volume ratio and so does the number of active sites. Perovskite oxides at the nanoscale have been displaying different properties than their bulk counterparts, leading to gains in their catalytic activities.[66,67] For example nanosized $La_{1-x}Sr_xMnO_3$ has shown remarkable ORR electrocatalytic performance, compared to conventional $La_{1-x}Sr_xMnO_3$ particles (1 μm).[68] Therefore, one can already see how pivotal nanostructuration can be. The design and control of the stoichiometry for specific nano-perovskites should be of great significance toward the development of efficient electrocatalysts for the ORR.

3. External stimuli for enhance electrocatalysis

We showed above how the compositional properties of perovskites are crucial for electrocatalysis but also how to select and design more efficient electrocatalysts. In this section, we show how non electrocatalytic properties can be used or activated under external stimuli for electrocatalytic purposes.

3.1. Gravity field enhanced electrocatalysis

The gravity field was used for electrocatalysis purposes, in order to facilitate the removal of gas produced and spillover on the surface of the electrode.[69–71] In a gas/liquid system, the heavy phase, i.e. the electrolyte, moves along the direction of the gravity acceleration while the lighter phase, herein gas bubbles, move along the opposite direction. Hence if the electrocatalytic reaction is carried out under a super gravity field the produced acceleration acts as a separation force between gas bubbles and the electrode surface as schematically shown **Figure 11**a-b by Wang *et al.*[70] The authors showed that the use of gravity field grandly enhanced the current density obtained for the hydrogen evolution reaction (HER) as a consequence of bubbles removal **Figure 11**c.

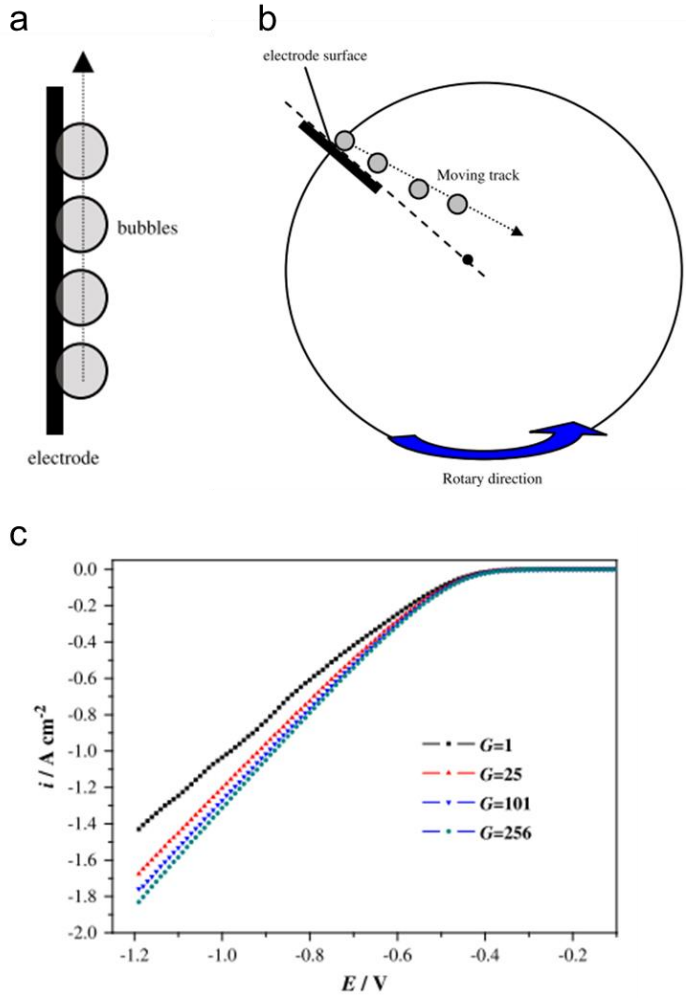

Figure 11. (a) moving track of bubbles on the electrode surface under normal gravity condition (b) and super gravity field. (c) polarization curves of HER.[70]

3.2. Light enhanced electrocatalysis

The surface plasmon resonance (SPR) has been investigated as a way to trigger electrocatalysis. Under light, energetic electrons are excited by resonant photons and then transferred to the nearby conductive or semiconductive surface. These electrons called "hot holes" are thus usable as energetic source for chemical reaction and leave energetic holes on the surface of the catalyst, which can act as electron trap to form higher active species.[72–76] Guigao *et al.*[77] coupled Au nanoparticles to $Ni(OH)_2$ nanosheets and observed under light a very large increase of the oxygen evolution reaction (OER) current density (**Figure 12**). This is explained by the coupling of Au as a plasmonic transducer to the nickel complex acting as the electrocatalyst. Indeed, Au nanoparticles are excited by light and the plasmon effect produces excited electrons, which facilitate the charge transfer from the catalyst to Au nanoparticles. Then, the nickel complex is easily oxidized from Ni^{2+} to an active $Ni^{3+/4+}$. Therefore, enhancing the electrocatalytic performance of the reaction. Xu *et al.*[78] were also able to enhance the OER activity of manganese oxide using Au-MnO_2 electrocatalysts activated by a green light. The development of electrocatalysis assisted by light field is still at an early stage but shows promising results.

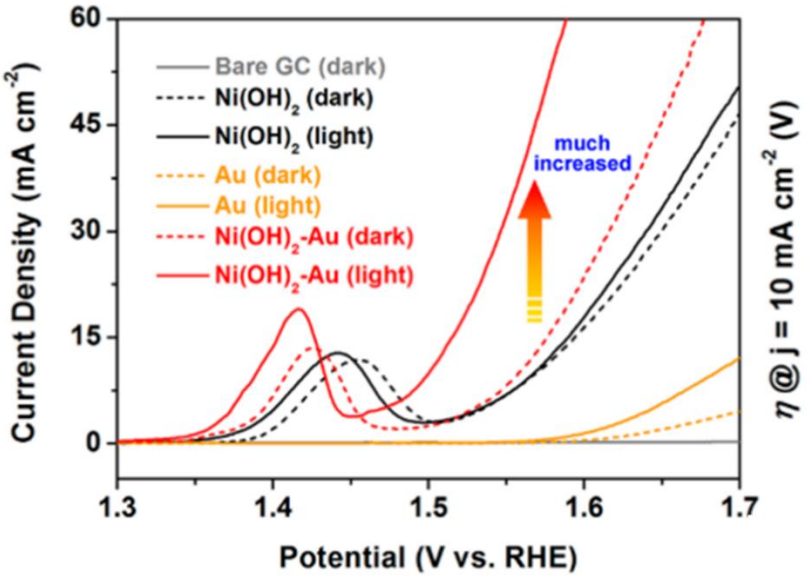

Figure 12. OER polarization curves of $Ni(OH)_2$-Au hybrid catalyst and control samples measured in 0.1 M KOH electrolyte with and without light irradiation (523 nm laser).[77]

3.3. Magnetic field enhanced electrocatalysis

a) The magnetothermal effect

The magnetothermal effect derives from magnetic hyperthermia, which consists in a local heating of magnetic nanoparticles by the use of an external high-frequency alternating field (AMF) as presented **Figure 13**.[79] Niether *et al.*[79] used FeC-Ni nanoparticles as electrocatalysts for the oxygen evolution reaction (OER). In these objects the iron carbide core is magnetic and the nickel shell acts as the catalytic surface. When exposed to an AMF the magnetic core instantly and strongly heat, the authors observed then that as the AMF is activated, the overpotential of the OER decreases from 2.12 down to 1.6 V vs. RHE. Therefore, the FeC-Ni catalyst approaches competitive value versus state-of-the-art OER electrocatalysts. Temperature is a primary factor affecting reaction kinetics, thus, when heated the activation energy is reached easily and the overpotential of the electrocatalytic reaction decreases.[80] However, an increase in temperature obtained by conventional heating process lead for batteries to the corrosion of the electrolyzer and gas pollution. Hence the ability to heat locally magnetic nanoparticles would avoid such degradation and yield higher electrocatalytic performances compared to traditional heating.

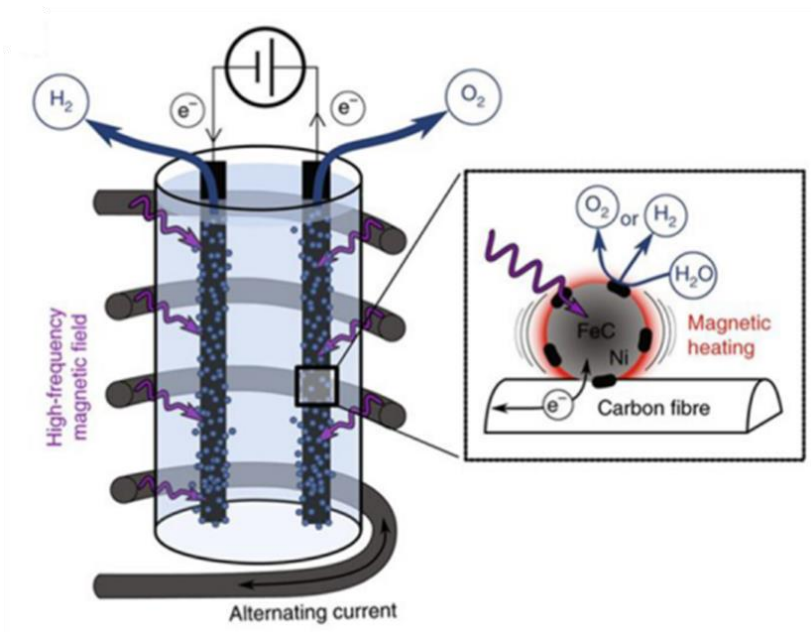

Figure 13. FeC-Ni catalyst heated locally in a high-frenquency alternating magnetic field (AMF).[79]

b) The magnetohydrodynamic effect

The magnetohydrodynamic effect (MHD) is the interaction of a local current density with a magnetic field. This effect is driven by the Lorentz force ($\boldsymbol{F}_L$), where $\boldsymbol{j}$ is the current density, $\boldsymbol{B}$ the magnetic field strength and $\boldsymbol{F}_L = \boldsymbol{j} \times \boldsymbol{B}$. This effect influences the gas produced at the electrode but also the ionic species in solution by orienting the flow in a certain direction. **Figure 14** represents the different magnetic convection achievable on the surface of an electrode. When $\boldsymbol{B}$ is perpendicular to $\boldsymbol{j}$, $\boldsymbol{F}_L$ reaches its maximum (**Figure 14**a). In the case of $\boldsymbol{B}$ parallel to $\boldsymbol{j}$, the flow obtained is null, but translates into a whirlpool movement at the surface of the electrode because of boundary effect on the flow of species (**Figure 14**b).[81,82] The orientation of the magnetic field versus the local current density can thus influence the flow of species near the electrode, hence the rate of the reaction for reactions different than ORR and producing gas.[83,84] Indeed, the whirlpool movement (**Figure 14**b) can contribute to evacuating the amount of gas produced, which can also enhance the yield of the reaction.

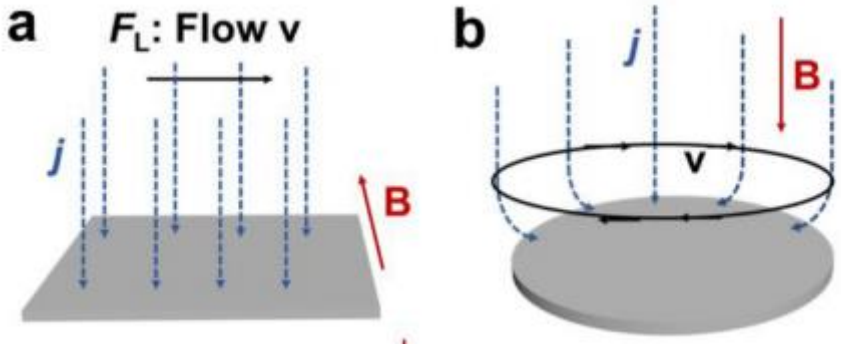

Figure 14. MHD flow types under homogeneous magnetic field. (a) MHD flow parallel to the electrode surface when B⊥j. (b) MHD whirlpool around the edge of the electrode when B//j.[85]

c) The Maxwell stress effect

The Maxwell stress effect is occurring when the dipole moment in an object interacts with a magnetic field. In the case of a paramagnetic droplet, a uniform magnetic field can cause deformation of the droplet shape. This deformation can be transverse or even longitudinal.[86] Depending on the orientation and the strength of the magnetic field applied, the stretching direction and degree are affected (**Figure 15**a-c). Therefore, the Maxwell stress effect can have an influence on the interfacial tension, contact angle, wettability or even the adhesion to the surface of the electrode.[87–89] Dunne and Coey[90] reported that the Maxwell stress effect changes the solvation of paramagnetic ions in the electrochemical double layer. Hence, it is possible under magnetic field to influence the shape of the ionic cloud near the electrode. To our

knowledge there has been no reported of modified electrocatalysis using the Maxwell stress effect so far. However, the ability to affect the electrochemical double layer may open up interesting perspectives for electrocatalysis.

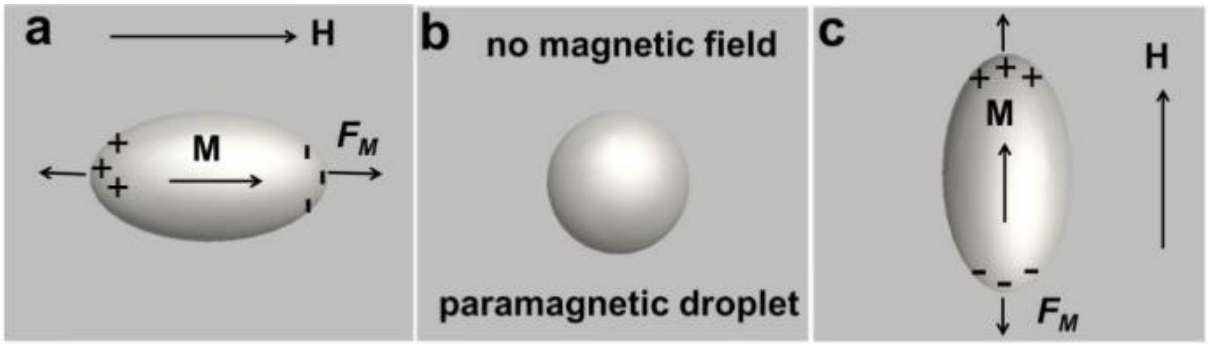

Figure 15. Distortion of a paramagnetic droplet induced by Maxwell stress in a magnetic field. The shape of a paramagnetic droplet changes from (a) parallel magnetic field, (b) zero magnetic field and (c) vertical magnetic field.[85]

d) The Kelvin force effect

The Kelvin force effect is another effect impacting the paramagnetic and diamagnetic species under magnetic field.[91] It requires a non-uniform magnetic field.[91–93] This effect can accelerate the mass transfer of the paramagnetic and diamagnetic species but also make the diffusion layer thinner and increase the limiting current.[94] For electrocatalytic application, the species targeted by the Kelvin force effect are paramagnetic O_2 molecules. When concentration gradients are observed in the electrolyte and a perpendicular non uniform magnetic field is applied, the paramagnetic species are attracted towards the strongest magnetic field strength. On the other hand, the diamagnetic species are repulsed to the lowest magnetic field strength area.[95] This effect can be applied to resolve issues encountered when diamagnetic species are poisoning active sites on the electrocatalyst surface or even to drag O_2 species towards the catalyst surface.[95,96]

4. Conclusion on electrocatalysis on perovskites

In this second part of the chapter, we have shown how ORR is a complex reaction with different reaction pathways. This is the reason why a better understanding of the mechanisms and how to improve the kinetics of this reaction is of great interest. We showed how manganese perovskite are of great interest for the ORR electrocatalysis and can be adjusted by compositional changes to provide the highest activity possible for the material. Finally, the use

of different stimuli impacting electrocatalysis has been presented. The use of external stimuli showed that intrinsic properties of material or triggered ones could greatly change the yields of the sluggish reactions in fuel cells and metal-air batteries. In this context, magnetic field-assisted electrocatalysis showed promising results and could be developed with manganese perovskites, making use of their magnetic properties.

Table 1 shows the scarce occurrences of ORR electrocatalysis assisted by magnetic field. These few cases have been mainly using the Kelvin effect[97–102] to influence the flow of oxygen species to the electrode. However, Shi *et al.*[99] and later Wang *et al.*[102] demonstrated that under magnetization, magnetic particles would form magnetic poles, which could interact together and disturb or weaken the oxygen transfer to the electrocatalytic surface and thus affect the Kelvin force. Likewise, Zeng *et al.*[103] worked with Co_3O_4 under magnetic field. The presence of mixed valence Co^{2+}/Co^{3+} resulted in enhancement of the electron exchange under magnetic field due to polarization of the unpaired electrons, facilitating the oxygen reduction. The electrocatalysis assisted by magnetic field has been thus mainly focus on the controlled diffusion of O_2 species towards the electrocatalytic surface.

Recently Garcés-Pineda *et al.*[104] studied the effect of a small magnet (<0.4 T) on Ni-based catalysts for the OER. They observed an increase of the OER current density with the magnetic field. By excluding the possibility of the magnetohydrodynamic effect, they affirmed that any enhancement observed was directly coming from the material by spin-polarization. However, the authors used a permanent magnet for electrocatalysis by simply approaching it from the electrochemical setup. This experiment results in the formation of a field gradient which can provoke the Kelvin force effect but was never mentioned. Overall, the comprehension of the mechanisms and effects involved in electrocatalysis under magnetic fields are still hard to apprehend and more thorough research are required on that matter. These experiments enlighten the importance of the use of a homogeneous magnetic field, the control of the electrolyte temperature and of the diffusion layer. These three parameters are taken into account in the following chapters.

Catalyst	*Field intensity*	*Redox reaction*	*Magnetic effect*	*References*
$Nd_2Fe_{14}B/C$	Tiny magnetic field	ORR	Kelvin force	97,98
Fe_3O_4/PANI	Tiny magnetic field	ORR	Kelvin force	99
Fe, Co and Zn microcrystals	360 mT	ORR	Kelvin force	100
CoPt nanowires	20-25 mT	ORR	Kelvin force	101
Fe_3O_4, γ-Fe_2O_3, and Fe-N-C	0-0.56 T	ORR	Kelvin force	102
Co_3O_4	0-1.32 mT	ORR	Polarization of unpaired electrons	103
Ni foil/Pt/NiW films	G= 1-541	HER	Gravity field	69–71
Au-MoS_2	808 nm laser excitation	HER	Light field	73
Ni$(OH)_2$-Au	532 nm laser excitation	OER	Light field	77
Au-MnO_2	100-200 mW	OER	Light field	78
Ni-based catalysts	<0.4 T	OER	Spin-polarization	104
FeC-Ni	24.3-48 mT	OER	Magnetothermal effect	79
Co-based catalysts	1 T	OER	Spin-polarization	105
Co_3O_4	125 mT	OER	Magnetohydrodynamic effect/Spin-polarization	106
Nickel electrode	06-4.5 T	Water splitting	Magnetohydrodynamic effect	83,84
Au nanorods	Visible light	Water splitting	Light field	76

Table 1. ORR, OER and HER performances of different catalysts under magnetic field, adapted from [85]

IV. The exsolution process

1. Introduction

The exsolution process consists in a phase segregation triggered into an initially single-phase material that results in the formation of particles protruding at the surface of the material. This segregation is mostly but not exclusively,[107] reported in perovskites doped with a reducible transition metal M on the B-site, with general formula $AB_{1-x}M_xO_{3-\delta}$. By applying reducing conditions as an external stimuli, the metallic cations are reduced, they migrate to the surface and form nanoparticles, dragged out of the parent $ABO_{3-\delta}$ perovskite lattice and socketed on the surface. This opens up a wide range of possibilities in terms of perovskite hosts but also reducible cations. However, a lot of parameters are involved to exsolute transition metals, and the understanding of this exsolution process is still ongoing.

The interest of the scientific community for the exsolution process has been mainly motivated by the environmental concerns we are nowadays facing. Indeed, the design of supported metal or oxide nanoparticles is of great interest for their key roles in catalysis, energy conversion and energy storage including batteries, fuel cells and electrocatalysis cells.[108–111] Such materials are usually prepared by impregnation where the catalyst precursors are deposited on the surface support followed by thermal and reductive treatments to form metallic nanoparticles. However, this widely applied method gives poor control over the particles interaction with the support and does not ensure strong anchoring at the surface, so that it often leads to deactivation by agglomeration, sintering and coking during industrial critical processes.[112,113] Exsoluted particles have been proven to be more uniformly dispersed on the surface of the substrate (the parent perovskite) but also partially immersed (or socketed) into the surface of the parent perovskite.[114] This last feature makes the particles highly resilient to agglomeration or coking[114,115] and thus could highly enhance and improve catalytic rates of numerous reactions as well as the stability of the materials and of their performances.

The interest in the exsolution process, also called solid-state recrystallization[116], started when it was first reported in 2002 by Tanaka's group and Daihatsu Motor Co.[117] Using a bulk perovskite $LaFe_{0.57}Co_{0.38}Pd_{0.05}O_3$ where palladium is extracted from the perovskite structure under reducing atmosphere and forms dispersed nanoparticles on the surface. By changing from reductive to oxidative atmosphere, Tanaka *et al.* were able to reincorporate Pd back into the perovskite and thus maintain a high catalyst activity after re-exsolution. For the past two

decades research on exsolution has advanced towards more understanding of the mechanisms underlying this process.

To our knowledge exsolution has been observed mostly on perovskites and rarely on other oxide families. This is mainly due to perovskites' fuel resistivity, carbon/sulfur tolerance and most importantly their structural stability under reducing and oxidizing atmosphere at high-temperature.[118,119] On the downside, most of the perovskite-based catalysts present lower catalytic activities than common industrial catalysts. This is where the exsolution process is very interesting. The possibility to increase the catalysis activity and stability of such stable materials and thus to enhance the cost/lifetime of the catalysts would be a major progress.

Most of the research on the exsolution has been focused on increasing efficacy in solid oxide fuel cell (SOFC) more specifically to provide highly active and durable anodes performing under high temperature and reductive atmosphere, which are perfect conditions to trigger exsolution.[120–123] The exsolution has been also used for electrodes of high-temperature electrolysis systems coupled with electrocatalysis[124], CO_2[125–127], steam[27,128,129] and electrochemical gas reforming.[130] Recent literature has stressed out the use of exsolution for chemical looping materials[131–133], oxygen permeation membranes[134,135], CO oxidation catalysis[136–138] and finally electrocatalysis in aqueous media using $(Ca_{0.92}Ni_{0.04})TiO_{2.96}$ and $Ca(Ti_{0.96}Ni_{0.04})O_{2.96}$.[139]

The exsolution can be sequenced in four different physical steps, diffusion, reduction, nucleation and growth. In order for the exsolution to happen the doping cations have to be reduced to a metallic state. This can be written such as:

$$\frac{1}{x}M_xO_y + \frac{y}{x}H_2(g) = M + \frac{y}{x}H_2O(g) \qquad (1)$$

Or in a Kröger-Vink notation:

$$M_M^{\times} + \frac{m}{2}O_O^{\times} \leftrightarrows M_{exsolution} + V_M^{m\prime} + \frac{m}{2}V_O^{\bullet\bullet} + \frac{m}{4}O_{2(g)} \qquad (2)$$

With $M_M^{\times}$ and $O_O^{\times}$, the metal M and oxygen ion in the oxide host, $M_{exsolution}$ being the exsolved metallic phase and $V_M^{m\prime}$ and $V_O^{\bullet\bullet}$ the cation and anion vacancies. *m* being the oxidation state of M. In an ideal model, under reductive atmosphere the oxygen ions form dioxygen gas, which creates positively charged O vacancies concomitant with reduction of the metal cations. If an oxidative atmosphere is afterwards applied, the reduced metal re-oxidize and dissolves back

into the host structure if the kinetics allow it. However, the reaction aforementioned can only occur if thermodynamically favored. This is associated to a negative Gibbs free energy of the reaction. On **Figure 16** it is visible that many oxides (e.g Ti, Mn, Fe, Cu oxides) exsolute as oxides, this is why exsolution is commonly performed with elements reducible into metals.

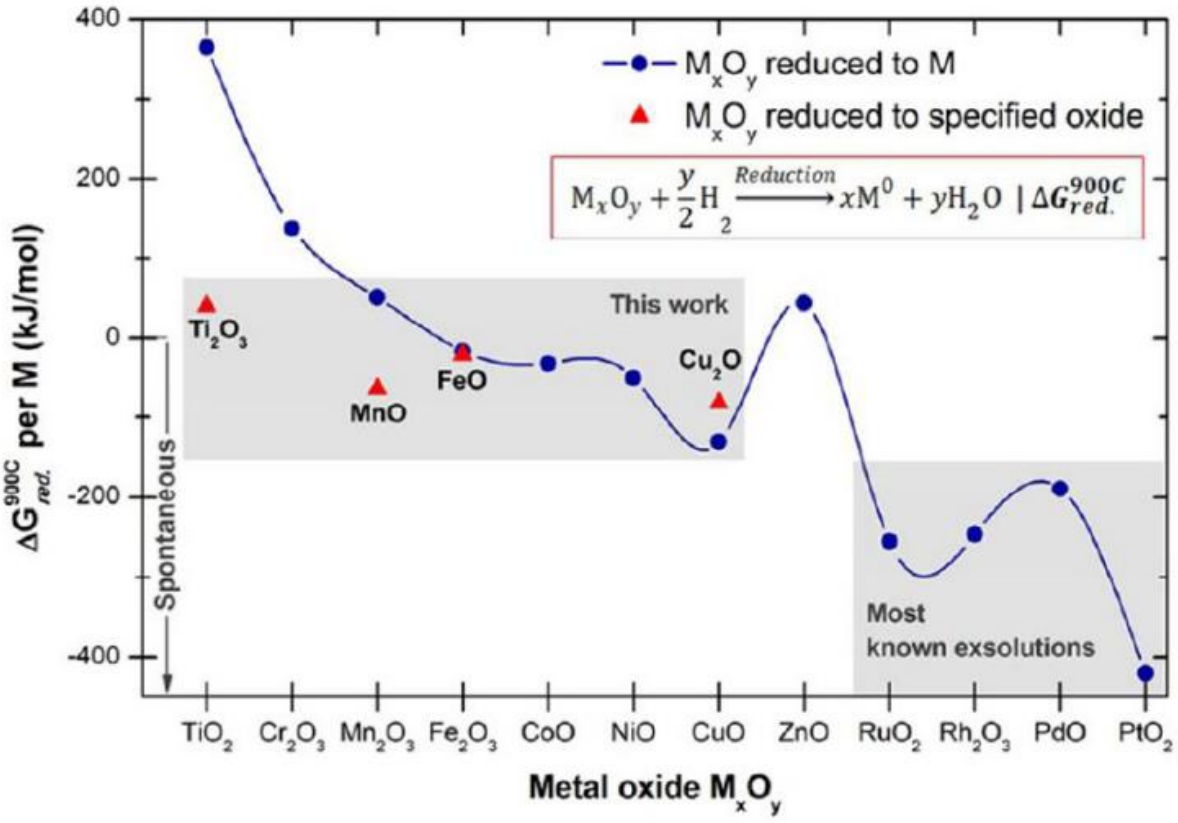

Figure 16. Calculated Gibbs free energy change of the reduction of transition metal oxides under reducing atmosphere at 900 °C.[140]

Apart from the thermodynamic aspect of the reduction of exsolvable cations, other parameters must be considered. The first one is the A-site deficiency. Indeed, the work of Tanaka *et al.*[117] was focused on stoichiometric perovskites with A/B=1 mole and restricted to few transition metals, which are easily reducible Ni, Rh, Pd, Pt.[141] Almost a decade ago Irvine's group has proven that by using an A-site deficient perovskite, the exsolution of hardly reducible transition metals becomes feasible.[114,141,142] By comparing the exsolution of an A-site deficient Ni-doped perovskite $La_{0.52}Sr_{0.28}Ni_{0.06}Ti_{0.94}$ with a stoichiometric one $(La_{0.3}Sr_{0.7})(Ni_{0.06}Ti_{0.94})O_3$, Irvine *et al.*[141] observed that exsolution only occurred in the case of A-site deficiency, even if both perovskites were doped with the same Ni ratio (6%). The fact that exsolution did not occur in the stoichiometric perovskite was considered as an evidence that the exsolution limiting factor cannot only be the presence of reducible ions in the lattice, but that other parameters are

impacting the exsolution process. Indeed, for a stoichiometric perovskite, exsolution of B-site cations will lead to an A-site rich perovskite, thus destabilizing the host lattice. A-site deficient perovskites can then be seen as B-site rich perovskites, which will drive the host perovskite under adequate conditions to exsolute B-site cations in order to reach the stoichiometric and stable state.

$$\underbrace{A_{1-x}BO_3}_{\text{A-deficient perovskite}} \leftrightarrows \underbrace{(1-x)ABO_3}_{\text{Residual perovskite}} + \underbrace{xB}_{\text{Exsolved metal}} + \frac{3}{2}xO_2 \qquad (3)$$

Irvine *et al.*[141] were able to form $La_{0.4}Sr_{0.4}M_xTi_{(1-x)}O_{(3-\delta)}$ where M = Mn, Ni, Fe, Cu and x=0.06. The authors noted that by introducing A site deficiency (site occupancy 0.8 in this case) and inserting B cations with lower charge than Ti(IV) leads to the formation of O_2^- vacancies. These vacancies, like A-site deficiency, will dynamically facilitate exsolution of B-site cations. However, a threshold in oxygen vacancies exists above which the perovskite structure is destabilized. According to these considerations, the optimal composition of a perovskite prone to exsolution is $A_{1-\alpha}M_xB_{1-x}O_{3-\delta}$ with α =0.2. The presence of oxygen vacancies clearly stands out as a major factor in exsolution, as Irvine *et al.*[141] have found that for a perovskite with A-site vacancies α=0.2, exsolution only occurs if the δ value above 0.05. The amount of oxygen vacancies (δ) can be adjusted independently from the B and A site occupancy by external factors such as the partial pressure of oxygen (PO_2) and temperature. During the reaction under reducing conditions, the oxygen ions from the perovskite structure are expelled, leading to the formation of oxygen vacancies and electrons, which reduce the metal and nucleate the particle. This can be summed up into two Schottky defects equations:

$$O_O^x \rightarrow V_O^{\bullet\bullet} + 2e^- + \frac{1}{2}O_{2(g)} \qquad (4)$$

$$M_B'' + 2e^- \rightarrow M_{(metal)} + V_B'' \qquad (5)$$

Once the threshold amount of oxygen vacancies mentioned above is reached through reduction and thermal treatment, and provided that the A-site occupancy is low enough, the doped perovskite is destabilized and evolves in an attempt to regain stability by reducing the B-site cation and exsoluting it to the surface. Tailoring of A-site and of O-site vacancies is therefore a prime strategy to tune the exsolution process.

2. Mechanistic approach

The mechanism of exsolution is still controversial. One of the important question is directly linked to whether exsolution is a surface process or a subsurface one. Irvine and Neagu performed morphological investigations of the exsolution process using atomic force resolution (AFM) and *in situ* transmission electron microscopy to shed some light on this question.[143,144] After mild reduction, pit-like structures are forming (**Figure 17**). This first step is followed by the emergence of metal particles from the pit centers. This observation suggests that nucleation of the particles is occurring beneath the surface of the perovskite inside the oxide matrix.[145] The formation of surface pits is unique to the exsolution process. If the experimental conditions are made harsher (higher temperature and time), the particles grow epitaxially and isotropically out of the surface from the pits (**Figure 17**).

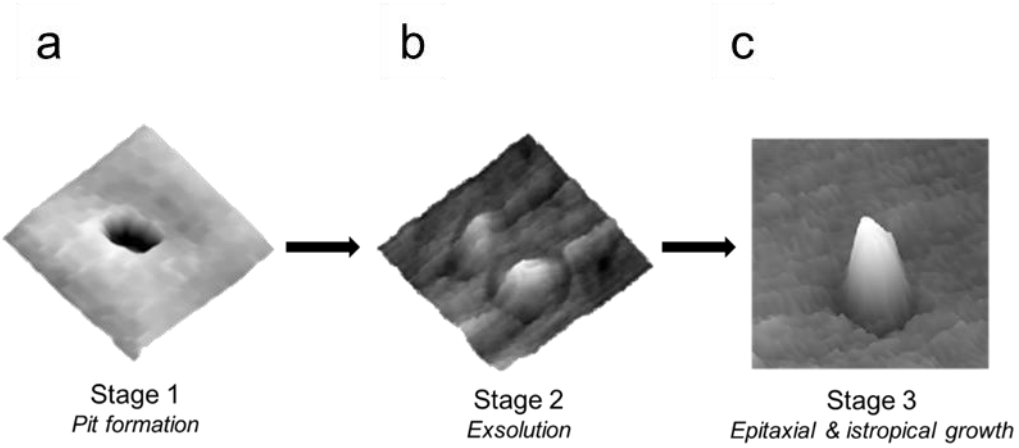

Figure 17. (a) 3D images of the formation of pit after reduction at 600 °C, (b) 3D view model of AFM image after reduction at 700 °C and (c) 3D view model of a nickel nanoparticle exsoluted.[143]

Trenches are then observed around the pits. As the particles emerge from the pits, the trenches soften until disappearance, followed by a rise of the surface at the junction with the particles, giving a volcano shape-like as represented **Figure 18**. This phenomenon results in particles partially socketed into the surface of the host perovskite. The fraction of the submerged surface of the particles has not been deeply investigated. However, approximately 30 to 40% of the Ni particles are submerged on a stannate substrate.[143,146] This fraction is a key factor in the efficiency of these new tuned catalysts against deactivation and the minimal submerged percentage required to keep the particles embedded is a must-known.

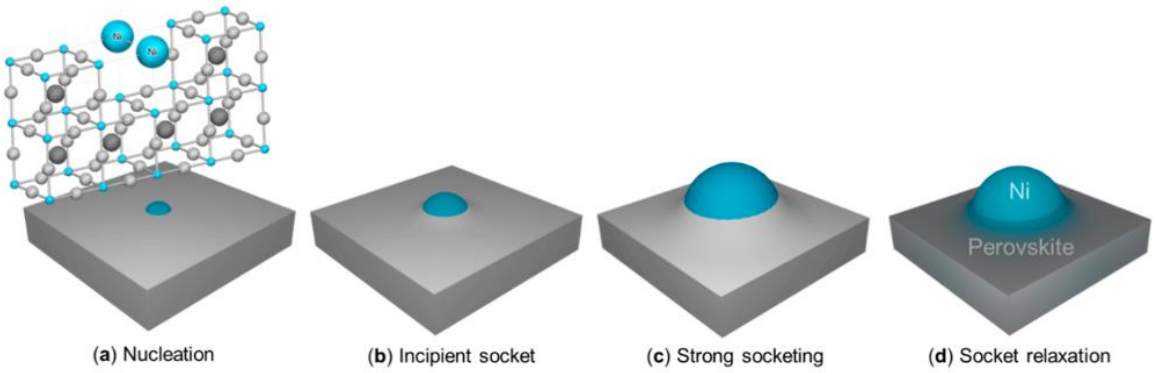

Figure 18. (a-d) Schematic illustration of particle-socket genesis during exsolution.[144]

A correlation between the height of the lattice rise during socketing and the size of the nanoparticles was described[144], showing that the host surface rises by lattice expansion until a third of the diameter of the particle is reached. In order to validate these observations, the authors used a strain field model. They first considered the interaction between the oxide matrix and a spherical metal nucleus dispersed in the bulk. The exsolution deforms the host lattice and thus imposes an elastic strain to it. As the particles approach the surface, the latter evolves towards the formation of a "pre-pit" in an attempt to lower the elastic strain, which also decreases the surface energy. Thus, a coordinated stabilization phenomenon arises to balance the increasing surface energy and the increasing elastic strain, as the particle rises.

The consequence of these considerations is that a threshold depth of nucleus exists, beyond which the particles are not able to reach the surface due to a high resistive elastic strain.[143] As mentioned above, the growth of the particles being isotropic, Irvine *et al.*[144] could estimate the amount of exsolved cations in their $La_{0.43}Ca_{0.37}Ti_{0.94}Ni_{0.06}O_3$ system at different steps during exsolution. Three different contributions, linked to plausible limiting factors of the exsolution are found in the literature. The first one considers the concentration of exsolvable cations as a limiting factor:

$$d_s(t) = d_{s0}\left(\ln\left(1 + \frac{t}{\tau_s}\right)\right)^{1/3} \qquad (6)$$

The second one accounts for the diffusion of exsolvable cations to the surface:

$$d_c(t) = d_{c0}\left(1 - \exp\left(-\frac{t}{\tau_r}\right)\right)^{1/3} \qquad (7)$$

Finally, the third contribution corresponds to the strain occurring at the particle-perovskite interface during formation of the particles:

$$d_d(t) = d_{d0}\left(\frac{t}{\tau_d}\right)^{1/6} \quad (8)$$

With d, t and τ being a particle dimension at a given time, time and time constant respectively. Using the experimental data of the amount of exsolved ions as a function of the time, the authors showed **Figure 19** that the main limiting factor of exsolution is the amount of exsolvable ions present in the host structure, the strain contribution being also close.

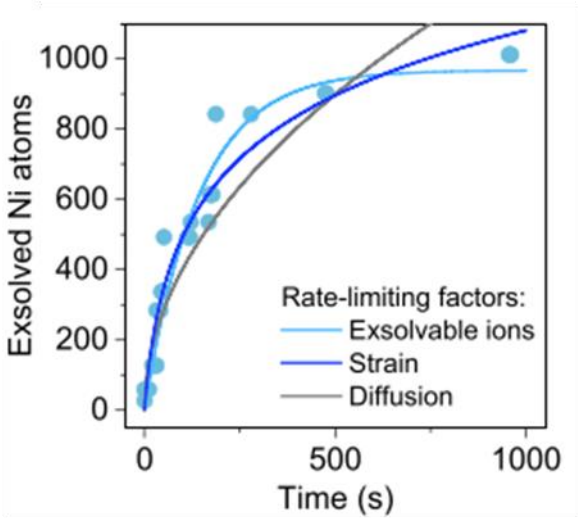

Figure 19. Plot of the number of Ni metal atoms contained within an exsolved particle as a function time, together with three models describing the rate-limiting processes that govern particle growth during exsolution.[144]

Following these considerations, Gao *et al.*[147] used three similar contributions to determine also the limiting factor of the exsolution of Ni on a $La_{0.4}Sr_{0.4}Sc_{0.9}Ni_{0.1}O_{3-\delta}$ perovskite. By using different reducing atmospheres, the authors were able to fit the experimental data to the models and found results similar to those of Irvine. Another study of Kim *et al.*[137] on $SrTi_{0.75}Co_{0.25}O_{3-\delta}$ once again showed that the reactant-limiting model is directly associated with the growth of exsoluted nanoparticles.

Aside from these basic thermodynamic and kinetic aspects related to the nucleation and growth of exsolved particles, other parameters are of interest. These parameters can be divided in two groups, intrinsic and extrinsic parameters. The intrinsic ones are directly associated to the host perovskite itself, the porosity and roughness of the surface[148], the mechanical stress and strain[143] mentioned earlier in this chapter, the surface wetting[149] and finally the

crystallographic orientation.[150,151] Regarding the extrinsic parameters, these are more classical, such as temperature, treatment time or the partial gas pressure.

We focus our attention to the partial gas pressure PO_2 and the surface orientation parameters. The partial gas pressure is of great importance in the exsolution process since a reducing atmosphere is required for exsolution. In addition, PO_2 has an influence on the growth and nucleation of the exsoluted particles.[152] Zhu *et al.*[120] created a model to predict the composition of exsoluted particles of Fe-Ni directly linked to PO_2. Through experimentation on $Sr_{0.95}Ti_{0.3}Fe_{0.63}Ni_{0.07}O_{3-\delta}$, they were able to predict the composition of the exsolved particles.

Kim *et al.*[151] investigated the role of the surface orientation on exsolution in $La_{0.2}Sr_{0.7}Ti_{0.9}Ni_{0.1}O_{3-\delta}$ thin films. The perovskite interfacial energy γ_{int}, with the (001) orientation is higher than the (111). This difference suggests that the nucleation barrier is lowered on (111) than on (001) surfaces. A lower γ_{int} translate into smaller and more numerous particles. Kim *et al*. confirmed their hypothesis by obtaining a larger pool of smaller nanoparticles on the (111) than on the (001) surfaces. However, Neagu *et al.*[114] observed a preferential exsolution on the (110) surface for Ni on the $La_{0.4+2x}Sr_{0.4-2x}Ni_xTi_{1-x}O_3$ (x=0.03/0.06) system. This discrepancy most likely comes from differences in lattice's strains, which are much more complex in polycrystalline perovskites than in thin films.

Overall, the most important factors driving exsolution are the partial O_2 pressure but also the crystallographic orientation of the perovskite facets.

3. Alternative methods to trigger exsolution

Exsolution has been first reported on perovskites dedicated to SOFC applications. It historically has been achieved at high temperatures for a long period and under reductant atmosphere.[153] These conditions bring some constraint, for example damage to the surface of the host material. They also narrow the pool of host materials and exsolvable elements. For this reason, researchers have not ceased to explore and discover other paths to exsolute metallic nanoparticles.

3.1. Electrochemical switching

Myung *et al.*[142] worked on electrochemical switching as an alternative way to exsolute particles. Indeed, they noticed that reduction under H_2 is usually a slow process. Therefore, they used electrical current in order to bring the reducing electrons into the host structure (**Figure 20**b). The team experimented on a fuel electrode $La_{0.43}Ca_{0.37}Ni_{0.06}Ti_{0.94}O_{3-\delta}$ using an electrical bias of 2V in 50% H_2O/N_2 at 700 °C and 900 °C. They observed nearly instant formation of a large amount of exsolved nanoparticles (**Figure 20**d), whereas lower particles density was observed for reduction by hydrogen at 900 °C for 20 h (**Figure 20**c). The larger observed particle density compared to classic exsolution (6.2 X 10^{-7} Ni nanoparticles μm^{-2} *vs* 3.7 X 10^{-7} Ni nanoparticles μm^{-2}), resulted in an increased power density of the fuel cell electrode. Zhou *et al.*[154] also reported the use of this concept on the cathode material $(La_{0.8}Sr_{0.2})_{0.95}Ag_{0.05}MnO_{3-\delta}$. By applying a cathodic bias, Ag nanoparticles were exsolved, leading to an increase of the electrocatalytic activity for the ORR. Overall, electrochemical switching allows fast and extensive *operando* production of exsolved nanoparticles, making this process of huge interest for the scientific community.

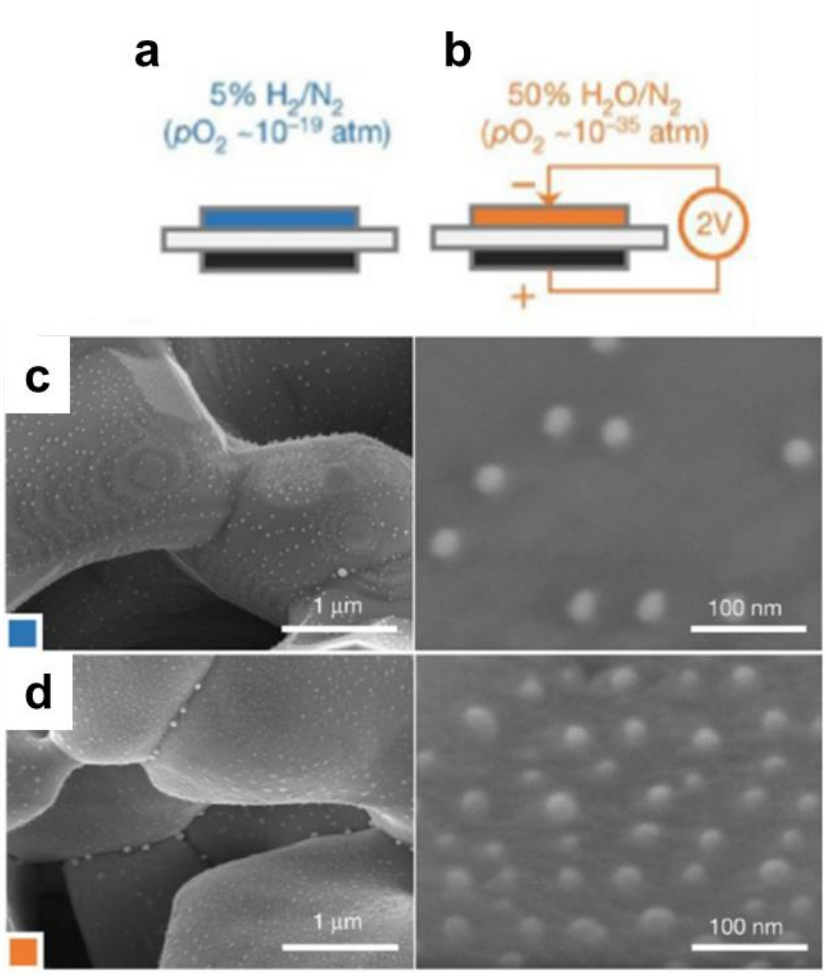

Figure 20. Conditions used to trigger exsolution in a solid oxide electrochemical cell at the fuel electrode by (a) reduction in 5% H_2/N_2 or (b) electrochemical switching while applying 2 V across the cell. (c) SEM micrographs of $La_{0.43}Ca_{0.37}Ni_{0.06}Ti_{0.94}O_{3-\delta}$ electrodes produced by reduction by hydrogen at 900 °C for 20 h and (d) electrochemical switching under 50% H_2O/N_2 at 900 °C for 150 s.[142]

3.2. Thermally induced exsolution

Thermally induced exsolution consists in heating the doped perovskite at high temperature under air. Tan *et al.*[155] triggered the exsolution of Ni nanoparticles out of $Gd_{1.5}Ni_{0.5}Ce_{0.8}O_{2-\delta}$ at 1250 °C. However, the fact no reducing atmosphere was used led to the oxidization of Ni into NiO nanoparticles at the surface. Furthermore, one should also consider that applying such high temperatures to the host structure can result in damage to the surface and/or the parent material itself. These techniques present advantages in terms of safety since no reducing gases are used, which at high temperatures are usually explosives and/or flammable. The use of vacuum can also be considered.[144] Tuning the heating rate is a simple way to tune particle size, as a high rate favors nucleation and then yields a high particles density with decreased sizes. In general

thermally induced exsolution can be considered only for temperature resistant materials and for high temperatures reaction such as chemical looping combustion or solar thermal applications.[156–158]

3.3. Heterogeneous doping

Heterogeneous doping leading to exsolution has been proposed recently by Kwak *et al.*[159] but already pointed out earlier by Harvey *et al.*[160] on $Ba_{0.5}Sr_{0.5}Co_{0.8}Fe_{0.2}O_{3-\delta}$ and by Beschnitt *et al.*[107] on non-perovskites oxides such as CeO_2 and ZrO_2. Indeed, this process consists in the insertion of metal cations (e.g. Ni into $Sm_{0.2}Ce_{0.8}O_{1.9-\delta}$) into grain boundaries of oxides (**Figure 21**a), so that there is no bulk doping. This allows to work beyond the scope of perovskites as the host does not have to be tolerant to doping. The metal source is sputtered onto the oxide followed by annealing at 700 °C under air. This treatment forces the foreign cations to disperse at the grain boundaries but not to diffuse into the bulk. A classic reductive treatment is then performed, resulting in nucleation of nanoparticles in corners of grain boundaries at the triple point "grain(I)-grain(II)-atmosphere leading to socketed particles (**Figure 21**b-c). This technique is of great interest for several reasons: the metal cations can be inserted homogenously in grain boundaries, since no diffusion of cations in the structure is involved, one could think of using a variety of oxides hosts which were so far unsuitable for exsolution. Finally grain boundaries have a larger capacity to incorporate cations than the bulk, meaning that larger densities of nanoparticles can be obtained, this is also very interesting if the cations present a low solubility into the host structure. To sum up, heterogeneous doping offers a lower exsolution temperature (700 °C) than classic homogeneous doping, a high production yield of nanoparticles but most importantly a wider number of usable structures to support exsolution.

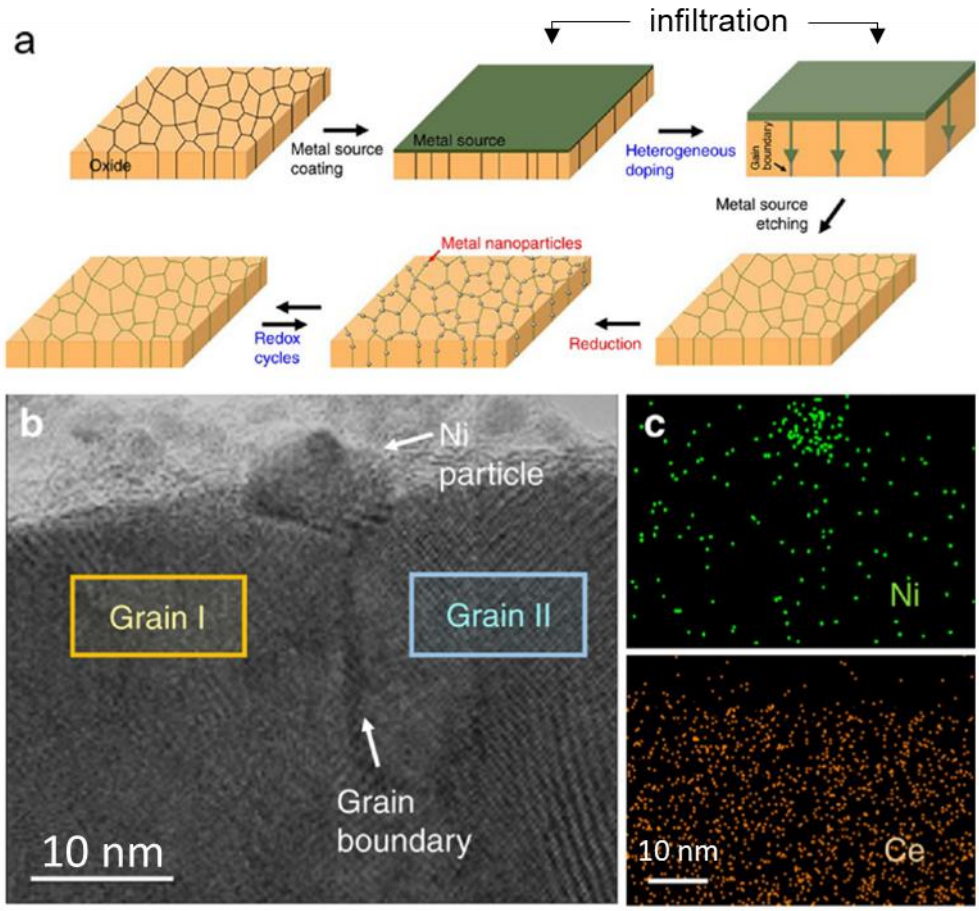

Figure 21. (a) schematic representation of the overall synthesis procedure for heterogeneous doping. (b) cross-sectional scanning transmission electron microscope (STEM) image, and (c) STEM-energy-dispersive X-ray spectroscopy (EDS) mapping results of Sn-doped CeO_2 film with a Ni particle.[159]

3.4. Topotactic exchange

Topotactic exchange relies on the stabilization of the host material by combining exsolution and doping. The usual technique for wet chemical deposition of metals at the surface of a host is the infiltration of the host/support by a liquid containing the doping metal salt, thus incorporating the metal at the surface of the host structure (**Figure 22**a).[161,162] Further thermal treatment triggers diffusion of surface deposited cations in the host structure. With this technique, various doping metal salt compositions can be introduce, representing then a major advantage *versus* simple exsolution in terms of cations diversity. As many techniques involving surface treatment, the wet chemical deposition leads to poor control over the size and distribution of particles at the opposite of exsolution which excels in formation of size controlled particles but lacks metal diversity. The combination of these two techniques was proposed by Joo *et al.*[161] under the denomination of topotactic ion exchange approach. The authors worked on $PrBaMn_{1.7}Co_{0.3}O_{3-\delta}$ systems with Fe as the infiltrating cations. In order for the topotactic ion exchange to work, the exsolvable cations must have a higher segregation energy than the infiltrating one. In this case Fe segregation energy is lower than Co (-0.15 eV *vs* -0.55 eV). Then, after reductive thermal treatment the authors observed exsolution of Co nanoparticles and the transformation of the host perovskite into $PrBaMn_{1.7}Fe_{0.3}O_{3-\delta}$. During topotactic ion exchange, the Co is exsoluted from the B site, which is filled by Fe cations, therefore no B-site vacancies are created and the stability of the host perovskite endures. In addition of the occupancy of the B-site, Fe was also reported[161] in the Co nanoparticles thus forming a Co-Fe alloy (**Figure 22**b).

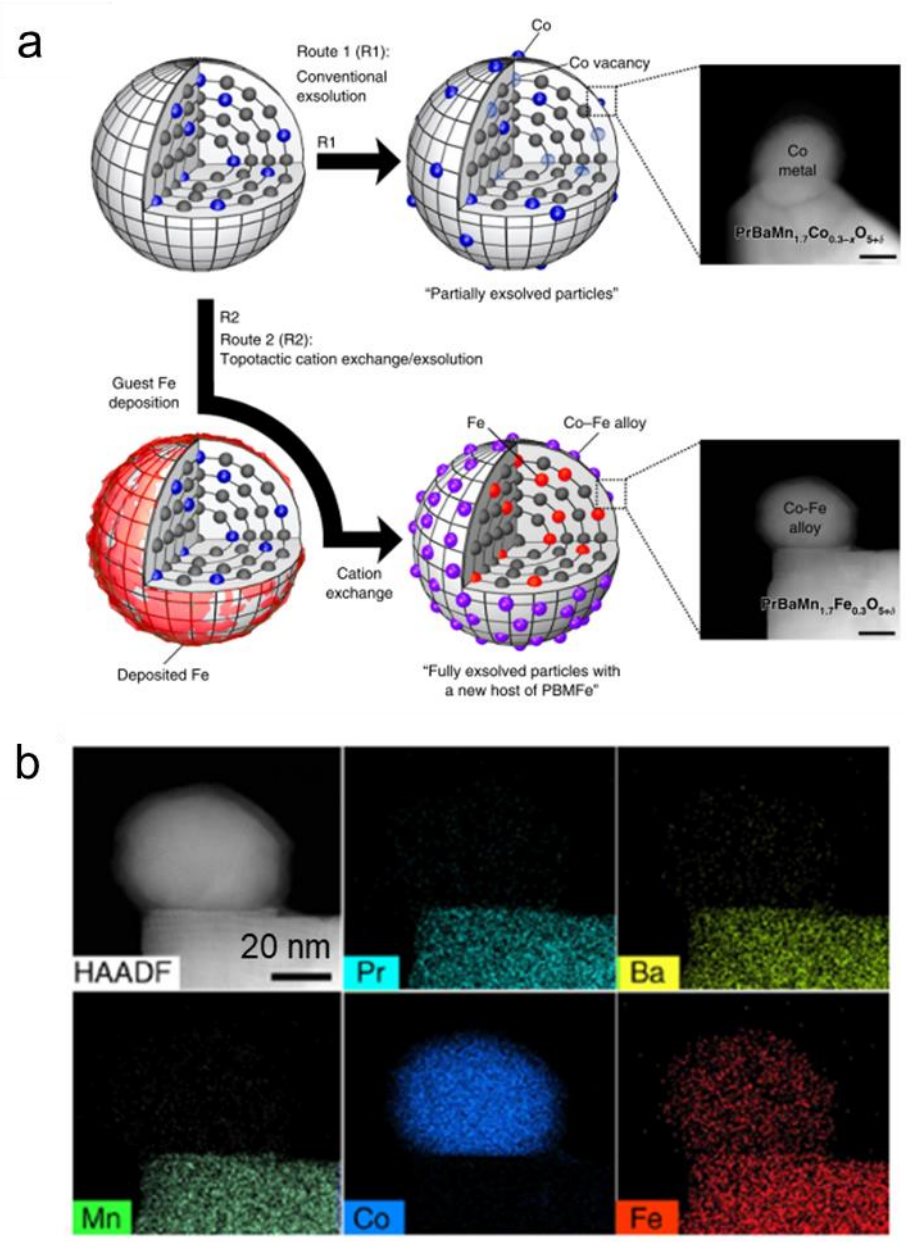

Figure 22. Topotactic ion exchange with infiltration to introduce guest cations: (a) exsolution process without and with topotactic ion exchange of Fe guest ion on $PrBaMn_{1.7}Co_{0.3}O_{5+\delta'}$. (b) EDS elemental maps of Pr, Ba, Mn, Co and Fe.[161]

Recent studies of Joo *et al.*[163] pushed the topotactic ion exchange method further by using atomic layer deposition (ALD) rather than infiltration. ALD yields uniform conformal layers independently of the morphology of the support. Moreover, this thin film technique creates high specific surface area and allows control over the rate of deposition. The authors were then able to deposit a uniform and controlled thickness layer of iron cations on to the host perovskite $La_{0.6}Sr_{0.2}Ti_{0.85}Ni_{0.15}O_{3-\delta}$. Since the diffusion rate in the host of the deposited cations is a determining factor for topotactic ion exchange, the uniformity brought out by ALD topotactic

ion exchange accelerate the exsolution and produce anchored nanoparticles of Ni-Fe alloy with an increase in the density population compared to classic exsolution.

4. Conclusion on exsolution in perovskite

Throughout this part we showed the complexity at work for the exsolution process. A phenomenon composed of four different physical steps, diffusion, reduction, nucleation, growth. The admitted mechanism for the exsolution involves reduction of cations beneath the surface of the host lattice, followed by formation pits-like structures and finally emergence of the metal particles from the pit centers.[144] This phenomenon results in particles socketed into the surface up to 30-40% of their heights.[143,146]

The exsolution process has been of high interest for the scientific community for the last two decades and thus new ways to exsolute have been proposed. The aforementioned pathways toward exsolution have all been performed on bulk perovskites systems but never on nanosized systems.

In the view to produce efficient electrocatalysts, the downscale from bulk to nanosized systems is attractive, and the exsolution process appears as a way to produce potentially enhanced electrocatalysts. However, questions can be raised: is exsolution feasible on nanosized system and will the properties of the exsolved particles be maintained? Is the mechanism observed in bulk system similar at the nanoscale? Finally, is the use of thermal treatments and reducing atmospheres a requirement to the formation of exsolved particles or could some other stimuli provoke the exsolution? In chapter IV we address these questions by using nano-objects as support to the exsolution.

V.Conclusion

In this chapter we provided the basic understanding for the magnetic properties of manganese perovskites through the example of the colossal magnetoresistance and the electronic phase separation. The determining factors of these magnetic properties have been highlighted by a thorough study of the literature. Thus, we showed that these properties are directly related to the electronic conductivity of manganese perovskite and how the use of external stimuli could change it through the case study of $La_{0.7}Sr_{0.3}MnO_3$. In a second part we showed how pivotal can be the use of manganese perovskite as electrocatalysts for the oxygen reduction reaction and what advantages the use of magnetic field can bring to the kinetics reaction. Finally, the

use of other stimuli towards the formation of new electrocatalysts is shown via the exsolution process.

In the following chapters of this manuscript, we will first show the synthesis of a new nano-electrocatalysts $La_{0.33}Pr_{0.33}Ca_{0.33}MnO_3$ (LPCMO), chosen for its peculiar magnetic properties. The benefits of the use of magnetic fields to directly stimulate the magnetic properties of LPCMO during electrocatalysis is presented in preliminary results. We will then investigate the effect of the magnetic field during ORR with $La_{0.7}Sr_{0.3}MnO_3$. Finally, the exsolution process will demonstrated at the nanoscale contrary to the literature on bulk perovskites. Indeed, we will present a guide through the exsolution at the nanoscale by using different external stimuli to produce new electrocatalysts This chapter enlighten the differences and advantages that nanosized object have for being tune by external stimuli.

References

(1) Rao, C. N. R. Colossal Magnetoresistance in Rare Earth Manganates. *Mater. Today* **1998**, *1* (3), 9–13. https://doi.org/10.1016/s1369-7021(98)80004-7.

(2) Loktev, V. M.; Pogorelov, Y. G. Peculiar Physical Properties and the Colossal Magnetoresistance of Manganites (Review). *Low Temp. Phys.* **2000**, *26* (3), 171–193. https://doi.org/10.1063/1.593890.

(3) Fontcuberta, J.; Martínez, B.; Seffar, A.; Piñol, S.; García-Muñoz, J. L.; Obradors, X. Colossal Magnetoresistance of Ferromagnetic Manganites: Structural Tuning and Mechanisms. *Phys. Rev. Lett.* **1996**, *76* (7), 1122–1125. https://doi.org/10.1103/PhysRevLett.76.1122.

(4) Tokura, Y.; Tomioka, Y.; Kuwahara, H.; Asamitsu, A.; Moritomo, Y.; Kasai, M. Origins of Colossal Magnetoresistance in Perovskite-Type Manganese Oxides (Invited). *J. Appl. Phys.* **1996**, *79* (8 PART 2A), 5288–5291. https://doi.org/10.1063/1.361353.

(5) Rodriguez-Martinez, L. M.; Attfield, J. P. Cation Disorder and Size Effects in Magnetoresistive Manganese Oxide Perovskites. *Phys. Rev. B - Condens. Matter Mater. Phys.* **1996**, *54* (22), R15622–R15625. https://doi.org/10.1103/PhysRevB.54.R15622.

(6) Moreo, A.; Verges, J.; Dagotto, E. Phase Separation Scenario for Manganese Oxides. *J. Magn. Magn. Mater.* **2001**, *226–230* (March), 773–774. https://doi.org/10.1016/S0304-8853(00)00745-9.

(7) Shao, J.; Liu, H.; Zhang, K.; Yu, Y.; Yu, W.; Lin, H.; Niu, J.; Du, K.; Kou, Y.; Wei, W.; Lan, F.; Zhu, Y.; Wang, W.; Xiao, J.; Plummer, E. W.; Yin, L.; Shen, J. Emerging Single-Phase State in Small Manganite Nanodisks. *Proc. Natl. Acad. Sci. U. S. A.* **2016**, *113* (33), 9228–9231. https://doi.org/10.1073/pnas.1609656113.

(8) Zhu, Y.; Du, K.; Niu, J.; Lin, L.; Wei, W.; Liu, H.; Lin, H.; Zhang, K.; Yang, T.; Kou, Y.; Shao, J.; Gao, X.; Xu, X.; Wu, X.; Dong, S.; Yin, L.; Shen, J. Chemical Ordering Suppresses Large-Scale Electronic Phase Separation in Doped Manganites. *Nat. Commun.* **2016**, *7*, 1–6. https://doi.org/10.1038/ncomms11260.

(9) Liang, L.; Li, L.; Wu, H.; Zhu, X. Research Progress on Electronic Phase Separation in Low-Dimensional Perovskite Manganite Nanostructures. *Nanoscale Res. Lett.* **2014**, *9* (1), 1–14. https://doi.org/10.1186/1556-276X-9-325.

(10) Urushibara, A.; Moritomo, Y.; Arima, T.; Asamitsu, A.; Kido, G.; Tokura, Y. Insulator-Metal Transition and Giant Magnetoresistance in $La_{1-X}Sr_xMnO_3$. *Phys. Rev. B* **1995**, *51* (20), 14103–14109. https://doi.org/10.1103/PhysRevB.51.14103.

(11) J.-H. Park; C. T. Chen; S-W. Cheong; W. Bao; G. Meigs; V. Chakarian; Y. U. Idzerda. Electronic Aspects of the Ferromagnetic Transition in Manganese Perovskites. *Phys. Rev. Lett.* **1996**, *76*, 4215.

(12) Kuwahara, H.; Tomioka, Y.; Moritomo, Y.; Asamitsu, A.; Kasai, M. Striction-Coupled Magnetoresistance in Perovskite-Type Manganese Oxides. *Science (80-.).* **2011**, *142* (3599), 1568–1569.

(13) Ward, T. Z.; Budai, J. D.; Gai, Z.; Tischler, J. Z.; Yin, L.; Shen, J. Elastically Driven Anisotropic Percolation in Electronic Phase-Separated Manganites. *Nat. Phys.* **2009**, *5* (12), 885–888. https://doi.org/10.1038/nphys1419.

(14) Jonker, G. H.; Van Santen, J. H. Ferromagnetic Compounds of Manganese with Perovskite Structure. *Physica* **1950**, *16* (3), 337–349. https://doi.org/10.1016/0031-8914(50)90033-4.

(15) Thi N'Goc, H. Le; Mouafo, L. D. N.; Etrillard, C.; Torres-Pardo, A.; Dayen, J. F.; Rano, S.; Rousse, G.; Laberty-Robert, C.; Calbet, J. G.; Drillon, M.; Sanchez, C.; Doudin, B.; Portehault, D. Surface-Driven Magnetotransport in Perovskite Nanocrystals. *Adv. Mater.* **2017**, *29* (9), 1–9. https://doi.org/10.1002/adma.201604745.

(16) Alonso, J. A.; Martínez-Lope, M. J.; Casais, M. T.; Fernández-Díaz, M. T. Evolution of the Jahn-Teller Distortion of MnO_6 Octahedra in $RMnO_3$ Perovskites (R = Pr, Nd, Dy, Tb, Ho, Er, Y): A Neutron Diffraction Study. *Inorg. Chem.* **2000**, *39* (5), 917–923. https://doi.org/10.1021/ic990921e.

(17) Belich, N.; Udalova, N.; Semenova, A.; Petrov, A.; Fateev, S.; Tarasov, A.; Goodilin, E. Perovskite Puzzle for Revolutionary Functional Materials. *Front. Chem.* **2020**, *8* (November), 1–9. https://doi.org/10.3389/fchem.2020.550625.

(18) Zhong, W.; Au, C. T.; Du, Y. W. Review of Magnetocaloric Effect in Perovskite-Type Oxides. *Chinese Phys. B* **2013**, *22* (5). https://doi.org/10.1088/1674-1056/22/5/057501.

(19) Asamitsu, A.; Moritomo, Y.; Tomioka, Y.; Arimat, T.; Tokura, Y. A Structural Phase Transition Induced by an External Magnetic Field. *Nature* **1995**, *373* (6513), 407–409.

https://doi.org/10.1038/373407a0.

(20) Martin, M. C.; Shirane, G.; Endoh, Y.; Hirota, K. Magnetism and Structural Distortion in $La_{0.7}Sr_{0.3}MnO_3$ Metallic Ferromagnet. *Phys. Rev. B - Condens. Matter Mater. Phys.* **1996**, *53* (21), 14285–14290. https://doi.org/10.1103/PhysRevB.53.14285.

(21) Nowotny, H.; Jeitschko, W.; Goretzki, H. Die Kristallstruktur Yon V_2PC Und V_5P_3N. *Monatshefte für Chemie* **1968**, *675*, 672–675.

(22) Damay, F.; Martin, C.; Maignan, A.; Raveau, B. Cation Disorder and Size Effects upon Magnetic Transitions in $Ln_{0.5}A_{0.5}MnO_3$ Manganites. *J. Appl. Phys.* **1997**, *82* (12), 6181–6185. https://doi.org/10.1063/1.366543.

(23) Matsumoto, H.; Sato, E. Electrocatalytic Properties of Transition Metal Oxides for Oxygen Evolution Reaction. *Mater. Chem. Phys.* **1986**, *14*, 397–426.

(24) Hwang, H. Y.; Cheong, S. W.; Radaelli, P. G.; Marezio, M.; Batlogg, B. Lattice Effects on the Magnetoresistance in Doped $LaMnO_3$. *Phys. Rev. Lett.* **1995**, *75* (5), 914–917. https://doi.org/10.1103/PhysRevLett.75.914.

(25) Attfield, J. P. A Simple Approach to Lattice Effects in Conducting Perovskite-Type Oxides. *Chem. Mater.* **1998**, *10* (11), 3239–3248. https://doi.org/10.1021/cm980221s.

(26) Guo, Z. B.; Du, Y. W.; Zhu, J. S.; Huang, H.; Ding, W. P.; Feng, D. Large Magnetic Entropy Change in Perovskite-Type Manganese Oxides. *Phys. Rev. Lett.* **1997**, *78* (6), 1142–1145. https://doi.org/10.1103/PhysRevLett.78.1142.

(27) Liu, T.; Zhao, Y.; Zhang, X.; Zhang, H.; Jiang, G.; Zhao, W.; Guo, J.; Chen, F.; Yan, M.; Zhang, Y.; Wang, Y. Robust Redox-Reversible Perovskite Type Steam Electrolyser Electrode Decorated with: In Situ Exsolved Metallic Nanoparticles. *J. Mater. Chem. A* **2020**, *8* (2), 582–591. https://doi.org/10.1039/c9ta06309a.

(28) Boschker, H.; Huijben, M.; Vailionis, A.; Verbeeck, J.; Van Aert, S.; Luysberg, M.; Bals, S.; Van Tendeloo, G.; Houwman, E. P.; Koster, G.; Blank, D. H. A.; Rijnders, G. Optimized Fabrication of High-Quality $La_{0.67}Sr_{0.33}MnO_3$ Thin Films Considering All Essential Characteristics. *J. Phys. D. Appl. Phys.* **2011**, *44* (20). https://doi.org/10.1088/0022-3727/44/20/205001.

(29) Ghivelder, L.; Parisi, F. Dynamic Phase Separation in $La_{5/8-y}Pr_yCa_{3/8}MnO_3$. *Phys. Rev. B - Condens. Matter Mater. Phys.* **2005**, *71* (18), 1–6.

https://doi.org/10.1103/PhysRevB.71.184425.

(30) Yunoki, S.; Hu, J.; Malvezzi, A. L.; Moreo, A.; Furukawa, N.; Dagotto, E. Phase Separation in Electronic Models for Manganites. *Phys. Rev. Lett.* **1998**, *80* (4), 845–848. https://doi.org/10.1103/PhysRevLett.80.845.

(31) Zhang, T.; Wang, X. P.; Fang, Q. F.; Li, X. G. Magnetic and Charge Ordering in Nanosized Manganites. *Appl. Phys. Rev.* **2014**, *1* (3). https://doi.org/10.1063/1.4895117.

(32) Valencia, S.; Peña, L.; Konstantinovic, Z.; Balcells, L.; Galceran, R.; Schmitz, D.; Sandiumenge, F.; Casanove, M.; Martínez, B. Intrinsic Antiferromagnetic/Insulating Phase at Manganite Surfaces and Interfaces. *J. Phys. Condens. Matter* **2014**, *26* (16). https://doi.org/10.1088/0953-8984/26/16/166001.

(33) Dulli, H.; Dowben, P. A.; Liou, S. H.; Plummer, E. W. Surface Segregation and Restructuring of Colossal-Magnetoresistant Manganese Perovskites $La_{0.65}Sr_{0.35}MnO_3$. *Phys. Rev. B - Condens. Matter Mater. Phys.* **2000**, *62* (22), R14629–R14632. https://doi.org/10.1103/PhysRevB.62.R14629.

(34) Nørskov, J. K.; Rossmeisl, J.; Logadottir, A.; Lindqvist, L.; Kitchin, J. R.; Bligaard, T.; Jónsson, H. Origin of the Overpotential for Oxygen Reduction at a Fuel-Cell Cathode. *J. Phys. Chem. B* **2004**, *108* (46), 17886–17892. https://doi.org/10.1021/jp047349j.

(35) Wang, H.; Xu, W.; Richins, S.; Liaw, K.; Yan, L.; Zhou, M.; Luo, H. Polymer-Assisted Approach to $LaCo_{1-x}Ni_xO_3$ Network Nanostructures as Bifunctional Oxygen Electrocatalysts. *Electrochim. Acta* **2019**, *296*, 945–953. https://doi.org/10.1016/j.electacta.2018.11.075.

(36) Xu, X.; Wang, W.; Zhou, W.; Shao, Z. Recent Advances in Novel Nanostructuring Methods of Perovskite Electrocatalysts for Energy-Related Applications. *Small Methods* **2018**, *2* (7), 1–35. https://doi.org/10.1002/smtd.201800071.

(37) Stoerzinger, K. A.; Risch, M.; Han, B.; Shao-Horn, Y. Recent Insights into Manganese Oxides in Catalyzing Oxygen Reduction Kinetics. *ACS Catal.* **2015**, *5* (10), 6021–6031. https://doi.org/10.1021/acscatal.5b01444.

(38) Suntivich, J.; Gasteiger, H. A.; Yabuuchi, N.; Shao-Horn, Y. Electrocatalytic Measurement Methodology of Oxide Catalysts Using a Thin-Film Rotating Disk Electrode. *J. Electrochem. Soc.* **2010**, *157* (8), B1263.

https://doi.org/10.1149/1.3456630.

(39) Peña, M. A.; Fierro, J. L. G. Chemical Structures and Performance of Perovskite Oxides. *Chem. Rev.* **2001**, *101* (7), 1981–2017. https://doi.org/10.1021/cr980129f.

(40) Lima, F. H. B.; Calegaro, M. L.; Ticianelli, E. A. Electrocatalytic Activity of Manganese Oxides Prepared by Thermal Decomposition for Oxygen Reduction. *Electrochim. Acta* **2007**, *52* (11), 3732–3738. https://doi.org/10.1016/j.electacta.2006.10.047.

(41) Roche, I.; Chaînet, E.; Chatenet, M.; Vondrák, J. Carbon-Supported Manganese Oxide Nanoparticles as Electrocatalysts for the Oxygen Reduction Reaction (ORR) in Alkaline Medium: Physical Characterizations and ORR Mechanism. *J. Phys. Chem. C* **2007**, *111* (3), 1434–1443. https://doi.org/10.1021/jp0647986.

(42) Cheng, F.; Shen, J.; Ji, W.; Tao, Z.; Chen, J. Selective Synthesis of Manganese Oxide Nanostructures for Electrocatalytic Oxygen Reduction. *ACS Appl. Mater. Interfaces* **2009**, *1* (2), 460–466. https://doi.org/10.1021/am800131v.

(43) Cheng, F.; Su, Y.; Liang, J.; Tao, Z.; Chen, J. MnO_2-Based Nanostructures as Catalysts for Electrochemical Oxygen Reduction in Alkaline Media. *Chem. Mater.* **2010**, *22* (3), 898–905. https://doi.org/10.1021/cm901698s.

(44) Mao, L.; Zhang, D.; Sotomura, T.; Nakatsu, K.; Koshiba, N.; Ohsaka, T. Mechanistic Study of the Reduction of Oxygen in Air Electrode with Manganese Oxides as Electrocatalysts. *Electrochim. Acta* **2003**, *48* (8), 1015–1021. https://doi.org/10.1016/S0013-4686(02)00815-0.

(45) El-Deab, M. S.; Ohsaka, T. Manganese Oxide Nanoparticles Electrodeposited on Platinum Are Superior to Platinum for Oxygen Reduction. *Angew. Chemie - Int. Ed.* **2006**, *45* (36), 5963–5966. https://doi.org/10.1002/anie.200600692.

(46) Kinoshita, K. *Electrochemical Oxygen Technology*; Wiley: New York, 1992.

(47) Suntivich, J.; Gasteiger, H. A.; Yabuuchi, N.; Nakanishi, H.; Goodenough, J. B.; Shao-Horn, Y. Design Principles for Oxygen-Reduction Activity on Perovskite Oxide Catalysts for Fuel Cells and Metal-Air Batteries. *Nat. Chem.* **2011**, *3* (7), 546–550. https://doi.org/10.1038/nchem.1069.

(48) Hong, W. T.; Risch, M.; Stoerzinger, K. A.; Grimaud, A.; Suntivich, J.; Shao-Horn, Y. Toward the Rational Design of Non-Precious Transition Metal Oxides for Oxygen

Electrocatalysis. *Energy Environ. Sci.* **2015**, *8* (5), 1404–1427. https://doi.org/10.1039/c4ee03869j.

(49) Goodenough, J. B.; Manoharan, R.; Paranthaman, M. Surface Protonation and Electrochemical Activity of Oxides in Aqueous Solution. *J. Am. Chem. Soc.* **1990**, *112* (6), 2076–2082. https://doi.org/10.1021/ja00162a006.

(50) Fabbri, E.; Mohamed, R.; Levecque, P.; Conrad, O.; Kötz, R.; Schmidt, T. J. Perovskite and Carbon toward Oxygen Reduction in Alkaline Media. *ACS Catal.* **2014**.

(51) Miyahara, Y.; Miyazaki, K.; Fukutsuka, T.; Abe, T. Catalytic Roles of Perovskite Oxides in Electrochemical Oxygen Reactions in Alkaline Media. *J. Electrochem. Soc.* **2014**, *161* (6), F694–F697. https://doi.org/10.1149/2.019406jes.

(52) Chen, D.; Chen, C.; Baiyee, Z. M.; Shao, Z.; Ciucci, F. Nonstoichiometric Oxides as Low-Cost and Highly-Efficient Oxygen Reduction/Evolution Catalysts for Low-Temperature Electrochemical Devices. *Chem. Rev.* **2015**, *115* (18), 9869–9921. https://doi.org/10.1021/acs.chemrev.5b00073.

(53) Poux, T.; Bonnefont, A.; Kéranguéven, G.; Tsirlina, G. A.; Savinova, E. R. Electrocatalytic Oxygen Reduction Reaction on Perovskite Oxides: Series versus Direct Pathway. *ChemPhysChem* **2014**, *15* (10), 2108–2120. https://doi.org/10.1002/cphc.201402022.

(54) Roche, I.; Chaînet, E.; Chatenet, M.; Vondrák, J. Durability of Carbon-Supported Manganese Oxide Nanoparticles for the Oxygen Reduction Reaction (ORR) in Alkaline Medium. *J. Appl. Electrochem.* **2008**, *38* (9), 1195–1201. https://doi.org/10.1007/s10800-008-9537-z.

(55) Bidault, F.; Brett, D. J. L.; Middleton, P. H.; Brandon, N. P. Review of Gas Diffusion Cathodes for Alkaline Fuel Cells. *J. Power Sources* **2009**, *187* (1), 39–48. https://doi.org/10.1016/j.jpowsour.2008.10.106.

(56) Trogadas, P.; Fuller, T. F.; Strasser, P. Carbon as Catalyst and Support for Electrochemical Energy Conversion. *Carbon N. Y.* **2014**, *75*, 5–42. https://doi.org/10.1016/j.carbon.2014.04.005.

(57) Ramaswamy, N.; Hakim, N.; Mukerjee, S. Degradation Mechanism Study of Perfluorinated Proton Exchange Membrane under Fuel Cell Operating Conditions.

Electrochim. Acta **2008**, *53* (8), 3279–3295. https://doi.org/10.1016/j.electacta.2007.11.010.

(58) Chen, C.; Levitin, G.; Hess, D. W.; Fuller, T. F. XPS Investigation of Nafion® Membrane Degradation. *J. Power Sources* **2007**, *169* (2), 288–295. https://doi.org/10.1016/j.jpowsour.2007.03.037.

(59) Ruvinskiy, P. S.; Bonnefont, A.; Pham-Huu, C.; Savinova, E. R. Using Ordered Carbon Nanomaterials for Shedding Light on the Mechanism of the Cathodic Oxygen Reduction Reaction. *Langmuir* **2011**, *27* (14), 9018–9027. https://doi.org/10.1021/la2006343.

(60) Gupta, S.; Kellogg, W.; Xu, H.; Liu, X.; Cho, J.; Wu, G. Bifunctional Perovskite Oxide Catalysts for Oxygen Reduction and Evolution in Alkaline Media. *Chem. - An Asian J.* **2016**, *11* (1), 10–21. https://doi.org/10.1002/asia.201500640.

(61) Hyodo, T.; Hayashi, M.; Miura, N.; Yamazoe, N. Catalytic Activities of Rare-Earth Manganites for Cathodic Reduction of Oxygen in Alkaline Solution. *J. Electrochem. Soc.* **1996**, *143* (11), L266–L267. https://doi.org/10.1149/1.1837229.

(62) Töpfer, J.; Goodenough, J. B. LaMnO3+δRevisited. *J. Solid State Chem.* **1997**, *130* (1), 117–128. https://doi.org/10.1006/jssc.1997.7287.

(63) Stoerzinger, K. A.; Lü, W.; Li, C.; Ariando; Venkatesan, T.; Shao-Horn, Y. Highly Active Epitaxial $La_{(1-x)}Sr_xMnO_3$ Surfaces for the Oxygen Reduction Reaction: Role of Charge Transfer. *J. Phys. Chem. Lett.* **2015**, *6* (8), 1435–1440. https://doi.org/10.1021/acs.jpclett.5b00439.

(64) Yuasa, M.; Nishida, M.; Kida, T.; Yamazoe, N.; Shimanoe, K. Bi-Functional Oxygen Electrodes Using $LaMnO_3/LaNiO_3$ for Rechargeable Metal-Air Batteries. *J. Electrochem. Soc.* **2011**, *158* (5), A605. https://doi.org/10.1149/1.3562564.

(65) Bockris, J. O.; Otagawa, T. The Electrocatalysis of Oxygen Evolution on Perovskites. *J. Electrochem. Soc.* **1984**, *131* (2), 290–302. https://doi.org/10.1149/1.2115565.

(66) Fernndez, E. M.; Moses, P. G.; Toftelund, A.; Hansen, H. A.; Martínez, J. I.; Abild-Pedersen, F.; Kleis, J.; Hinnemann, B.; Rossmeisl, J.; Bligaard, T.; Nørskov, J. K. Scaling Relationships for Adsorption Energies on Transition Metal Oxide, Sulfide, and Nitride Surfaces. *Angew. Chemie - Int. Ed.* **2008**, *47* (25), 4683–4686. https://doi.org/10.1002/anie.200705739.

(67) Zhao, B.; Zhang, L.; Zhen, D.; Yoo, S.; Ding, Y.; Chen, D.; Chen, Y.; Zhang, Q.; Doyle, B.; Xiong, X.; Liu, M. A Tailored Double Perovskite Nanofiber Catalyst Enables Ultrafast Oxygen Evolution. *Nat. Commun.* **2017**, *8*, 1–9. https://doi.org/10.1038/ncomms14586.

(68) Miyazaki, K.; Kawakita, K. I.; Abe, T.; Fukutsuka, T.; Kojima, K.; Ogumi, Z. Single-Step Synthesis of Nano-Sized Perovskite-Type Oxide/Carbon Nanotube Composites and Their Electrocatalytic Oxygen-Reduction Activities. *J. Mater. Chem.* **2011**, *21* (6), 1913–1917. https://doi.org/10.1039/c0jm02600j.

(69) Wang, M.; Wang, Z.; Guo, Z. Water Electrolysis Enhanced by Super Gravity Field for Hydrogen Production. *Int. J. Hydrogen Energy* **2010**, *35* (8), 3198–3205. https://doi.org/10.1016/j.ijhydene.2010.01.128.

(70) Wang, M.; Wang, Z.; Guo, Z. Understanding of the Intensified Effect of Super Gravity on Hydrogen Evolution Reaction. *Int. J. Hydrogen Energy* **2009**, *34* (13), 5311–5317. https://doi.org/10.1016/j.ijhydene.2009.05.043.

(71) Wang, M.; Wang, Z.; Guo, Z.; Li, Z. The Enhanced Electrocatalytic Activity and Stability of NiW Films Electrodeposited under Super Gravity Field for Hydrogen Evolution Reaction. *Int. J. Hydrogen Energy* **2011**, *36* (5), 3305–3312. https://doi.org/10.1016/j.ijhydene.2010.12.116.

(72) Zheng, Z.; Tachikawa, T.; Majima, T. Plasmon-Enhanced Formic Acid Dehydrogenation Using Anisotropic Pd-Au Nanorods Studied at the Single-Particle Level. *J. Am. Chem. Soc.* **2015**, *137* (2), 948–957. https://doi.org/10.1021/ja511719g.

(73) Shi, Y.; Wang, J.; Wang, C.; Zhai, T. T.; Bao, W. J.; Xu, J. J.; Xia, X. H.; Chen, H. Y. Hot Electron of Au Nanorods Activates the Electrocatalysis of Hydrogen Evolution on MoS_2 Nanosheets. *J. Am. Chem. Soc.* **2015**, *137* (23), 7365–7370. https://doi.org/10.1021/jacs.5b01732.

(74) Liu, G.; Wang, T.; Zhou, W.; Meng, X.; Zhang, H.; Liu, H.; Kako, T.; Ye, J. Crystal-Facet-Dependent Hot-Electron Transfer in Plasmonic-Au/Semiconductor Heterostructures for Efficient Solar Photocatalysis. *J. Mater. Chem. C* **2015**, *3* (29), 7538–7542. https://doi.org/10.1039/c5tc01406a.

(75) Mubeen, S.; Hernandez-Sosa, G.; Moses, D.; Lee, J.; Moskovits, M. Plasmonic Photosensitization of a Wide Band Gap Semiconductor: Converting Plasmons to Charge

Carriers. *Nano Lett.* **2011**, *11* (12), 5548–5552. https://doi.org/10.1021/nl203457v.

(76) Lee, J.; Mubeen, S.; Ji, X.; Stucky, G. D.; Moskovits, M. Plasmonic Photoanodes for Solar Water Splitting with Visible Light. *Nano Lett.* **2012**, *12* (9), 5014–5019. https://doi.org/10.1021/nl302796f.

(77) Liu, G.; Li, P.; Zhao, G.; Wang, X.; Kong, J.; Liu, H.; Zhang, H.; Chang, K.; Meng, X.; Kako, T.; Ye, J. Promoting Active Species Generation by Plasmon-Induced Hot-Electron Excitation for Efficient Electrocatalytic Oxygen Evolution. *J. Am. Chem. Soc.* **2016**, *138* (29), 9128–9136. https://doi.org/10.1021/jacs.6b05190.

(78) Xu, J.; Gu, P.; Birch, D. J. S.; Chen, Y. Plasmon-Promoted Electrochemical Oxygen Evolution Catalysis from Gold Decorated MnO_2 Nanosheets under Green Light. *Adv. Funct. Mater.* **2018**, *28* (31). https://doi.org/10.1002/adfm.201801573.

(79) Niether, C.; Faure, S.; Bordet, A.; Deseure, J.; Chatenet, M.; Carrey, J.; Chaudret, B.; Rouet, A. Improved Water Electrolysis Using Magnetic Heating of FeC-Ni Core-Shell Nanoparticles. *Nat. Energy* **2018**, *3* (6), 476–483. https://doi.org/10.1038/s41560-018-0132-1.

(80) Masa, J.; Andronescu, C.; Antoni, H.; Sinev, I.; Seisel, S.; Elumeeva, K.; Barwe, S.; Marti-Sanchez, S.; Arbiol, J.; Roldan Cuenya, B.; Muhler, M.; Schuhmann, W. Role of Boron and Phosphorus in Enhanced Electrocatalytic Oxygen Evolution by Nickel Borides and Nickel Phosphides. *ChemElectroChem* **2019**, *6* (1), 235–240. https://doi.org/10.1002/celc.201800669.

(81) Monzon, L. M. A.; Coey, J. M. D. Magnetic Fields in Electrochemistry: The Lorentz Force. A Mini-Review. *Electrochem. commun.* **2014**, *42*, 38–41. https://doi.org/10.1016/j.elecom.2014.02.006.

(82) Mohan, S.; Saravanan, G.; Bund, A. Role of Magnetic Forces in Pulse Electrochemical Deposition of Ni-nanoAl_2O_3 Composites. *Electrochim. Acta* **2012**, *64*, 94–99. https://doi.org/10.1016/j.electacta.2011.12.123.

(83) Lin, M. Y.; Hourng, L. W.; Kuo, C. W. The Effect of Magnetic Force on Hydrogen Production Efficiency in Water Electrolysis. *Int. J. Hydrogen Energy* **2012**, *37* (2), 1311–1320. https://doi.org/10.1016/j.ijhydene.2011.10.024.

(84) Lin, M. Y.; Hourng, L. W.; Hsu, J. S. The Effects of Magnetic Field on the Hydrogen

Production by Multielectrode Water Electrolysis. *Energy Sources, Part A Recover. Util. Environ. Eff.* **2017**, *39* (3), 352–357. https://doi.org/10.1080/15567036.2016.1217289.

(85) Zhang, Y.; Liang, C.; Wu, J.; Liu, H.; Zhang, B.; Jiang, Z.; Li, S.; Xu, P. Recent Advances in Magnetic Field-Enhanced Electrocatalysis. *ACS Appl. Energy Mater.* **2020**, *3* (11), 10303–10316. https://doi.org/10.1021/acsaem.0c02104.

(86) Dodoo, J.; Stokes, A. A. Field-Induced Shaping of Sessile Paramagnetic Drops. *Phys. Fluids* **2020**, *32* (6). https://doi.org/10.1063/5.0011612.

(87) Latikka, M.; Backholm, M.; Timonen, J. V. I.; Ras, R. H. A. Wetting of Ferrofluids: Phenomena and Control. *Curr. Opin. Colloid Interface Sci.* **2018**, *36* (January), 118–129. https://doi.org/10.1016/j.cocis.2018.04.003.

(88) Afkhami, S.; Tyler, A. J.; Renardy, Y.; Renardy, M.; St. Pierre, T. G.; Woodward, R. C.; Riffle, J. S. Deformation of a Hydrophobic Ferrofluid Droplet Suspended in a Viscous Medium under Uniform Magnetic Fields. *J. Fluid Mech.* **2010**, *663*, 358–384. https://doi.org/10.1017/S0022112010003551.

(89) Theis-Bröhl, K.; Gutfreund, P.; Vorobiev, A.; Wolff, M.; Toperverg, B. P.; Dura, J. A.; Borchers, J. A. Self Assembly of Magnetic Nanoparticles at Silicon Surfaces. *Soft Matter* **2015**, *11* (23), 4695–4704. https://doi.org/10.1039/c5sm00484e.

(90) Dunne, P.; Coey, J. M. D. Influence of a Magnetic Field on the Electrochemical Double Layer. *J. Phys. Chem. C* **2019**, *123* (39), 24181–24192. https://doi.org/10.1021/acs.jpcc.9b07534.

(91) Lioubashevski, O.; Katz, E.; Willner, I. Effects of Magnetic Field Directed Orthogonally to Surfaces on Electrochemical Processes. *J. Phys. Chem. C* **2007**, *111* (16), 6024–6032. https://doi.org/10.1021/jp069055z.

(92) Ragsdale, S. R.; Grant, K. M.; White, H. S. Electrochemically Generated Magnetic Forces. Enhanced Transport of a Paramagnetic Redox Species in Large, Nonuniform Magnetic Fields. *J. Am. Chem. Soc.* **1998**, *120* (51), 13461–13468. https://doi.org/10.1021/ja982540q.

(93) Monzon, L. M. A.; Coey, J. M. D. Magnetic Fields in Electrochemistry: The Kelvin Force. A Mini-Review. *Electrochem. commun.* **2014**, *42*, 42–45. https://doi.org/10.1016/j.elecom.2014.02.005.

(94) Dunne, P.; Coey, J. M. D. Patterning Metallic Electrodeposits with Magnet Arrays. *Phys. Rev. B - Condens. Matter Mater. Phys.* **2012**, *85* (22), 1–21. https://doi.org/10.1103/PhysRevB.85.224411.

(95) Wang, L. B.; Wakayama, N. I.; Okada, T. Numerical Simulation of a New Water Management for PEM Fuel Cell Using Magnet Particles Deposited in the Cathode Side Catalyst Layer. *Electrochem. commun.* **2002**, *4* (7), 584–588. https://doi.org/10.1016/S1388-2481(02)00383-1.

(96) Wang, L. B.; Wakayama, N. I.; Okada, T. Numerical Simulation of Enhancement of Mass Transfer in the Cathode Electrode of a PEM Fuel Cell by Magnet Particles Deposited in the Cathode-Side Catalyst Layer. *Chem. Eng. Sci.* **2005**, *60* (16), 4453–4467. https://doi.org/10.1016/j.ces.2005.03.007.

(97) Shi, J.; Xu, H.; Lu, L.; Sun, X. Study of Magnetic Field to Promote Oxygen Transfer and Its Application in Zinc-Air Fuel Cells. *Electrochim. Acta* **2013**, *90*, 44–52. https://doi.org/10.1016/j.electacta.2012.11.088.

(98) Shi, J.; Xu, H.; Zhao, H.; Lu, L.; Wu, X. Preparation of $Nd_2Fe_{14}B$/C Magnetic Powder and Its Application in Proton Exchange Membrane Fuel Cells. *J. Power Sources* **2014**, *252*, 189–199. https://doi.org/10.1016/j.jpowsour.2013.11.106.

(99) Shi, J.; Xu, H.; Zhao, H.; Lu, L. Synthesis and Properties of Fe_3O_4/Polyaniline and Its Tiny Magnetic Field Functions during Oxygen Transfer Processes. *J. Power Sources* **2012**, *205*, 129–135. https://doi.org/10.1016/j.jpowsour.2012.01.046.

(100) Monzon, L. M. A.; Rode, K.; Venkatesan, M.; Coey, J. M. D. Electrosynthesis of Iron, Cobalt, and Zinc Microcrystals and Magnetic Enhancement of the Oxygen Reduction Reaction. *Chem. Mater.* **2012**, *24* (20), 3878–3885. https://doi.org/10.1021/cm301766s.

(101) Chaure, N. B.; Rhen, F. M. F.; Hilton, J.; Coey, J. M. D. Design and Application of a Magnetic Field Gradient Electrode. *Electrochem. commun.* **2007**, *9* (1), 155–158. https://doi.org/10.1016/j.elecom.2006.08.059.

(102) Wang, L.; Yang, H.; Yang, J.; Yang, Y.; Wang, R.; Li, S.; Wang, H.; Ji, S. The Effect of the Internal Magnetism of Ferromagnetic Catalysts on Their Catalytic Activity toward Oxygen Reduction Reaction under an External Magnetic Field. *Ionics (Kiel).* **2016**, *22* (11), 2195–2202. https://doi.org/10.1007/s11581-016-1746-6.

(103) Zeng, Z.; Zhang, T.; Liu, Y.; Zhang, W.; Yin, Z.; Ji, Z.; Wei, J. Magnetic Field-Enhanced 4-Electron Pathway for Well-Aligned Co3O4/Electrospun Carbon Nanofibers in the Oxygen Reduction Reaction. *ChemSusChem* **2018**, *11* (3), 580–588. https://doi.org/10.1002/cssc.201701947.

(104) Garcés-pineda, F. A.; Blasco-ahicart, M.; Nieto-castro, D.; López, N.; Galán-mascarós, J. R. Direct Magnetic Enhancement of Electrocatalytic Water Oxidation in Alkaline Media. *Nat. Energy* **2019**, *4* (June), 519–525.

(105) Ren, X.; Wu, T.; Sun, Y.; Li, Y.; Xian, G.; Liu, X.; Gracia, J.; Gao, H.; Yang, H.; Xu, Z. J.; Shen, C. Spin-Polarized Oxygen Evolution Reaction under Magnetic Field. *Nat. Commun.* **2021**, 1–12. https://doi.org/10.1038/s41467-021-22865-y.

(106) Li, Y.; Zhang, L.; Peng, J.; Zhang, W.; Peng, K. Magnetic Field Enhancing Electrocatalysis of Co_3O_4/NF for Oxygen Evolution Reaction. *J. Power Sources* **2019**, *433* (May), 226704. https://doi.org/10.1016/j.jpowsour.2019.226704.

(107) Beschnitt, S.; De Souza, R. A. Impurity Diffusion of Hf and Zr in Gd-Doped CeO_2. *Solid State Ionics* **2017**, *305*, 23–29. https://doi.org/10.1016/j.ssi.2017.03.029.

(108) Farmer, J. A.; Campbell, C. T. Ceria Maintains Smaller Metal Catalyst Particles by Strong Metal-Support Bonding. *Science (80-.).* **2010**, *329* (5994), 933–936. https://doi.org/10.1126/science.1191778.

(109) Yamada, Y.; Tsung, C. K.; Huang, W.; Huo, Z.; Habas, S. E.; Soejima, T.; Aliaga, C. E.; Somorjai, G. A.; Yang, P. Nanocrystal Bilayer for Tandem Catalysis. *Nat. Chem.* **2011**, *3* (5), 372–376. https://doi.org/10.1038/nchem.1018.

(110) Cargnello, M.; Doan-Nguyen, V. V. T.; Gordon, T. R.; Diaz, R. E.; Stach, E. A.; Gorte, R. J.; Fornasiero, P.; Murray, C. B. Control of Metal Nanocrystal Size Reveals Metal-Support Interface Role for Ceria Catalysts. *Science (80-.).* **2013**, *341* (6147), 771–773. https://doi.org/10.1126/science.1240148.

(111) Irvine, J. T. S.; Neagu, D.; Verbraeken, M. C.; Chatzichristodoulou, C.; Graves, C.; Mogensen, M. B. Evolution of the Electrochemical Interface in High-Temperature Fuel Cells and Electrolysers. *Nat. Energy* **2016**, *1* (1), 1–13. https://doi.org/10.1038/nenergy.2015.14.

(112) Helveg, S.; López-Cartes, C.; Sehested, J.; Hansen, P. L.; Clausen, B. S.; Rostrup-

Nielsen, J. R.; Abild-Pedersen, F.; Nørskov, J. K. Atomic-Scale Imaging of Carbon Nanofibre Growth. *Nature* **2004**, *427* (6973), 426–429. https://doi.org/10.1038/nature02278.

(113) Abild-Pedersen, F.; Nørskov, J. K.; Rostrup-Nielsen, J. R.; Sehested, J.; Helveg, S. Mechanisms for Catalytic Carbon Nanofiber Growth Studied by Ab Initio Density Functional Theory Calculations. *Phys. Rev. B - Condens. Matter Mater. Phys.* **2006**, *73* (11), 1–13. https://doi.org/10.1103/PhysRevB.73.115419.

(114) Neagu, D.; Oh, T. S.; Miller, D. N.; Ménard, H.; Bukhari, S. M.; Gamble, S. R.; Gorte, R. J.; Vohs, J. M.; Irvine, J. T. S. Nano-Socketed Nickel Particles with Enhanced Coking Resistance Grown in Situ by Redox Exsolution. *Nat. Commun.* **2015**, *6*. https://doi.org/10.1038/ncomms9120.

(115) Papaioannou, E. I.; Neagu, D.; Ramli, W. K. W.; Irvine, J. T. S.; Metcalfe, I. S. Sulfur-Tolerant, Exsolved Fe–Ni Alloy Nanoparticles for CO Oxidation. *Top. Catal.* **2019**, *62* (17–20), 1149–1156. https://doi.org/10.1007/s11244-018-1053-8.

(116) Takehira, K. Highly Dispersed and Stable Supported Metal Catalysts Prepared by Solid Phase Crystallization Method. *Catal. Surv. from Asia* **2002**, *6* (1–2), 19–32. https://doi.org/10.1023/a:1020589132547.

(117) Mizuki, J.; Akao, T.; Tanaka, H.; Uenishi, M.; Kimura, M.; Okamoto, T.; Hamadak, N. Self-Regeneration of a Pd-Perovskite Catalyst for Automotive Emissions Control. *Nature* **2002**, *418* (x), 12–15. https://doi.org/10.1038/nature00875.1.

(118) Su, C.; Wang, W.; Liu, M.; Tadé, M. O.; Shao, Z. Progress and Prospects in Symmetrical Solid Oxide Fuel Cells with Two Identical Electrodes. *Adv. Energy Mater.* **2015**, *5* (14), 1–19. https://doi.org/10.1002/aenm.201500188.

(119) Ni, C.; Ni, J.; Zhou, Z.; Jin, M. Structural and Chemical Stability of Sr-, Nb- and Zr-Doped Calcium Manganite as Oxygen-Storage Materials. *J. Alloys Compd.* **2017**, *709*, 789–795. https://doi.org/10.1016/j.jallcom.2017.03.214.

(120) Zhu, T.; Troiani, H. E.; Mogni, L. V.; Han, M.; Barnett, S. A. Ni-Substituted $Sr(Ti,Fe)O_3$ SOFC Anodes: Achieving High Performance via Metal Alloy Nanoparticle Exsolution. *Joule* **2018**, *2* (3), 478–496. https://doi.org/10.1016/j.joule.2018.02.006.

(121) Xue, S.; Shi, N.; Wan, Y.; Xu, Z.; Huan, D.; Zhang, S.; Xia, C.; Peng, R.; Lu, Y. Novel

Carbon and Sulfur-Tolerant Anode Material $FeNi_3$@$PrBa(Fe,Ni)_{1.9}Mo_{0.1}O_{5+\delta}$ for Intermediate Temperature Solid Oxide Fuel Cells. *J. Mater. Chem. A* **2019**, *7* (38), 21783–21793. https://doi.org/10.1039/c9ta07027c.

(122) Kim, K. J.; Rath, M. K.; Kwak, H. H.; Kim, H. J.; Han, J. W.; Hong, S. T.; Lee, K. T. A Highly Active and Redox-Stable $SrGdNi_{0.2}Mn_{0.8}O_{4\pm\delta}$ Anode with in Situ Exsolution of Nanocatalysts. *ACS Catal.* **2019**, *9* (2), 1172–1182. https://doi.org/10.1021/acscatal.8b03669.

(123) Du, Z.; Zhao, H.; Yi, S.; Xia, Q.; Gong, Y.; Zhang, Y.; Cheng, X.; Li, Y.; Gu, L.; Świerczek, K. High-Performance Anode Material $Sr_2FeMo_{0.65}Ni_{0.35}O_{6-\delta}$ with in Situ Exsolved Nanoparticle Catalyst. *ACS Nano* **2016**, *10* (9), 8660–8669. https://doi.org/10.1021/acsnano.6b03979.

(124) Tsekouras, G.; Neagu, D.; Irvine, J. T. S. Step-Change in High Temperature Steam Electrolysis Performance of Perovskite Oxide Cathodes with Exsolution of B-Site Dopants. *Energy Environ. Sci.* **2013**, *6* (1), 256–266. https://doi.org/10.1039/c2ee22547f.

(125) Li, Y.; Xie, K.; Chen, S.; Li, H.; Zhang, Y.; Wu, Y. Efficient Carbon Dioxide Electrolysis Based on Perovskite Cathode Enhanced with Nickel Nanocatalyst. *Electrochim. Acta* **2015**, *153*, 325–333. https://doi.org/10.1016/j.electacta.2014.11.151.

(126) Choi, J.; Park, S.; Han, H.; Kim, M.; Park, M. Highly Efficient CO_2 Electrolysis to CO on Ruddlesden – Popper Perovskite Oxide with in Situ Exsolved Fe Nanoparticles. *J. Mater. Chem. A* **2021**. https://doi.org/10.1039/d0ta11328j.

(127) Lv, H.; Lin, L.; Zhang, X.; Song, Y.; Matsumoto, H.; Zeng, C.; Ta, N.; Liu, W.; Gao, D.; Wang, G.; Bao, X. In Situ Investigation of Reversible Exsolution/Dissolution of CoFe Alloy Nanoparticles in a Co-Doped $Sr_2Fe_{1.5}Mo_{0.5}O_{6-\delta}$ Cathode for CO_2 Electrolysis. *Adv. Mater.* **2020**, *32* (6), 1–9. https://doi.org/10.1002/adma.201906193.

(128) Kyriakou, V.; Neagu, D.; Papaioannou, E. I.; Metcalfe, I. S.; van de Sanden, M. C. M.; Tsampas, M. N. Co-Electrolysis of H_2O and CO_2 on Exsolved Ni Nanoparticles for Efficient Syngas Generation at Controllable H_2/CO Ratios. *Appl. Catal. B Environ.* **2019**, *258* (February), 117950. https://doi.org/10.1016/j.apcatb.2019.117950.

(129) Qi, W.; Ruan, C.; Wu, G.; Zhang, Y.; Wang, Y.; Xie, K.; Wu, Y. Reversibly In-Situ Anchoring Copper Nanocatalyst in Perovskite Titanate Cathode for Direct High-

Temperature Steam Electrolysis. *Int. J. Hydrogen Energy* **2014**, *39* (11), 5485–5496. https://doi.org/10.1016/j.ijhydene.2014.01.108.

(130) Zhu, C.; Hou, S.; Hu, X.; Lu, J.; Chen, F.; Xie, K. Electrochemical Conversion of Methane to Ethylene in a Solid Oxide Electrolyzer. *Nat. Commun.* **2019**, *10* (1), 1–8. https://doi.org/10.1038/s41467-019-09083-3.

(131) Zeng, D.; Cui, D.; Lv, Y.; Qiu, Y.; Li, M.; Zhang, S.; Xiao, R. A Mixed Spinel Oxygen Carrier with Both High Reduction Degree and Redox Stability for Chemical Looping H_2 Production. *Int. J. Hydrogen Energy* **2019**, No. xxxx, 1–9. https://doi.org/10.1016/j.ijhydene.2019.11.062.

(132) Hosseini, D.; Donat, F.; Abdala, P. M.; Kim, S. M.; Kierzkowska, A. M.; Müller, C. R. Reversible Exsolution of Dopant Improves the Performance of $Ca_2Fe_2O_5$ for Chemical Looping Hydrogen Production. *ACS Appl. Mater. Interfaces* **2019**, *11* (20), 18276–18284. https://doi.org/10.1021/acsami.8b16732.

(133) Cui, D.; Qiu, Y.; Lv, Y.; Li, M.; Zhang, S.; Tippayawong, N.; Zeng, D.; Xiao, R. A High-Performance Oxygen Carrier with High Oxygen Transport Capacity and Redox Stability for Chemical Looping Combustion. *Energy Convers. Manag.* **2019**, *202* (October), 112209. https://doi.org/10.1016/j.enconman.2019.112209.

(134) Papargyriou, D.; Miller, D. N.; Irvine, J. T. S. Exsolution of Fe-Ni Alloy Nanoparticles from (La,Sr)(Cr,Fe,Ni)O_3 Perovskites as Potential Oxygen Transport Membrane Catalysts for Methane Reforming. *J. Mater. Chem. A* **2019**, *7* (26), 15812–15822. https://doi.org/10.1039/c9ta03711j.

(135) Dimitrakopoulos, G.; Ghoniem, A. F.; Yildiz, B. In Situ Catalyst Exsolution on Perovskite Oxides for the Production of CO and Synthesis Gas in Ceramic Membrane Reactors. *Sustain. Energy Fuels* **2019**, *3* (9), 2347–2355. https://doi.org/10.1039/c9se00249a.

(136) Tang, C.; Kousi, K.; Neagu, D.; Portolés, J.; Papaioannou, E. I.; Metcalfe, I. S. Towards Efficient Use of Noble Metals: Via Exsolution Exemplified for CO Oxidation. *Nanoscale* **2019**, *11* (36), 16935–16944. https://doi.org/10.1039/c9nr05617c.

(137) Jo, Y. R.; Koo, B.; Seo, M. J.; Kim, J. K.; Lee, S.; Kim, K.; Han, J. W.; Jung, W. C.; Kim, B. J. Growth Kinetics of Individual Co Particles Ex-Solved on $SrTi_{0.75}Co_{0.25}O_{3-\delta}$ Polycrystalline Perovskite Thin Films. *J. Am. Chem. Soc.* **2019**, *141* (16), 6690–6697.

https://doi.org/10.1021/jacs.9b01882.

(138) Kim, J. K.; Jo, Y. R.; Kim, S.; Koo, B.; Kim, J. H.; Kim, B. J.; Jung, W. C. Exceptional Tunability over Size and Density of Spontaneously Formed Nanoparticles via Nucleation Dynamics. *ACS Appl. Mater. Interfaces* **2020**, *12* (21), 24039–24047. https://doi.org/10.1021/acsami.0c05215.

(139) Lee, J. G.; Myung, J. H.; Naden, A. B.; Jeon, O. S.; Shul, Y. G.; Irvine, J. T. S. Replacement of Ca by Ni in a Perovskite Titanate to Yield a Novel Perovskite Exsolution Architecture for Oxygen-Evolution Reactions. *Adv. Energy Mater.* **2020**, *10* (10), 1–6. https://doi.org/10.1002/aenm.201903693.

(140) Kim, J. H.; Kim, J. K.; Liu, J.; Curcio, A.; Jang, J. S.; Kim, I. D.; Ciucci, F.; Jung, W. C. Nanoparticle Ex-Solution for Supported Catalysts: Materials Design, Mechanism and Future Perspectives. *ACS Nano* **2021**. https://doi.org/10.1021/acsnano.0c07105.

(141) Neagu, D.; Tsekouras, G.; Miller, D. N.; Ménard, H.; Irvine, J. T. S. In Situ Growth of Nanoparticles through Control of Non-Stoichiometry. *Nat. Chem.* **2013**, *5* (11), 916–923. https://doi.org/10.1038/nchem.1773.

(142) Myung, J. H.; Neagu, D.; Miller, D. N.; Irvine, J. T. S. Switching on Electrocatalytic Activity in Solid Oxide Cells. *Nature* **2016**, *537* (7621), 528–531. https://doi.org/10.1038/nature19090.

(143) Oh, T. S.; Rahani, E. K.; Neagu, D.; Irvine, J. T. S.; Shenoy, V. B.; Gorte, R. J.; Vohs, J. M. Evidence and Model for Strain-Driven Release of Metal Nanocatalysts from Perovskites during Exsolution. *J. Phys. Chem. Lett.* **2015**, *6* (24), 5106–5110. https://doi.org/10.1021/acs.jpclett.5b02292.

(144) Neagu, D.; Kyriakou, V.; Roiban, I.; Aouine, M.; Tang, C.; Caravaca, A.; Kousi, K.; Schreur-piet, I.; Metcalfe, I. S.; Vernoux, P.; Tsampas, M. N. In Situ Observation of Nanoparticle Exsolution Mechanistic Insight to Nanostructure Tailoring. *ACS Nano* **2019**, *13*, 12996–13005. https://doi.org/10.1021/acsnano.9b05652.

(145) Katz, M. B.; Zhang, S.; Duan, Y.; Wang, H.; Fang, M.; Zhang, K.; Li, B.; Graham, G. W.; Pan, X. Reversible Precipitation/Dissolution of Precious-Metal Clusters in Perovskite-Based Catalyst Materials: Bulk versus Surface Re-Dispersion. *J. Catal.* **2012**, *293*, 145–148. https://doi.org/10.1016/j.jcat.2012.06.017.

(146) Yu, S.; Yoon, D.; Lee, Y.; Yoon, H.; Han, H.; Kim, N.; Kim, C. J.; Ihm, K.; Oh, T. S.; Son, J. Metal Nanoparticle Exsolution on a Perovskite Stannate Support with High Electrical Conductivity. *Nano Lett.* **2020**, *20* (5), 3538–3544. https://doi.org/10.1021/acs.nanolett.0c00488.

(147) Gao, Y.; Chen, D.; Saccoccio, M.; Lu, Z.; Ciucci, F. From Material Design to Mechanism Study: Nanoscale Ni Exsolution on a Highly Active A-Site Deficient Anode Material for Solid Oxide Fuel Cells. *Nano Energy* **2016**, *27*, 499–508. https://doi.org/10.1016/j.nanoen.2016.07.013.

(148) Adamson, A.; Gast, A. *Physical Chemistry of Surfaces*, 2nd editio.; Wiley-Interscience Publication, 1967.

(149) Blander, M.; Katz, J. L. Bubble Nucleation in Liquids. *AIChE J.* **1975**, *21* (5), 833–848. https://doi.org/10.1002/aic.690210502.

(150) Han, H.; Park, J.; Nam, S. Y.; Kim, K. J.; Choi, G. M.; Parkin, S. S. P.; Jang, H. M.; Irvine, J. T. S. Lattice Strain-Enhanced Exsolution of Nanoparticles in Thin Films. *Nat. Commun.* **2019**, *10* (1), 1–8. https://doi.org/10.1038/s41467-019-09395-4.

(151) Kim, K. J.; Han, H.; Defferriere, T.; Yoon, D.; Na, S.; Kim, S. J.; Dayaghi, A. M.; Son, J.; Oh, T. S.; Jang, H. M.; Choi, G. M. Facet-Dependent in Situ Growth of Nanoparticles in Epitaxial Thin Films: The Role of Interfacial Energy. *J. Am. Chem. Soc.* **2019**, *141* (18), 7509–7517. https://doi.org/10.1021/jacs.9b02283.

(152) Jiang, G.; Yan, F.; Wan, S.; Zhang, Y.; Yan, M. Microstructure Evolution and Kinetics of B-Site Nanoparticle Exsolution from an A-Site-Deficient Perovskite Surface: A Phase-Field Modeling and Simulation Study. *Phys. Chem. Chem. Phys.* **2019**, *21* (21), 10902–10907. https://doi.org/10.1039/c8cp07883a.

(153) Nishihata, Y.; Mizuki, J.; Akao, T.; Tanaka, H.; Uenishi, M.; Kimura, M.; Okamoto, T.; Hamada, N. Self-Regeneration of a Pd-Perovskite Catalyst for Automotive Emissions Control. *Nature* **2002**, *418* (6894), 164–167. https://doi.org/10.1038/nature00893.

(154) Zhou, W.; Shao, Z.; Liang, F.; Chen, Z. G.; Zhu, Z.; Jin, W.; Xu, N. A New Cathode for Solid Oxide Fuel Cells Capable of in Situ Electrochemical Regeneration. *J. Mater. Chem.* **2011**, *21* (39), 15343–15351. https://doi.org/10.1039/c1jm12660a.

(155) Tan, J.; Lee, D.; Ahn, J.; Kim, B.; Kim, J.; Moon, J. Thermally Driven in Situ Exsolution

of Ni Nanoparticles from (Ni, Gd)CeO2 for High-Performance Solid Oxide Fuel Cells. *J. Mater. Chem. A* **2014**. https://doi.org/10.1039/c.d.oxide.

(156) Kousi, K.; Neagu, D.; Bekris, L.; Papaioannou, E. I.; Metcalfe, I. S. Endogenous Nanoparticles Strain Perovskite Host Lattice Providing Oxygen Capacity and Driving Oxygen Exchange and CH_4 Conversion to Syngas . *Angew. Chemie* **2020**, *132* (6), 2531–2540. https://doi.org/10.1002/ange.201915140.

(157) Zhang, X.; Pei, C.; Chang, X.; Chen, S.; Liu, R.; Zhao, Z. J.; Mu, R.; Gong, J. FeO_6 Octahedral Distortion Activates Lattice Oxygen in Perovskite Ferrite for Methane Partial Oxidation Coupled with CO_2 Splitting. *J. Am. Chem. Soc.* **2020**, *142* (26), 11540–11549. https://doi.org/10.1021/jacs.0c04643.

(158) Carrillo, A. J.; Kim, K. J.; Hood, Z. D.; Bork, A. H.; Rupp, J. L. M. $La_{0.6}Sr_{0.4}Cr_{0.8}Co_{0.2}O_3$ Perovskite Decorated with Exsolved Co Nanoparticles for Stable CO_2 Splitting and Syngas Production. *ACS Appl. Energy Mater.* **2020**, *3* (5), 4569–4579. https://doi.org/10.1021/acsaem.0c00249.

(159) Kwak, N. W.; Jeong, S. J.; Seo, H. G.; Lee, S.; Kim, Y. J.; Kim, J. K.; Byeon, P.; Chung, S. Y.; Jung, W. C. In Situ Synthesis of Supported Metal Nanocatalysts through Heterogeneous Doping. *Nat. Commun.* **2018**, *9* (1), 1–8. https://doi.org/10.1038/s41467-018-07050-y.

(160) Harvey, S. P.; De Souza, R. A.; Martin, M. Diffusion of La and Mn in $Ba_{0.5}Sr_{0.5}Co_{0.8}Fe_{0.2}O_{3-\delta}$ Polycrystalline Ceramics. *Energy Environ. Sci.* **2012**, *5* (2), 5803–5813. https://doi.org/10.1039/c1ee02740a.

(161) Joo, S.; Kwon, O.; Kim, K.; Kim, S.; Kim, H.; Shin, J.; Jeong, H. Y.; Sengodan, S.; Han, J. W.; Kim, G. Cation-Swapped Homogeneous Nanoparticles in Perovskite Oxides for High Power Density. *Nat. Commun.* **2019**, *10* (1), 1–9. https://doi.org/10.1038/s41467-019-08624-0.

(162) Joo, S.; Kwon, O.; Kim, S.; Jeong, H. Y.; Kim, G. Ni-Fe Bimetallic Nanocatalysts Produced by Topotactic Exsolution in Fe Deposited $PrBaMn_{1.7}Ni_{0.3}O_{5+\delta}$ for Dry Reforming of Methane . *J. Electrochem. Soc.* **2020**, *167* (6), 064518. https://doi.org/10.1149/1945-7111/ab8390.

(163) Joo, S.; Seong, A.; Kwon, O.; Kim, K.; Lee, J. H.; Gorte, R. J.; Vohs, J. M.; Han, J. W.; Kim, G. Highly Active Dry Methane Reforming Catalysts with Boosted in Situ Grown

Ni-Fe Nanoparticles on Perovskite via Atomic Layer Deposition. *Sci. Adv.* **2020**, *6* (35), 1–9. https://doi.org/10.1126/sciadv.abb1573.

Chapitre II:

Synthesis of quaternary phase manganite perovskite $La_{0.33}Pr_{0.33}Ca_{0.33}MnO_3$ using molten salt

I. Introduction

Manganite perovskites such as $La_{0.7}Sr_{0.3}MnO_3$ are known to be efficient metal-free electrocatalysts for the oxygen reduction reaction.[1] They also exhibit the so-called electronic phase separation (EPS), which leads to the co-existence of different magnetic domains inside the material, paramagnetic insulating and ferromagnetic conductive domains. These perovskites can also exhibit large change of their electrical resistivity under a magnetic field (colossal magnetoresistance effect). One of the largest EPS known (1 μm) in the bulk state has been for $La_{0.33}Pr_{0.33}Ca_{0.33}MnO_3$ (LPCMO).[2] By producing defect-free particles below that EPS length, the formation of a single ferromagnetic domain would be possible. The combination of these two phenomena brings up interesting perspectives for electrocatalysis under magnetic field. However, the perquisite to study such properties is to design crystalline nano-objects of this material. Such an achievement has not been reached according to the literature. In this chapter we demonstrate the synthesis of highly crystalline nanoparticles of LPCMO for the first time, using molten salt synthesis. We also show the difficulties arising from the synthesis of quaternary manganese perovskites throughout the variations of numerous parameters. The importance of the heating process and of the choice of adequate molten salt media is demonstrated. Finally, early results of the use of LPCMO nanoparticles as electrocatalysts for the ORR under magnetic field are shown.

II. Original synthesis

As a first attempt to synthesize LPCMO nanoparticles we have adapted the synthesis of LSMO nanoparticles reported by H. Le Thi N'Goc *et al.*[3]. Potassium nitrate (10 eq), lanthanum nitrate hexahydrate (0.3 eq), praseodymium nitrate hexahydrate (0.3 eq), calcium nitrate tetrahydrate (0.27 eq) and manganese nitrate tetrahydrate (1 eq) were heated at 750 °C for 1h, this synthesis is labelled A-750 °C. The powder was then analyzed by X-ray diffraction (XRD) as

shown **Figure 1**. The pattern is overall consistent with the LPCMO phase but also exhibits an asymmetry of peaks at ca. 33.5°, 49.1° and 61° (2θ) ascribed to $CaMnO_3$ by-product.

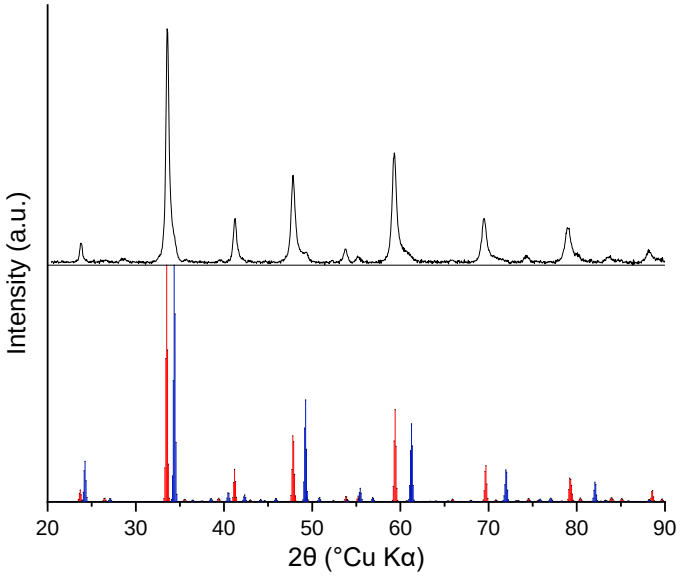

Figure 1. Powder XRD pattern of synthesis A-750 °C (black), LPCMO reference (red) and $CaMnO_3$ reference (blue).

The morphology of the nanoparticles was then analyzed by transmission electron microscopy (TEM), scanning electron microscopy (SEM) and high-resolution transmission electron microscopy (HRTEM) (**Figure 2**). The TEM and HRTEM images (**Figure 2**a-e) showed highly crystalline cubical particles ascribed to a perovskite phase, according to XRD and HRTEM. SEM analysis (**Figure 2b**) confirms the cubical morphology of these particles, but also highlights a second type of morphology consisting in foils, which seem to arise from single particles fused together. **Figure 2c** shows that these foils have the thickness of single particles, and confirms their presence all over the sample. Selective sedimentation was realized to separate single nanoparticles from the large foils. The latter were then studied with energy dispersive X-ray analysis (EDX) in a scanning electron microscope (**Figure 2d**). The cationic composition of the foils was estimated to $La_{0.68}Pr_{0.33}Ca_{0.1}MnO_3$ (LPMO). This calcium-poor phase was not detected by XRD, because of the close lattice parameters for LPCMO and LPMO. Nonetheless, the formation of $CaMnO_3$ as a side-product hinted at the presence of an additional side-product poor in calcium. We then embarked in a study to avoid the formation of these two secondary phases during synthesis.

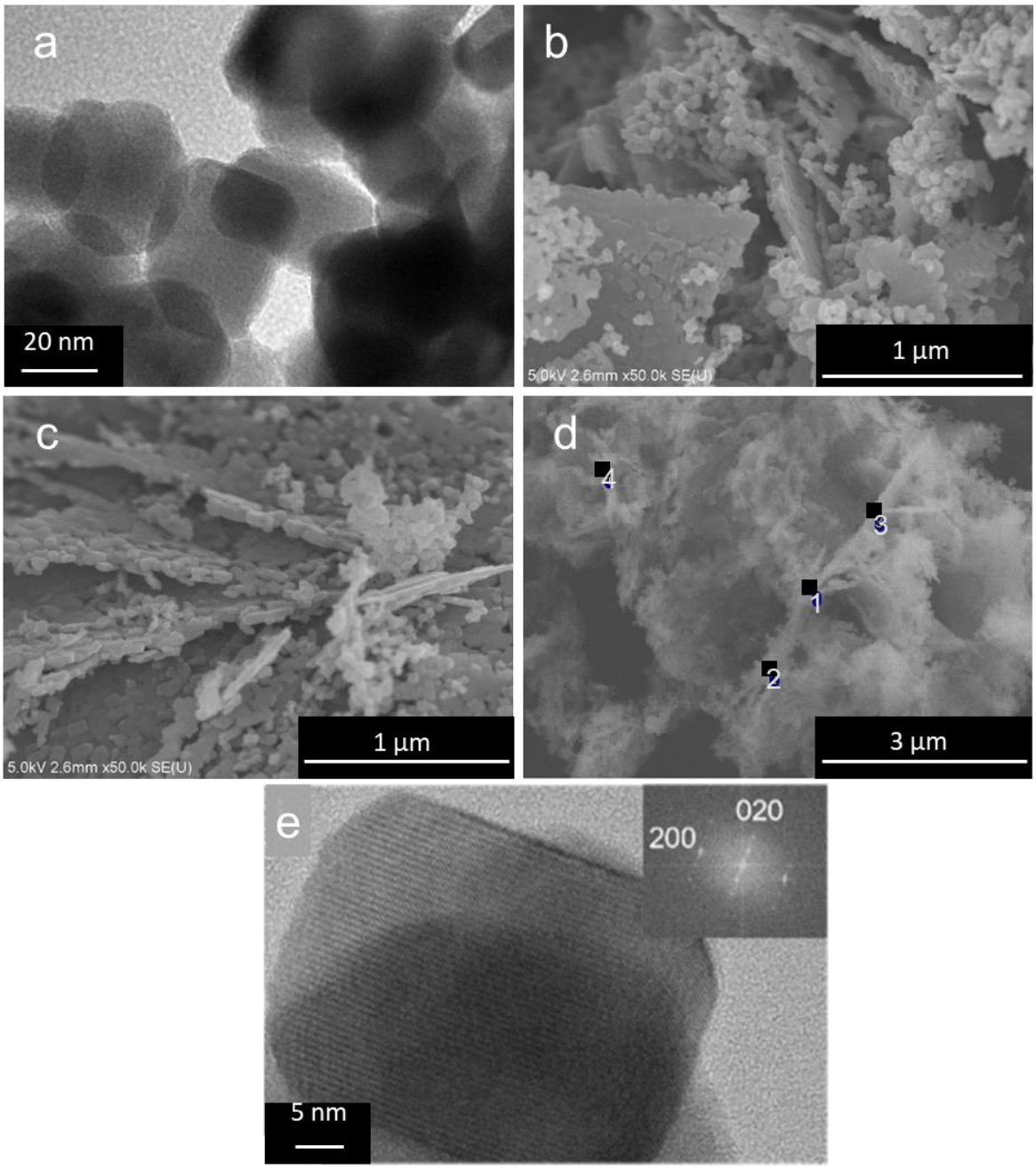

Figure 2. (a) TEM, (b, c, d) SEM and (e) HRTEM images of a sample obtained at 750 °C for 1 h in molten potassium nitrate: (a) LPCMO nanoparticles, (b) LPCMO nanoparticles and foils, (c) foils, (d) 4 spots analyzed by EDX, (e) LPCMO nanoparticle. Inset: corresponding FFT indexed along the LPCMO structure.

1. Influence of the reaction temperature

The first parameter studied in order to synthesize phase pure LPCMO nanoparticles was the temperature, which was screened according to the previously described protocol of synthesis A-750 °C. The synthesis was performed at 600 °C (A-600 °C), 650 °C (A-650 °C), 700 °C (A-700 °C) and 800 °C (A-800 °C). From the powder XRD diffractograms presented **Figure 3**, it

is visible that increasing the temperature above 750 °C leads to the formation of impurities, which are ascribed to a praseodymium oxide. The optimal temperature is then 750 °C, which minimizes the relative intensities of the $CaMnO_3$ peaks described in section 1.1. We then adopted this temperature and moved on to the second parameter, the heating time.

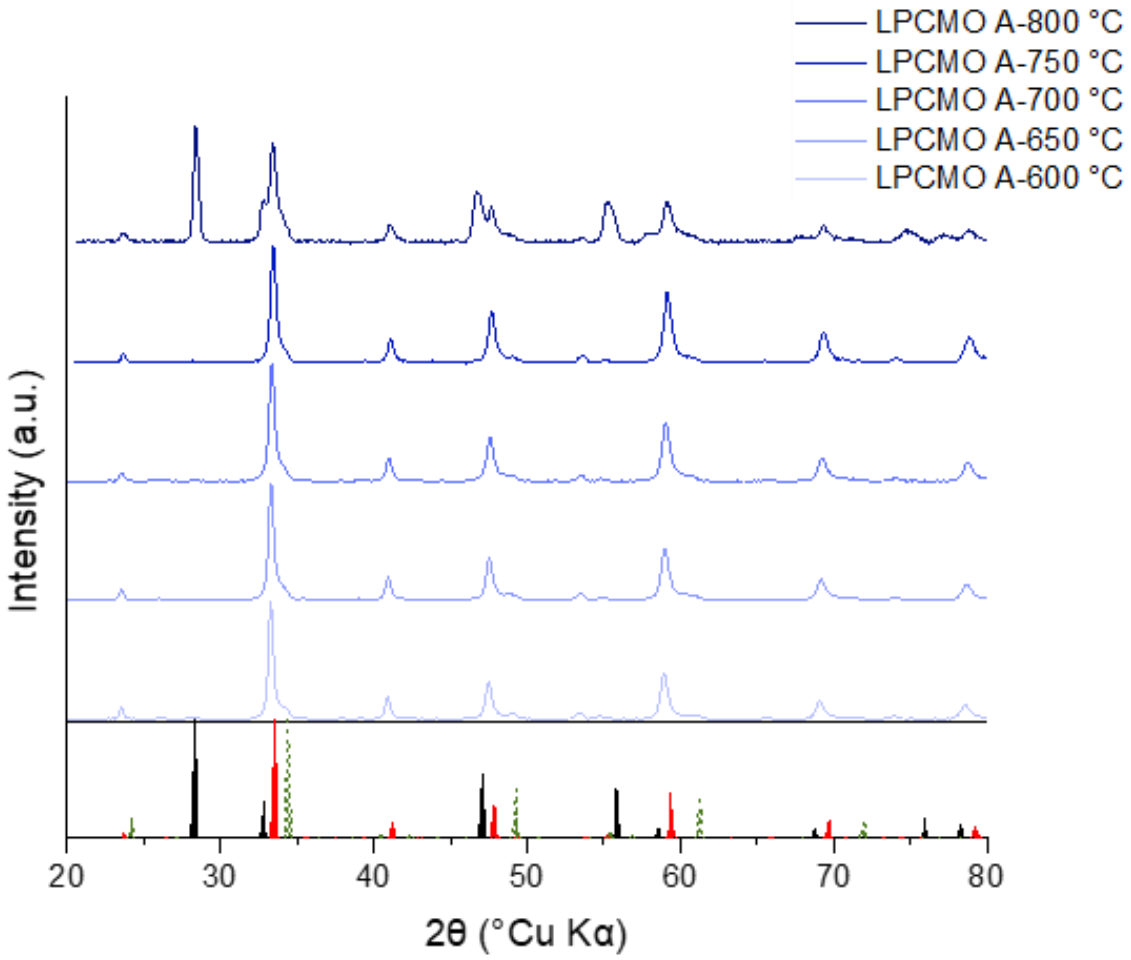

Figure 3. Powder XRD patterns of the products of syntheses at different temperatures: A-600 °C, A-650 °C, A-700 °C, A-750 °C, A-800 °C. The reference patterns of LPCMO, $PrO_{1.88}$ and $CaMnO_3$ are displayed in red, black and green dashes respectively.

2. Influence of the reaction time

The protocol described in synthesis A-750 °C was adopted by screening the reaction time from 30 min (B-30min) to 4 h (B-4h) and 8 h (B-8h). XRD (**Figure 4**) shows that increasing the reaction time above 1 h leads to the formation of a praseodymium oxide impurity while 30 min heating leads to the LPCMO phase and the $CaMnO_3$ impurity. SEM (**Figure 5**) indicates the presence in all samples of the characteristic foil morphology ascribed to a Ca-poor perovskite. The optimal reaction time then appears to be 1 h (A-750°C).

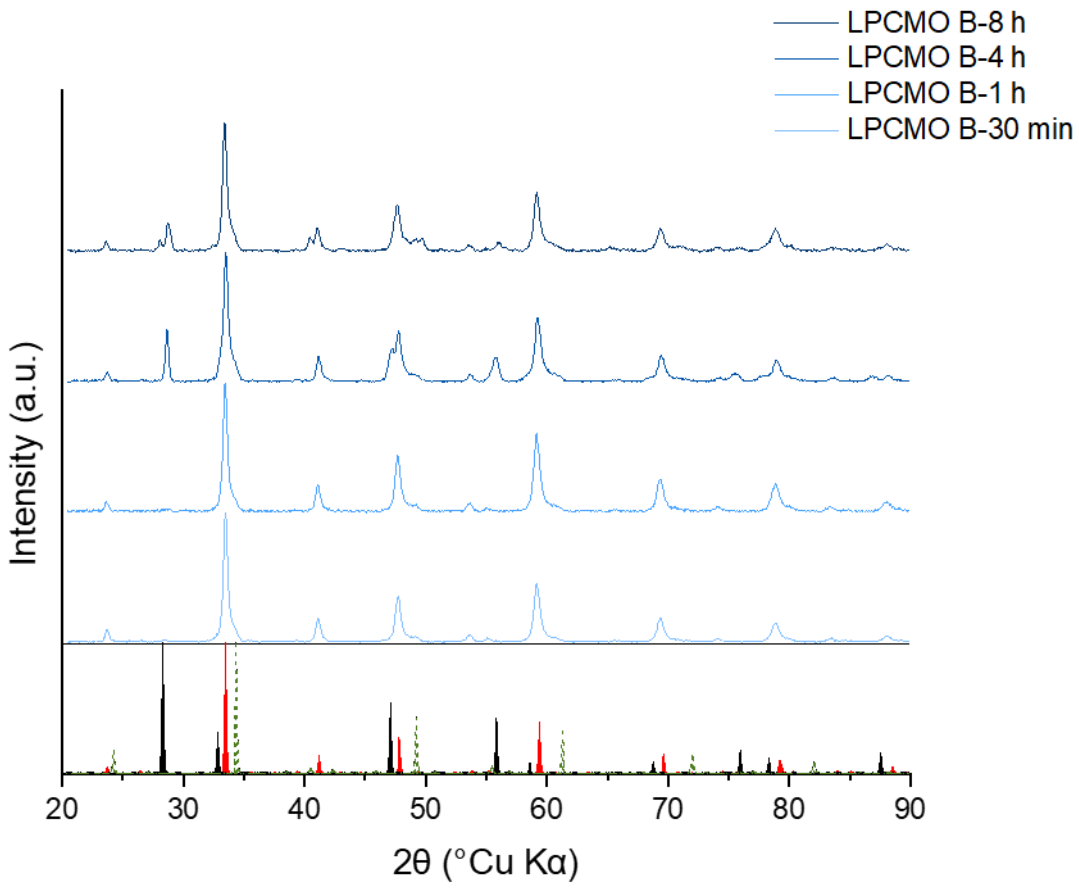

Figure 4. Powder XRD patterns of the products of syntheses at 750 °C with different reaction times. The reference patterns of LPCMO, $PrO_{1.88}$ and $CaMnO_3$ are displayed in red, black and green dashes respectively.

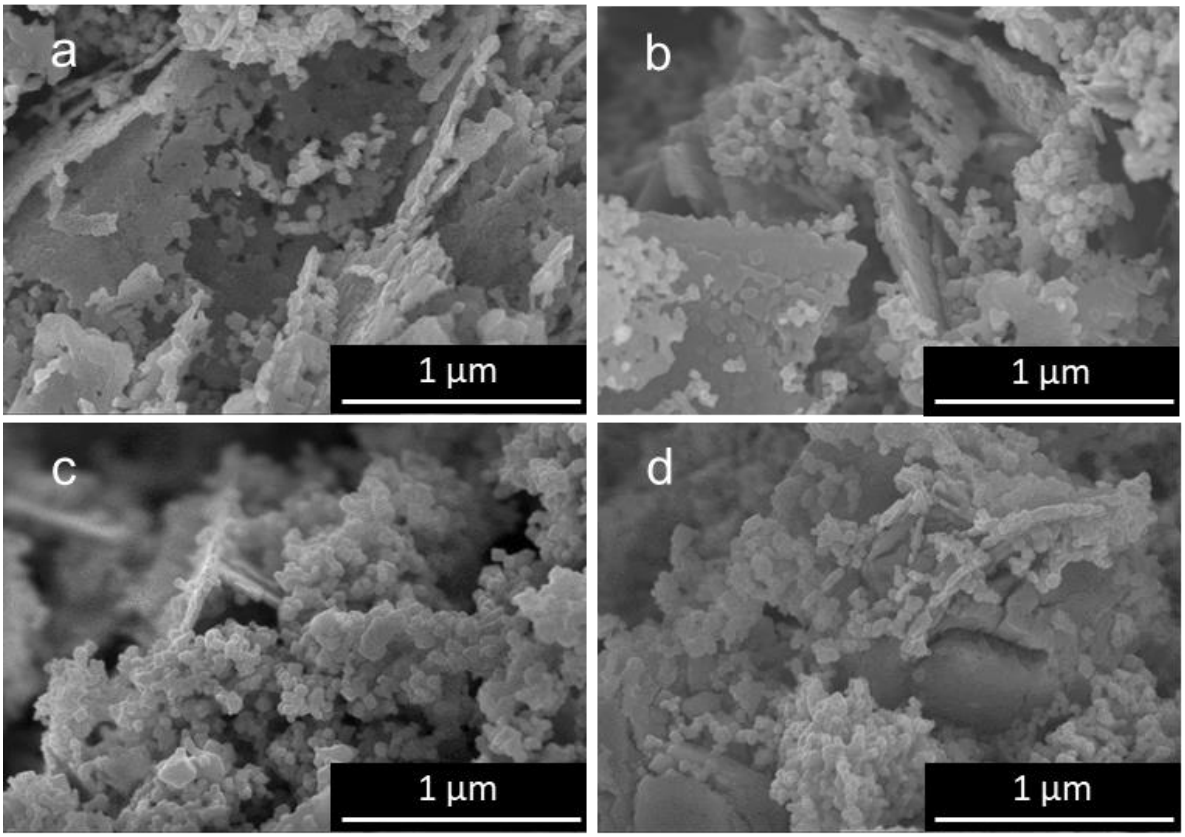

Figure 5. SEM images of LPCMO samples obtained at 750 °C and different reaction times: (a) B-30 min, (b) B-1 h, (c) B-4 h, (d) B-8 h.

3. Influence of the reagent ratios

Since the formation of the secondary phases Ca-poor LPCMO (LPMO) and $CaMnO_3$ cannot be avoided by varying the reaction temperature and time, the issue was approached differently. The LPCMO structure desired is composed in its A-site of three different elements, La, Pr and Ca. The two side-products detected indicate a tendency of segregation of Ca versus La and Pr, which readily coprecipitate. We then modified the reagent ratios between La, Pr, and Ca to impact this coprecipitation affinity.

Firstly, we decreased the Pr reagent content, to favor coprecipitation of Ca with La, by targeting reagents ratios corresponding to $La_{0.43}Pr_{0.23}Ca_{0.33}MnO_3$ (A-$Pr_{0.2}$) and $La_{0.53}Pr_{0.13}Ca_{0.33}MnO_3$ (A-$Pr_{0.1}$). The samples were synthesized using the protocol from synthesis A-750, i.e. 750 °C for 1 h in potassium nitrate. XRD (**Figure 6)** shows that a decrease in the Pr reagent content led to the formation of a more pronounced peak asymmetry around 33.5° ascribed to the $CaMnO_3$ (CMO) phase, which shows that Ca still segregates from the La and Pr phase, even at low Pr content.

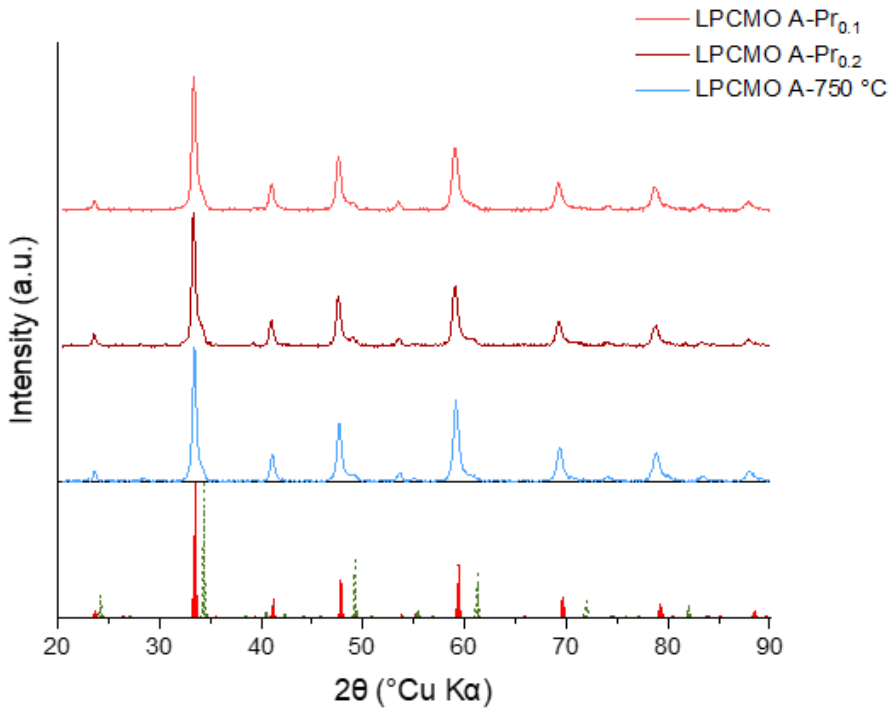

Figure 6. Powder XRD patterns of samples obtained during LPCMO synthesis with different Pr reagent stoichiometries. The reference patterns of LPCMO and $CaMnO_3$ are displayed in red and green dashes respectively

Then, the La and Ca contents were modified: the La content was decreased (A-La) and the Ca content was increased (A-Ca), by maintaining the original Pr/Mn ratio. By decreasing the La content, we can expect to favor coprecipitation of Ca with Pr. Furthermore, by increasing the Ca content we aimed at changing the coprecipitation affinity of La and Pr and yielding a complete coprecipitation of Ca with Pr and La. The XRD patterns of both powders (**Figure 7**) show again the presence of the LPCMO phase and of the $CaMnO_3$ impurity. The increase in calcium content and decrease in La content did not lead to the formation of a more distinct CMO phase. However, by decreasing the La content, another impurity was formed corresponding to a praseodymium oxide observed at 28.5° (2θ Cu Kα). Overall, we conclude that the variation of the reagents ratios did not enable avoiding the CMO sub-product, which indicates that its counter-part, a Ca-poor perovskite in the form of foils, should also be present.

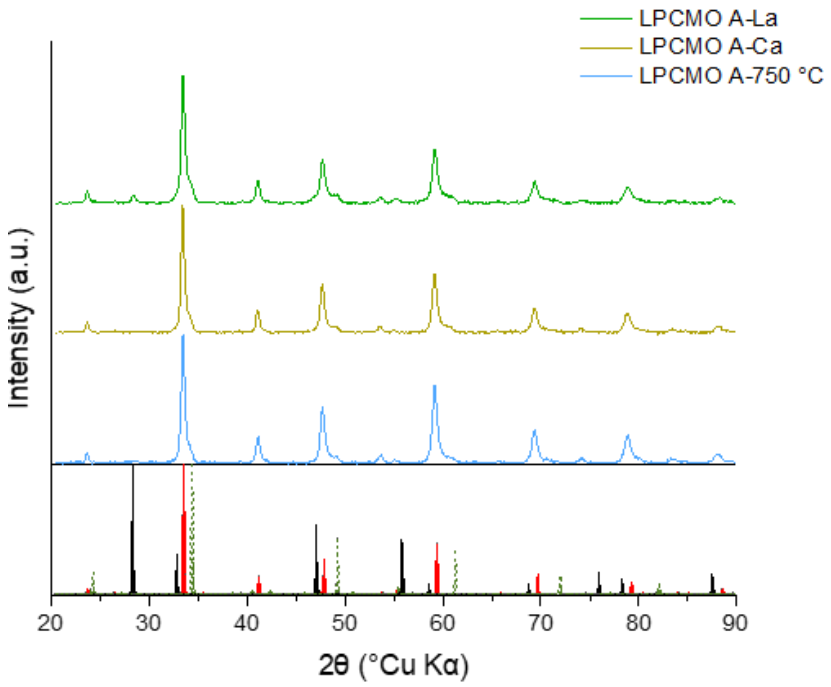

Figure 7. Powder XRD patterns of samples obtained during LPCMO synthesis with Ca excess and La default, respectively. The reference patterns of LPCMO, $PrO_{1.88}$ and $CaMnO_3$ are displayed in red, black and green dashes respectively.

4. Influence of the reagents concentration

Finally, we investigated the effect of the concentration of reagents. Indeed, this parameter classically impacts nucleation and growth kinetics, but could have a specific effect in the procedure described herein, since the molten salt not only plays the role of liquid medium at high temperatures, but also provides O^{2-} ions for the formation of the perovskite. Increasing the O^{2-} content versus the amount of metal cations could favor coprecipitation of La, Ca, and Pr cations. Thus, the quantity of precursors was divided by 10 by maintaining the potassium nitrate amount, to obtain a 10-times diluted medium. The protocol (A-D10) followed the synthesis A-750, i.e. 750 °C for 1 h heating. The XRD pattern (**Figure 8**) of this diluted synthesis shows the presence of the desired LPCMO phase. The contribution of the CMO phase is still present, although with a decreased relative intensity, which could be ascribed to an increase in the O^{2-} content of the reaction medium versus the metal cations. Nonetheless, a praseodymium oxide impurity also appears with a characteristic peak at 28.5°. TEM (**Figure 9)** shows that by diluting the medium, the cubical aspect of the LPCMO nanoparticles is partially lost and the particles are aggregated, so that the sample does not meet the requirements for a phase pure and morphologically controlled nanomaterial.

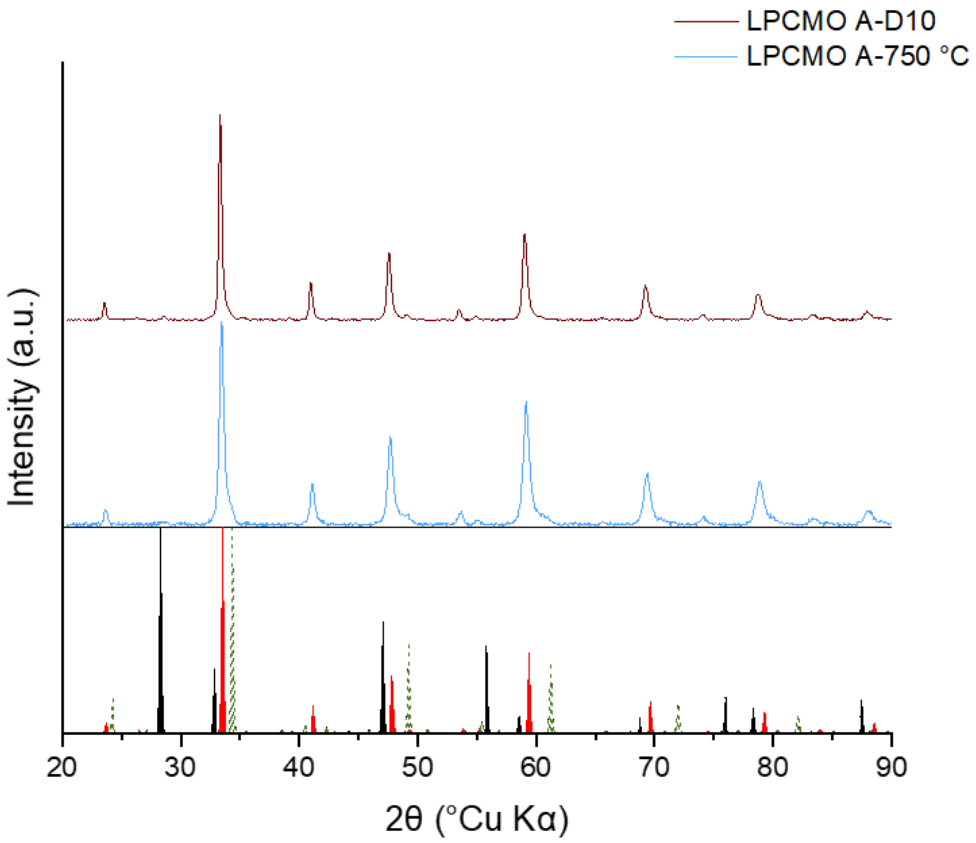

Figure 8. Powder XRD patterns of samples obtained during LPCMO synthesis with reagents concentration divided by 10. The reference pattern of LPCMO, $PrO_{1.88}$ and $CaMnO_3$ are displayed in red, black and green dashes respectively.

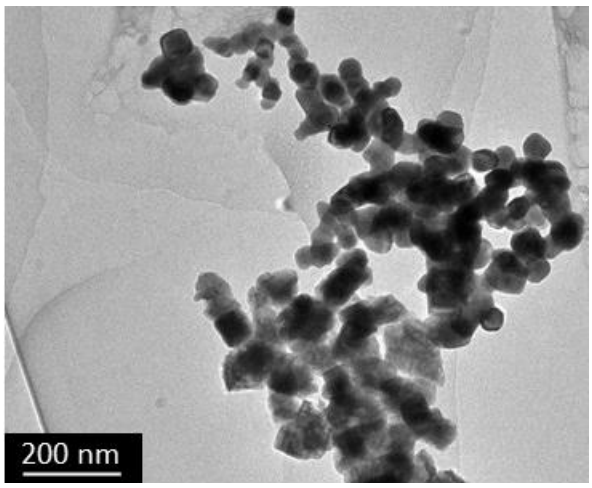

Figure 9. TEM image of nanoparticles obtained during LPCMO synthesis with reagents concentration divided by 10.

We have then modified the molten salt itself. Al Raihani *et al.*[4] reported that molten $NaNO_2$ exhibits a much higher oxo-basicity than molten nitrates, due to the dissociative constant of NO_2^- that is 10^{10} times more important than NO_3^-. This basicity increase is expected to level the reactivity of the different cations, as observed in water with Brönstedt basicity[5]. In this case, all cations would have a stronger tendency to coprecipitate together. Sodium nitrite (10 eq),

lanthanum nitrate hexahydrate (0.3 eq), praseodymium nitrate hexahydrate (0.3 eq), calcium nitrate tetrahydrate (0.27 eq) and manganese nitrate tetrahydrate (1eq) were then introduced into an alumina crucible and heated at 750 °C for 1 h. (*Synthesis Cx).*

To study the effect of the change of molten salt, the reaction temperature has been screened again from 600 °C to 850 °C (C-600 °C, C-750 °C, C-800 °C, C-850 °C) to compare with *synthesis Ax*, **Figure 3**. The XRD patterns (**Figure 10**) revealed that above 750 °C, the LPCMO phase is not obtained and several impurities of praseodymium oxide and manganese oxide are formed. The syntheses at 600 °C and 750 °C did not lead to the formation of the CMO subphase, however the praseodymium oxide impurity is detected at 750 °C (C-750 °C). Therefore, XRD indicates that the use of molten $NaNO_2$ instead of KNO_3 led to single phase LPCMO at 600 °C (C-600 °C). The samples from synthesis C-600 °C and C-750 °C were observed by TEM and SEM (**Figure 11**), to assess the presence of Ca-poor perovskite foils undetectable in routine XRD (**Figure 10**). Both samples do not show any foil morphology, but a new architecture that we name filaments, made of a tortuous wire-like morphology. SEM and TEM images suggest that the fraction of filaments increases from 750 °C down to 600 °C. The filaments were observed by HRTEM and STEM-EDS mapping (**Figure 12**) to assess their crystallinity and composition. The filament structure shows high crystallinity (Figure **12b**), the STEM-EDS mapping (**Figure 12c**) exhibits all the elements of LPCMO. Therefore, the change of molten salt from KNO_3 to $NaNO_2$ was efficient to avoid the formation of $CaMnO_3$ and Ca-poor perovskite phases. However, it led to a polydisperse sample in terms of morphology, encompassing not only LPCMO cube-shape nanoparticles, but also LPCMO anisotropic filaments.

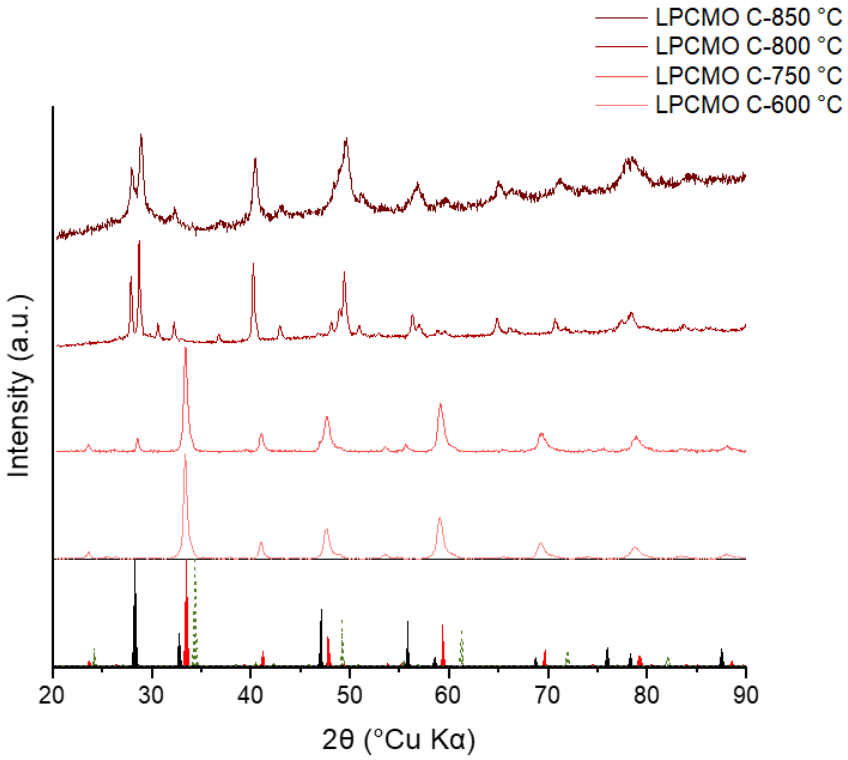

Figure 10. Powder XRD patterns of samples obtained in molten $NaNO_2$ at different temperatures during 1 h. The reference pattern of LPCMO, $PrO_{1.88}$ and $CaMnO_3$ are displayed in red, black and green dashes respectively.

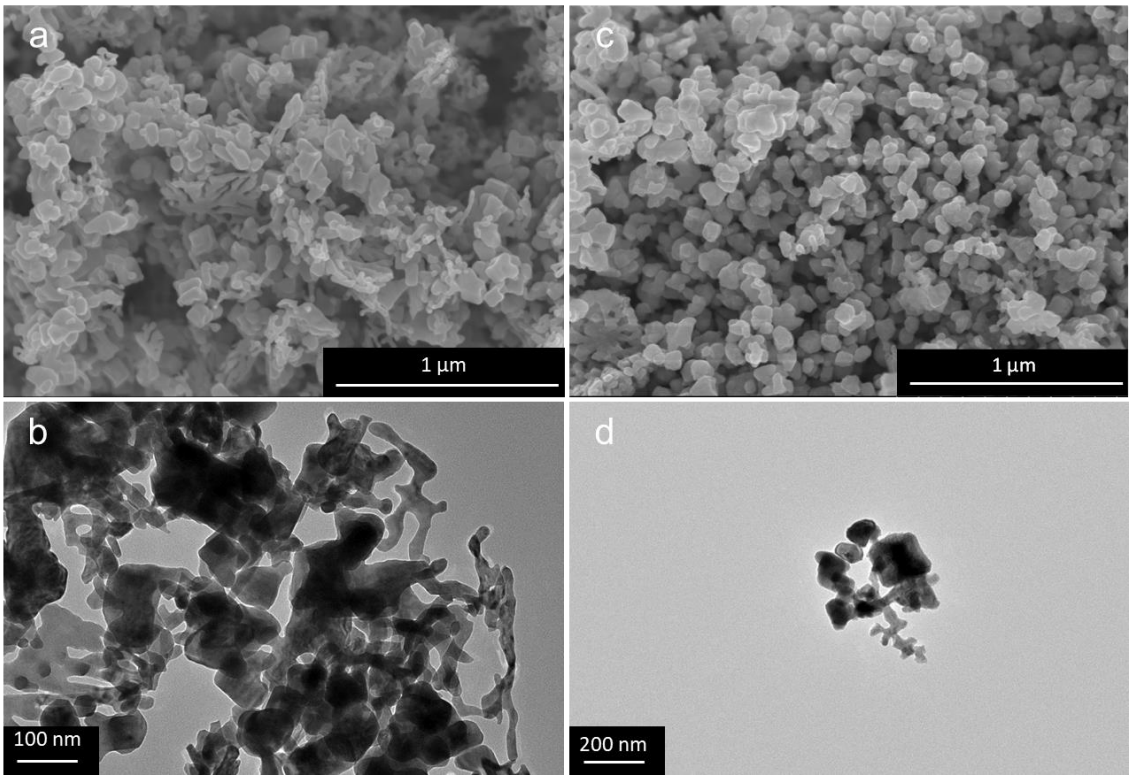

Figure 11. (a, c) SEM and (b, d) TEM images of samples obtained in molten $NaNO_2$ during 1 h at (a-b) 600 °C and (c-d) 750 °C.

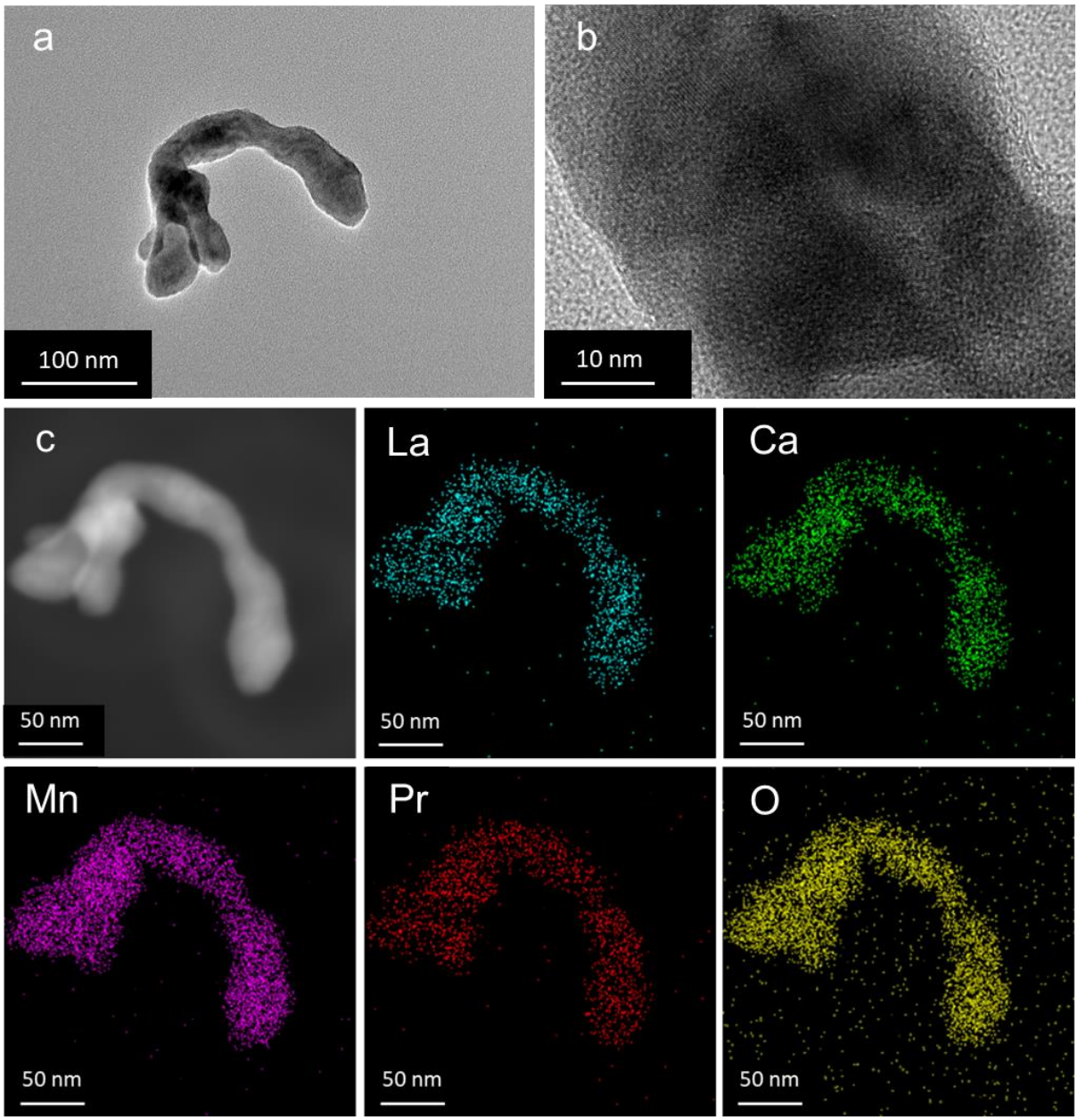

Figure 12. TEM images (a-b) and EDS mapping (c) of filament structure obtained in molten salt $NaNO_2$ during 1 h at 750 °C.

We then assessed in molten $NaNO_2$ at 750 °C the impact of the reaction time, from 15 min (synthesis C-15min) to 30 min (synthesis C-30min) and 1 h (synthesis C-1h). XRD (**Figure 13**) indicates that a reduction of the reaction time to 15 and 30 min yields the $CaMnO_3$ impurity and a decrease of the relative intensity of the characteristic peaks (e.g. at 28.5°) of the praseodymium oxide impurity, which even disappeared at 15 min. The nanoscale morphology of these samples was investigated by SEM (**Figure 14**), which showed that a decrease in the reaction time reduced the amount of filaments observed. Nonetheless, lowering the reaction time does not enable full coprecipitation of La, Ca, and Pr cations as $CaMnO_3$ is detected by

XRD. We observed that increasing the temperature of the synthesis above 750 °C yields impurities and even the loss of the LPCMO aimed phase (**Figure 10**). However, decreasing the temperature down to 600 °C yields LPCMO and $CaMnO_3$ phases with two types of morphologies. We showed in **Figure 13** and that reducing the reaction time led to less impurities (C-15 min) and less filaments structures. Therefore, increasing the temperature and reducing the reaction time both yield fewer filaments.

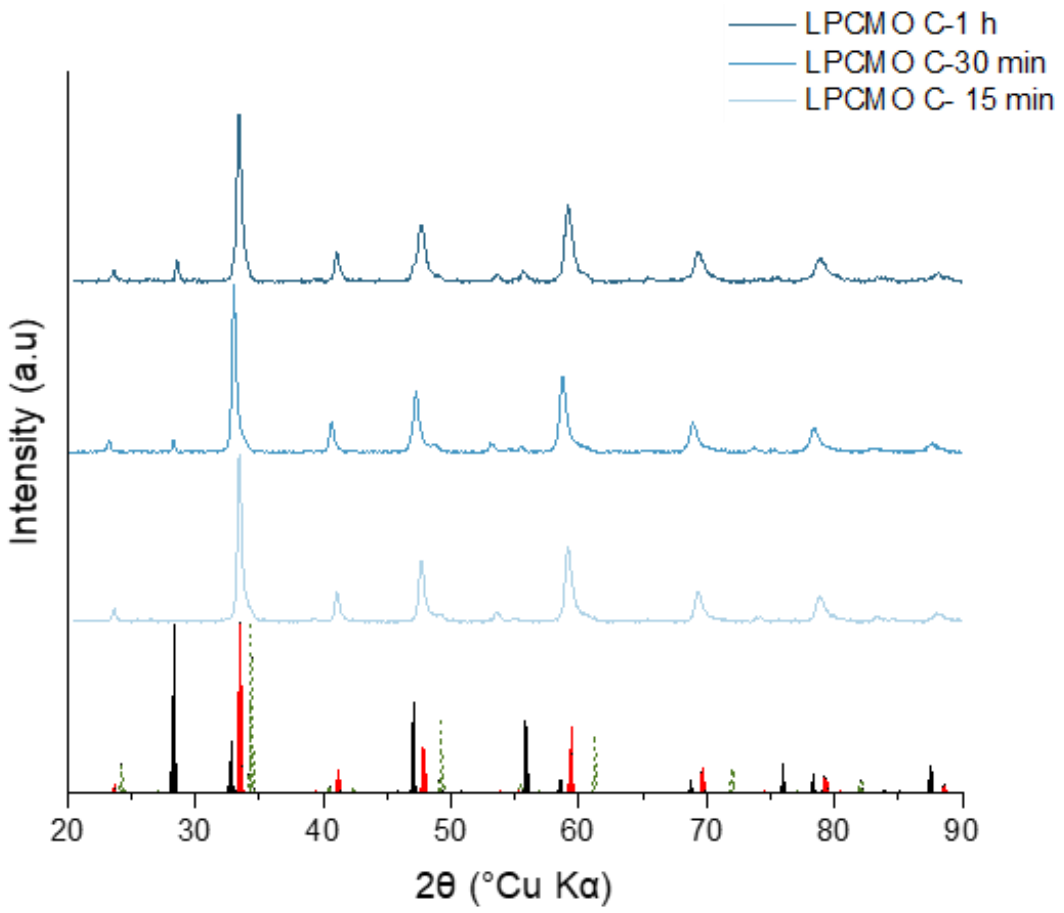

Figure 13. Powder XRD patterns of samples obtained in molten $NaNO_2$ at 750 °C during different reaction times. The reference patterns of LPCMO, $PrO_{1.88}$ and $CaMnO_3$ are displayed in red, black and green dashes respectively

.

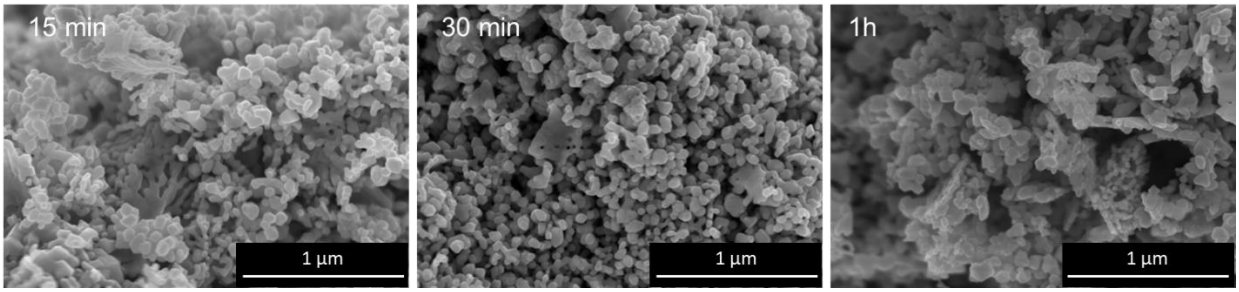

Figure 14. SEM images of samples obtained in molten $NaNO_2$ at 750 °C during different reaction times.

We then screened the reaction temperature from 650 °C (D-650 °C), 700 °C (D-700 °C) and 800 °C (D-800 °C) (**Figure 15**) at short reaction time, 15 min, to react all cations together, while still limiting the formation of filaments. The XRD patterns revealed the same behavior observed before, i.e. increasing the temperature above 750 °C leads to the formation of additional impurities, while below 750 °C down to 650 °C, the $CaMnO_3$ by-product is detected. Thus, competitive coprecipitation is still present during synthesis below 750 °C. TEM images (**Figure 16**) shows that lowering the temperature and the reaction time did not prevent the formation of the filaments.

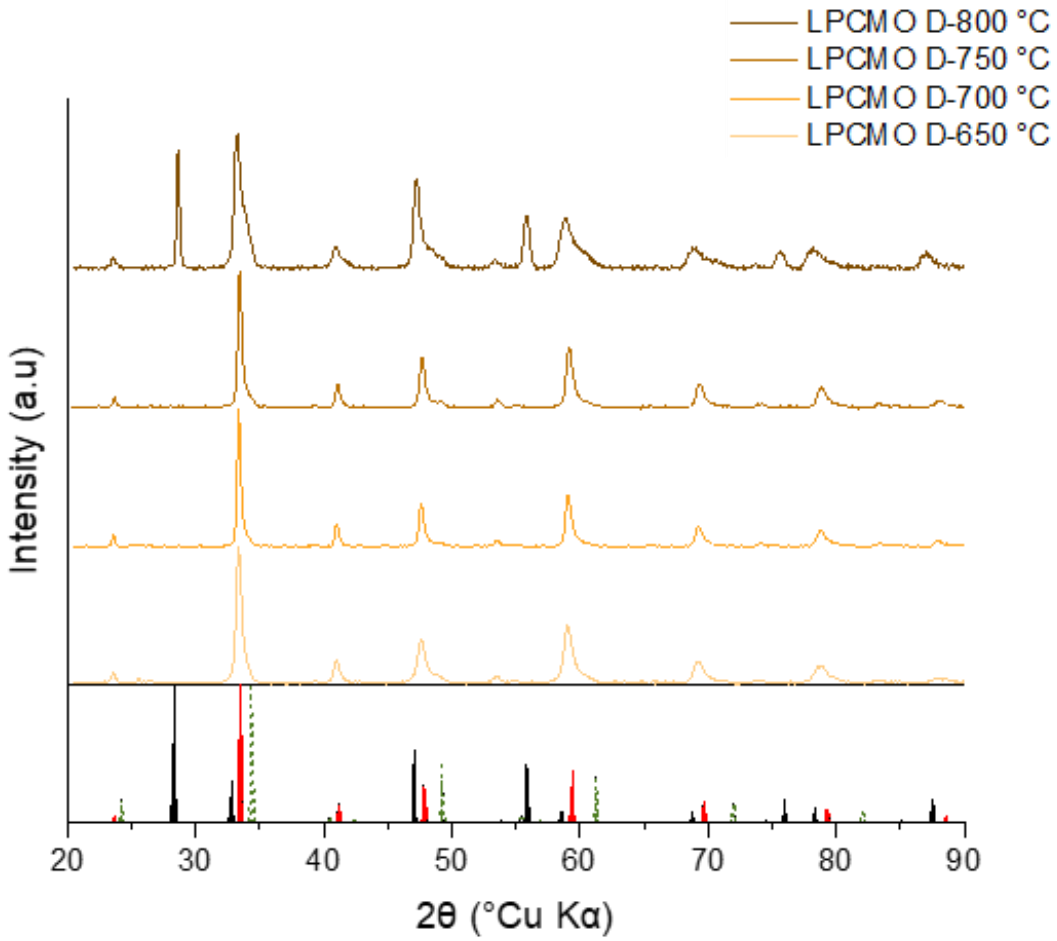

Figure 15. Powder XRD patterns of samples obtained in molten $NaNO_2$ during 15 min at different reaction temperatures. The reference pattern of LPCMO, $PrO_{1.88}$ and $CaMnO_3$ are displayed in red, black and green dashes respectively.

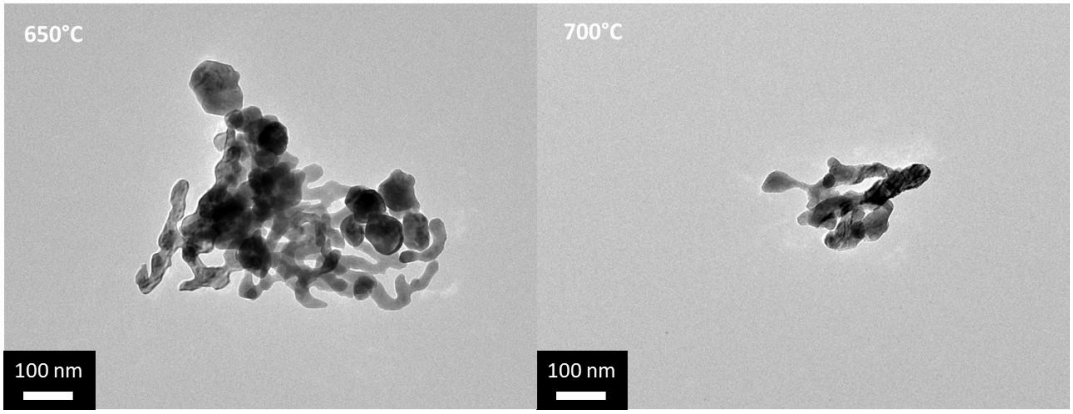

Figure 16. TEM images of samples obtained in molten $NaNO_2$ during 15 min at 650 °C (synthesis D-650) and at 750 °C (synthesis D-750).

To sum up, the experiments in molten sodium nitrite $NaNO_2$ discussed above showed that increasing reaction time and/or temperature yielded impurities and even loss of the targeted LPCMO phase above 1h and 750 °C. When lowering the temperature and/or diminishing reaction time below 1h and 750 °C, $CaMnO_3$ was formed and filaments were observed. The latter behavior can be ascribed to incomplete reaction between all cationic precursors, and to coalescence of the single particles. Both phenomena can be related to heating not efficient enough to react all cations and to trigger crystallization of the perovskite phase before coalescence of the particles. Therefore, by seeking for a more efficient heating process, we turned toward microwave-assisted synthesis. This process is well developed for hydrothermal and solvothermal syntheses of nanoparticles. Especially, Niederberger *et al.*[6] reviewed and explained how microwave heating enables efficient and fast heating to yield smaller nanoparticles, less polydisperse samples, shorter synthesis time, and faster nucleation rate, compared to conventional heating.

5. Influence of the heating process: microwave heating

The synthesis was performed using a patented microwave oven[7] suited to perform high temperature synthesis. Microwave-assisted synthesis presents several advantages to the synthesis of crystalline and homogeneous nanoparticles. First the heating ramp is faster than conventional heating devices. Second the whole reaction volume is heated homogeneously rather than by heat diffusion. This leads to shorter dwelling times for the obtention of crystalline material. The homogeneous temperature inside the medium avoids temperature gradients and heterogeneities thus allowing a better control over the particle morphology and size.[6] Sodium nitrite (10 eq), lanthanum nitrate hexahydrate (0.3 eq), praseodymium nitrate hexahydrate

(0.3 eq), calcium nitrate tetrahydrate (0.27 eq) and manganese nitrate tetrahydrate (1 eq) were used as reported for previous procedures. (*Syntheses Ex).*

For microwave-assisted syntheses, the reaction media were heated from room temperature to the targeted temperature over a ramping time noted X_{ramp}. The temperature was then dwelled over a time noted $X'_{plateau}$. The overall reaction time is then noted $X_{ramp}+X'_{plateau}$. Syntheses were performed at 750 °C for 2+2min (synthesis E-2+2), 4+2min (synthesis E-4+2), 4+5min (synthesis E-4+5). According to powder XRD patterns (**Figure 17**), no $CaMnO_3$ phase was detected for 4+2min and 4+5min synthesis. A low intensity peak at 25° ascribed to $CaMnO_3$ is visible only for the synthesis at shortest reaction time (E-2+2). Noteworthy, reaction times are strongly reduced compared to conventional heating. Nonetheless, according to TEM (**Figure 18**), microwave heating did not avoid the formation of the filament structures.

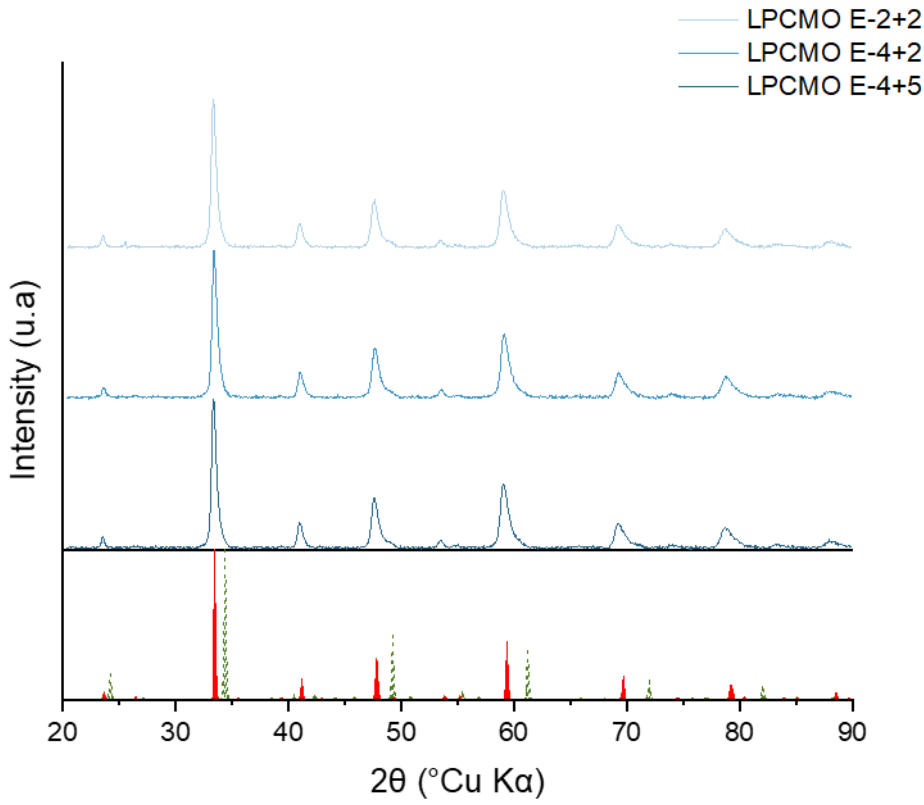

Figure 17. Powder XRD patterns of samples obtained by microwave heating in molten $NaNO_2$ at 750 °C during different ramping and dwelling times. The reference patterns of LPCMO and $CaMnO_3$ are displayed in red and green dashes respectively.

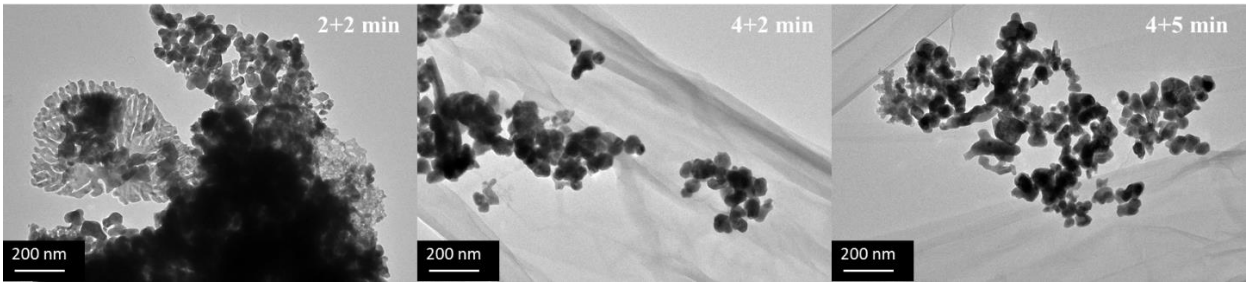

Figure 18. TEM images of samples obtained by microwave heating in molten $NaNO_2$ at 750 °C during different ramping and dwelling times.

We have underlined above that changing the molten salt from KNO_3 (syntheses A) to $NaNO_2$ (syntheses C, D and E) enabled avoiding the formation of Ca-poor perovskite foils, through an increase of the oxo-basicity of the molten salt. Because we hypothesized that the filaments observed in $NaNO_2$ were originating from overlapped nucleation and growth stages, we have sought to further increase the nucleation rate by further increasing the oxo-basicity of the medium. To do so, 3 equivalents of Na_2O versus Mn were added to the initial salt mixture. The corresponding XRD diffractogram (**Figure 19**) shows that the addition of Na_2O prevented the formation of any detectable impurities at 800 °C, including $CaMnO_3$. TEM (**Figure 19**a-b) shows the disappearance of the filaments when Na_2O is added to the reactive media. Regarding the particles shapes, they appeared to be either spherical or cubical. The HRTEM image (**Figure 20**c) shows a high crystallinity for a LPCMO nanoparticle. Finally, the size distribution from TEM (**Figure 20**d) gave an average size of 25 nm and clearly showed a high polydispersity. The general composition was assessed by EDS mapping (**Figure 20**e) and we observed the presence of the five compositional elements with a calculated composition of $La_{0.35\pm0.1}Pr_{0.35\pm0.1}Ca_{0.29\pm0.1}MnO_3$. X-ray photoelectron spectroscopy (XPS) analysis reported in **Appendix 2** gave an elemental ratio of $La_{0.2\pm0.1}Pr_{0.2\pm0.1}Ca_{0.4\pm0.1}MnO_3$ which is close to the $La_{1/3}Pr_{1/3}Ca_{1/3}MnO_3$ targeted. Despite shape and size disparity, the synthesis of single-phase nanoparticles of LPCMO was achieved.

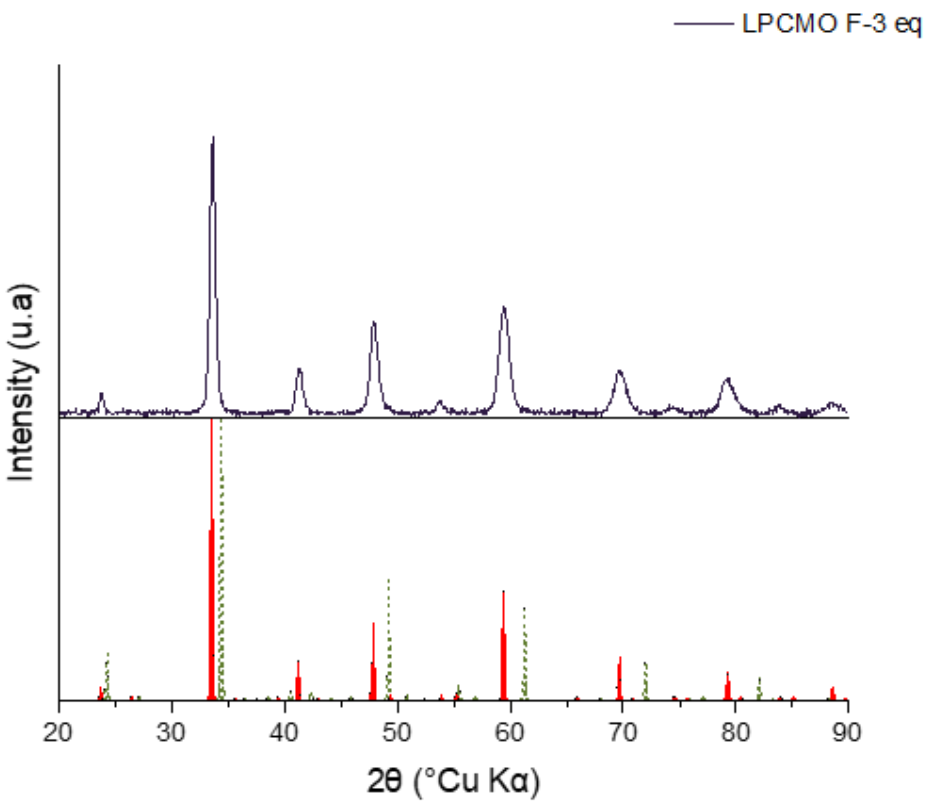

Figure 19. Powder XRD pattern of the sample obtained by microwave heating in molten $NaNO_2$ at 800 °C for 3 min by addition of 3 equivalents of Na_2O (synthesis F-3eq). The reference patterns of LPCMO and $CaMnO_3$ are displayed in red and green dashes respectively

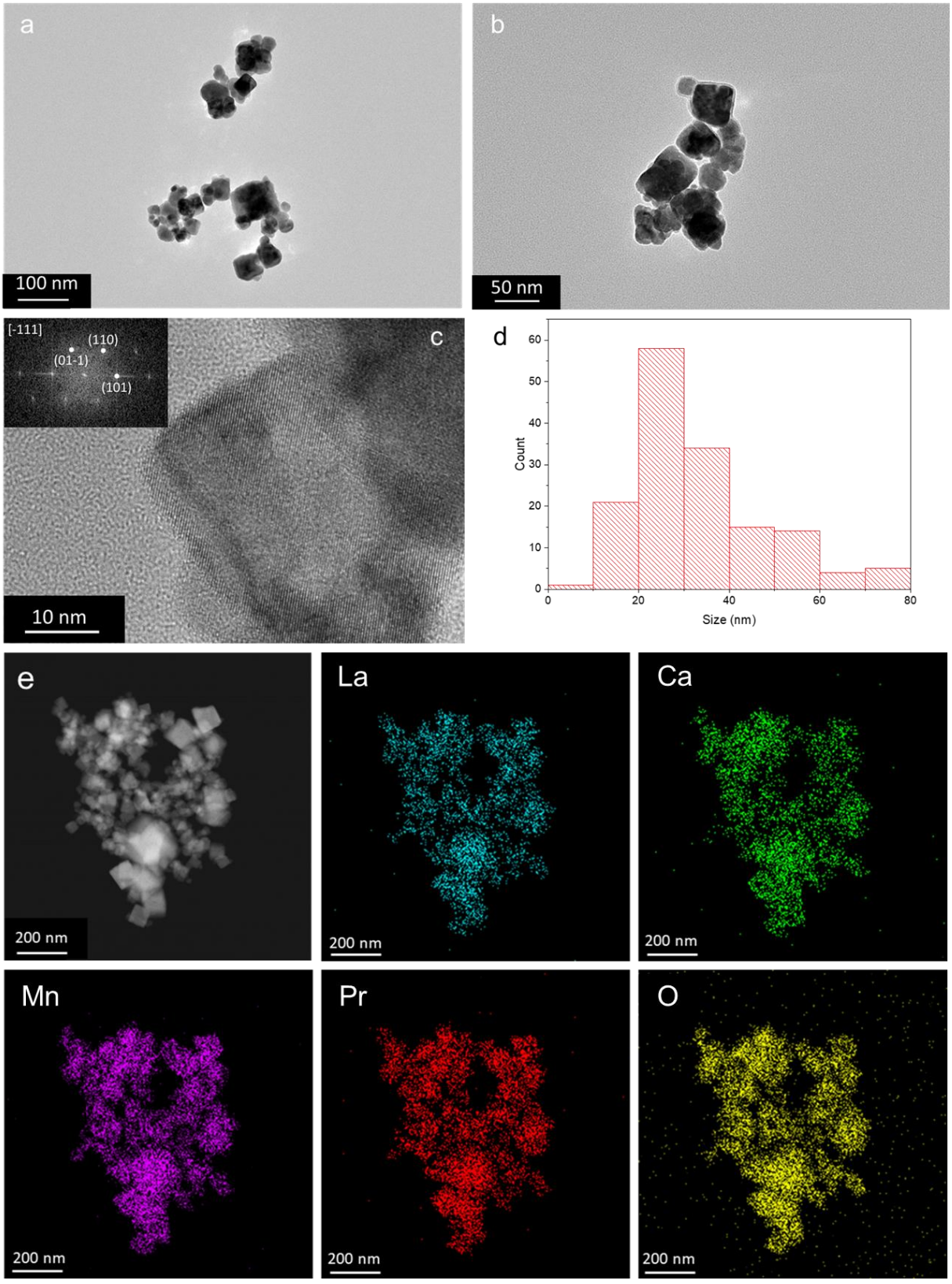

Figure 20. (a-b) TEM images, (d) corresponding diameter distribution, (c) HRTEM images and (d) EDS mapping of the sample obtained from synthesis F-3eq with 3 eq of Na_2O.

III. Conclusion

To sum up, the synthesis of single phase $La_{0.33}Pr_{0.33}Ca_{0.33}MO_3$ nanoparticles has been attempted in KNO_3 molten salt, which resulted in the formation of the aforementioned nanoparticles but also $CaMnO_3$ (CMO) impurities and $La_{0.66}Pr_{0.33}MnO_3$ foils. To avoid a competitive coprecipitation between Pr and Ca responsible for the formation of $CaMnO_3$ and the calcium-poor perovskite, the molten salt was changed from KNO_3 to $NaNO_2$. $NaNO_2$ increased the oxo-basicity of the reactive media due to its faster dissociative constant, thus, lowered the Ca solubility. The change of molten salt hindered the formation of LPMO foils and of the CMO phase but led to the formation of LPCMO filaments. It was hypothesized that changing the heating process of these syntheses from conventional heating to microwave heating would help the formation of well-defined $La_{0.33}Pr_{0.33}Ca_{0.33}MO_3$ nanoparticles. However, the filament kept being formed during the synthesis. Finally, more oxygen was added to the reactive media using Na_2O. It resulted in the disappearance of the filament structures and the obtention of single-phase LPCMO nanoparticles close to the one aimed for in the first place. Hence, the oxo-basicity of the flux is the key factor for enabling the synthesis of phase-pure multicationic oxides.

The electrocatalytic properties of LPCMO nanoparticles were investigated in preliminary measurements for the oxygen reduction reaction (**Appendix 1**). We observed a clear response of the nanoparticles to the magnetic field, which cannot yet be unambiguously ascribed to the colossal magnetoresistance effect. Several results are open for discussion such as the high number of electrons measured by Koutecky-Levich analysis (**Appendix 3**) during ORR. Also, the reason for the higher response of $La_{0.33}Pr_{0.33}Ca_{0.33}MO_3$ under magnetic field in a 4 M KOH (**Appendix 4**) and the mechanism behind is yet to be established. Electrochemical impedance spectroscopy measurements are required for the understandings of the mechanisms involved in ORR with LPCMO under magnetic field. The next chapter will provide a more indepth study of the entanglement between electrocatalysis and a magnetic field with the case study of $La_{0.7}Sr_{0.3}MnO_3$.

References

(1) Stoerzinger, K. A.; Risch, M.; Han, B.; Shao-Horn, Y. Recent Insights into Manganese Oxides in Catalyzing Oxygen Reduction Kinetics. *ACS Catal.* **2015**, *5* (10), 6021–6031. https://doi.org/10.1021/acscatal.5b01444.

(2) Shao, J.; Liu, H.; Zhang, K.; Yu, Y.; Yu, W.; Lin, H.; Niu, J.; Du, K.; Kou, Y.; Wei, W.; Lan, F.; Zhu, Y.; Wang, W.; Xiao, J.; Yin, L.; Plummer, E. W.; Shen, J. Emerging Single-Phase State in Small Manganite Nanodisks. *Proc. Natl. Acad. Sci.* **2016**, *113* (33), 9228–9231. https://doi.org/10.1073/pnas.1609656113.

(3) Thi N'Goc, H. Le; Mouafo, L. D. N.; Etrillard, C.; Torres-Pardo, A.; Dayen, J. F.; Rano, S.; Rousse, G.; Laberty-Robert, C.; Calbet, J. G.; Drillon, M.; Sanchez, C.; Doudin, B.; Portehault, D. Surface-Driven Magnetotransport in Perovskite Nanocrystals. *Adv. Mater.* **2017**, *29* (9), 1–9. https://doi.org/10.1002/adma.201604745.

(4) Raihani, H. Al; Durand, B.; Chassagneux, F.; Kerridged, D. H. Zirconia Formation by Reaction of Zirconium Sulfate in Molten Alkali-Metal Nitrates or Nitrites. **1994**, *4* (8), 1331–1336.

(5) Jolivet, J. P.; Tronc, É.; Chanéac, C. Synthesis of Iron Oxide-Based Magnetic Nanomaterials and Composites. *Comptes Rendus Chim.* **2002**, *5* (10), 659–664. https://doi.org/10.1016/S1631-0748(02)01422-4.

(6) Bilecka, I.; Niederberger, M. Microwave Chemistry for Inorganic Nanomaterials Synthesis. *Nanoscale* **2010**, *2* (8), 1358–1374. https://doi.org/10.1039/b9nr00377k.

(7) Portehault, D.; Marinel, S.; Savary, E. Method for Melting a Salt Sample by Microwave. W0/2018/104187A1, 2018.

(1) Stoerzinger, K. A.; Risch, M.; Han, B.; Shao-Horn, Y. Recent Insights into Manganese Oxides in Catalyzing Oxygen Reduction Kinetics. *ACS Catal.* **2015**, *5* (10), 6021–6031. https://doi.org/10.1021/acscatal.5b01444.

(2) Shao, J.; Liu, H.; Zhang, K.; Yu, Y.; Yu, W.; Lin, H.; Niu, J.; Du, K.; Kou, Y.; Wei, W.; Lan, F.; Zhu, Y.; Wang, W.; Xiao, J.; Yin, L.; Plummer, E. W.; Shen, J. Emerging Single-Phase State in Small Manganite Nanodisks. *Proc. Natl. Acad. Sci.* **2016**, *113* (33), 9228–9231. https://doi.org/10.1073/pnas.1609656113.

(3) Thi N'Goc, H. Le; Mouafo, L. D. N.; Etrillard, C.; Torres-Pardo, A.; Dayen, J. F.; Rano,

S.; Rousse, G.; Laberty-Robert, C.; Calbet, J. G.; Drillon, M.; Sanchez, C.; Doudin, B.; Portehault, D. Surface-Driven Magnetotransport in Perovskite Nanocrystals. *Adv. Mater.* **2017**, *29* (9), 1–9. https://doi.org/10.1002/adma.201604745.

(4) Raihani, H. Al; Durand, B.; Chassagneux, F.; Kerridged, D. H. Zirconia Formation by Reaction of Zirconium Sulfate in Molten Alkali-Metal Nitrates or Nitrites. **1994**, *4* (8), 1331–1336.

(5) Jolivet, J. P.; Tronc, É.; Chanéac, C. Synthesis of Iron Oxide-Based Magnetic Nanomaterials and Composites. *Comptes Rendus Chim.* **2002**, *5* (10), 659–664. https://doi.org/10.1016/S1631-0748(02)01422-4.

(6) Bilecka, I.; Niederberger, M. Microwave Chemistry for Inorganic Nanomaterials Synthesis. *Nanoscale* **2010**, *2* (8), 1358–1374. https://doi.org/10.1039/b9nr00377k.

(7) Portehault, D.; Marinel, S.; Savary, E. Method for Melting a Salt Sample by Microwave. W0/2018/104187A1, 2018.

Chapter III:

$La_{0.7}Sr_{0.3}MnO_3$ nanoparticles, towards interplay between magnetic fields and the oxygen reduction reaction electrocatalysis

I. Introduction

Manganese perovskites composed of mixed-valence $Mn^{3+/4+}$ are of great interest for the scientific community due to their peculiar properties described in the previous chapter. Some of them are considered as best precious-metal free electrocatalysts for the oxygen reduction reaction (ORR), especially $La_{0.7}Sr_{0.3}MnO_3$ (LSMO).[1] Besides LSMOs' interesting electrocatalytic properties, this perovskite also possesses gripping magnetic properties. The special magnetic behavior of LSMO nanocrystals has been reported by Thi N'Goc *et al.*[2], who showed that under a magnetic field, the nanoparticles resistivity strongly decreases (**Figure 1Figure** a). This magnetoresistance effect (MR) at temperatures far away from the bulk Curie temperature has been ascribed to the magnetic structure of the particles. Indeed, the magnetization curves could be decomposed into two different magnetic components (**Figure 1**b), one ferromagnetic component ascribed to the core and another paramagnetic-like component from a 4 nm-thick shell. This behavior relates to the electronic phase separation (EPS), well documented for manganese perovskite oxides.[3–6]

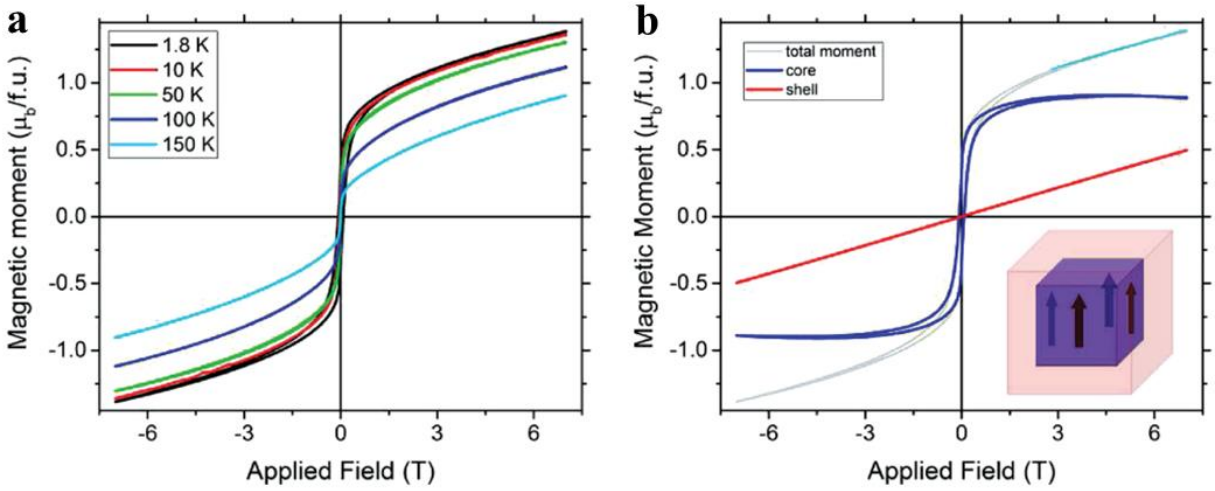

Figure 1. Magnetic characterization of LSMO nanoparticles. a) Magnetization curves at several temperatures. b) Decomposition of the magnetization at 1.8K into a ferromagnetic core component (blue curve) dominant at low field and a paramagnetic-like shell (red curve) dominant at high field.

The presence of both MR and EPS in LSMO nanoparticles adds a new dimension to the electrocatalytic properties of this system. Applying a magnetic field to LSMO nanoparticles leads to a decrease of the electrical resistivity (MR effect) and more specifically of the electrical resistivity of the shell of the particles (EPS). Hence, under a magnetic field, a fully conductive ferromagnetic system would form, thus enhancing charge transport that is directly linked to the electrocatalytic activity. In this chapter we first present the synthesis of highly crystalline

nanoparticles of LSMO using a molten salt synthesis. Then the electrocatalytic activity of these LSMO nanoparticles for the oxygen reduction reaction is shown. The electrocatalytic properties measured in standard conditions are then compared to those measured under magnetic field.

II. Synthesis of $La_{0.7}Sr_{0.3}MnO_3$ nanoparticles

The synthesis of $La_{0.77}Sr_{0.33}MnO_3$ (LSMO) nanoparticles was performed following the protocol reported by N'Goc *et al*.[2]. Manganese nitrate tetrahydrate (1 eq), lanthanum nitrate hexahydrate (0.6 eq), strontium nitrate (0.3eq), and potassium nitrate (10 eq) were heated at 600 °C for 2 h. After washing with water, the powder was analyzed by X-ray diffraction (XRD) (**Figure 2**) The pattern obtained is consistent with LSMO, as the sole crystalline phase.

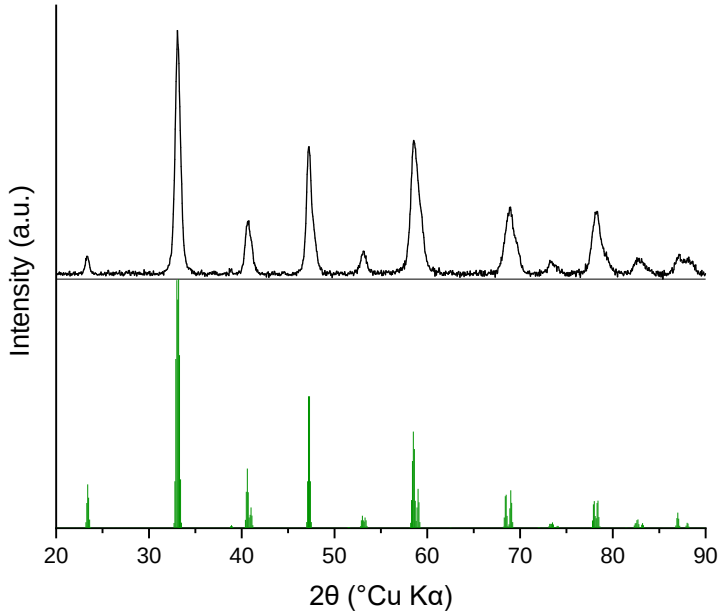

Figure 2. Powder XRD pattern of a LSMO sample synthetized in molten KNO_3 (black) and LSMO reference (green).

The morphology of the nanoparticles was then analyzed by transmission electron microscopy (TEM) and scanning electron microscopy (SEM) (**Figure 3**). TEM (**Figure 3**a) and SEM (**Figure 3**b) show highly crystalline cubical particles as expected from a perovskite structure. HRTEM (**Figure 3**c) confirms the LSMO pseudo-cubic perovskite structure. Analysis of several HRTEM images enables identifying facets of the particles, leading to the morphology shown in **Figure 3**e-f. The size distribution from TEM (**Figure 3**d) gives an average size of 20 nm.

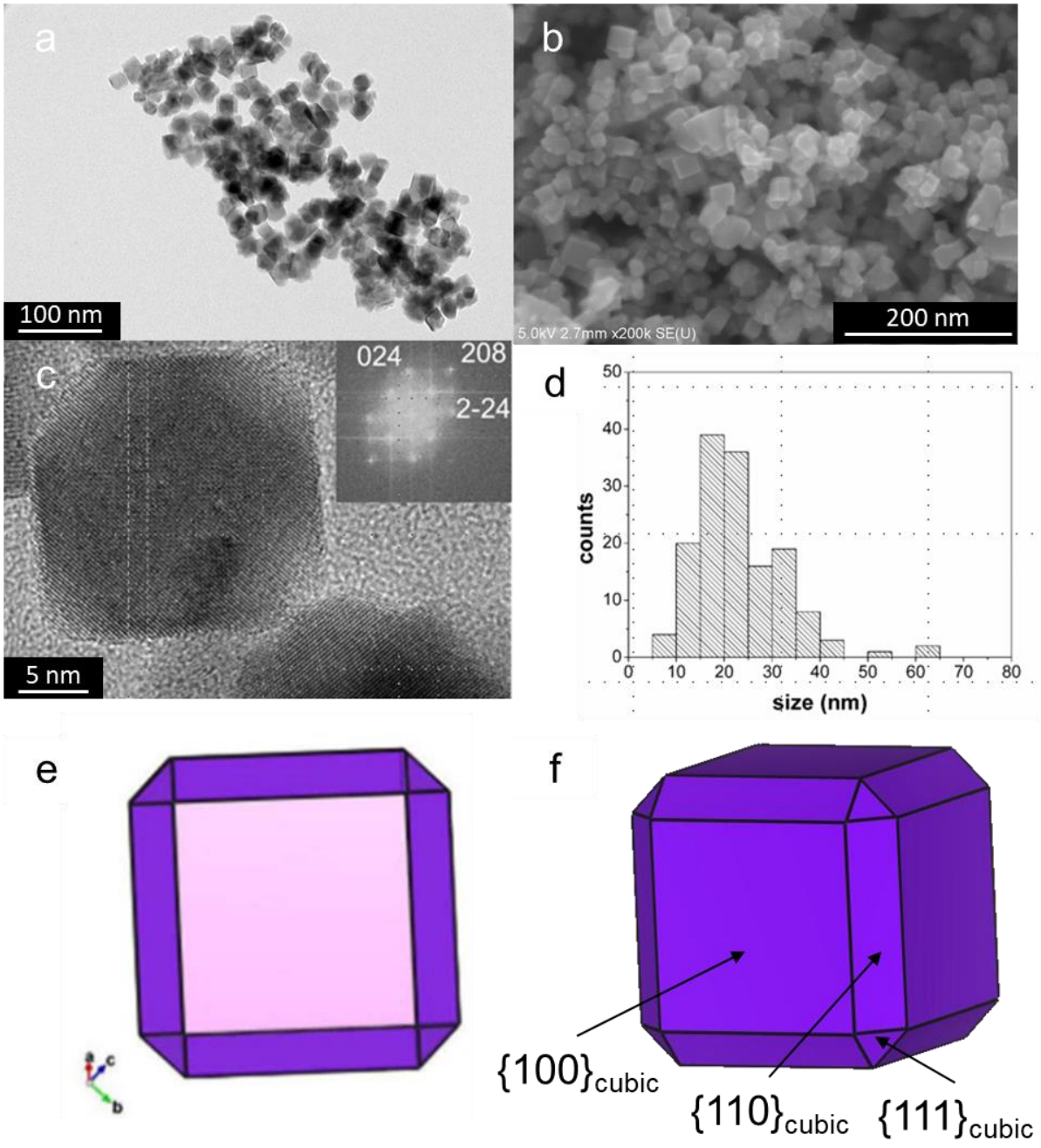

Figure 3. (a) TEM and (b) SEM images of LSMO nanoparticles obtained at 600 °C for 2 h in molten potassium nitrate. (c) HRTEM image of a LSMO nanocube and (e) its corresponding projection. (d) size distribution of LSMO nanoparticles. (f) 3D model of a LSMO nanocrystal.[7]

III. Electrochemical behavior of LSMO in a rotating disk electrode (RDE) configuration

The LSMO nanoparticles were deposited on a glassy carbon rotating disk electrode (RDE), as a catalyst/Nafion/carbon black composite electrode film. The use of the RDE allows the control of the diffusion barrier, which drives the flux of reactive species/products towards/from the catalytic surface.

Cyclovoltammetry cycles (CVs) in 0.1 M KOH saturated with O_2 were performed at 15 °C, below the Curie temperature of LSMO (≃87 °C)[8]. The CVs were recorded at different speed to control the aforementioned diffusion barrier (**Figure 4**). The ORR onset potential was found to be of 0.9 V vs. RHE and the diffusion plateau was obtained at 0.47 V vs. RHE. According to Koutecky-Levich (KL) analysis at 0.4 V vs. RHE, 4.1 electrons were transferred per O_2 molecule, which is close to the theoretical 4-electrons value for the overall reduction reaction of O_2 into H_2O.

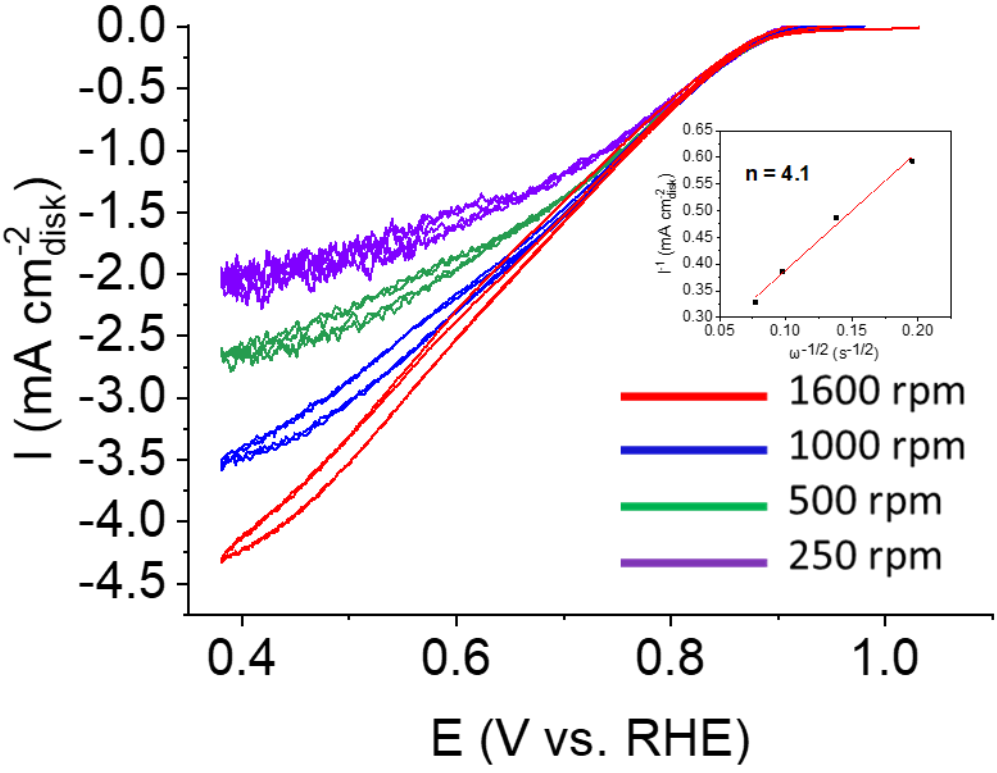

Figure 4. Last cyclovoltammetry cycles obtained after cycling 15 times a LSMO RDE at 15 °C in O_2- saturated 0.1M KOH. Inset shows the Koutecky-Levich analysis and the number of exchanged electron per O_2.

We then assessed the effect of the magnetic field on the ORR with LSMO. To do so, a Haalbaar permanent magnet of 1 T was installed around the electrochemical cell for magnetic field experiments (**Figure 5**a). The magnetic field was then parallel to the surface of the

composite electrode film. Finally, such magnet has the particularity to have a contained and homogeneous field. The use of such magnet avoids the formation of magnetic field gradient during the experiments contrary to what can be found in the literature.[9]

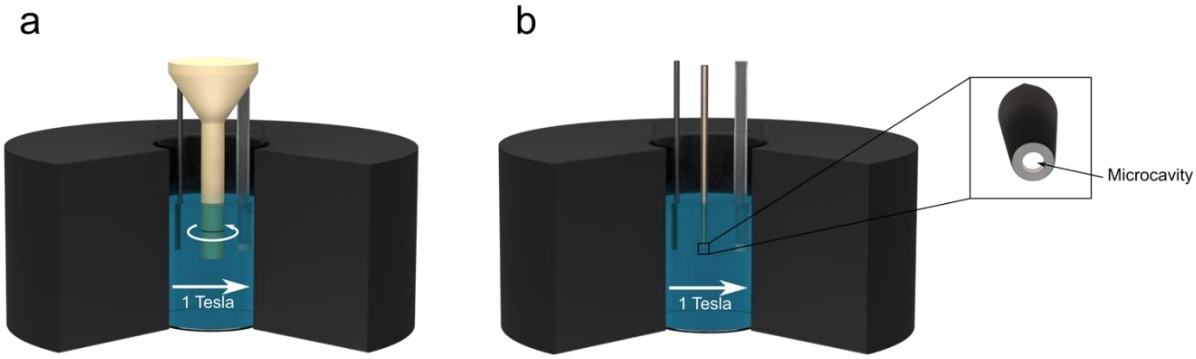

Figure 5. Representation of the experimental setup under magnetic field using (a) a RDE and (b) a microelectrode (ME).

Experiments have been sequenced in three steps, to observe the effect of a permanent magnetic field of 1T onto the electrocatalytic activity of LSMO nanoparticles. The first phase is described as “no magnetic field” (NMF), followed by the use of the “magnetic field” (MF) and finally, by removal of the magnetic field, described as “no magnetic field recovered” (NMFR).

The results are shown **Figure 6.** Firstly, increasing the rotation speed from 250 rpm to 1600 rpm increases the cathodic current density by almost twice for each phase. This increase of the cathodic current with the speed arises from the thinning of the diffusion layer by the rotation of the RDE, resulting in an increase of the reagents flux to the electrode. Secondly, under magnetic field (MF) (**Figure 6**b) perturbations are creating a periodic signal rendering hard to distinguish the exact values of the cathodic current density. This periodic signal is most likely due to the induced current in the rotating device within the magnetic field. Thirdly, the current density in MF conditions is lower than in NMF conditions (**Figure 6**a). Then, once the LSMO composite electrode undergoes again cyclovoltammetry measurements without magnetic field (NMFR) (**Figure 6**c), the initial activity (NMF) is not recovered. The current density observed for NMFR at each rotation speed is close to the one obtained under MF. The number of electrons transferred during ORR was measured by KL analysis of the diffusion current at 0.4 V vs. RHE for the three steps. For MF and NMFR, KL analysis indicates that 4.3 and 5.5 electrons are transferred, respectively, which is higher than in NMF (**Figure 4**) and larger than expected for ORR.

Overall, we did not observe any enhancement of the electrocatalytic activity of LSMO under magnetic field at 15 °C, and the signal was very noisy. Nonetheless, we observed a clear effect of the magnetic field.

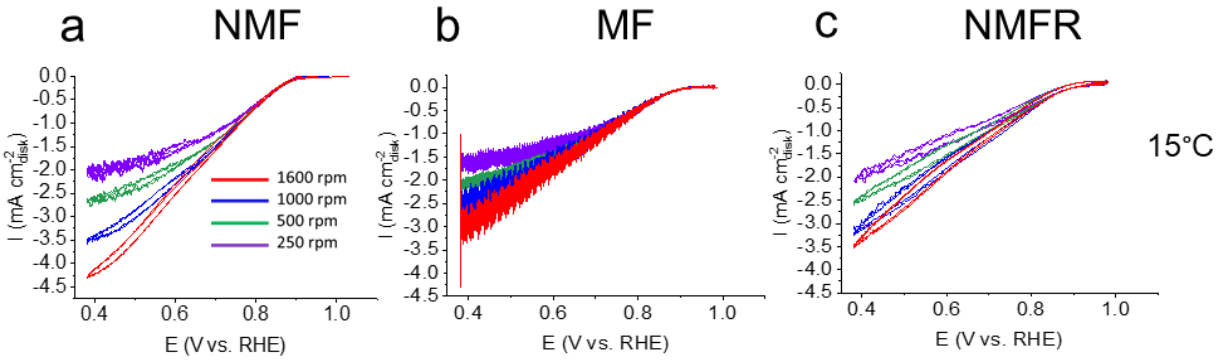

Figure 6. Last cyclovoltammetry cycles obtained after cycling 15 times a LSMO RDE at 15 °C in O_2- saturated 0.1M KOH. a) no magnetic field (NMF), b) under magnetic field (MF) and c) with no magnetic field recovered (NMFR).

Based on the magnetization curves expressing an increase of the magnetoresistance effect of LSMO at low temperatures and shown in the state-of-the-art chapter (part I.4).a), we then decided to decrease the operation temperature to 10 and 5 °C. The results at 10 °C and 5 °C were similar to those obtained at 15 °C. Increasing the rotation speed increases the current density values. Under magnetic field (MF) (**Figure 7**b-e) the activity of the electrocatalyst is lower than without magnetic field (NMF) (**Figure 7**a-b). Upon cycling again with no magnetic field (NMFR) (**Figure 7**c-f), the initial activity is not recovered. Hence, decreasing the temperature had no positive effect, the maximal cathodic current values obtained decreased with the temperature. The Koutecky-Levich analysis performed at 10 °C and 5 °C gave an electron number close to 4 for NMF and MF experiments. However, this amount increased to values close to 5 electrons for NMFR experiments.

Three different issues were brought up by these experiments. First the decrease in activity observed across the three different steps of measurement could come from damage or loss of the LSMO composite film. The second issue is the periodic noise observed while cycling for all speed rates under magnetic field (**Figure 6**b and **Figure 7**b-e). Due to the periodicity of the signal, we supposed that it was a consequence of the induced current in the rotating device within the magnetic field. Finally, the impossibility to recover the initial activity observed during the third step (NMFR) could come from a low kinetics of the mechanisms bringing back the particles to their initial state. In order to test these hypotheses and seek further effect of the magnetic field on the catalytic properties of LSMO nanoparticles, the RDE system was changed to microelectrodes, which enable control of the diffusion layer without any moving part.

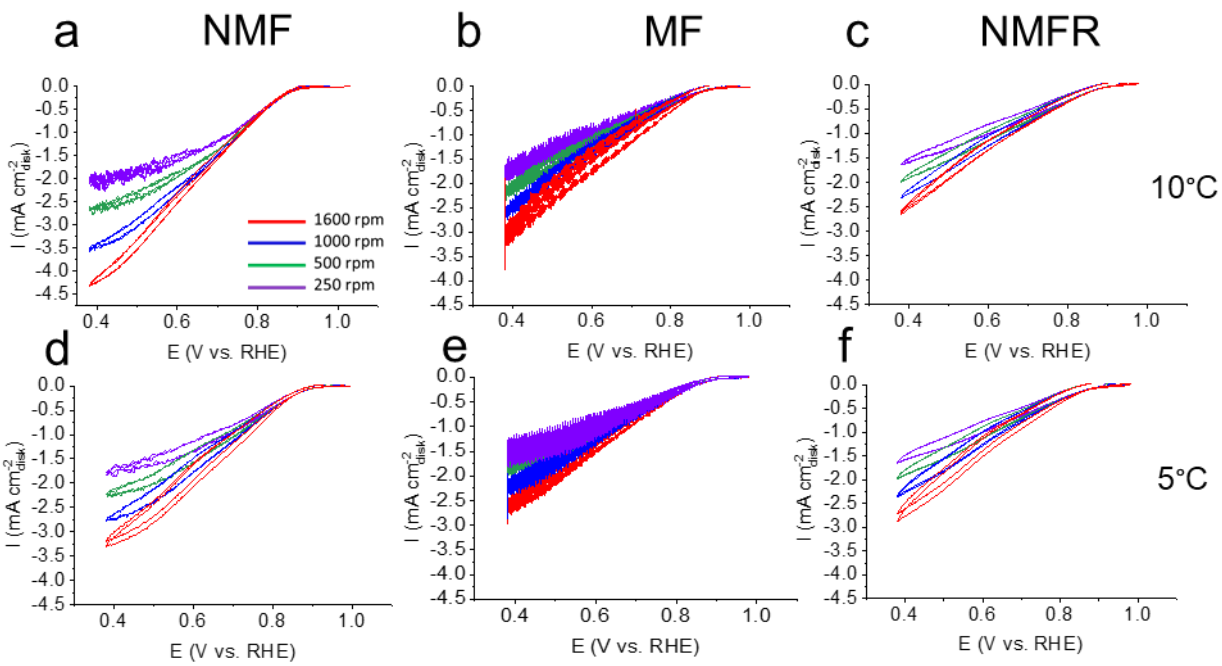

Figure 7. Last cyclovoltammetry cycles obtained after cycling 15 times a LSMO RDE at 10 °C (a, b, c) and 5 °C (d, e, f) in O_2-saturated 0.1M KOH at 250, 500, 100, 1600 rpm, a & d) no magnetic field (NMF), b & e) under magnetic field (MF) and c & f) no magnetic field recovered (NMFR).

IV. Cyclic voltammetry studies of LSMO using a microelectrode (ME)

Microelectrodes enable detecting small variations of current and do not encompass any moving parts. The absence of moving part should eliminate the noise observed under magnetic field with the RDE (**Figure 5**b). In addition, microelectrodes do not require anything else than the nanoparticles, freeing the system from other electrode components such as carbon black or Nafion. Thus, we ensure that any magnetic response directly arises from the electrocatalyst. Copper microelectrodes have been prepared following a protocol reported by Cachet-Vivier *et al.*[10]. The microelectrode is then set operational following oxidative etching of the copper wire up to few micrometers, thus creating a microcavity where nanoparticles are inserted by manual stamping. Note however that microelectrodes have downsides. Indeed, due to the manual stamping to fill the microcavity, precision and reproducibility concerning the amount of nanoparticles inserted are hard to achieve. This results in the impossibility to compare current-wise different experiments. Nonetheless, responses to a magnetic field should still be detectable. We then assessed the role of the O_2 saturation.

1. ORR activity in ME configuration

We first assessed the occurrence of ORR in the microelectrode configuration. To do so, cyclovoltammetry cycles were recorded using a microelectrode at 15°C in 0.1 M KOH first saturated by Ar, then by O_2. **Figure 8** shows that changing the electrolyte saturation from Ar to O_2 without magnetic field increases the cathodic current. We ascribe this effect to the occurrence of the ORR.

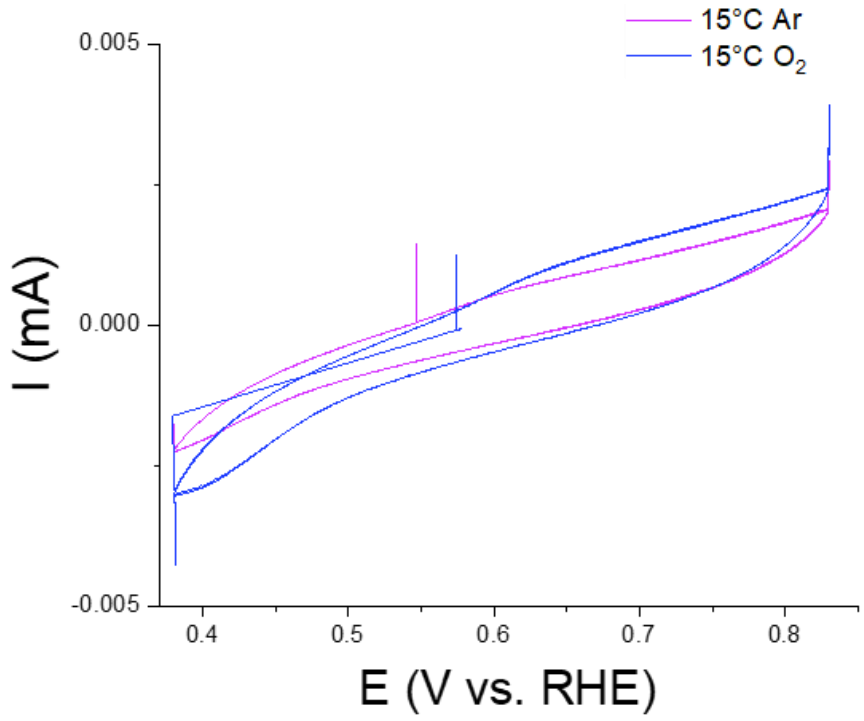

Figure 8. Last cyclovoltammetry cycles obtained after cycling 15 times a LSMO microelectrode at 15°C in KOH 0.1M saturated first by Ar (purple) then by O_2 (blue).

2. Purity of the electrolyte

The standard 0.1M KOH electrolyte used in the previous experiments is known to contain small quantities of paramagnetic iron cations.[11] Therefore, the electrolyte was purified in order to ensure that this impurity had negligible impact on the electrocatalytic activity and on the effect of the magnetic field. The protocol used was described by Trotochaud *et al.*[11] and allowed obtaining Fe-free KOH. Cyclovoltammetry cycles were then recorded with microelectrodes at 20 °C, 15 °C and 5 °C (**Figure 9)**. The CVs show that purifying the electrolyte did not change the responses of LSMO under magnetic field (**Figure 9**) as we observed the same behavior

reported previously with a rotating disk electrode (**Figure 6**-**Figure 7**). Thus, small traces of Fe in the electrolyte are of no influence on LSMO surface changes.

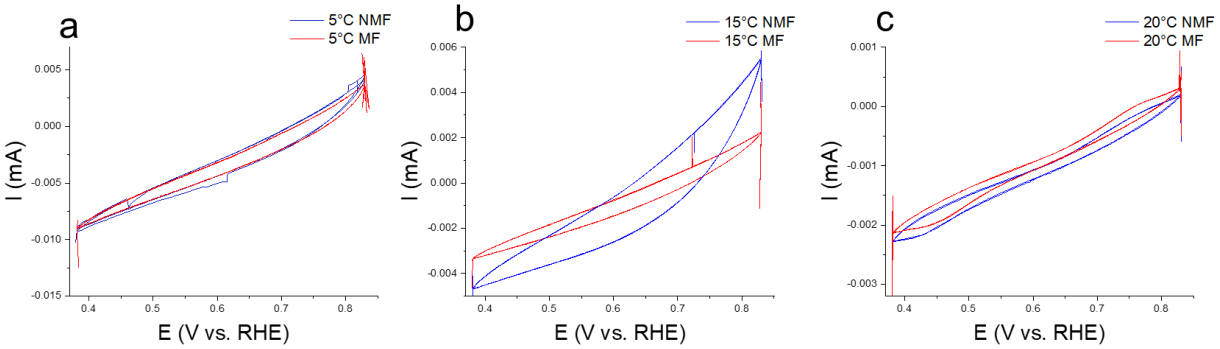

Figure 9. Last cyclovoltammetry cycles obtained after cycling 15 times a LSMO microelectrode at (a) 5 °C, (b) 15 °C and (c) 20 °C in O_2-saturated 0.1M KOH and purified, without magnetic field (NFM-blue) and under magnetic field (MF-red).

3. Impact of the magnetic field

We then assessed LSMO filled Cu microelectrodes and their response to a 1T magnetic field. The microelectrode electrochemical response was studied by CV in 0.1M KOH at 15 °C. First, argon-saturated electrolyte was used to deprive the material from the ORR reagent and then obtain the LSMO magnetic response (**Figure 10**) in the absence of electrochemical reaction.

The cyclovoltammetry cycles **Figure 10** show an increase of the overall current density under a magnetic field. The enhancement observed can originate from either the aforementioned magnetoresistance effect or the magnetohydrodynamic effect. Observation of a magnetic field effect in microelectrodes confirms their sensitivity and utility to detect small variations of current. We then moved to the study of this effect during ORR.

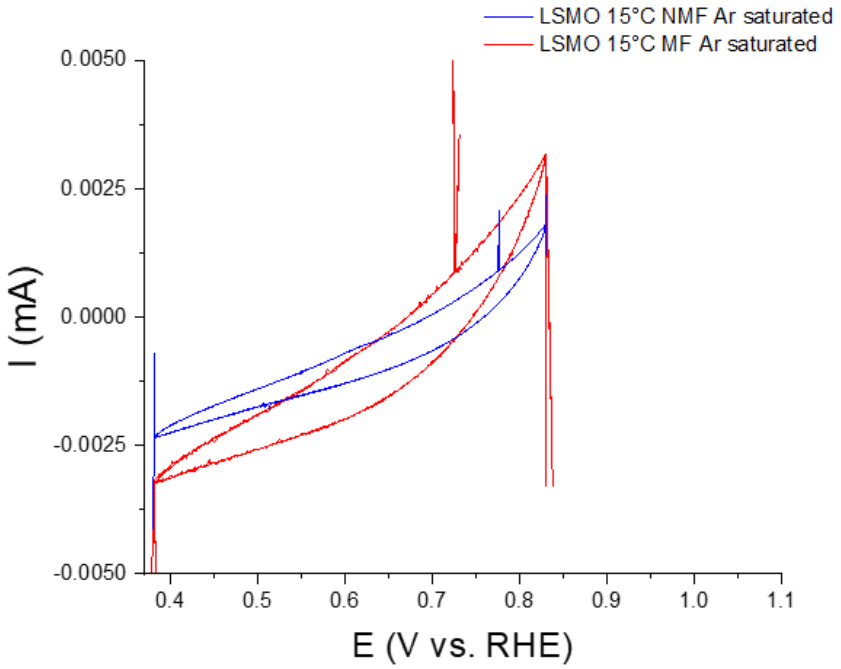

Figure 10. Last cyclovoltammetry cycles obtained after cycling 15 times a LSMO microelectrode at 15 °C in Ar-saturated 0.1M KOH, without magnetic field (NMF-blue) and with a magnetic field of 1T (MF-red).

4. Impact of the magnetic field on the ORR

A LSMO microelectrode was studied at 20 °C in O_2-saturated 0.1M KOH using a 1 T magnetic field. The cyclovoltammograms (**Figure 11**) indicate a decrease of the current under magnetic field. The microelectrode was left 2 h in the electrolyte to observe if a resting time had an impact on the current and then the activity. The activity further decreased after this resting time. We then decided to verify if the activity of LSMO would change if the sample was put under magnetic field without applying current for a long period of time and then investigated the electrochemical response right after removal of the magnetic field.

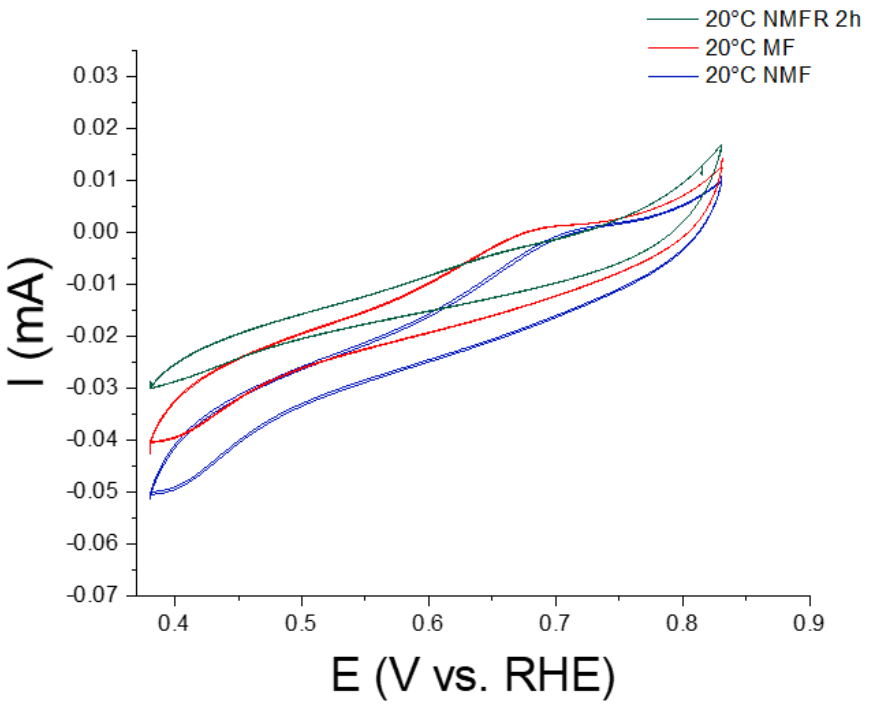

Figure 11. Last cyclovoltammetry cycles obtained after cycling 15 times a LSMO microelectrode at 20 °C in O_2-saturated 0.1M KOH, without magnetic field (NMF-blue), magnetic field (MF-red) and without magnetic field after 2 hours resting (NMFR-green).

CVs were recorded first without magnetic field. Then the electrochemical cell was placed under magnetic field for an hour, the electrochemical response was investigated after removal of the magnetic field (**Figure 12**). The measurements were done in O_2-saturated 0.1M KOH at 5 °C to enhance the magnetic response of LSMO as mentioned before.

Figure 12 shows that the cyclovoltammetry cycles of LSMO pre and post-magnetization are similar, the magnetic field had then no persistent effect on the electrocatalytic activity. Therefore, it is concluded that the impossibility to retrieve the initial activity after MF is not coming from an irreversible change due to a magnetic interaction. We then measured electrochemical responses at 15 °C and 5 °C by the same three steps operation using a microelectrode to confirm that decreasing the temperature does not enhance the magnetic response.

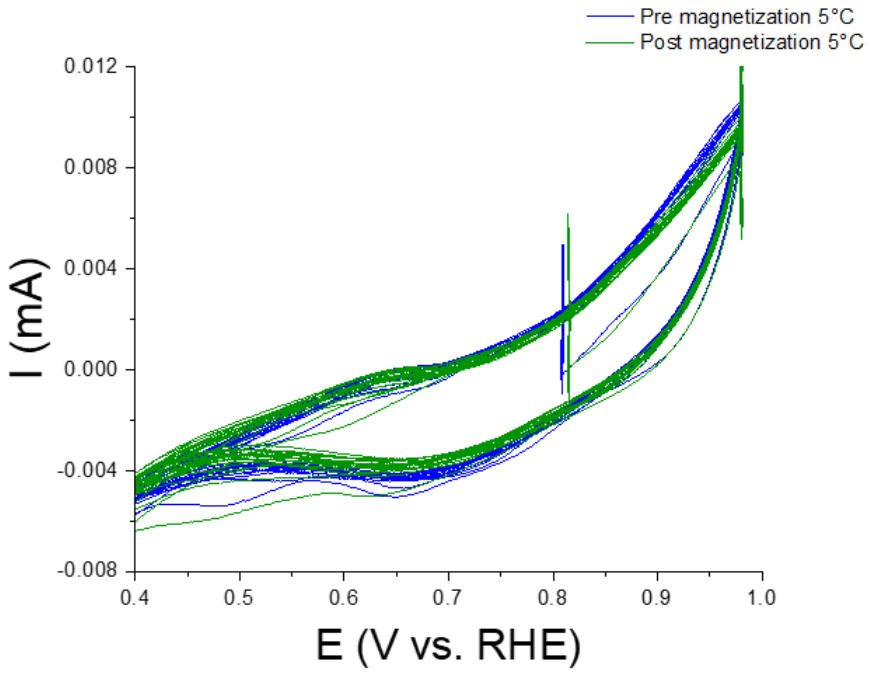

Figure 12. Last cyclovoltammetry cycles obtained after cycling 15 times a LSMO microelectrode at 5°C in O_2-saturated 0.1M KOH without magnetic field (blue), and without magnetic field after staying 1h under magnetic field (green).

We observed at 5 °C (**Figure 13**a) a decrease in the absolute value of the cathodic current when the sample was put under magnetic field. Once the magnetic field was removed (NMFR-green), the initial current was not retrieved (NMF-blue) but stayed the same as under magnetic field (MF-red). At 15 °C (**Figure 13**b-c) we observed two different responses depending on the electrode used. Over 10 experiments we obtained 25 % of the cases where the behavior of LSMO followed the same trend as for the other temperatures, meaning a decrease in the current density under magnetic field (MF-red) that is maintained upon removal of the magnet (NMFR-green). However, 75% of the experiments at 15 °C showed an increase of the absolute cathodic current value under magnetic field (MF-red). The cathodic current once the magnetic field was removed did not recover its initial value either (NMF-blue) but as at 5 °C, remained steady as under magnetic field. It is worth noticing that between 0.7-0.8 (V vs. RHE) for both experiments, MF and NMFR curves (**Figure 13**a-c) showed a reduction wave that is reversible. This wave is characteristic of the reduction from Mn^{4+} to Mn^{3+} that occurs during the ORR cycle. This phenomenon was not observed at 20 °C (**Figure 11**).

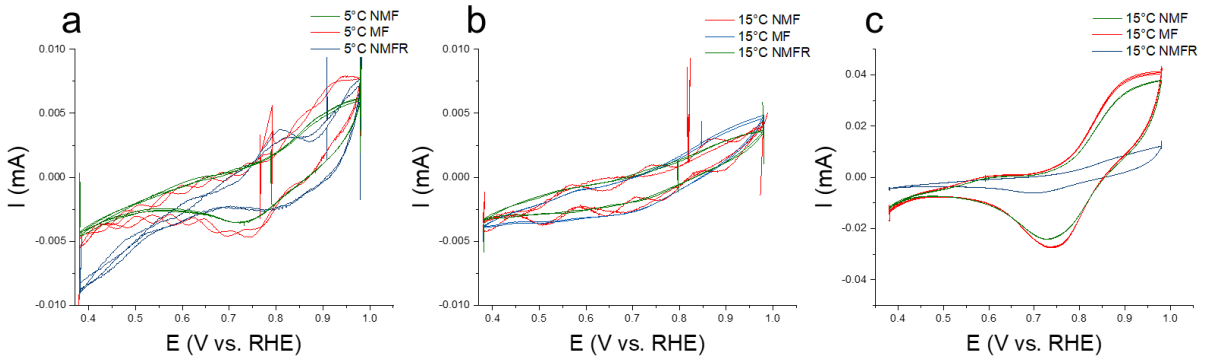

Figure 13. Last cyclovoltammetry cycles obtained after cycling 15 times a LSMO microelectrodes at a) 5°C b-c) 15°C in O_2-saturated 0.1M KOH 0.1 M without magnetic field (NMF-Blue), magnetic field (MF-red) and without magnetic field after 1h relaxation (NMFR-green). (b) and (c) correspond to two different microelectrodes.

In order to assess the origin of changes in the electrochemical response in the magnetic field, electrochemical impedance spectroscopy (EIS) was performed on an LSMO electrode at 15 °C. EIS measurements (**Figure 14**) were implemented at the open circuit voltage between cyclovoltammetry cycles following the same protocol as described above. LSMO after cycling without magnetic field did not exhibit any significant change of the gain and phase, as observed in the Bode diagrams (**Figure 14**a). However, once the material was cycled under magnetic field, the gain component changed, which can be ascribed to a decrease in the resistance of the material. Indeed, CVs acquired for an empty microelectrode (**Appendix 5**), do not exhibit any impact of the magnetic field. Hence, we attribute the change measured by EIS to the material itself. This impact of the magnetic field is confirmed by the evolution of the phase component, again differing from the NMF counterpart (**Figure 14**b). Finally, once the magnet is removed and cyclovoltammetry performed again, both gain and phase show a trend towards the recovery of the initial behavior. This indicates that LSMO under magnetic field and at the open circuit voltage, is transitioning reversibly to a different state. These preliminary observations require further studies, especially at different electrochemical potentials, to provide insights into materials changes in ORR electrocatalytic conditions under magnetic field.

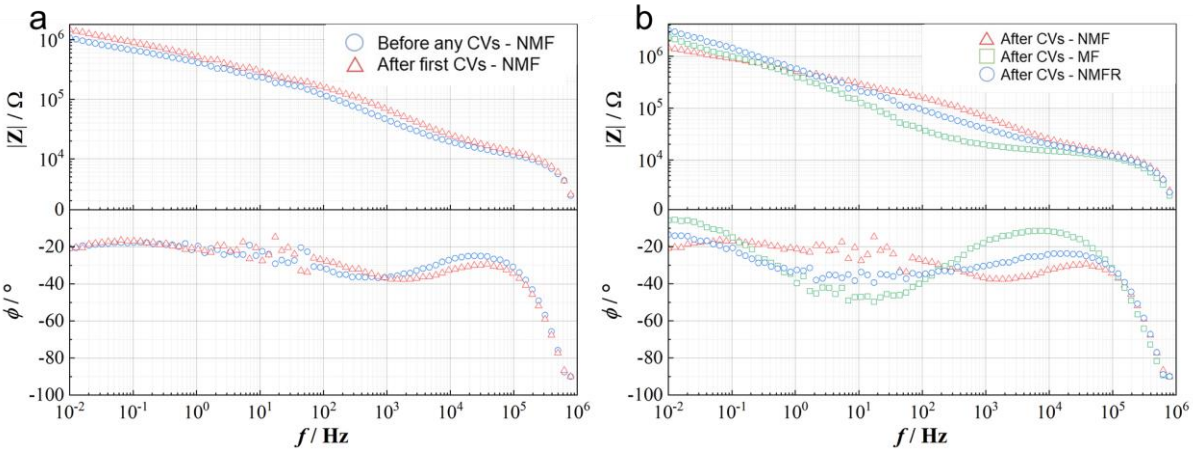

Figure 14. Bode diagrams of LSMO microelectrode at 15°C in O_2-saturated 0.1M KOH (a) before and after ten CVs without magnetic field (NMF), (b) after ten CVs without magnetic field (NMF), after ten CVs with magnetic field and after ten CVs post recovering (NMFR).

According to EIS results, LSMO is changing only under magnetic field upon cycling in O_2-saturated KOH. This change leads to a decrease in the electrocatalytic activity which is irreversible or in some case at 15 °C to the opposite. However, the transformation happening to LSMO is hard to study due to the microelectrode device making difficult any recovery of the material for *post mortem* analysis. If such variations of the cathodic current are related to the surface of LSMO, any parameters affecting it could be of importance to understand the mechanism behind these changes. We then investigated the role of the concentration of the 0.1 M KOH electrolyte.

5. Concentration of the electrolyte

The usual concentration for ORR electrocatalytic tests reported in the literature is 0.1 M KOH. However, for practical metal-air batteries, the ORR is performed in very concentrated alkaline media.[12] The activity of manganite perovskites has been found to be enhanced in concentrated alkaline media, while maintaining the 4-electron pathway. This activity enhancement was ascribed to the formation of surface oxygen vacancies after the hydroxylation decomposition of the adsorbed peroxide species.[13] We then decided to increase the concentration of the KOH electrolyte in order to act on the interplay between vacancies, conductivity and magnetism.

The cyclovoltammetry cycles were recorded at 20 °C, 15 °C and 5 °C by using a microelectrode in O_2-saturated 4 M KOH. The cyclovoltammetry cycles at 5 °C and 15 °C under magnetic field (**Figure 15**) show that the cathodic current increases. The CVs recorded at 20 °C, however, did not show any improvement upon application of the magnetic field to the

LSMO microelectrode. An important oxidation wave is visible at each temperature around 0.75 V vs. RHE and ascribed to the oxidation of the copper wire from the microelectrode itself (**Appendix 6**). The increase in the KOH concentration led to an obvious magnetic field effect at 5 °C and 15 °C. We are yet unable to give a proper mechanistic reason for this enhancement at 5 °C 4M KOH compared to the 0.1M KOH electrolyte. Based on the literature the increase of alkaline concentration led to change of the surface of LSMO. In these specific conditions if the CMR effect occurs, this property of LSMO should be retrieved also at 0.1M. The fact that an effect under magnetic field was observed only at 15 °C for 75% of the experiments in 0.1M KOH confirms the hypotheses of competitive trends occurring during ORR, which could be related to the surface of the catalyst.

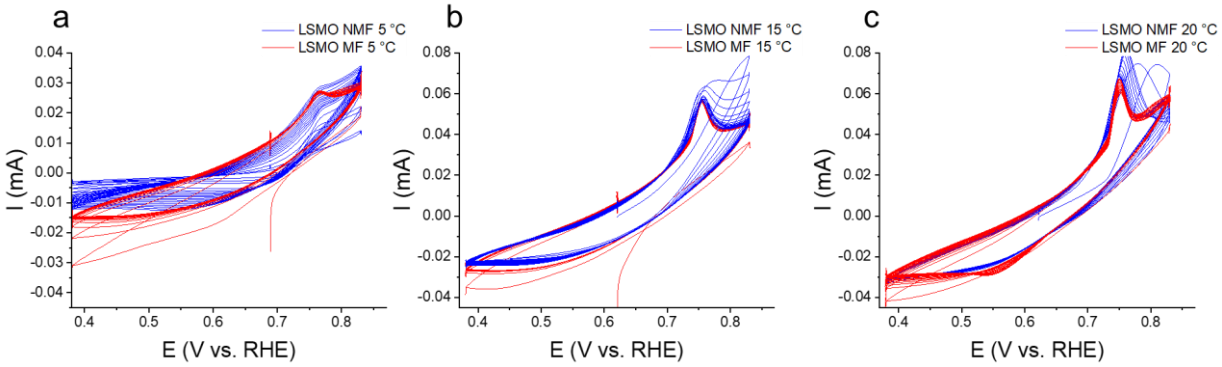

Figure 15. Cyclovoltammetry of the LSMO microelectrode at (a) 5 °C, (b) 15 °C and (c) 20 °C in O_2-saturated 4M KOH, without magnetic field (NFM-blue) and magnetic field (MF-red).

IV. Conclusion

In this chapter, we first design an experimental set-up enabling to apply a high strength and homogeneous magnetic field while providing low noise during electrochemical measurements. The set-up relied especially on microelectrodes instead of classical rotating disk electrodes. We observed an increase of the cathodic current at 15 °C in O_2-saturated 0.1M KOH in 75% of the cases. Electrochemical impedance spectroscopy (EIS) at the open circuit voltage evidenced changes occurring in the LSMO electrode within a 1 T magnetic field. On the contrary to what was observed with cyclovoltammetry cycles, EIS preliminary results showed the reversibility of this behavior at the open circuit voltage. Further EIS experiments at different potential in ORR conditions are now required to provide deeper insights into the changes occurring in LSMO under magnetic field. We then sought to understand what parameters was key to influence the LSMO response to the magnetic field. An important observation is the increase

of the cathodic current under a magnetic field in a highly alkaline electrolyte. Overall concluding on the mechanism occurring during ORR with LSMO and under magnetic field is still presumptuous. Further EIS experiments are at this point required in order to understand the change in LSMO.

References

(1) Suntivich, J.; Gasteiger, H. A.; Yabuuchi, N.; Nakanishi, H.; Goodenough, J. B.; Shao-Horn, Y. Design Principles for Oxygen-Reduction Activity on Perovskite Oxide Catalysts for Fuel Cells and Metal-Air Batteries. *Nat. Chem.* **2011**, *3* (7), 546–550. https://doi.org/10.1038/nchem.1069.

(2) Thi N'Goc, H. Le; Mouafo, L. D. N.; Etrillard, C.; Torres-Pardo, A.; Dayen, J. F.; Rano, S.; Rousse, G.; Laberty-Robert, C.; Calbet, J. G.; Drillon, M.; Sanchez, C.; Doudin, B.; Portehault, D. Surface-Driven Magnetotransport in Perovskite Nanocrystals. *Adv. Mater.* **2017**, *29* (9), 1–9. https://doi.org/10.1002/adma.201604745.

(3) Zhu, Y.; Du, K.; Niu, J.; Lin, L.; Wei, W.; Liu, H.; Lin, H.; Zhang, K.; Yang, T.; Kou, Y.; Shao, J.; Gao, X.; Xu, X.; Wu, X.; Dong, S.; Yin, L.; Shen, J. Chemical Ordering Suppresses Large-Scale Electronic Phase Separation in Doped Manganites. *Nat. Commun.* **2016**, *7*, 1–6. https://doi.org/10.1038/ncomms11260.

(4) Shao, J.; Liu, H.; Zhang, K.; Yu, Y.; Yu, W.; Lin, H.; Niu, J.; Du, K.; Kou, Y.; Wei, W.; Lan, F.; Zhu, Y.; Wang, W.; Xiao, J.; Yin, L.; Plummer, E. W.; Shen, J. Emerging Single-Phase State in Small Manganite Nanodisks. *Proc. Natl. Acad. Sci.* **2016**, *113* (33), 9228–9231. https://doi.org/10.1073/pnas.1609656113.

(5) Liang, L.; Li, L.; Wu, H.; Zhu, X. Research Progress on Electronic Phase Separation in Low-Dimensional Perovskite Manganite Nanostructures. *Nanoscale Res. Lett.* **2014**, *9* (1), 1–14. https://doi.org/10.1186/1556-276X-9-325.

(6) Wu, J. H.; Lin, J. G. Study on the Phase Separation of La0.7Sr0.3MnO3 Nanoparticles by Electron Magnetic Resonance. *J. Magn. Magn. Mater.* **2006**, *304* (1), 7–9. https://doi.org/10.1016/j.jmmm.2006.02.024.

(7) Gonell, F.; Alem, N.; Dunne, P.; Crochet, G.; Beaunier, P.; Méthivier, C.; Montero, D.; Laberty-Robert, C.; Doudin, B.; Portehault, D. Versatile Molten Salt Synthesis of Manganite Perovskite Oxide Nanocrystals and Their Magnetic Properties. *ChemNanoMat* **2019**, *5* (3), 358–363. https://doi.org/10.1002/cnma.201800632.

(8) Coey, J. M. D.; Viret, M.; Molnar, S. Mixed-Valence Manganites. *Adv. Phys.* **1999**, *48* (2), 167–293.

(9) Garcés-pineda, F. A.; Blasco-ahicart, M.; Nieto-castro, D.; López, N.; Galán-mascarós,

J. R. Direct Magnetic Enhancement of Electrocatalytic Water Oxidation in Alkaline Media. *Nat. Energy* **2019**, *4* (June), 519–525.

(10) Cachet-Vivier, C.; Keddam, M.; Vivier, V.; Yu, L. T. Development of Cavity Microelectrode Devices and Their Uses in Various Research Fields, Université Pierre et Marie Curie, 2015. https://doi.org/10.1016/j.jelechem.2012.09.011.

(11) Trotochaud, L.; Young, S. L.; Ranney, J. K.; Boettcher, S. W. Nickel-Iron Oxyhydroxide Oxygen-Evolution Electrocatalysts: The Role of Intentional and Incidental Iron Incorporation. *J. Am. Chem. Soc.* **2014**, *136* (18), 6744–6753. https://doi.org/10.1021/ja502379c.

(12) Mainar, A. R.; Iruin, E.; Colmenares, L. C.; Kvasha, A.; de Meatza, I.; Bengoechea, M.; Leonet, O.; Boyano, I.; Zhang, Z.; Blazquez, J. A. An Overview of Progress in Electrolytes for Secondary Zinc-Air Batteries and Other Storage Systems Based on Zinc. *J. Energy Storage* **2018**, *15*, 304–328. https://doi.org/10.1016/j.est.2017.12.004.

(13) Aoki, Y.; Takase, K.; Kiuchi, H.; Kowalski, D.; Sato, Y.; Toriumi, H.; Kitano, S.; Habazaki, H. In Situ Activation of a Manganese Perovskite Oxygen Reduction Catalyst in Concentrated Alkaline Media. *J. Am. Chem. Soc.* **2021**, *143* (17), 6505–6515. https://doi.org/10.1021/jacs.1c00449.

Chapter IV:

The exsolution process, towards enhanced new catalysts

I. Introduction

This chapter retrace the experiments and the methodology for the exsolution of several metals out of a commonly used for exsolution structure, $SrTiO_3$ (STO).[1–4] We then attempt to trigger exsolution from another perovskite material $La_{0.7}Sr_{0.3}MnO_3$ (LSMO), widely discussed in the previous chapters for its interest as electrocatalyst in the oxygen reduction reaction (ORR). As mentioned above, several metals have already been exsoluted out of bulk perovskites, therefore to achieve the exsolution from nanosystems we used several reference metals. We started with Pt as a model, then extend the scope of metallic exsolution to other compounds such as nickel, copper and silver.

The aim of this PhD project was to synthesize nano-catalysts enhanced by external stimuli and more specifically during electrocatalysis. Reducing conditions are required to trigger exsolution of the doping metal atoms as nanoparticles at the surface of the matrix. Three different ways to produce exsolution by stimuli have been investigated. The first method is the use of electron irradiation in a transmission electron microscope (TEM), which allows both occurrence and observation of exsolution and has never been done before. The second way investigated in this chapter consists in heating the synthesized doped nanoparticles under a H_2 atmosphere. This method is the most used in the literature as routine exsolution process, nevertheless it requires high temperatures and long reaction time, which are suited for bulk perovskites but not for maintaining nanoparticles.[1,3–6] We will show how going to the nanoscale highly increases the sensibility of the systems towards exsolution in milder conditions but also facilitate the exsolution by providing a higher strain tolerance enabling a decrease of atomic diffusion lengths, which opens up numerous possibilities of host structures. Finally, a third way is explored: exsolution during electrocatalysis. This last method is of great interest for further work on exsolution, as the possibility to enhance electrocatalysts *in situ* is very attractive. Overall, this chapter is a guide through the exsolution from nanoparticles and the possibility to create long lifetime electrocatalysts for the oxygen reduction reaction.

II. $SrTiO_3$ synthesis

Firstly, the supporting matrix $SrTiO_3$ (STO) chosen as reference for the exsolution was synthetized in molten salts. We used a eutectic mix of potassium chloride (2.6 eq) and sodium chloride salts (2.6 eq), TiO_2 nanoparticles (1 eq) and strontium nitrate (1.2 eq). After heating a 700 °C for 6 h the powder was washed and dried. The XRD pattern (**Figure 1**a) is consistent

with the sole STO phase. TEM images (**Figure 1**b-c) show cubical nanoparticles ascribed to STO. The size distribution (**Figure 1**d) reveals a particle size of average 45 nm.

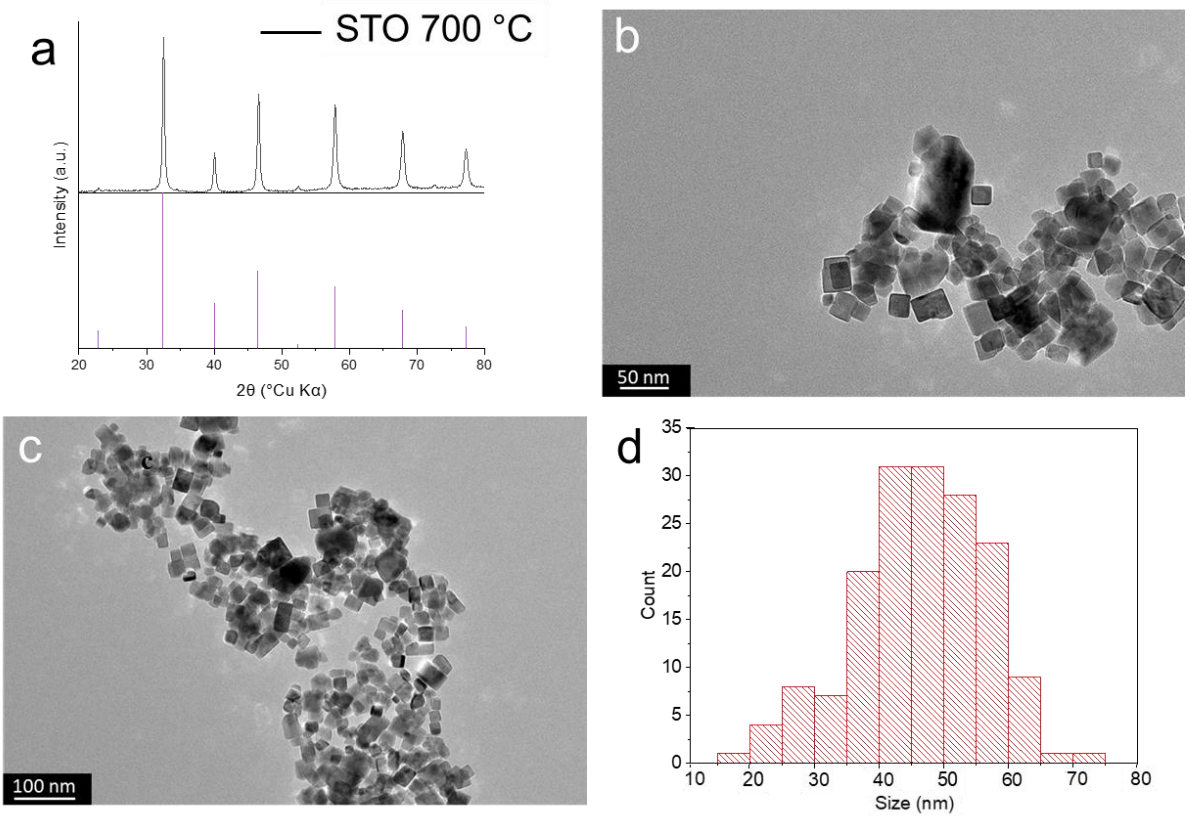

Figure 1. (a) Powder XRD pattern of STO particles (black) with the corresponding reference pattern (purple), (b-c) TEM images of STO nanoparticles at 700 °C for 6 h, and (d) corresponding size distribution.

III. $SrTi_{1-x}O_3$ doped with platinum

We have then modified the synthesis protocol by incorporating platinum tetrachloride as dopant metal precursor. The doping ratios targeted were 20 at.%, 10 at.%, 5 at.% and 2 at.% of platinum over the B site cations, herein titanium ($SrTi_{1-x}Pt_xO_3$). The XRD patterns (**Figure 2**) show that from 2 at.% to 10 at.%, Pt doping leads to STO as the sole crystalline phase. However, at 20%, peak impurities at 25° and 40° (Cu Kα 2θ) are observed. They are respectively ascribed to titanium oxide anatase and metallic platinum. Therefore, a limit exists between 10 at% and 20 at% doping rate, for reaching a homogeneous perovskite compound. According to X-ray fluorescence (WDXRF), the composition of STO-Pt 2% is $Sr_{0.97\pm0.05}Ti_{0.99\pm0.05}Pt_{0.01\pm0.05}O_3$ in agreement with the expected value.

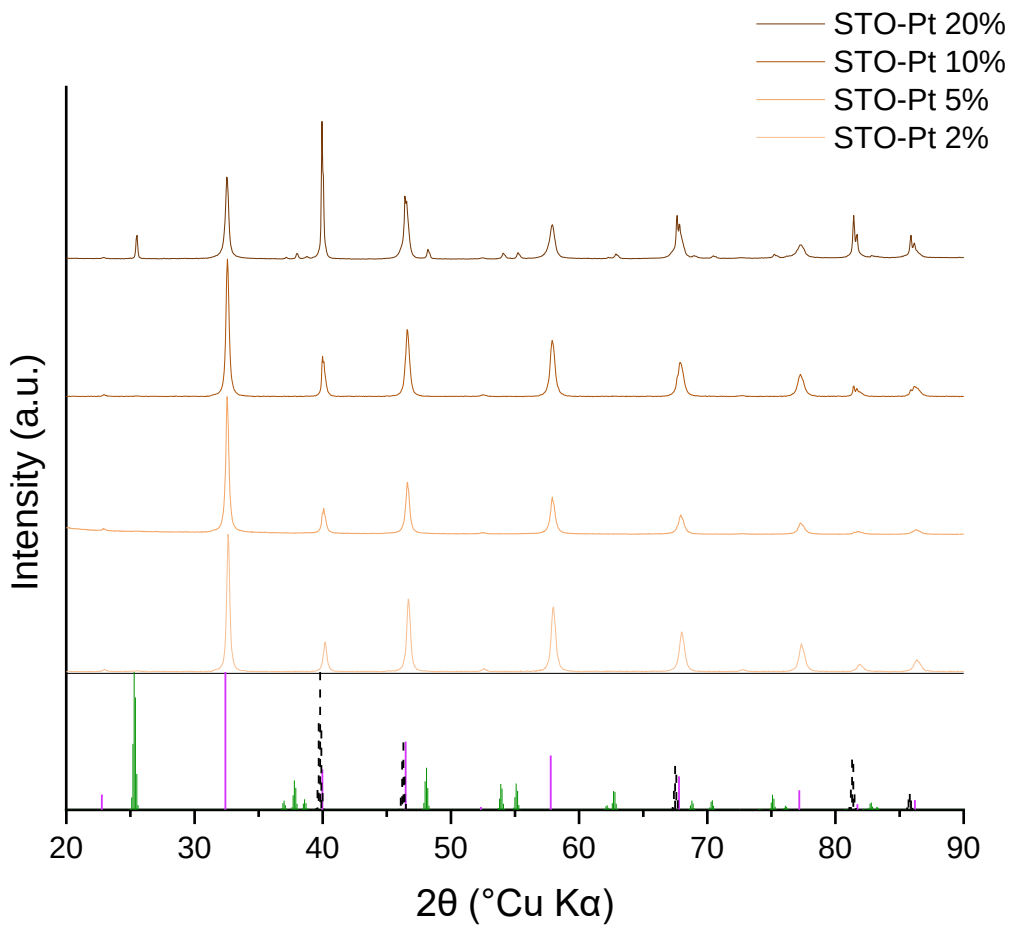

Figure 2. Powder XRD patterns of STO samples at different platinum doping ratio with $SrTi_{1-x}Pt_xO_3$ nominal composition. STO, Pt and TiO_2 reference patterns are displayed in purple, black dashes and green respectively.

The TEM (**Figure 3**) images show cubical particles ascribed to the STO perovskite for each doping ratio, which shows that doping does not impact significantly the nanoparticles morphology (**Figure**).

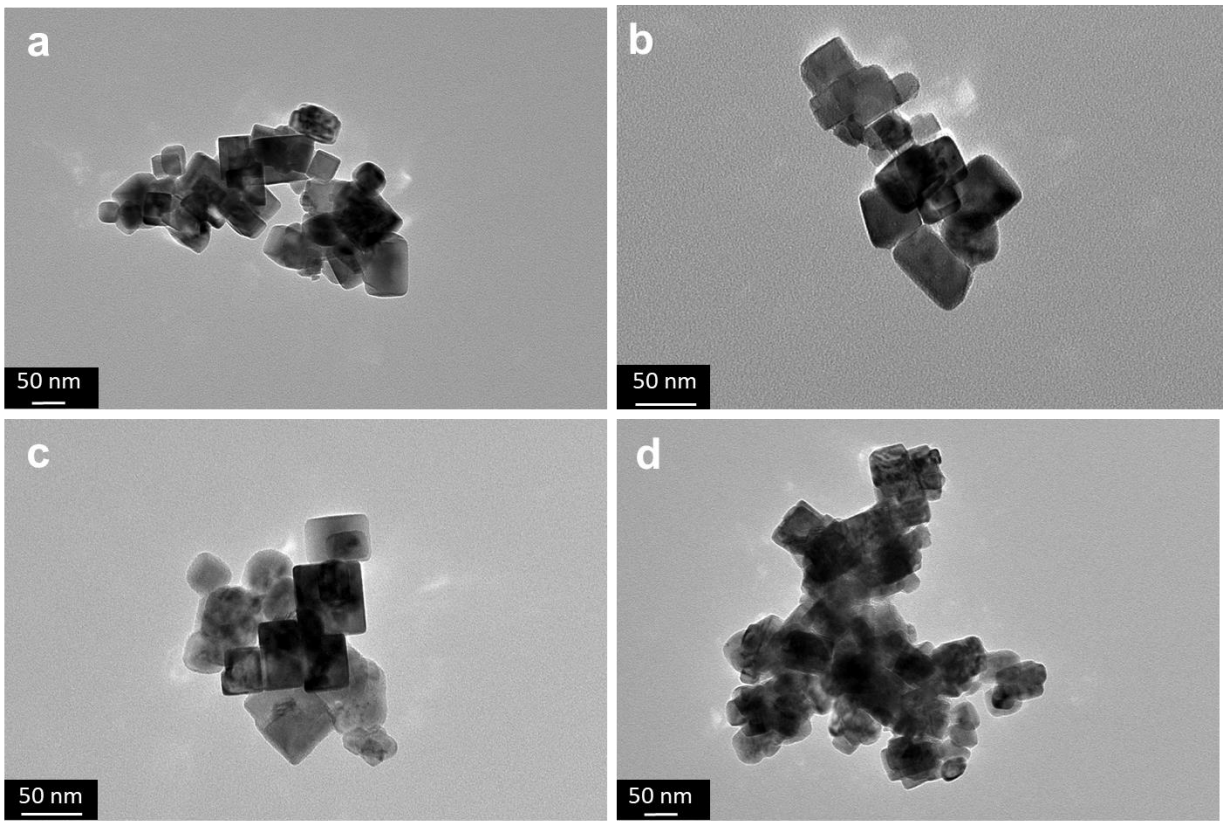

Figure 3. TEM images of Pt doped STO samples with different ratio in platinum: (a) 2 at.%, (b) 5 at.%, (c) 10 at.% and (d) 20 at.%.

In order to confirm the incorporation of platinum in the structure, STEM-EDS mapping (**Figure 4**) was performed on the sample doped at 10 at.%. Strontium, titanium and platinum are collocated, thus confirming homogeneous incorporation of Pt into the STO structure.

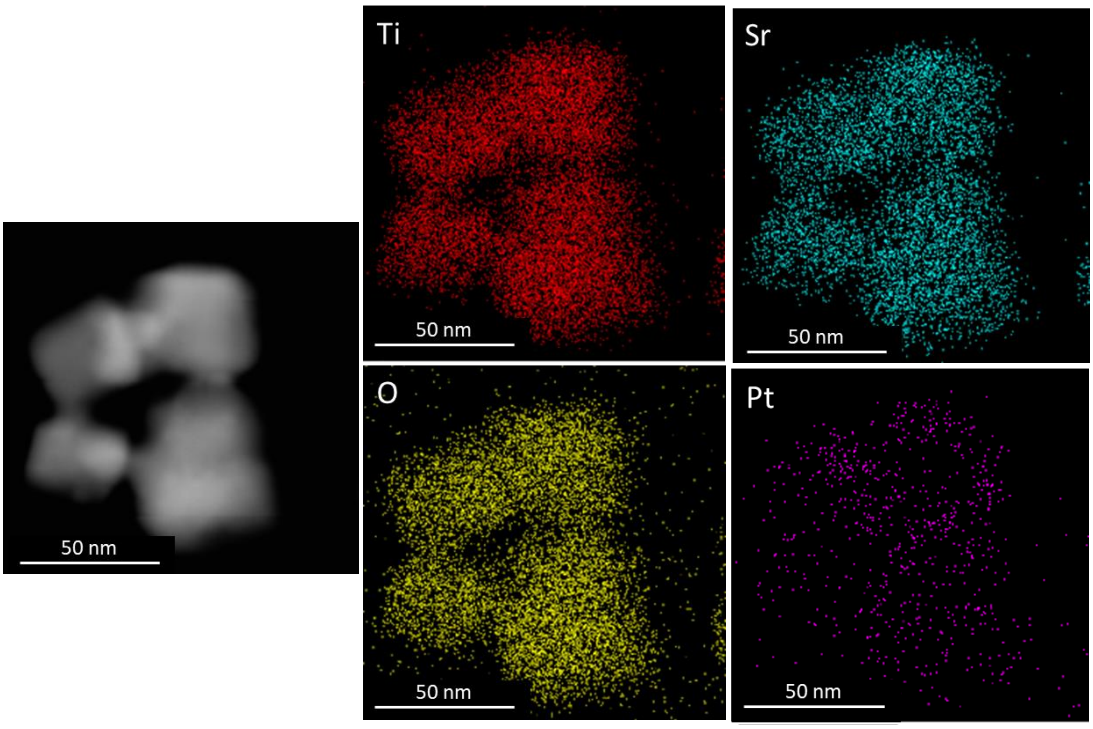

Figure 4. EDS images of STO nanoparticles doped with 10 at.% platinum

1. Exsolution assisted by transmission electron microscopy

Exsolution was first triggered in the 10 at.% Pt doped STO by using the electron beam of a transmission electron microscope operation at 120 kV. The TEM images (**Figure 5**b) show that after 2 min, small defects can be detected, but the exsolution is not yet visible. At 4 min (**Figure 5**c-d) small black dots of about 1-2 nm appear over the surface of the STO nanoparticles. HRTEM (**Figure 5**e-f) confirms that the perovskite structure is maintained during this process. The composition of the small objects protruding on the surface was then analyzed by STEM coupled to high-angle annular dark-field (HAADF) detection, which is sensitive to the atomic number.

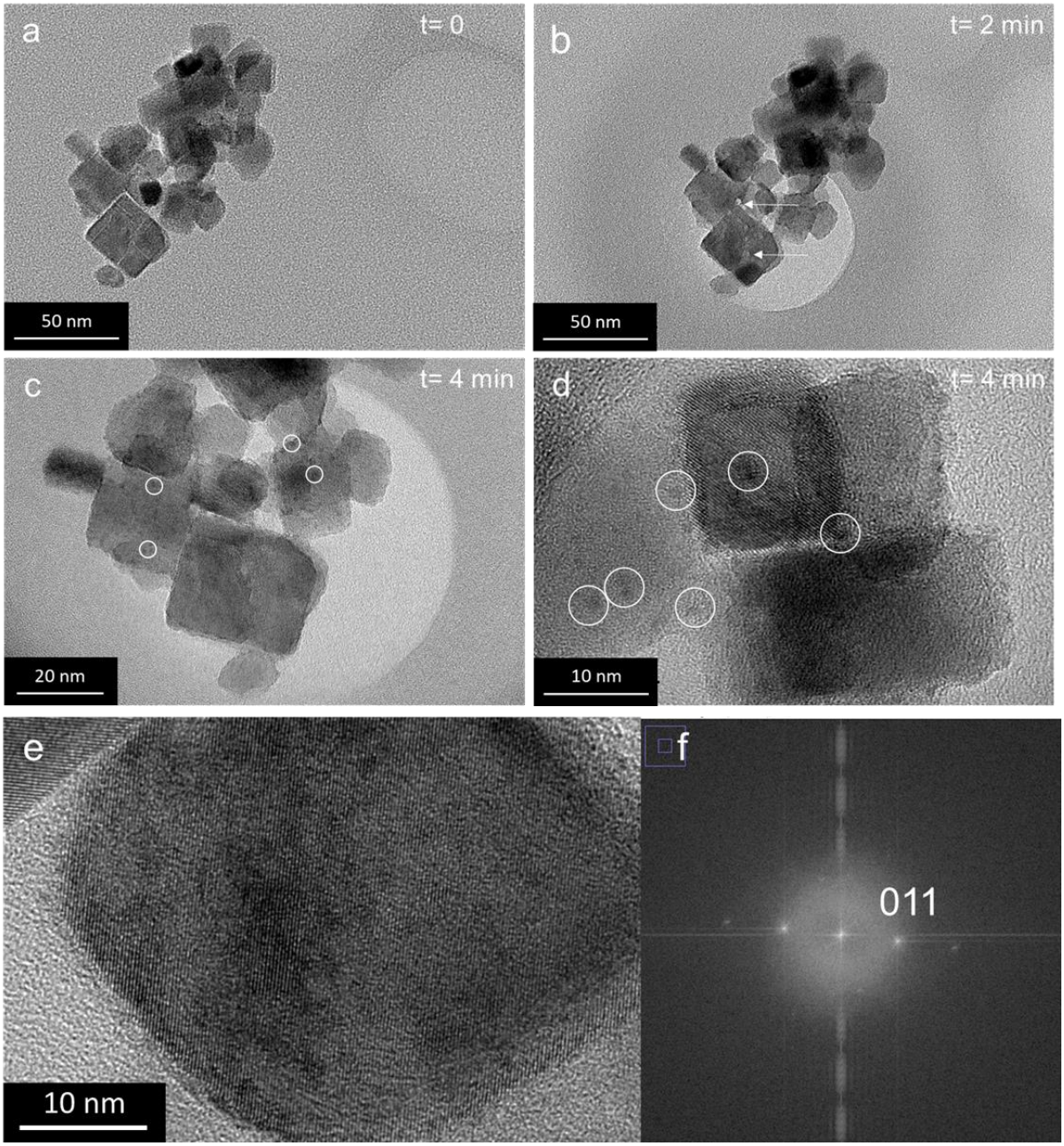

Figure 5. TEM images of STO-Pt 10 at.% sample at (a) t=0, (b) t=2 min, (c- d) t=4 min and (e) HRTEM image of STO-Pt 10 at.%, with (f) corresponding FFT indexed along the STO structure.

STEM-HAADF images obtained with a Cs-corrected JEOL ARM at 200 kV are shown **Figure 6**, after irradiation over 20 min. **Figure 6**a-c show bright spots all over the surface. **Figure 6**b-d clearly indicate the presence of 1-2 nm bright nanoparticles at the surface of the perovskite nanocrystals. The high contrast indicates that the particles are made of platinum. Thus, exsolution was successfully performed using an electron beam.

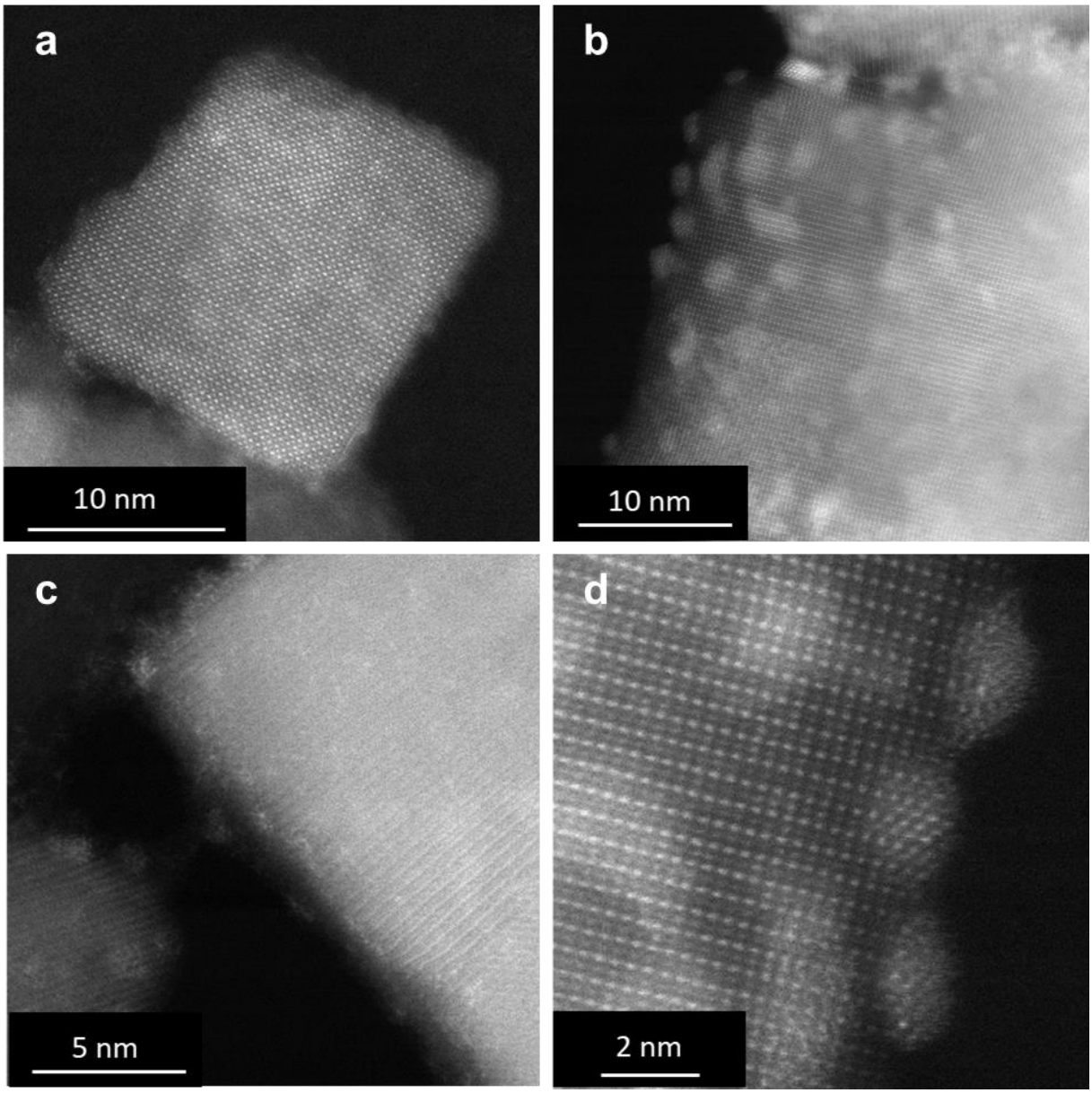

Figure 6. STEM-HAADF images of STO doped with 10 at.% platinum after 20 minutes of irradiation in a Cs-corrected JEOL ARM at 200 kV.

We then probed the occurrence of exsolution at lower doping ratios by electron irradiation. The 2 at.% platinum doped STO was first observed using TEM (**Figure 7**). **Figure 7**a show particles in their original state, no black dots are observed and the surface of the particles is soft. After 1 minute of beam irradiation (**Figure 7**b), the surface of the STO nanocrystals starts to change and become more rugous. Besides, black dots are appearing in the bright field images. At 2 and 3 min of irradiation (**Figure 7**c-d) the rugosity of the surfaces is more visible and indicate the formation of ≈ 2 nm nanoparticles over all the facets of the nanoparticles. According to observation made for the STO sample doped at 10 at.%, we ascribe these nanoparticles to Pt. Thus, a 2 at.% Pt doping rate is high enough for Pt particles to undergo exsolution. Moreover,

the exsolution does not provoke any change of the morphology and crystalline structure (**Figure 5**e-f) of nanoscaled perovskite structure.

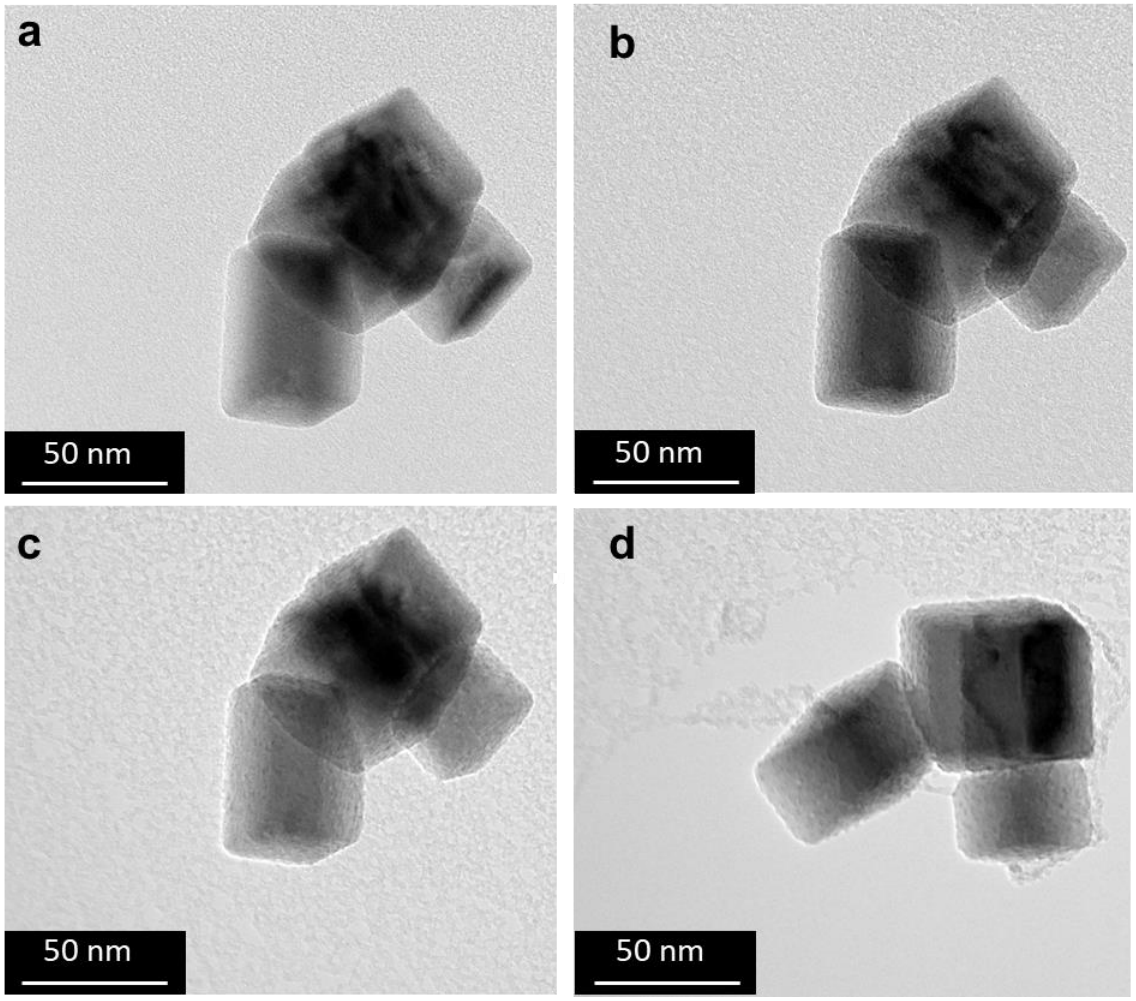

Figure 7. TEM images of STO doped with 2 at.% platinum at different times under a 120 kV beam, (a) t= 0, (b) t= 1 min, (c) t= 2 min, (d) t= 3 min.

We so far demonstrated exsolution of platinum out of STO nanocrystals by using an electron beam. However, this approach is hardly transferable to materials production and then for electrochemical measurements. We then embarked in triggering exsolution through other ways. Exsolution is performed classically in the literature by heating the material under a reducing atmospheres which allows to retrieve the material afterwards. We then attempted to adapt this method to the STO nanoparticles doped with Pt.

2. Exsolution under reductant atmosphere

Conventionally, bulk perovskites are exsoluted at high temperatures (900-1200 °C)[7,8] and for long times (24 h) as explained in the bibliography chapter. However, such long and harsh treatments would lead to sintering of the STO nanoparticles. Interestingly, using nanoscaled perovskite matrixes could facilitate exsolution by providing more strain tolerance and by enabling a decrease of atomic diffusion lengths. Therefore, Pt doped STO nanoparticles may undergo exsolution at lower temperature than reported for the bulk. To test this hypothesis, we then studied exsolution on STO doped by 5 at.% platinum under reducing atmosphere (5 %H_2/95 %Ar). The reaction time was set to 4 h for 3 different temperatures: 600, 700 and 800 °C. The XRD pattern of the resulting samples (**Figure 8**) showed that no change occurred during exsolution in the 3 samples, as STO is the only detected crystalline phase.

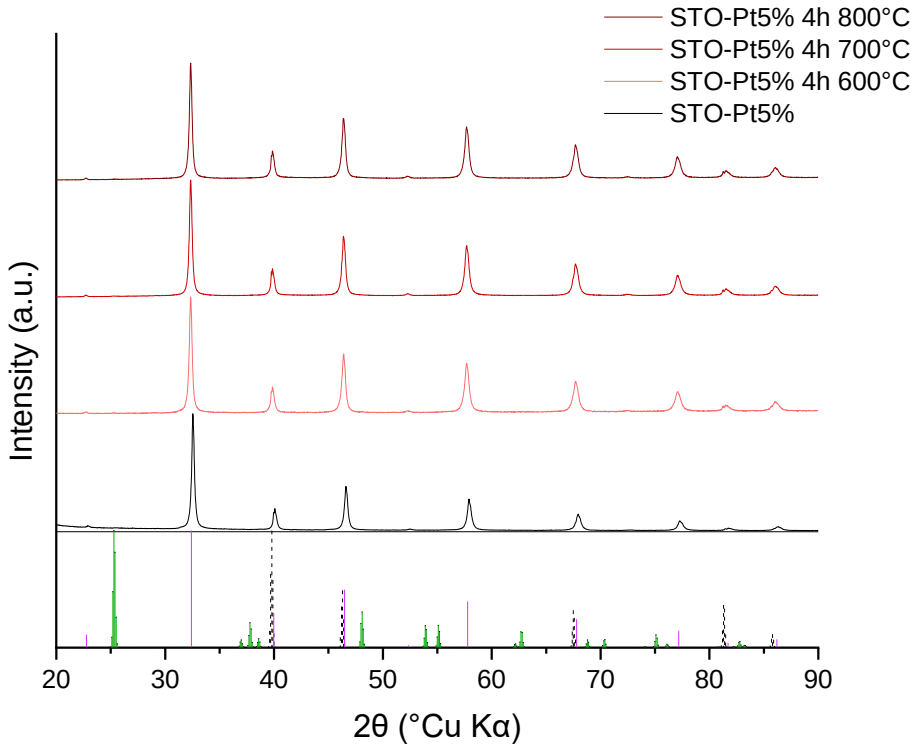

Figure 8. Powder XRD patterns of 5 at.% Pt doped STO after treatment at different temperatures for 4 h in reducing atmosphere 5 %H2/95 %Ar. STO and Pt reference patterns are displayed in purple and black dashes respectively.

TEM (**Figure 9**) indicates that the sample exsoluted at 600 °C (**Figure 9**a) exhibits black dots characteristic of platinum nanoparticles exsoluted. The size distribution (**Figure 9**b) highlights an average of 2 nm platinum nanoparticles. At 700 °C (**Figure 9**c), the Pt nanoparticles size distribution shifts towards bigger nanoparticles (**Figure 9**d). At 800 °C (**Figure 9**e) the size

distribution is widened and indicates a significant amount of nanoparticles larger than 3 nm (**Figure 9**f).

Two hypotheses can be invoked to explain the growth of Pt nanoparticles. First, the feeding of the particles by Pt species remaining in the STO host structure at low temperature. Second, the diffusion of the Pt nanoparticles at the surface of STO particles. This process is thermally activated and would yield to aggregation and sintering of the Pt objects. This phenomenon is well-known for classical deposited materials.[9,10] However, this second hypothesis is in opposition to the knowledge on exsolution in bulk perovskites. Indeed, Irvine *et al*.[11,12] have proved that the exsolution resulted in the exsoluted particles being anchored on the surface of the host structure, because they are socked in the surface. We then attempted to clarify if the temperature impacted the migration of the platinum nanoparticles.

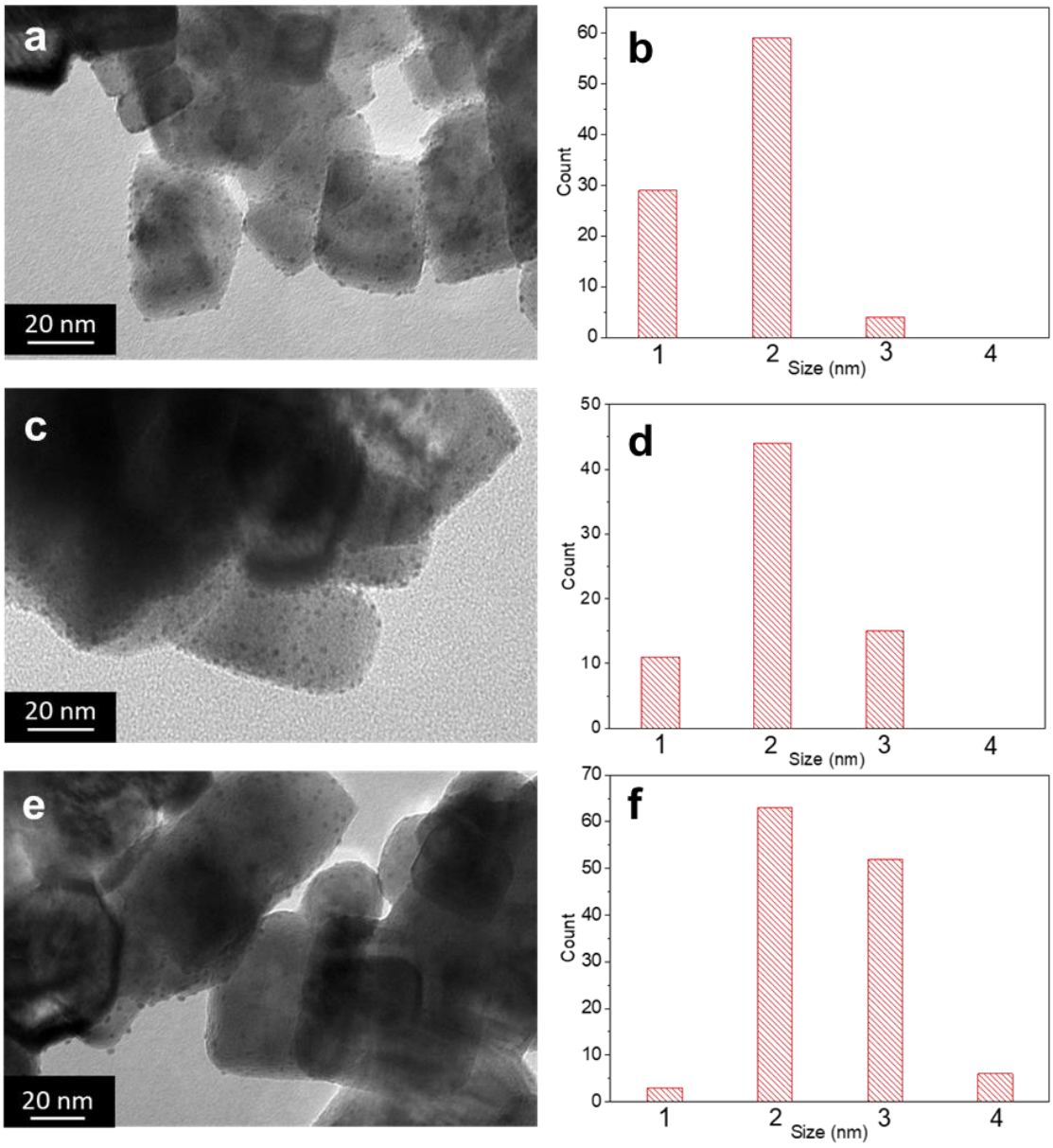

Figure 9. TEM images of 5 at.% Pt-doped STO and corresponding size distributions of platinum nanoparticles exsoluted at (a-b) 600 °C, (c-d) 700 °C, (e-f) 800 °C after 4 hours.

To do so, we acquired snapshots of the 10 at.% Pt-doped STO sample during exsolution. The sample was irradiated in a JEOL JEM2100Plus Lab 6 at 200 kV and analyzed by STEM-HAADF for 20 min (**Figure 10)**. These observations show no significant movement of the Pt nanoparticles over the STO surface after 20 min irradiation. This surface immobility is similar to the aforementioned bulk counterpart. Although the exsolution stimulus is different, we then ascribed the growth of the Pt particles observed **Figure 9** to the migration of the platinum out of the core structure of the perovskite nanocrystals hosts.

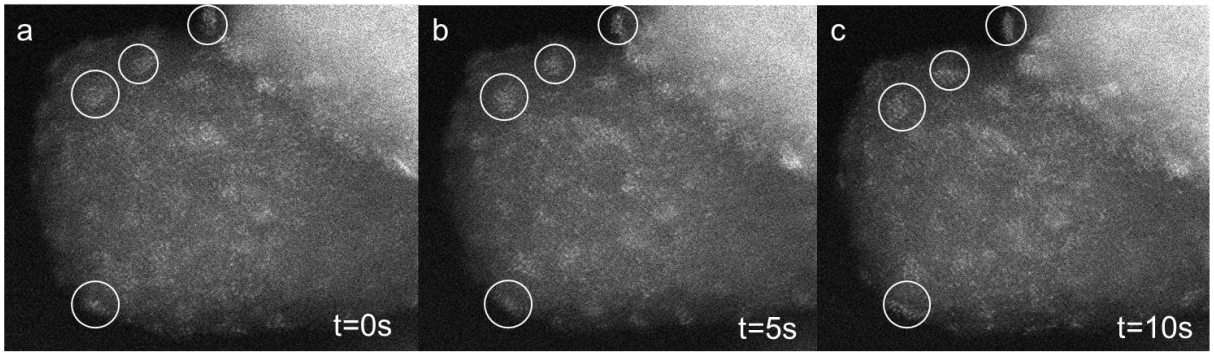

Figure 10. Snapshots acquired by TEM of STO-Pt 10 at.% at (a) t=0, (b) t=5 s and (c) t=10 s.

So far, we have been able to exsolute nanoparticles of platinum using TEM but also by heating under reductant atmosphere. We also showed no differences of stability of the resulting heterostructures between bulk exsolution and the nanoscale. The last way to trigger exsolution is by using an electrochemical stimulus. Indeed, under reducing potential, electrons are transferred to the material, thus providing the possibility to reduce the doping metal and provoke exsolution. The cyclovoltammetry cycles were performed using a composite of carbon black, Nafion and STO doped with 10 at.% platinum deposited on a glassy carbon electrode in 0.5M H_2SO_4. **Figure 11**a shows that the CVs measured for STO undoped and doped were identical for a scan rate of 10 mV s^{-1}. However, reducing the scan rate down to 1 mV s^{-1} led to a large increase in the current density of doped STO after 3 cycles. This large change was ascribed to the exsolution of platinum nanoparticles on the surface of the STO nanocubes. Noteworthy the shape of the curves show that the material has a strong ohmic character, which indicates its low electrical conductivity, reminiscent of the insulating behavior of the STO matrix.

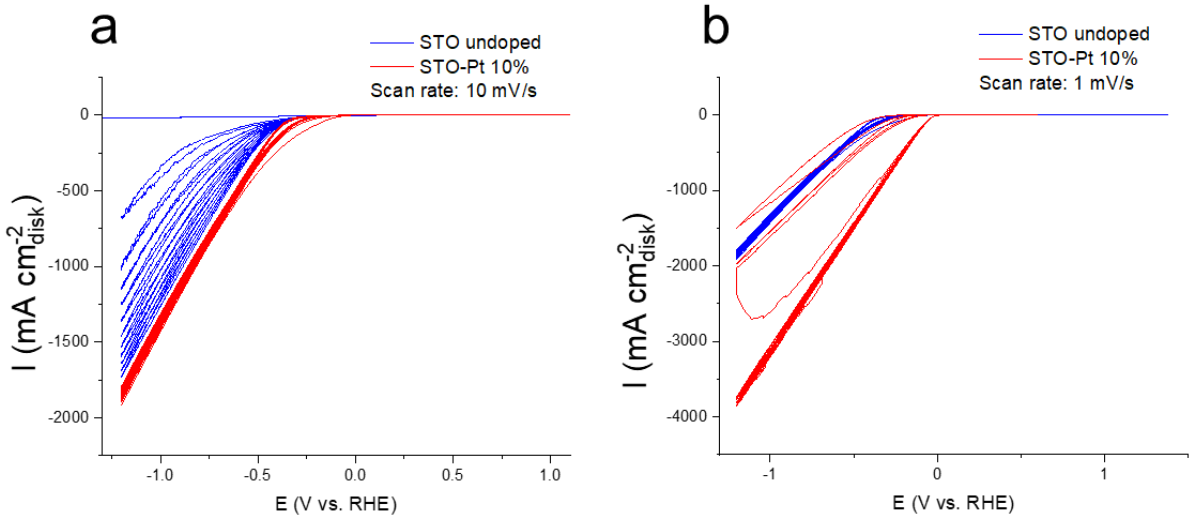

Figure 11. Cyclovoltammetry cycles of STO-Pt 10 at.% (a) 10 mV s^{-1} and (b) 1 mV s^{-1}.

3. Exsolution of other doping metals

The exsolution of platinum presented above has been done throughout 3 different techniques: electron irradiation, heating under reducing atmosphere and finally electrochemistry. We then assessed the versatility of the process by exsoluting other metals such as nickel, copper and silver. The choice of these metals has been made out of the perspective of electrochemical exsolution, and catalytic active metals were selected to be incorporate in the host perovskite. The same STO system was used as the host structure. We aimed for doping ratios of 10, 5 and 2 at.% of nickel, copper and silver as we previously showed that above 10 at.%, platinum doping resulted in impurities. The STO syntheses adjusted for nickel, copper and silver incorporation were performed at 700 °C for 6 h. XRD (**Figure 12**) shows that the nickel-doped (**Figure 12**a) samples have the STO structure, however the 10 at.% sample also exhibited small impurity peaks ascribed to NiO at 37°, 43° and 62° (Cu Kα 2θ). Regarding copper-doped STO (**Figure 12**b), we observed the same behavior, where targeting 10 at.% doping ratio resulted in the formation of a CuO side product visible at 37° and 39° (Cu Kα 2θ). Finally, the STO-Ag system (**Figure 12**c) also led to the formation of AgCl impurities at 28° and 54° (Cu Kα 2θ) but for all doping ratios targeted. AgCl is coming from the reaction of Ag nitrate with the molten chloride. From the powder XRD patterns presented **Figure 2** and **Figure 12**, we observed that above a doping ratio threshold at 10 at.%, segregation of the doping cations occurred and led to the formation of oxide impurities. Furthermore, silver doping revealed that some metals are harder to insert into the STO perovskite structure by using molten salt synthesis, because of a competitive reaction with the salt constituents.

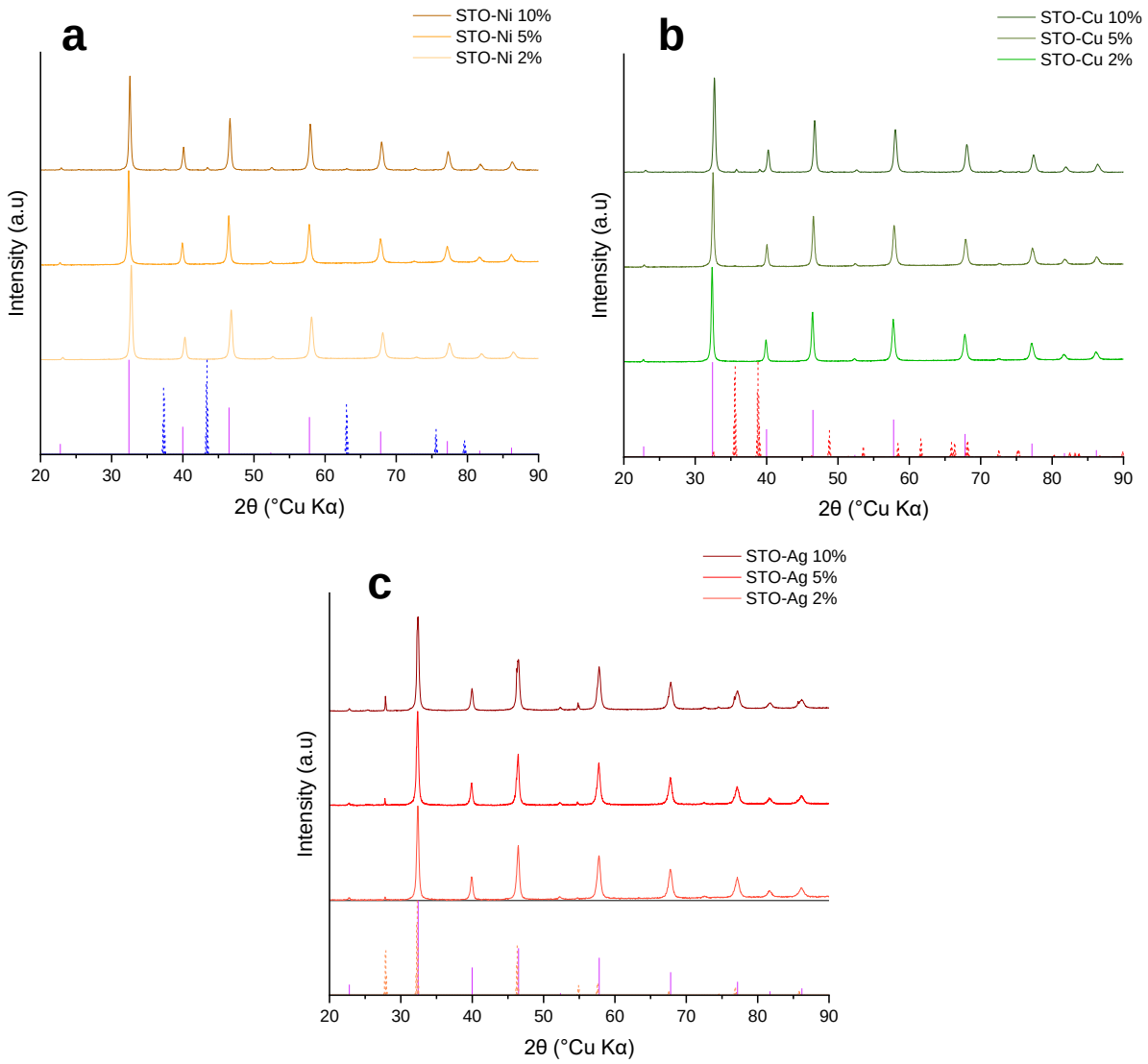

Figure 12. Powder XRD patterns of STO samples by targeting doping ratio of 10, 5 and 2 at.% for (a) nickel, (b) copper, (c) silver. The STO, NiO, CuO and AgCl reference patterns are displayed in purple, blue dashes, red dashes and orange dashes respectively.

The presence of impurities does not refute the partial insertion of the doping cations inside the host STO. The exsolution of nickel, copper and silver was then performed on the 10 at.% doped systems using electron beam irradiation (**Figure 13**). After few minutes under the beam, the exsolution of nickel (**Figure 13**a-b), copper (**Figure 13**c-d) and silver (**Figure 13**e-f) was observed as small objects formed on the surface of STO particles.

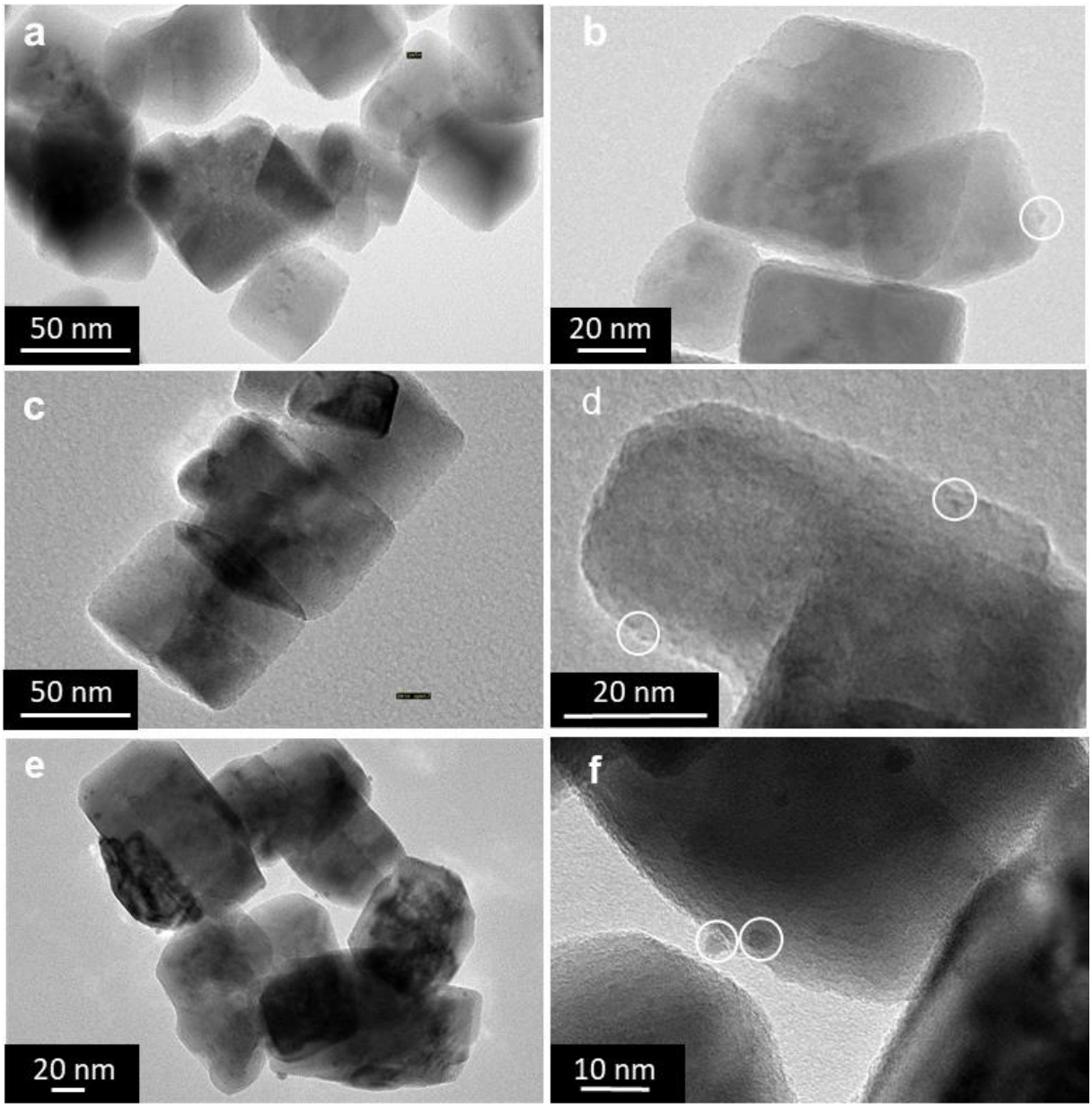

Figure 13. TEM images of exsoluted STO doped at 10 at.% with (a-b) nickel, (c-d) copper and (e-f) silver.

We have synthetized homogeneous systems composed of STO and different doping metal cations. We also observed the limits of this doping strategy with thresholds above which segregations and formation of impurities occurred. Besides we showed that exsolution was successfully obtained either by electron irradiation, thermal treatment under reducing atmosphere or electrochemical reduction. In a next step, in order to use the exsolution process to yield higher electrocatalytic activities we moved to a new perovskite host, which is more conductive than STO. Choice was made to focus on $La_{0.7}Sr_{0.3}MnO_3$ (LSMO) nanocubes, widely

discussed in a previous chapter for its interesting magnetic properties but also efficient electrocatalytic activity.[13]

IV. Synthesis of $La_{0.7}Sr_{0.3}MnO_3$ doped for the exsolution process

The synthesis of doped $La_{0.7}Sr_{0.3}MnO_3$ (LSMO) nanoparticles was performed by adapting the protocol of N'Goc *et al*[14]. As for the STO system, we first chose to insert platinum into LSMO. We then assessed the threshold of doping rate enabling the recovery of a homogenous perovskite. The XRD patterns (**Figure 14**) show that the doping ratios of 20 and 10 at.% both presented peaks at 39, 46 and 68° (Cu Kα 2θ) ascribed to metallic platinum. These peaks were not detected for 5 and 2 at.%, suggesting that platinum was fully inserted. However, a peak at 25° was detected on 2, 5 and 10 at.% sample. We could not identify this peak, but we note that it was also reported in a previous work[15] on LSMO synthesis. Wavelength dispersive X-ray fluorescence (WDXRF) analysis of the 2 at.% Pt-doped sample gave a nominal composition of $La_{0.7\pm0.05}Sr_{0.3\pm0.05}Mn_{0.98\pm0.05}Pt_{0.02\pm0.05}O_3$, in agreement with expected value.

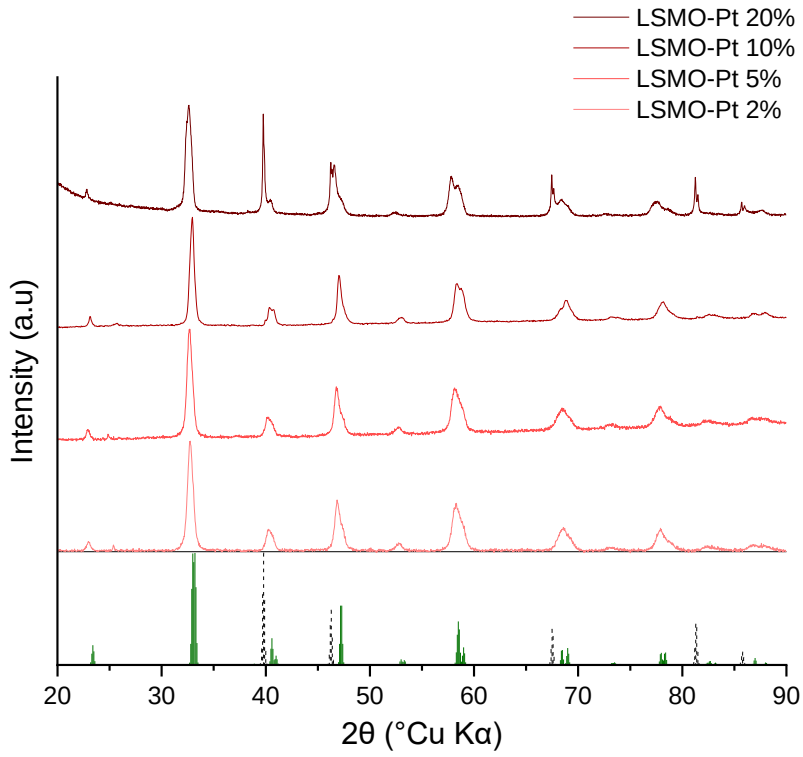

Figure 14. Powder XRD patterns of LSMO sample doped at 20 at.%, 10 at.%, 5 at.% and 2 at.% of platinum. The LSMO and Pt reference patterns are displayed in green and black dashes respectively.

The exsolution process was then studied on LSMO doped with 2% platinum, by using beam irradiation (**Figure 15**). TEM (**Figure 15**a) shows that the sample was in the early stage of the exsolution visible by very small (~ 1 nm) black dots after 30 s. After 2 min (**Figure 15**b), Pt nanoparticles were visible over the surface of LSMO nanocubes, thus demonstrating successful exsolution. Finally, the crystallinity of the LSMO perovskite nanocrystals after exsolution was confirmed by TEM (**Figure 15**c-d).

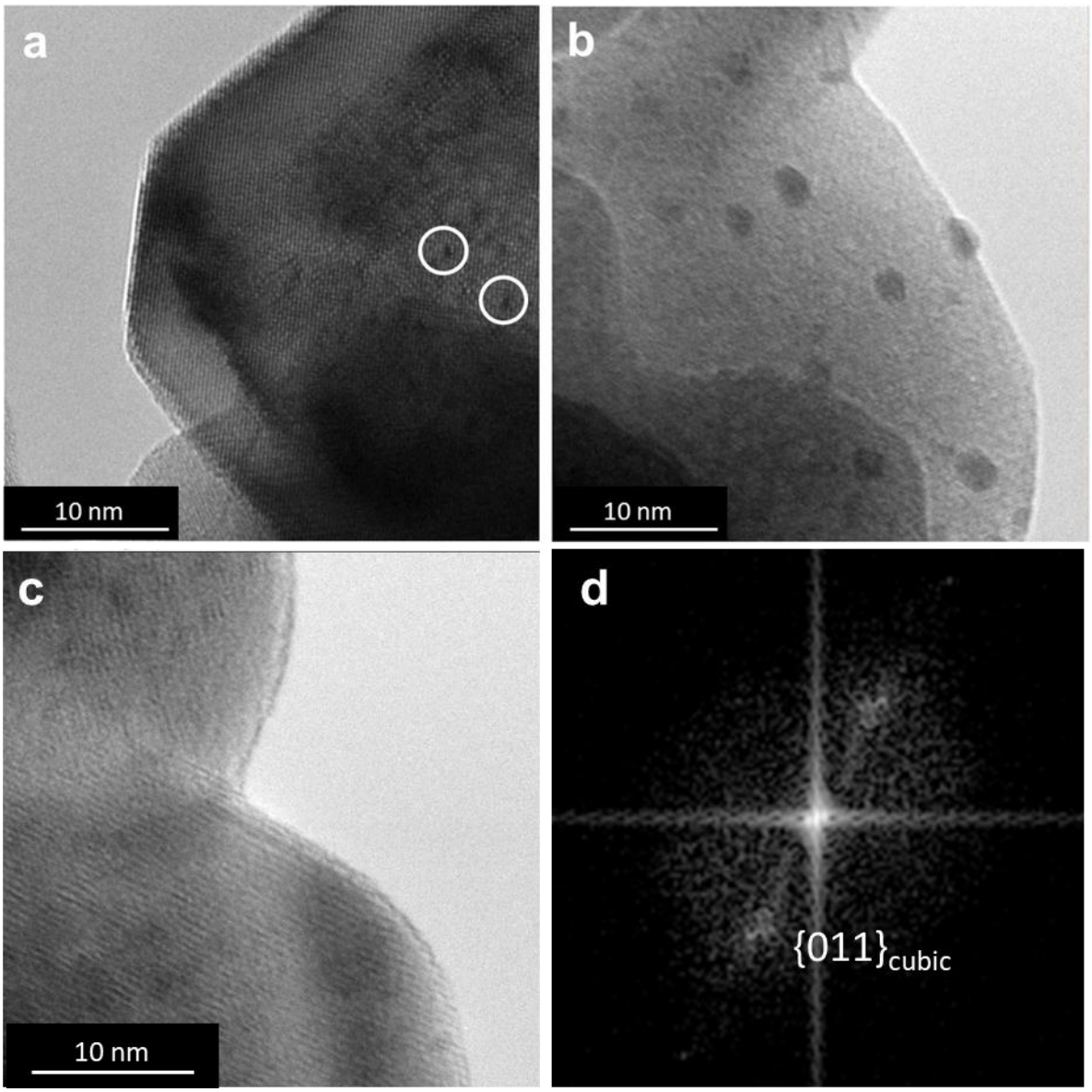

Figure 15. HRTEM images of LSMO doped with 2.% platinum (a) after 30 s and (b-c-d) after 2 min.

We then attempted the exsolution of the same sample under heating and reducing atmosphere. XRD patterns (**Figure 16**) show that the LSMO structure was kept. However, a secondary phase ascribed to $La_{0.1}Sr_{0.9}MnO_3$ appeared at 47°, 59° 79° (Cu Kα 2θ), indicating that this method led to a phase segregation of the host perovskite. Finally, no platinum was detected even after

reductive treatment. Note that a small amount of platinum was inserted and probably fewer exsoluted for this sample doped with 2 at%, hence the difficulty to detect platinum even post exsolution by XRD.

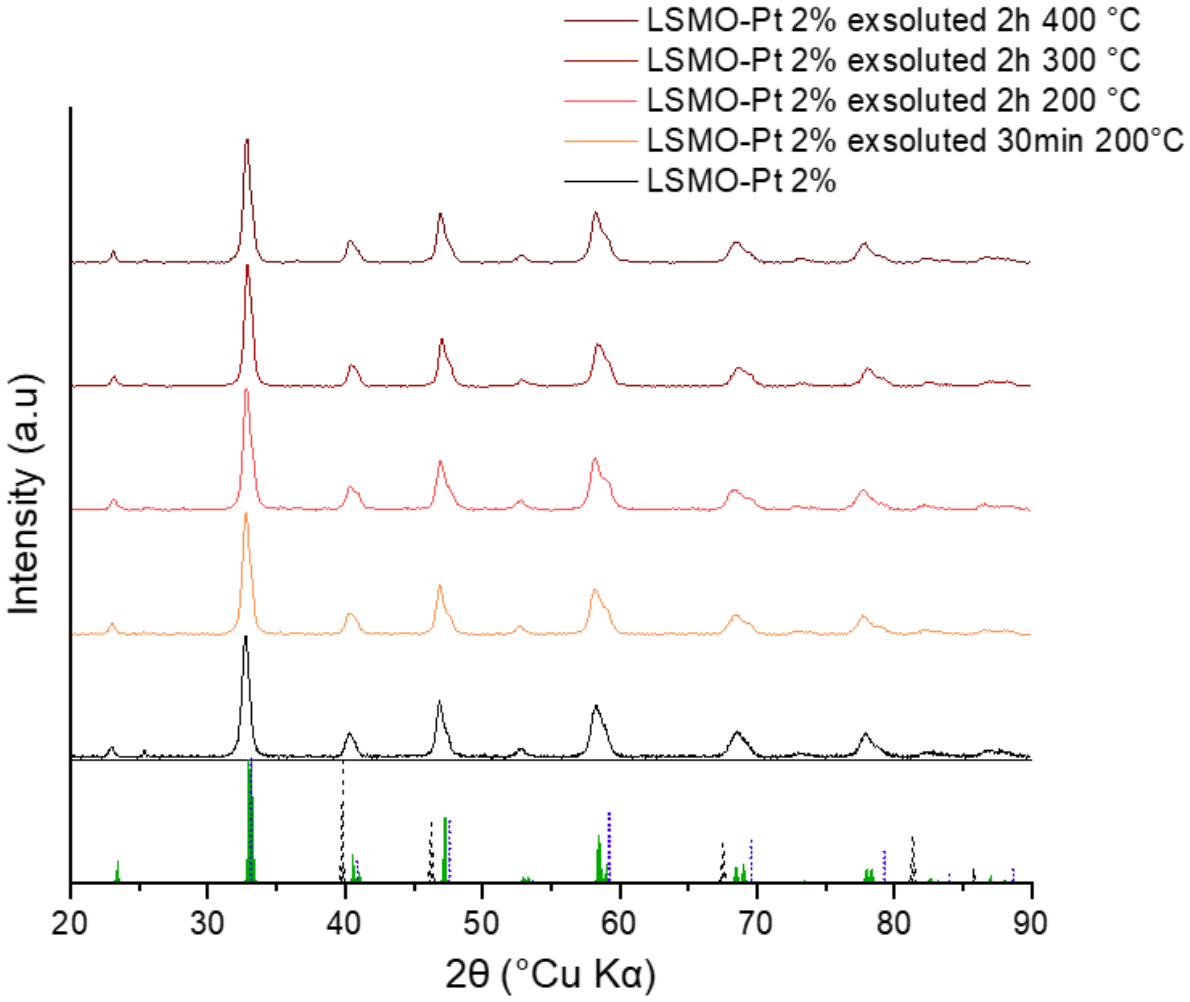

Figure 16. Powder XRD patterns of LSMO samples doped with 2 at% platinum before and after thermal treatment and reducing atmosphere. LSMO, Pt and $La_{0.1}Sr_{0.9}MnO_3$ references are displayed in green, black dashes and blue dots respectively.

To assess the occurrence of exsolution we observed by TEM the samples thermally treated H_2 The sample reduced for 30 min does not show evidence of exsolution (**Figure 17**a). However, exsolution was detected after 2 h of reducing treatment at temperature ranging from 200 to 400 °C.

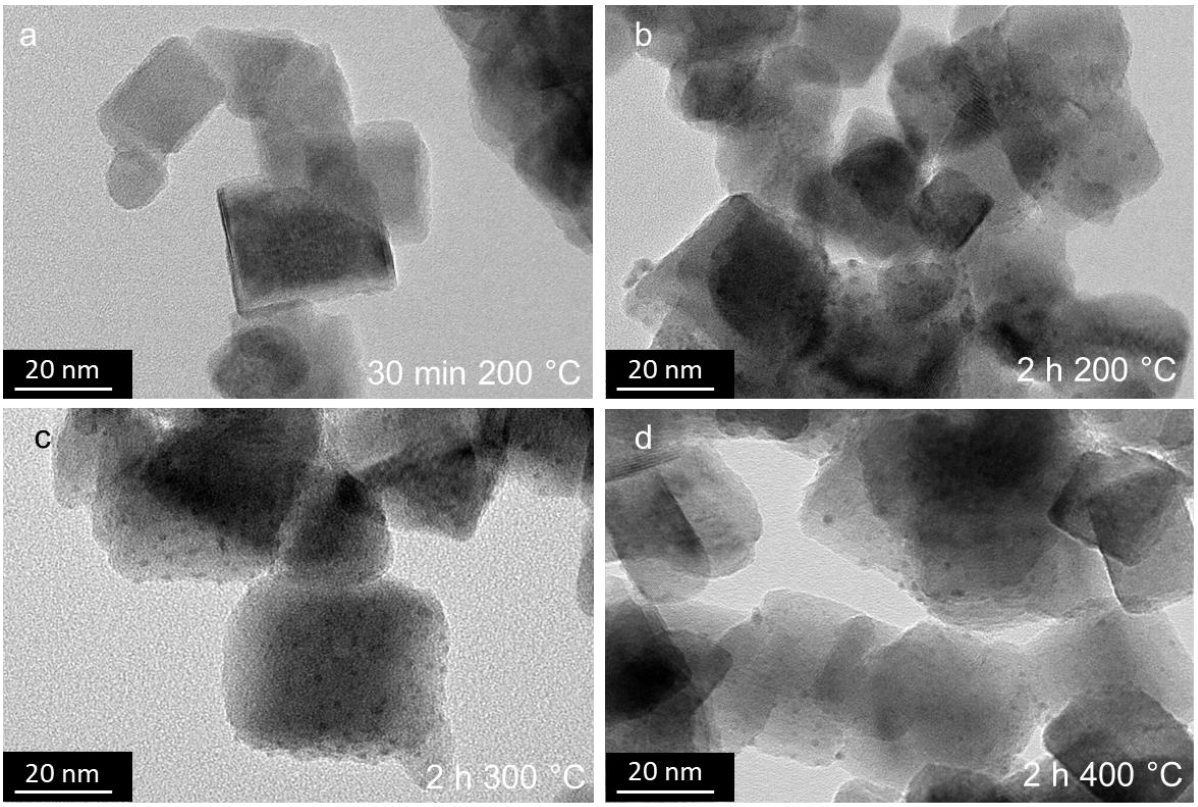

Figure 17. TEM images LSMO Pt 2 at.% post exsolution at several times and temperatures.

We showed that insertion of platinum into the LSMO perovskite structure and its exsolution was possible. The electron irradiation method as well as the reductive thermal treatment method led to the exsolution of platinum nanoparticles. The fact that exsolution was successfully obtained at 200 °C for only 2 h under reducing atmosphere shows how nanoscaled perovskite are more reactive than bulk perovskite. It also suggests the possibility to trigger exsolution in very mild conditions, thus enabling the use of perovskite hosts sensitive to reducing conditions, which could not be used in conventional high temperature exsolution. However, under heat and reducing atmosphere the LSMO perovskite seems to segregate while exsoluting.

V. Conclusion

To conclude, the exsolution process has been performed first on a reference perovskite $SrTiO_3$ host at the nanoscale by insertion of platinum. We showed that the doped structure was indeed able to exsolute nanoparticles of platinum at its surface, which to our knowledge has not been reported in the literature for nanoscaled perovskites. We also proved that other doping cations could be exsoluted from this nanoscaled perovskite. While exsolution on bulk perovskite has been reported during reductive thermal treatment, we showed that nanoparticles could also be

exsoluted in these conditions, but in milder conditions. Less harsh method was also usable such as electrochemical reduction to obtain the desired phenomenon. We showed a similar behavior of the exsoluted nanoparticles compared to bulk perovskites, where exsoluted nanoparticles are immobilized on the surface of the host perovskite. Hence, this phenomenon, was preserved, even if larger amount of surfaces and edges defects for the nanoscaled perovskite are present. This may also relate to the higher strain tolerance of nano-objects compared to the bulk which could be considered as an advantage from a catalysis point of view. Indeed, the immobility of exsoluted particles over particle deposition during chemical reaction, avoid aggregation and thus loss of activity. Exsolution was then applied to $La_{0.7}Sr_{0.3}MnO_3$. We showed that LSMO was also able to accept platinum in its structure and to undergo exsolution under an electron beam and reducing atmosphere. However, the reducing thermal treatment led to a phase segregation in LSMO.

Overall we developed a protocol using molten salt synthesis able to produce doped perovskite nanocrystals enabling exsolution. The perspectives of these results are vast, but first doping and exsolution in LSMO with other doping cations is of great interest for catalytic applications such as the oxygen reduction reaction. Secondly the use of other systems at the nanoscale could open a larger pool of catalytic reaction enhancement. Finally, 3 major points are left to investigate deeper. The first one is the dynamics of the exsoluted nanoparticles observed on STO: is it specific to STO? Can it be limited at low temperature? Secondly, coupling electrochemical exsolution to electrocatalysis, as suggested for STO-Pt 10% (**Figure 11**) would be of great interest. The use of milder treatment would also be worth investigating for other host perovskites as LSMO as we showed that exsolution on nanosystems was prone to occurs at lower temperatures compared to the bulk. The final point is the ability to reoxidized exsoluted nanoparticles and reinsert them into the host structure. This last point would open the possibility to reactivate catalysts *in situ* hence reducing the cost of catalysis overall.

References

(1) Takehira, K. Highly Dispersed and Stable Supported Metal Catalysts Prepared by Solid Phase Crystallization Method. *Catal. Surv. from Asia* **2002**, *6* (1–2), 19–32. https://doi.org/10.1023/a:1020589132547.

(2) Zhu, T.; Troiani, H. E.; Mogni, L. V.; Han, M.; Barnett, S. A. Ni-Substituted $Sr(Ti,Fe)O_3$ SOFC Anodes: Achieving High Performance via Metal Alloy Nanoparticle Exsolution. *Joule* **2018**, *2* (3), 478–496. https://doi.org/10.1016/j.joule.2018.02.006.

(3) Gao, Y.; Lu, Z.; You, T. L.; Wang, J.; Xie, L.; He, J.; Ciucci, F. Energetics of Nanoparticle Exsolution from Perovskite Oxides. *J. Phys. Chem. Lett.* **2018**, *9* (13), 3772–3778. https://doi.org/10.1021/acs.jpclett.8b01380.

(4) Neagu, D.; Oh, T. S.; Miller, D. N.; Ménard, H.; Bukhari, S. M.; Gamble, S. R.; Gorte, R. J.; Vohs, J. M.; Irvine, J. T. S. Nano-Socketed Nickel Particles with Enhanced Coking Resistance Grown in Situ by Redox Exsolution. *Nat. Commun.* **2015**, *6*. https://doi.org/10.1038/ncomms9120.

(5) Madsen, B. D.; Kobsiriphat, W.; Wang, Y.; Marks, L. D.; Barnett, S. A. Nucleation of Nanometer-Scale Electrocatalyst Particles in Solid Oxide Fuel Cell Anodes. *J. Power Sources* **2007**, *166* (1), 64–67. https://doi.org/10.1016/j.jpowsour.2006.12.080.

(6) Myung, J. H.; Neagu, D.; Miller, D. N.; Irvine, J. T. S. Switching on Electrocatalytic Activity in Solid Oxide Cells. *Nature* **2016**, *537* (7621), 528–531. https://doi.org/10.1038/nature19090.

(7) Tanaka, H.; Uenishi, M.; Taniguchi, M.; Tan, I.; Narita, K.; Kimura, M.; Kaneko, K.; Nishihata, Y.; Mizuki, J. The Intelligent Catalyst Having the Self-Regenerative Function of Pd, Rh and Pt for Automotive Emissions Control. *Catal. Today* **2006**, *117* (1–3), 321–328. https://doi.org/10.1016/j.cattod.2006.05.029.

(8) Uenishi, M.; Taniguchi, M.; Tanaka, H.; Kimura, M.; Nishihata, Y.; Mizuki, J.; Kobayashi, T. Redox Behavior of Palladium at Start-up in the Perovskite-Type $LaFePdO_x$ Automotive Catalysts Showing a Self-Regenerative Function. *Appl. Catal. B Environ.* **2005**, *57* (4), 267–273. https://doi.org/10.1016/j.apcatb.2004.11.011.

(9) Helveg, S.; López-Cartes, C.; Sehested, J.; Hansen, P. L.; Clausen, B. S.; Rostrup-

Nielsen, J. R.; Abild-Pedersen, F.; Nørskov, J. K. Atomic-Scale Imaging of Carbon Nanofibre Growth. *Nature* **2004**, *427* (6973), 426–429. https://doi.org/10.1038/nature02278.

(10) Abild-Pedersen, F.; Nørskov, J. K.; Rostrup-Nielsen, J. R.; Sehested, J.; Helveg, S. Mechanisms for Catalytic Carbon Nanofiber Growth Studied by Ab Initio Density Functional Theory Calculations. *Phys. Rev. B - Condens. Matter Mater. Phys.* **2006**, *73* (11), 1–13. https://doi.org/10.1103/PhysRevB.73.115419.

(11) Oh, T. S.; Rahani, E. K.; Neagu, D.; Irvine, J. T. S.; Shenoy, V. B.; Gorte, R. J.; Vohs, J. M. Evidence and Model for Strain-Driven Release of Metal Nanocatalysts from Perovskites during Exsolution. *J. Phys. Chem. Lett.* **2015**, *6* (24), 5106–5110. https://doi.org/10.1021/acs.jpclett.5b02292.

(12) Neagu, D.; Kyriakou, V.; Roiban, I.; Aouine, M.; Tang, C.; Caravaca, A.; Kousi, K.; Schreur-piet, I.; Metcalfe, I. S.; Vernoux, P.; Tsampas, M. N. In Situ Observation of Nanoparticle Exsolution Mechanistic Insight to Nanostructure Tailoring. *ACS Nano* **2019**, *13*, 12996–13005. https://doi.org/10.1021/acsnano.9b05652.

(13) Suntivich, J.; Gasteiger, H. A.; Yabuuchi, N.; Nakanishi, H.; Goodenough, J. B.; Shao-Horn, Y. Design Principles for Oxygen-Reduction Activity on Perovskite Oxide Catalysts for Fuel Cells and Metal-Air Batteries. *Nat. Chem.* **2011**, *3* (7), 546–550. https://doi.org/10.1038/nchem.1069.

(14) Thi N'Goc, H. Le; Mouafo, L. D. N.; Etrillard, C.; Torres-Pardo, A.; Dayen, J. F.; Rano, S.; Rousse, G.; Laberty-Robert, C.; Calbet, J. G.; Drillon, M.; Sanchez, C.; Doudin, B.; Portehault, D. Surface-Driven Magnetotransport in Perovskite Nanocrystals. *Adv. Mater.* **2017**, *29* (9), 1–9. https://doi.org/10.1002/adma.201604745.

(15) Alem, N. Synthesis of Perovskite Oxide Nanocrystals: Towards Magnetic Field-Based Energy Conversion, Sorbonne Université, 2018.

General conclusion

This PhD work aimed at using original synthesis strategies based on molten salts media in order to develop nanomaterials able to interact with their environment and then to exhibit stimuli-dependent electrocatalytic properties.

We first developed the first occurrence of nanoparticles of a quaternary manganese perovskite, $La_{0.33}Pr_{0.33}Ca_{0.33}MnO_3$. We showed that the usual experimental parameters, such as temperature, reaction time and reagents ratio were not adapted to avoid the formation of byproducts and of ill-defined objects. Instead, we highlighted the key role of two parameters: heating ramps and molten salt solvent oxo-basicity. We hypothesized that media with strong oxo-basicity, thanks to the choice of the salt itself and to the use of additives, enabled forcing coprecipitation of all cations in the same crystal structure and enhancing nucleation rates for a better morphological control. Likewise, very high heating ramps were instrumental in triggering coprecipitation of all cations, and then avoiding the formation of byproducts. Because the synthesis of this material appeared very challenging, the electrocatalytic and magnetic properties could not be addressed thoroughly within the timeframe of this PhD work. This is the major medium-term perspective for this quaternary oxide.

We specifically addressed the relationship between magnetism and electrocatalysis on the case study of $La_{0.7}Sr_{0.3}MnO_3$ nanocrystals derived from molten salts. To do so, we first designed an original dedicated set-up enabling to control the diffusion layer in the vicinity of the electrode, to bypass the use of any composite electrodes with multiple components, and to ensure a highly homogeneous magnetic field in the electrode area. We then observed a sporadic and poorly reproducible increase of the cathodic current under magnetic field at 15 °C and in a KOH electrolyte with conventional 0.1 M concentration. Preliminary electrochemical impedance spectroscopy (EIS) measurements suggest a reversible change of the material under magnetic field, although more in-depth studies will be performed on the short-term to understand the behavior of the material in electrocatalysis conditions. We also highlighted a dramatic impact of the electrolyte concentration, where a 40 fold increase of the KOH concentration (4 M) ensured a reproducible positive effect of the magnetic field (1 T) on the cathodic current. According to the literature, we ascribe this effect to the occurrence of anionic vacancies in the perovskite, although more EIS experiments and a screening of electrolyte compositions will be required on the short term to understand the origin of this current enhancement in the potential region of the oxygen reduction reaction.

Finally, we addressed another way to trigger "externally" the properties of nanoscaled perovskite oxides by modifying their intrinsic properties. We showed that platinum nanoparticles can be exsoluted from Pt-doped $SrTiO_3$ (STO) crystalline nanocubes initially produced by molten salts synthesis. To our knowledge, exsolution from nano-objects has never been reported in the literature. The synthesis protocol we developed enabled versatile doping of perovskite nanocrystals, in terms of doping cation nature and concentration. Hence, we were able to trigger exsolution of a wide range of reducible metals, although with varying behavior. Thermal exsolution could be triggered hundreds of degrees below the temperatures reported for bulk perovskite matrices, so that using nano-objects with enhanced reactivity provides a way to perform exsolution in mild conditions and to explore a wider range of perovskite compositions, even among the compounds chemically sensitive to reducing conditions, as shown for the $La_{0.7}Sr_{0.3}MnO_3$ perovskite. We showed that various reducing conditions can be envisioned, including electron irradiation, reducing thermal treatment and electrochemical reduction. Then, several perspectives emerge from these promising results. Firstly, electrochemically triggered reduction needs to be deeply investigated as it could yield *in situ* efficient electrocatalysts provided the choice of a sufficiently conductive perovskite matrix is chosen. Secondly, the reversibility of electrochemical exsolution in oxidative conditions should be addressed, as it might provide the ability to regenerate the catalysts. Thirdly, we showed that nanoscaled materials enable using mild conditions to exsolve a wide pool of cations from a large range of host perovskites. This enhanced diversity opens an avenue towards additional properties coupling, like e.g. probing how magnetic fields can impact the exsolution behavior.

Overall, in this work we explored different pathways towards the synthesis of new nanoscaled electrocatalysts responsive to external stimuli. We showed and discussed how different stimuli could be used to tune the properties of perovskites and more specifically, in the case of magnetic fields, the complexity that aroused from combining external stimuli with electrocatalysis. Finally, this manuscript can be considered as a prequel to a wider project englobing the synthesis of nanoscaled electrocatalysts and their use under external stimuli.

Materials and methods

I. Synthesis

1. $La_{0.7}Sr_{0.33}MnO_3$ synthesis

The LSMO synthesis was carried out as follows, according to a previously described procedure.[1] First, potassium nitrate (65 mmol), strontium nitrate (1.99 mmol), manganese nitrate tetrahydrate (6.5 mmol), lanthanum nitrate hexahydrate (3.86 mmol) were ball milled in a Retsch MM400 ball miller (50 mL stainless steel irons with one 25 mm ball) for 2 min and then dried at 40 °C under vacuum overnight. The powder was then put into an alumina crucible and heated at 600 °C for 2 h. After cooling at room temperature the product was redispersed with deionized water and stirred for 10 min and a reddish black solution was obtained, which was separated by centrifugated (20 000 rpm, 10 min) 8 times, washed with deionized water untill a conductance around 10 µS cm^{-1} was reached. The product was dried under vacuum at 40 °C overnight.

2. $La_{0.33}Pr_{0.33}Ca_{0.33}MnO_3$ original synthesis A-750 °C

First, potassium nitrate (65 mmol), lanthanum nitrate hexahydrate (1.99 mmol), praseodymium nitrate hexahydrate (1.99 mmol), calcium nitrate tetrahydrate (1.79 mmol) and manganese nitrate tetrahydrate (6.5 mmol) were ball milled in a Retsch MM400 ball miller (50 mL stainless steel irons with one 25 mm ball) for 2 min and then dried at 40 °C under vacuum overnight. The powder was then put into an alumina crucible and heated at 750 °C for 1 h. After cooling at room temperature, the product was redispersed with deionized water and stirred for 10 min. The suspension was then separated by centrifugation (21 000 rpm, 10 min) 5 times, washed with deionized water until a conductance around 10 µS cm^{-1} was reached. The product was dried under vacuum at 40 °C overnight and a powder was recovered.

2.1. Synthesis A-X °C 1 h, temperature screening

First, potassium nitrate (65 mmol), lanthanum nitrate hexahydrate (1.99 mmol), praseodymium nitrate hexahydrate (1.99 mmol), calcium nitrate tetrahydrate (1.79 mmol) and manganese nitrate tetrahydrate (6.5 mmol) were ball milled in a Retsch MM400 ball miller (50 mL stainless steel irons with one 25 mm ball) for 2 min and then dried at 40 °C under vacuum overnight. The powder was then put into an alumina crucible and heated at 600, 700 or 800 °C for 1 h. After cooling at room temperature, the product was redispersed with deionized water and stirred for 10 min. The suspension was then separated by centrifugation (21 000 rpm, 10 min) 5 times,

washed with deionized water until a conductance around 10 µS cm^{-1} was reached. The product was dried under vacuum at 40 °C overnight and a powder was recovered.

2.2. Synthesis B-Y 750 °C, time screening

First, potassium nitrate (65 mmol), lanthanum nitrate hexahydrate (1.99 mmol), praseodymium nitrate hexahydrate (1.99 mmol), calcium nitrate tetrahydrate (1.79 mmol) and manganese nitrate tetrahydrate (6.5 mmol) were ball milled in a Retsch MM400 ball miller (50 mL stainless steel irons with one 25 mm ball) for 2 min and then dried at 40 °C under vacuum overnight. The powder was then put into an alumina crucible and heated at 750 °C for 0.5, 4 or 8 h. After cooling at room temperature, the product was redispersed with deionized water and stirred for 10 min. The suspension was then separated by centrifugation (21 000 rpm, 10 min) 5 times, washed with deionized water until a conductance around 10 µS cm^{-1} was reached. The product was dried under vacuum at 40 °C overnight and a powder was recovered.

With Y = 30 min or 4 h or 8 h.

2.3. Synthesis A-Pr_x',

First, potassium nitrate (65 mmol), lanthanum nitrate hexahydrate (1.99 mmol), praseodymium nitrate hexahydrate (1.25 or 0.545 mmol), calcium nitrate tetrahydrate (1.79 mmol) and manganese nitrate tetrahydrate (6.5 mmol) were ball milled in a Retsch MM400 ball miller (50 mL stainless steel irons with one 25 mm ball) for 2 min and then dried at 40 °C under vacuum overnight. The powder was then put into an alumina crucible and heated at 750 °C for 1 h. After cooling at room temperature, the product was redispersed with deionized water and stirred for 10 min. The suspension was then separated by centrifugation (21 000 rpm, 10 min) 5 times, washed with deionized water until a conductance around 10 µS cm^{-1} was reached. The product was dried under vacuum at 40 °C overnight and a powder was recovered.

2.4. Synthesis A-La defect

First, potassium nitrate (65 mmol), lanthanum nitrate hexahydrate (1.69 mmol), praseodymium nitrate hexahydrate (1.99 mmol), calcium nitrate tetrahydrate (1.79 mmol) and manganese nitrate tetrahydrate (6.5 mmol) were ball milled in a Retsch MM400 ball miller (50 mL stainless steel irons with one 25 mm ball) for 2 min and then dried at 40 °C under vacuum overnight. The powder was then put into an alumina crucible and heated at 750 °C for 1 h. After cooling at room temperature, the product was redispersed with deionized water and stirred for 10 min. The suspension was then separated by centrifugation (21 000 rpm, 10 min) 5 times, washed

with deionized water until a conductance around 10 µS cm^{-1} was reached. The product was dried under vacuum at 40 °C overnight and a powder was recovered.

2.5. Synthesis A-Ca excess

First, potassium nitrate (65 mmol), lanthanum nitrate hexahydrate (1.99 mmol), praseodymium nitrate hexahydrate (1.99 mmol), calcium nitrate tetrahydrate (2.99 mmol) and manganese nitrate tetrahydrate (6.5 mmol) were ball milled in a Retsch MM400 ball miller (50 mL stainless steel irons with one 25 mm ball) for 2 min and then dried at 40 °C under vacuum overnight. The powder was then put into an alumina crucible and heated at 750 °C for 1 h. After cooling at room temperature, the product was redispersed with deionized water and stirred for 10 min. The suspension was then separated by centrifugation (21 000 rpm, 10 min) 5 times, washed with deionized water until a conductance around 10 µS cm^{-1} was reached. The product was dried under vacuum at 40 °C overnight and a powder was recovered.

2.6. Synthesis A-D10

First, potassium nitrate (65 mmol), lanthanum nitrate hexahydrate (0.199 mmol), praseodymium nitrate hexahydrate (0.199 mmol), calcium nitrate tetrahydrate (0.179 mmol) and manganese nitrate tetrahydrate (0.65 mmol) were ball milled in a Retsch MM400 ball miller (50 mL stainless steel irons with one 25 mm ball) for 2 min and then dried at 40 °C under vacuum overnight. The powder was then put into an alumina crucible and heated at 750 °C for 1 h. After cooling at room temperature, the product was redispersed with deionized water and stirred for 10 min. The suspension was then separated by centrifugation (21 000 rpm, 10 min) 5 times, washed with deionized water until a conductance around 10 µS cm^{-1} was reached. The product was dried under vacuum at 40 °C overnight and a powder was recovered.

2.7. Synthesis C-X °C 1h, temperature screening

First, sodium nitrite (65 mmol), lanthanum nitrate hexahydrate (1.99 mmol), praseodymium nitrate hexahydrate (1.99 mmol), calcium nitrate tetrahydrate (1.79 mmol) and manganese nitrate tetrahydrate (6.5 mmol) were ball milled in a Retsch MM400 ball miller (50 mL stainless steel irons with one 25 mm ball) for 2 min and then dried at 40 °C under vacuum overnight. The powder was then put into an alumina crucible and heated at 600, 750, 800 or 850 °C for 1 h. After cooling at room temperature, the product was redispersed with deionized water and stirred for 10 min. The suspension was then separated by centrifugation (21 000 rpm, 10 min)

5 times, washed with deionized water until a conductance around 10 µS cm^{-1} was reached. The product was dried under vacuum at 40 °C overnight and a powder was recovered.

2.8. Synthesis C-Y 750 °C, time screening

First, sodium nitrite (65 mmol), lanthanum nitrate hexahydrate (1.99 mmol), praseodymium nitrate hexahydrate (1.99 mmol), calcium nitrate tetrahydrate (1.79 mmol) and manganese nitrate tetrahydrate (6.5 mmol) were ball milled in a Retsch MM400 ball miller (50 mL stainless steel irons with one 25 mm ball) for 2 min and then dried at 40 °C under vacuum overnight. The powder was then put into an alumina crucible and heated at 750 °C for 15, 30 min or 1 h. After cooling at room temperature, the product was redispersed with deionized water and stirred for 10 min. The suspension was then separated by centrifugation (21 000 rpm, 10 min) 5 times, washed with deionized water until a conductance around 10 µS cm^{-1} was reached. The product was dried under vacuum at 40 °C overnight and a powder was recovered.

2.9. Synthesis D-X °C 15 min, temperature screening

First, sodium nitrite (65 mmol), lanthanum nitrate hexahydrate (1.99 mmol), praseodymium nitrate hexahydrate (1.99 mmol), calcium nitrate tetrahydrate (1.79 mmol) and manganese nitrate tetrahydrate (6.5 mmol) were ball milled in a Retsch MM400 ball miller (50 mL stainless steel irons with one 25 mm ball) for 2 min and then dried at 40 °C under vacuum overnight. The powder was then put into an alumina crucible and heated at 650, 700, 750 or 800 °C for 15 min. After cooling at room temperature, the product was redispersed with deionized water and stirred for 10 min. The suspension was then separated by centrifugation (21 000 rpm, 10 min) 5 times, washed with deionized water until a conductance around 10 µS cm^{-1} was reached. The product was dried under vacuum at 40 °C overnight and a powder was recovered.

With X = 650 °C, 700 °C, 750 °C or 800 °C.

2.10. Synthesis E-Xramp+X'plateau, 750 °C, time screening

First, sodium nitrite (65 mmol), lanthanum nitrate hexahydrate (1.99 mmol), praseodymium nitrate hexahydrate (1.99 mmol), calcium nitrate tetrahydrate (1.79 mmol) and manganese nitrate tetrahydrate (6.5 mmol) were ball milled in a Retsch MM400 ball miller (50 mL stainless steel irons with one 25 mm ball) for 2 min and then dried at 40 °C under vacuum overnight. For microwave-assisted syntheses, the reaction media were heated from room temperature to the targeted temperature over a ramping time noted X_{ramp}. The temperature was then dwelled over a time noted $X'_{plateau}$. The overall reaction time is then noted $X_{ramp}+X'_{plateau}$. 2g of the prepared

powder was then put into a SiC crucible and 0.13g of Na_2O were added. The mixture was then heated at 750 °C for $X_{ramp}+X'_{plateau}$. After cooling at room temperature, the product was redispersed with deionized water and stirred for 10 min. The suspension was then separated by centrifugation (21 000 rpm, 10 min) 5 times, washed with deionized water until a conductance around 10 µS cm^{-1} was reached. The product was dried under vacuum at 40 °C overnight and a powder was recovered.

With $X_{ramp}+X'_{plateau}$ = 2 + 2 min, 4 + 2 min or 4 + 5 min.

2.11. Synthesis F-3 eq, 3 min ramp at 800 °C

First, sodium nitrite (65 mmol), lanthanum nitrate hexahydrate (1.99 mmol), praseodymium nitrate hexahydrate (1.99 mmol), calcium nitrate tetrahydrate (1.79 mmol) and manganese nitrate tetrahydrate (6.5 mmol) were ball milled in a Retsch MM400 ball miller (50 mL stainless steel irons with one 25 mm ball) for 2 min and then dried at 40 °C under vacuum overnight. For microwave-assisted syntheses, the reaction media were heated from room temperature to the targeted temperature over a ramping time noted X_{ramp}. The temperature was then dwelled over a time noted $X'_{plateau}$. The overall reaction time is then noted $X_{ramp}+X'_{plateau}$. 2g of the prepared powder was then put into a SiC crucible and 0.39g of Na_2O were added. The mixture was then heated at 750 °C for only 3 min ramping time. After cooling at room temperature, the product was redispersed with deionized water and stirred for 10 min. The suspension was then separated by centrifugation (21 000 rpm, 10 min) 5 times, washed with deionized water until a conductance around 10 µS cm^{-1} was reached. The product was dried under vacuum at 40 °C overnight and a powder was recovered.

3. $SrTiO_3$ original synthesis

First, commercial 0.24 titanium oxide (3.0 mmol), 0.76 g strontium nitrate tetrahydrate (3.6 mmol) and 1.0 g of equimolar NaCl/KCl (0.448g/0.571g) were ball milled in a Retsch MM400 ball miller (50 mL stainless steel irons with one 25 mm ball) for 2 min and then dried at 40 °C under vacuum overnight. The powder was then put into an alumina crucible and heated at 700 °C for 6 h. After cooling at room temperature, the product was redispersed with deionized water and stirred for 10 min. The suspension was then separated by centrifugation (21 000 rpm, 10 min) 5 times, washed with deionized water until a conductance around 10 µS cm^{-1} was reached. The product was dried under vacuum at 40 °C overnight and a powder was recovered.

3.1. $SrTi_{1-x}Pt_xO_3$ synthesis

First, commercial x_{gTi} g titanium oxide (x_{molTi} mmol), 0.76 g strontium nitrate tetrahydrate (3.6 mmol), x_{gPt} platinum tetrachloride (x_{molPt} mmol) and 1.0 g of equimolar NaCl/KCl (0.45g/0.57g) were ball milled in a Retsch MM400 ball miller (50 mL stainless steel irons with one 25 mm ball) for 2 min and then dried at 40 °C under vacuum overnight. The powder was then put into an alumina crucible and heated at 700 °C for 6 h. After cooling at room temperature, the product was redispersed with deionized water and stirred for 10 min. The suspension was then separated by centrifugation (21 000 rpm, 10 min) 5 times, washed with deionized water until a conductance around 10 µS cm^{-1} was reached. The product was dried under vacuum at 40 °C overnight and a powder was recovered.

	$PtCl_4$ (g)	*$PtCl_4$ (mmol)*	*TiO_2 (g)*	*TiO_2 (mmol)*
X = 20 at%	0.2	0.06	0.19	2.4
X = 10 at%	0.1	0.03	0.22	2.7
X = 5 at%	0.05	0.015	0.23	2.85
X = 2 at%	0.02	0.006	0.24	2.94

3.2. $SrTi_{1-x}Ni_xO_3$ synthesis

First, commercial x_{gTi} g titanium oxide (x_{molTi} mmol), 0.85 g strontium nitrate tetrahydrate (4 mmol), x_{gNi} nickel chloride hexahydrate (x_{molNi} mmol) and 1.0 g of equimolar NaCl/KCl (0.59g/0.76g) were ball milled in a Retsch MM400 ball miller (50 mL stainless steel irons with one 25 mm ball) for 2 min and then dried at 40 °C under vacuum overnight. The powder was then put into an alumina crucible and heated at 700 °C for 6 h. After cooling at room temperature, the product was redispersed with deionized water and stirred for 10 min. The suspension was then separated by centrifugation (21 000 rpm, 10 min) 5 times, washed with deionized water until a conductance around 10 µS cm^{-1} was reached. The product was dried under vacuum at 40 °C overnight and a powder was recovered.

	x_{gPt} *$NiCl_2.6H_2O$ (g)*	*x_{molPt}* *$NiCl_2.6H_2O$ (mmol)*	*x_{gTi}* *TiO_2 (g)*	*x_{molTi}* *TiO_2 (mmol)*
X = 10 at%	0.095	0.4	0.29	3.6
X = 5 at%	0.048	0.2	0.30	3.8
X = 2 at%	0.019	0.08	0.31	3.9

3.3. $SrTi_{1-x}Cu_xO_3$ synthesis

First, commercial x_{gTi} g titanium oxide (x_{molTi} mmol), 0.85 g strontium nitrate tetrahydrate (4 mmol), x_{gCu} copper chloride (x_{molCu} mmol) and 1.0 g of equimolar NaCl/KCl (0.59g/0.76g) were ball milled in a Retsch MM400 ball miller (50 mL stainless steel irons with one 25 mm ball) for 2 min and then dried at 40 °C under vacuum overnight. The powder was then put into an alumina crucible and heated at 700 °C for 6 h. After cooling at room temperature, the product was redispersed with deionized water and stirred for 10 min. The suspension was then separated by centrifugation (21 000 rpm, 10 min) 5 times, washed with deionized water until a conductance around 10 µS cm^{-1} was reached. The product was dried under vacuum at 40 °C overnight and a powder was recovered.

	x_{gCu}	x_{molCu}	x_{gTi}	x_{molTi}
	$CuCl_2$ (g)	*$CuCl_2$ (mmol)*	*TiO_2 (g)*	*TiO_2 (mmol)*
X = 10 at%	0.054	0.4	0.29	3.6
X = 5 at%	0.027	0.2	0.30	3.8
X = 2 at%	0.011	0.08	0.31	3.9

3.4. $SrTi_{1-x}Ag_xO_3$ synthesis

First, commercial x_{gTi} g titanium oxide (x_{molTi} mmol), 0.85 g strontium nitrate tetrahydrate (4 mmol), x_{gAg} silver chloride (x_{molAg} mmol) and 1.0 g of equimolar NaCl/KCl (0.59g/0.76g) were ball milled in a Retsch MM400 ball miller (50 mL stainless steel irons with one 25 mm ball) for 2 min and then dried at 40 °C under vacuum overnight. The powder was then put into an alumina crucible and heated at 700 °C for 6 h. After cooling at room temperature, the product was redispersed with deionized water and stirred for 10 min. The suspension was then separated by centrifugation (21 000 rpm, 10 min) 5 times, washed with deionized water until a conductance around 10 µS cm^{-1} was reached. The product was dried under vacuum at 40 °C overnight and a powder was recovered.

	x_{gAg}	x_{molAg}	x_{gTi}	x_{molTi}
	AgCl (g)	*AgCl (mmol)*	*TiO_2 (g)*	*TiO_2 (mmol)*
X = 10 at%	0.057	0.4	0.29	3.6
X = 5 at%	0.029	0.2	0.30	3.8
X = 2 at%	0.011	0.08	0.31	3.9

4. $La_{0.7}Sr_{0.3}Mn_{1-x}Pt_xO_3$ synthesis

First, potassium nitrate (65 mmol), strontium nitrate (1.99 mmol), manganese nitrate tetrahydrate (x_{molMn} mmol), lanthanum nitrate hexahydrate (3.86 mmol) and platinum chloride (x_{molPt} mmol) were ball milled in a Retsch MM400 ball miller (50 mL stainless steel irons with one 25 mm ball) for 2 min and then dried at 40 °C under vacuum overnight. The powder was then put into an alumina crucible and heated at 600 °C for 2 h. After cooling at room temperature, the product was redispersed with deionized water and stirred for 10 min and a reddish black solution was obtained, which was separated by centrifugated (20 000 rpm, 10 min) 8 times, washed with deionized water until a conductance around 10 µS/cm was reached. The product was dried under vacuum at 40 °C overnight.

	x_{molMn}	x_{molPt}
	$Mn(NO_3)_2.4H_2O$ (mmol)	*$PtCl_4$ (mmol)*
X = 20 at%	5.2	1.3
X = 10 at%	5.9	0.7
X = 5 at%	6.2	0.2
X = 2 at%	6.4	0.1

II. Material characterization

1. Furnace oven

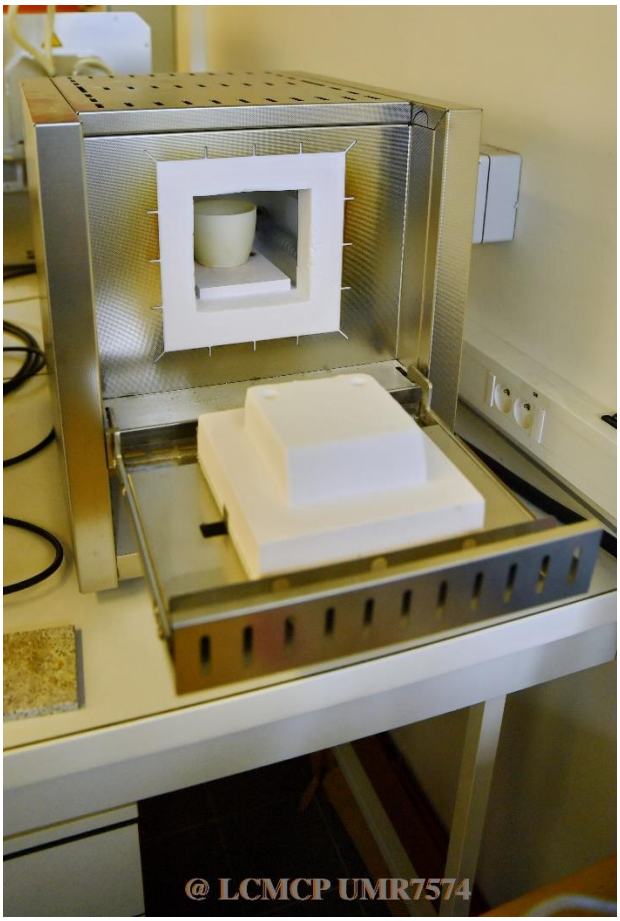

Syntheses were performed using a L 3/11/B410 Nabertherm GmbH muffle furnace oven under air.

2. Microwave oven (MW)

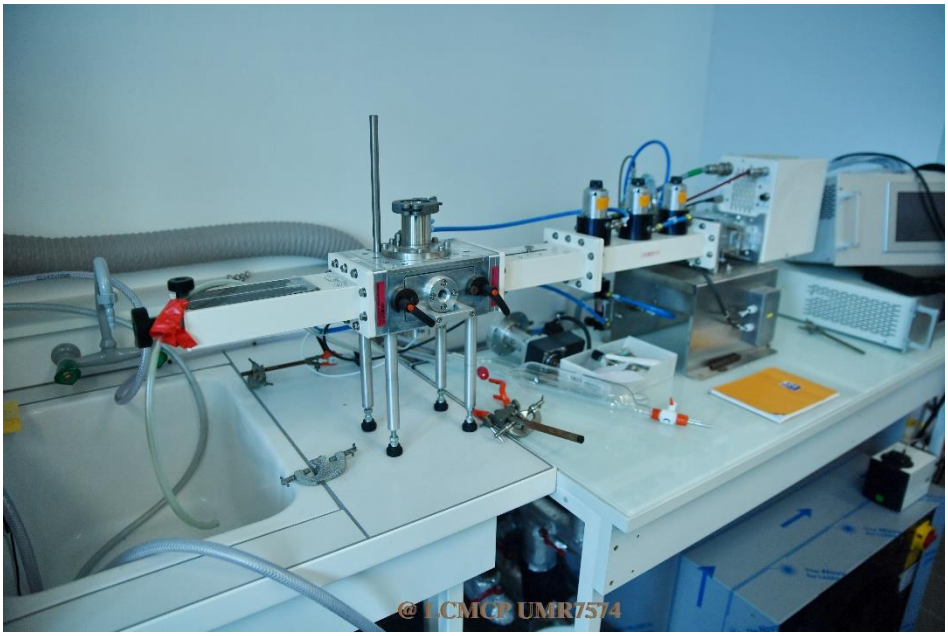

Syntheses were performed using a patented high temperature microwave from SAIREM.[2]

3. Powder X-ray diffraction (XRD)

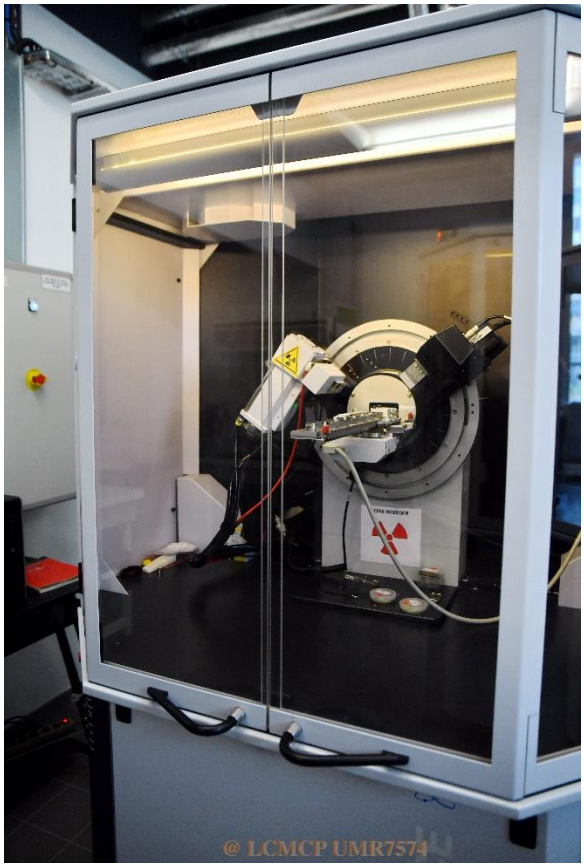

Powder XRD patterns were recorded on a Bruker D8 advance diffractometer operating at the Cu Kα source. ICSD references used for indexation were ICSD 35218, ICSD 18513,

PDF 04-021-6265, PDF 04-011-2398, PDF 01-089-3080, PDF 00-031-1238, PDF 00-064-0863, PDF 00-004-0802, PDF 00-035-0734, PDF 01-078-0428, PDF 04-020-2759 for $CaMnO_3$, $PrO_{1.88}$, $La_{0.7}Sr_{0.3}MnO_3$, $La_{0.275}Ca_{0.375}Pr_{0.35}MnO_3$, NiO, AgCl, TiO_2, Pt, $SrTiO_3$, CuO and $La_{0.1}Sr_{0.9}MnO_3$ respectively.

4. Transmission electron microscopy (TEM)

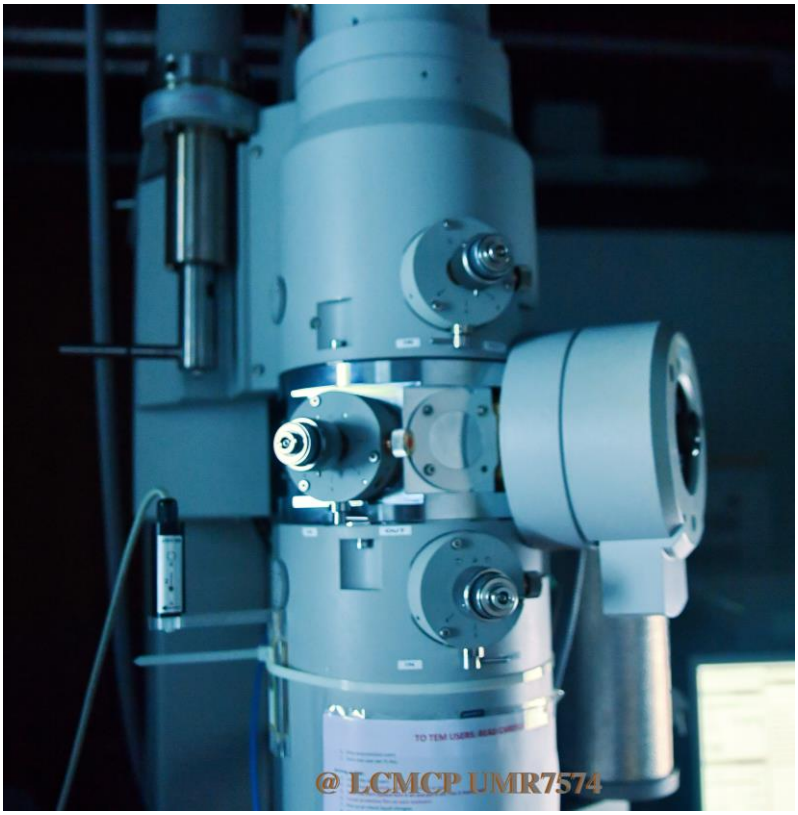

Transmission electron microscopy (TEM) was performed on a JEOL JEM2100Plus LaB 6 working at an accelerating voltage of 200 kV.

5. X-ray fluorescence (WDXRF)

Atomic compositions were assessed by wavelength-dispersive X-ray fluorescence (WDXRF) measured on a Bruker S8 Tiger spectrometer after pelletizing the powder.

III. Electrochemical Characterization

1. Magnet

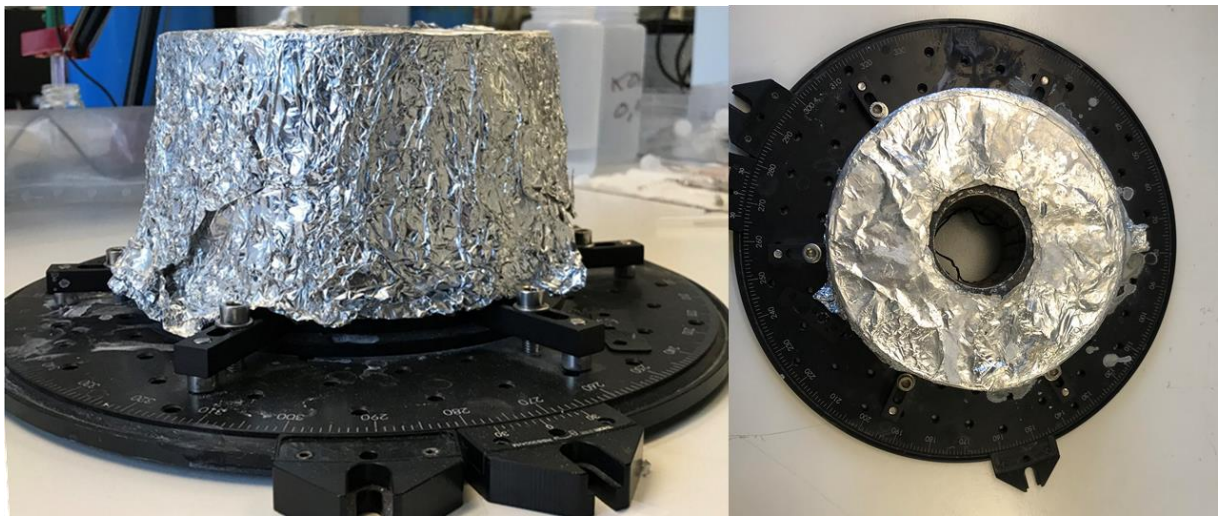

The magnet used for all experiments under magnetic field is a Haalbaar magnet. The magnetic field is contained and homogeneous in the cylindrical aperture with a value of 1 T.

2. Rotating disk electrode (RDE)

The electrocatalytic properties of the materials were studied through a three-electrode setup in an electrochemical cell using a Pt wire as a counter electrode, a saturated Ag/AgCl reference electrode, and a glassy carbon (GC) rotating disk electrode (RDE) as a working electrode, connected to a VPS Biologic potentiostat. All potentials are referred in the text to the reversible hydrogen electrode (RHE, ERHE = $E_{Ag/AgCl(sat)}$ + 0.197 + 0.059pH). The GC RDE (geometrical disk area (0.07 cm^2), Radiometer Analytical) was polished with diamond paste (1 μm, BAS Inc.) followed by diamond paste (0.05 μm, BAS inc.) to reach mirror grade before each experiment. Then the GC disk was coated with a conductive ink that contains the different perovskite catalysts. This ink was composed by the perovskite catalyst powder, hydrophilized Acetylene Black carbon (AB, Alfa Aesar) (99.9+%, 75 $m^2\ g^{-1}$), and Nafion-117 (5 wt % solution in aliphatic alcohols, Sigma-Aldrich). AB was hydrophilized by treating 0.5 g of AB in 50 mL of HNO_3 20% at 80 °C under stirring overnight, followed by centrifugation, washing with water, and vacuum drying. A 10 mg amount of the perovskite catalyst powder, 10 mg of the modified AB, and 10 mL of absolute ethanol were mixed and sonicated for 2 h. Then 435 μL of ion- exchanged Nafion solution (5 wt % in aliphatic alcohols, Aldrich) was added, and the suspension was sonicated for 5 min. A 10 μL (for cyclic voltammetry (CV)) amount of the ink (catalyst:acetylene black (AB) = 1:1) was deposited on the polished GC electrode and dried for 1 h.

3. Cavity microelectrode (ME)

ME were made of a glass tube (5–6 mm diameter with a total length ranging from 80 to 150 mm) containing a Cu-wire (diameter: 25–50 mm, length 3 cm). Before making the cavity, the ME head was made planar with a micro- grained sandpaper (Norton, TUFBAK, ADALOX, P1000) and Al_2O_3 paste (Prolabo). After polishing, the electrode was washed with distilled water until it was free of Al_2O_3. With the help of a microscope, the formation of a metal disk free of residual impurities was checked. It was then verified that the connection between the platinum and graphite does not induce an ohmic drop at contact. Typically, the resistance of this homemade electrode was less than 10 V. The cavity was obtained by controlled dissolution of the Cu-wire in a 0.5M H_2SO_4 solution for 3 min by applying a voltage of 0.4 V vs. SCE. The connection between the Cu-wire and the Cu-wire collector was achieved by embedding the end of the two wires with compacted graphite powder. The diameter, and the depth, of the microcavity were measured with an optical microscope. This arrangement allowed checking the material inclusion too. The usual height diameter ratio is between 0.4 and 1. If larger than 1, then establishing the contact between the grains and Cu is difficult. With a ratio smaller than 0.4, the grains could easily escape out of the cavity during the experiment. The cavity was filled up with material grains using the electrode as a pestle. The amount of grains included within the microcavity depended on the hardness of the surface on which the powder was spread. The filling of the cavity was controlled with the microscope, and at the same time, it was verified that no grain remains on the head outside the cavity. The first CV scan was started a few seconds after the electrode was immersed in the electrolytic solution. After the electrochemical experiments, the material was dissolved by immersing the electrode head in an appropriate solution.[3]

(1) Thi N'Goc, H. Le; Mouafo, L. D. N.; Etrillard, C.; Torres-Pardo, A.; Dayen, J. F.; Rano, S.; Rousse, G.; Laberty-Robert, C.; Calbet, J. G.; Drillon, M.; Sanchez, C.; Doudin, B.; Portehault, D. Surface-Driven Magnetotransport in Perovskite Nanocrystals. *Adv. Mater.* **2017**, *29* (9), 1–9. https://doi.org/10.1002/adma.201604745.

(2) Portehault, D.; Marinel, S.; Savary, E. Method for Melting a Salt Sample by Microwave. W0/2018/104187A1, 2018.

(3) Cachet-Vivier, C.; Keddam, M.; Vivier, V.; Yu, L. T. Development of Cavity Microelectrode Devices and Their Uses in Various Research Fields, Université Pierre et Marie Curie, 2015. https://doi.org/10.1016/j.jelechem.2012.09.011.

Appendix

$La_{0.33}Pr_{0.33}Ca_{0.33}MnO_3$ as electrocatalyst for the oxygen reduction reaction

LPCMO possesses one of the largest EPS as mentioned in the introduction, by reducing its size to the nanoscale the possibility to obtain only single ferromagnetic domains per particles is possible. Moreover, as LSMO the electrical resistance of LPCMO decreases under influence of a magnetic field (CMR effect). The Curie temperature in room conditions is ≃ -121 °C. Both aforementioned electrocatalysts are of great interest for the oxygen reduction reaction and we expected that LPCMO nanoparticles would be stronger impacted by magnetic field compared to LSMO, due to the formation of these single ferromagnetic domains.

The number of electrons transferred during ORR was measured by Koutecky-Levich analysis of the diffusion current at 0.4 V/RHE for 20 °C, 15 °C and 5 °C on a rotating disk electrode in 0.1 M KOH. The number of electrons measured was of 6.6, 5.6 and 5 for 20 °C, 15 °C and 5 °C respectively. CVs cycles of the analysis are shown **Appendix 3**. We are so far unable to explain why such high number of electrons are transferred for the ORR and also why this number is decreasing with the temperature.

The ORR on LPCMO was then performed in the same conditions as for LSMO using a microelectrode in 0.1 M KOH saturated in O_2 at 15°C and 5°C and a magnet of 1T. **Appendix 1** shows that once LPCMO is put under a magnetic field, the current density increases significantly for both experiments. The response of LPCMO to the magnetic field cannot be ascribed now to the colossal magnetoresistance effect. Electrochemical impedance spectroscopy measurements are required. These preliminary results suggest that by reaching the nanoscale we were able to obtain single ferromagnetic domain which are more responsive than LSMO multi-domains to the magnetic field. Moreover, experiments in 4 M KOH saturated in O_2 (**Appendix 4**) show a promising response of LPCMO microelectrodes under magnetic field. We are yet unable to explain this different behavior observed at such concentration nor what type of mechanism is involved.

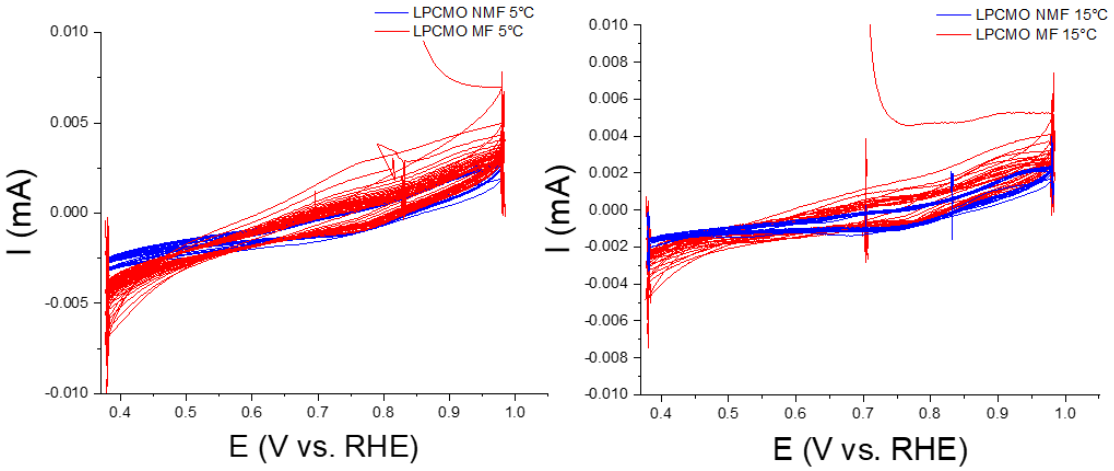

Appendix 1. Cyclovoltammetry of LPCMO nanoparticles at 5°C and 15°C in KOH 0.1 M saturated in O_2, without magnetic field (NMF-blue) and with magnetic field (MF-red).

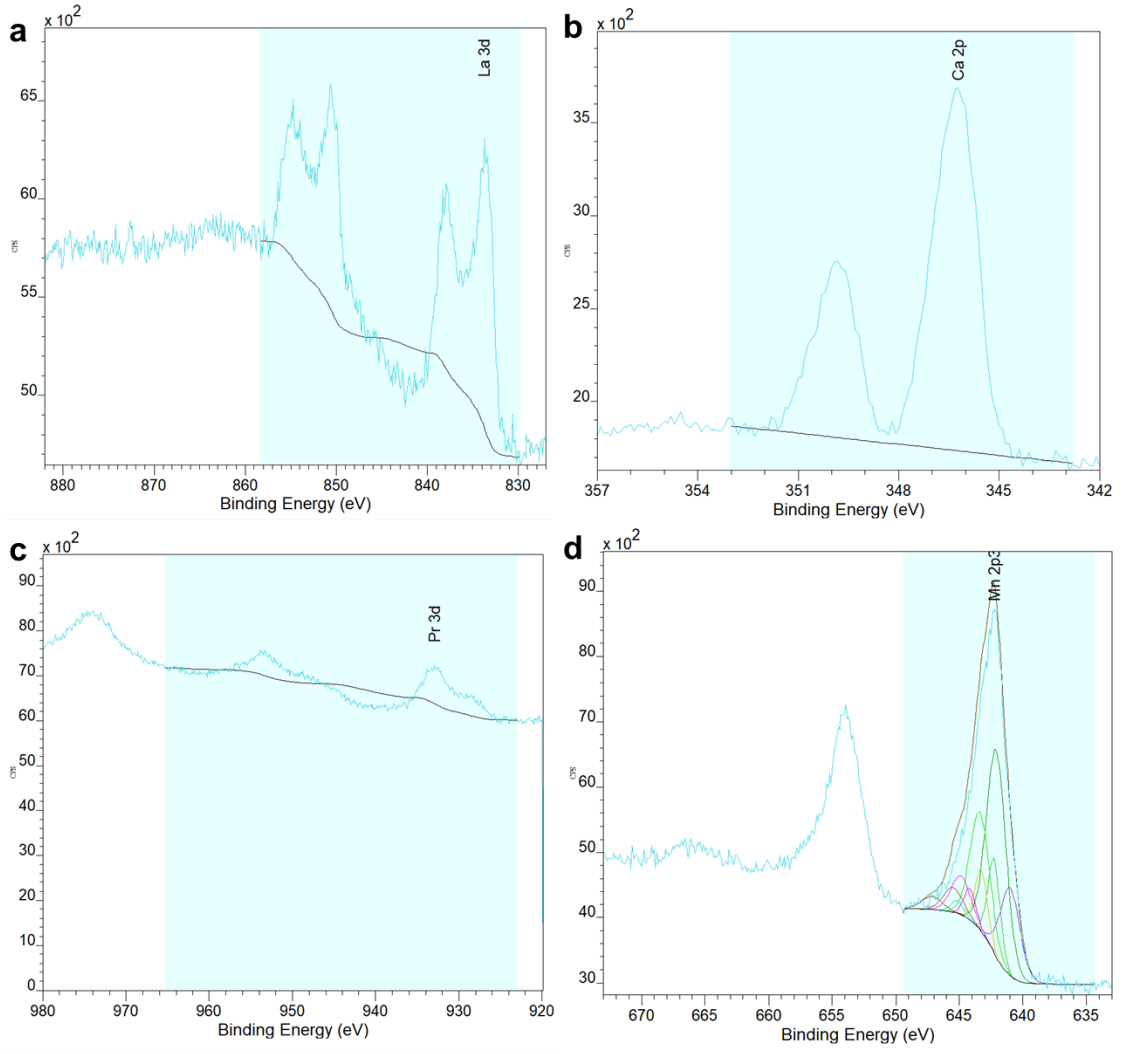

Appendix 2. XPS spectra of LPCMO nanoparticles with (a) La 3d region, (b) Ca 2p region, (c) Pr 3d region and (d) Mn $2p_{3/2}$ region.

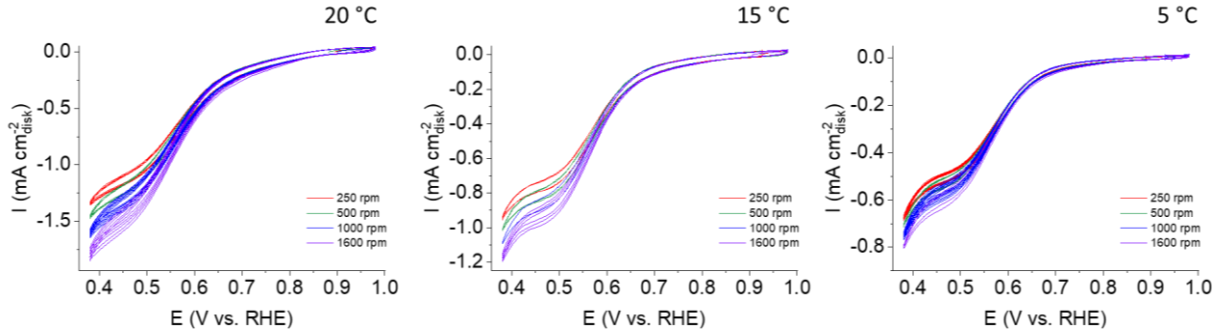

Appendix 3. Cyclovoltammetry cycles of LPCMO RDE at 20 °C, 15 °C and 5°C in O_2-saturated 0.1M KOH.

Cyclovoltammetry cycles in 0.1 M KOH O_2-saturated with were performed at 20, 15 and 5 °C. The CVs were recorded at different speed to control the diffusion barrier. The oxygen reduction reaction onset potential was found to be of 0.7 V vs. RHE, the ORR reaction was observed at 0.46 V vs. RHE. However, the diffusion plateau does not seem to be reached at 0.4 V vs. RHE. According to Koutecky-Levich analysis at 0.4 V vs. RHE 6.6, 5.6 and 5 electrons were transferred for 20, 15 and 5 °C respectively.

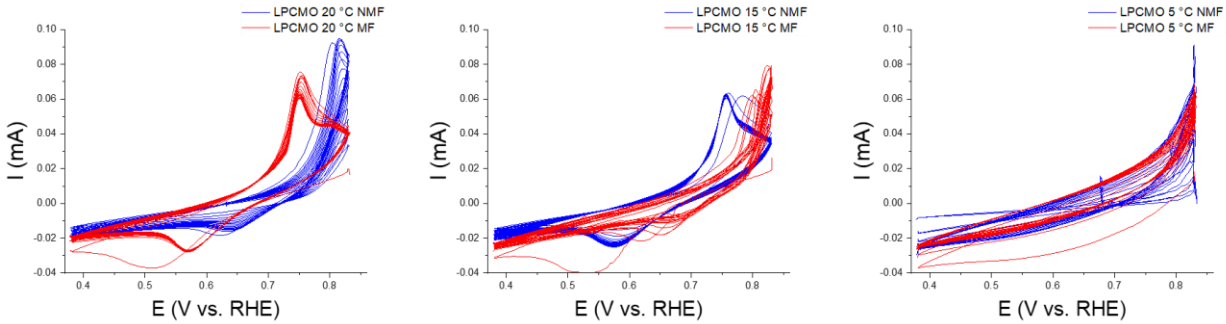

Appendix 4. Cyclovoltammetry cycles of LPCMO microelectrode at 20 °C, 15 °C and 5°C in O_2-saturated 4 M KOH.

$La_{0.7}Sr_{0.3}MnO_3$ electrochemical measurements-raw data

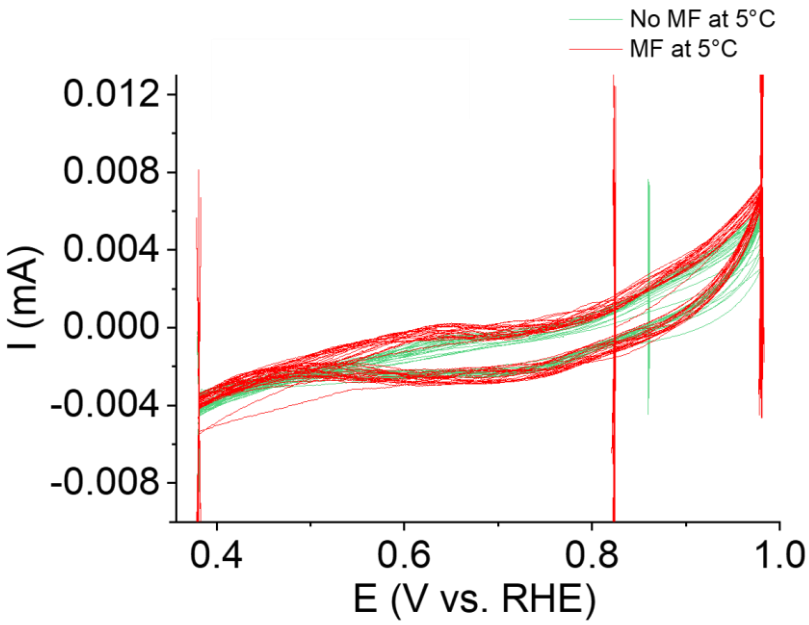

Appendix 5. Cyclovoltammograms of empty microelectrode at 5 °C in O_2-saturated 0.1 M KOH without magnetic field (green) and with magnetic field (red).

Appendix 5 shows that empty microelectrode are not affected by the magnetic field while conducting ORR.

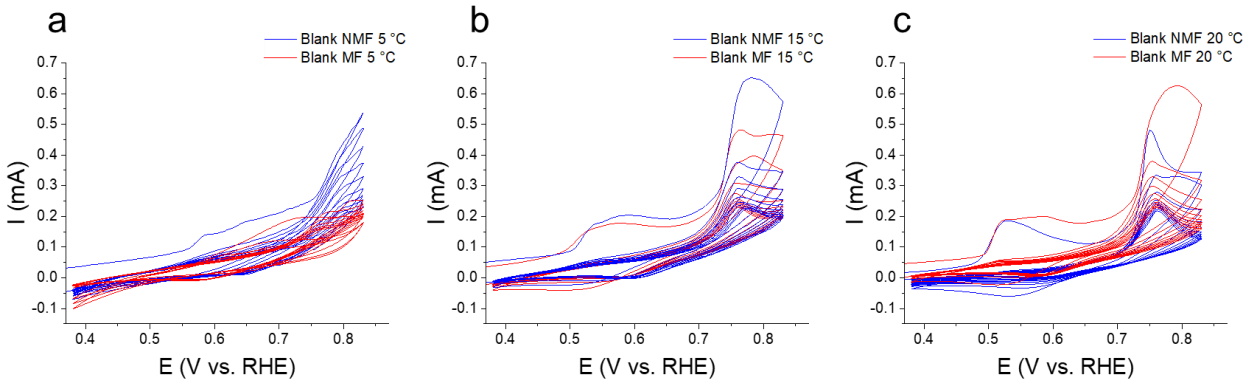

Appendix 6. Cyclovoltammograms of empty microelectrodes at (a) 5 °C, (b) 15 °C and (c) 20 °C in O_2-saturated 4 M KOH without magnetic field (blue) and with magnetic field (red).

The CVs in **Appendix 6** were obtained by using microelectrodes in 4 M KOH without electrocatalysts loading. The oxidation waves observed with and without magnetic field at 0.7-0.8 (V vs. RHE) are ascribed to the oxidation of the copper wire of the microelectrodes.

All cycles of the previously shown cyclovoltammograms can be found in the following appendix.

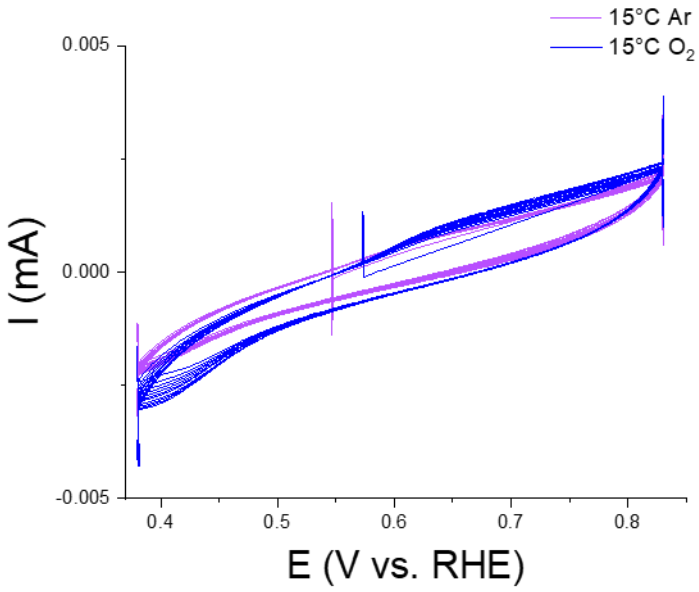

Appendix 7. Cyclovoltammetry cycles obtained after cycling 15 times a LSMO microelectrode at 15°C in KOH 0.1M saturated first by Ar (purple) then by O_2 (blue).

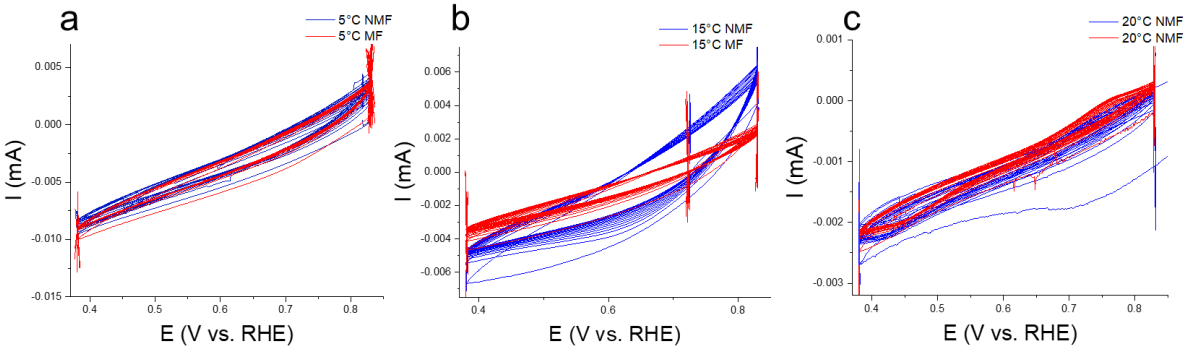

Appendix 8. Cyclovoltammetry cycles obtained after cycling 15 times a LSMO microelectrode at (a) 5 °C, (b) 15 °C and (c) 20 °C in O_2-saturated 0.1M KOH and purified, without magnetic field (NFM-blue) and under magnetic field (MF-red).

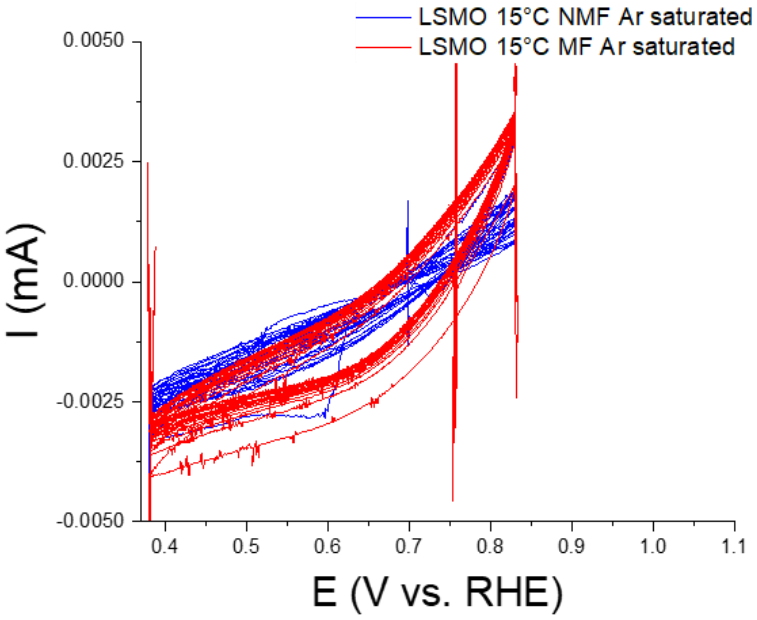

Appendix 9. Cyclovoltammetry cycles obtained after cycling 15 times a LSMO microelectrode at 15 °C in Ar-saturated 0.1M KOH, without magnetic field (NMF-blue) and with a magnetic field of 1T (MF-red).

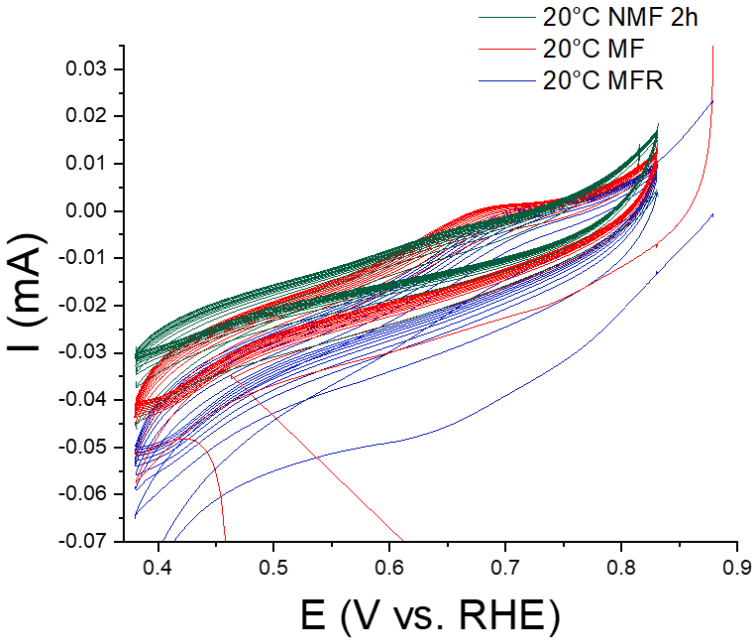

Appendix 10. cyclovoltammetry cycles obtained after cycling 15 times a LSMO microelectrode at 20 °C in O_2-saturated 0.1M KOH, without magnetic field (NMF-blue), magnetic field (MF-red) and without magnetic field after 2 hours resting (NMFR-green).

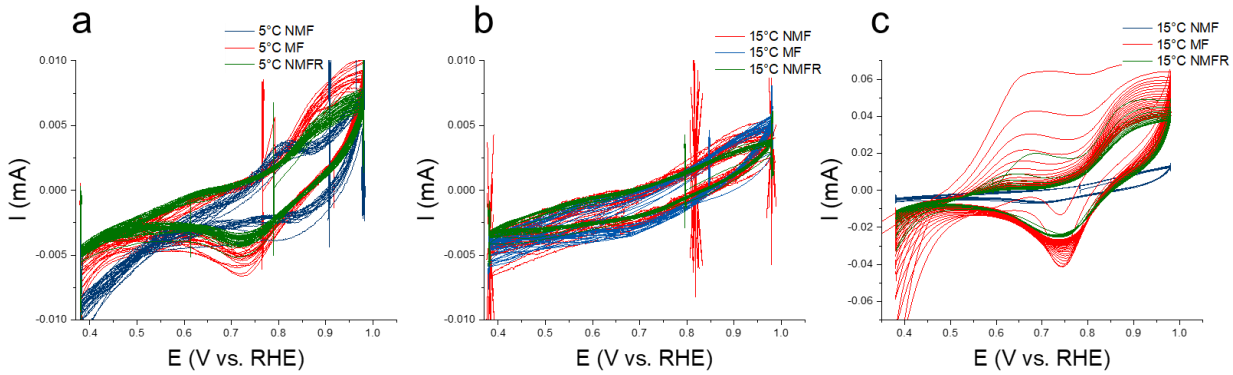

Appendix 11. Cyclovoltammetry cycles obtained after cycling 15 times a LSMO microelectrodes at a) 5°C b-c) 15°C in O_2-saturated 0.1M KOH without magnetic field (NMF-Blue), magnetic field (MF-red) and without magnetic field after 1h relaxation (NMFR-green). (b) and (c) correspond to two different microelectrodes.

Crochet Guillaume – Thèse de doctorat - 2021

Abstract:

Perovskite oxides are studied since decades for their magnetic properties and more recently for their electrocatalytic properties in the context of energy conversion, within fuel cells and water electrolyzers, for instance. In this work, we have aimed at developing new perovskite-based electrocatalysts operating in aqueous media, by targeting nanoscaled perovskites able to interact with their environment and then to exhibit stimuli-dependent electrocatalytic properties. This work was then at crossroad between the development of synthesis strategies, the design of nanomaterials, the study of their electrochemical and magnetic properties and of their interplay. We first describe a synthesis strategy suitable to reach quaternary perovskites by using molten salt media, innovative microwave heating and precise tuning of the oxo-basicity of the melt. We then address the relationship between magnetism and electrocatalysis on the case study of $La_{0.7}Sr_{0.3}MnO_3$ nanocrystals derived from molten salts, through the development of an original set-up enabling triggering changes in the oxygen reduction reaction electrocatalysis by application of a magnetic field. We especially stress out the important of the composition of the electrolyte for magnetic enhancement of electrocatalytic activity. Finally, we address another way to trigger "externally" the properties of nanoscaled perovskite oxides, by developing a synthesis of doped perovskite nanocrystals and then by triggering under reducing conditions the exsolution of the metal cation dopants as metal nanoparticles at the surface of perovskite nanocrystal hosts, for the first time.

Keywords: [manganese perovskites, oxides, nanoparticles, synthesis in molten salts, oxygen reduction reaction, electrocatalysis, exsolution, magnetism]

Résumé :

Les oxydes pérovskites sont étudiés depuis des décennies pour leurs propriétés magnétiques et plus récemment leurs propriétés électrocatalytiques dans le contexte de la conversion d'énergie, dans les piles à combustibles et les électrolyseurs, notamment. Dans ce travail, nous avons cherché à développer de nouveaux électrocatalyseurs à base de pérovskites opérant en milieu aqueux, en visant des objets nanométriques capables d'interagir avec leur environnement et donc de présenter des propriétés électrocatalytiques dépendant de stimuli extérieurs. Ce travail se situe donc au croisement entre le développement de méthodes de synthèse, la conception de nanomatériaux, l'étude de leurs propriétés électrochimiques et magnétiques et du lien entre ces propriétés. En premier lieu, nous décrivons une stratégie de synthèse adaptée à l'obtention de pérovskites quaternaires en utilisant des milieux sels fondus, un chauffage micro-ondes innovant, et l'ajustement des conditions d'oxo-basicité du milieu fondu. Nous étudions ensuite la relation entre magnétisme et électrocatalyse dans le cas d'école de nanocristaux de $La_{0.7}Sr_{0.3}MnO_3$ obtenus en sels fondus. Nous développons ainsi un dispositive permettant de déclencher des changements de propriétés électrocatalytiques pour la reduction du dioxygène en appliquant un champ magnétique. Nous mettons en avant l'importance de la composition de l'électrolyte pour l'amélioration des propriétés électrocatalytiques sous champ magnétique. Enfin, nous abordons un autre moyen de modifier par un stimulus les propriétés de pérovskites nanométriques, en développant la synthèse de nanocristaux de perovskite dopées avec divers métaux, puis en déclenchant pour la première fois l'exsolution de ces cations métalliques à la surface des matrices perovskites nanométriques.

Mots clés : [pérovskite manganèse, oxyde, nanoparticules, synthèse en sels fondus, réaction de réduction de l'oxygène, exsolution, magnétisme]